Magic-angle Spinning NMR of paramagnetic metalloproteins

Andrea Bertarello

Numéro National de Thèse : 2018LYSEN004

THÈSE de DOCTORAT DE L'UNIVERSITÉ DE LYON
opérée par
L'École Normale Supérieure de Lyon

École Doctorale N° 206
École Doctorale de Chimie (Chimie, Procédés, Environnement)

Spécialité de doctorat : Chimie
Discipline : Chimie

Soutenue publiquement le 06/04/2018, par :
Andrea BERTARELLO

Magic-angle spinning NMR of paramagnetic metalloproteins

RMN en rotation à l'angle magique de métalloprotéines paramagnétiques

---

Devant le jury composé de :

Henrike HEISE	Professeure, Heinrich-Heine-Universität, Düsseldorf	Rapporteure
Paola TURANO	Professeure, Università di Firenze – CERM, Firenze	Rapporteure
Bruno GUIGLIARELLI	Professeur, Aix – Marseille Université, Marseille	Examinateur
Christophe MORELL	Professeur, Université Lyon 1, Lyon	Examinateur
Hartmut OSCHKINAT	Professeur, Leibniz – FMP, Berlin	Examinateur
Roberta PIERATTELLI	Professeure, Università di Firenze – CERM, Firenze	Examinatrice
Tatyana POLENOVA	Professeure, University of Delaware, Newark	Examinatrice
Guido PINTACUDA	Directeur de Recherche, CNRS, Lyon	Directeur de thèse

Acknowledgements

First of all, let me thank Henrike Heise and Paola Turano who agreed to be the two referees of this dissertation, and all the jury members for accepting to be part of the jury.

I arrived in Lyon in November 2013. It was foggy, rainy, and I was living in a small studio directly facing at the CNRS "delegation", which is notoriously not an example of a wonderful building. My English was horrible, my French covered with dust, I did not know a single person in the city, every time someone tried to explain me something related to NMR my eyes were invaded by a mixture of fear and desperation. I seriously wondered what was I doing with my life.

When writing these words, it is cold and snowy, and from my desk I can see my former studio. So not a big improvement concerning weather and landscape. But in more than four years I think my English and French improved a lot, I met many wonderful people, and from time to time a more intelligent expression is observable in my eyes when discussing NMR.

I can say that during these four and half years of PhD I grew a lot, probably as a scientist, surely as a person. And if doubts accompanied me for a while during the first years, now I say no regrets, I did the right thing. And this is also thanks to people that I met and with whom I spent my time during this adventure. With whom I shared positive, and also negative, experiences, which nevertheless brought me where I am now.

So let me thank first of all my supervisor, Guido. Thanks for having given me this brilliant opportunity, for your contagious enthusiasm in doing things, and your constant support as a scientist and as a person. Even if sometimes I could not understand you, and I was upset at you. Even if sometimes you could not understand me, and you were upset at me. I am really glad you were my supervisor during these years. And I apologize for all the times I could have done better.

Many thanks also to Lyndon Emsley. For having supported my application as a PhD student, and for the positive encouragement I always received from you when we discussed together. Many thanks to Anne Lesage and Moreno Lelli, for all the, sometimes very long, but always fruitful scientific discussions.

I would like also to thank all the collaborators I had the opportunity to work with, in particular Roberta Pierattelli, Claudio Luchinat, Giacomo Parigi, Isabella Felli, Leonardo

Gonnelli and Enrico Ravera from Florence, Martin Kaupp and Vladimir Pelmenschikov from Berlin, and Tatyana Polenova from Newark.

A special mention is also needed for all the people I met within the PNMR network. I am really glad of having been part of this wonderful project that allowed us to travel all around Europe, and having very interesting meetings with the most influent scientists of our fields. In particular, I really want to thank all the people I met during my secondments at GIOTTO Biotech and CERM in Florence, and at the Technische Universität in Berlin. For this, I should also thank the European Union for funding this project, and express my full support to the Europeanist vision, especially now that different political groups in all Europe are fighting against that with increasing consensus among people.

And now all the people in the CRMN. I really need to thank first of all Cécile G., for her big help at work, and for being a unique friend (even if I am really upset that you will not make it for my defense), for having fought together against "sangliers", for the improvised hiking on Sunday afternoons, for the mutual support in looking for a decent mojito in the city. And thanks to Kevin, who has been and is a wonderful colleague and friend, always ready to help me when I need. Really thanks. Thanks to Ladislav and Tobias, especially for their precious support in some difficult parts of my project. To Daniela, for the all the long conversations and for having encouraged me in difficult moments. And also to all other friends and colleagues from the CRMN and the ISA: Tanguy, Marta, Diane, Hugh, Andy, Judith, Elodie, Pierrick, Debora, Jan, Loren, Kristaps, Cécile C., Lenaïc, Dorothea, Alicia, David, Houda, Manhal, Audrey, Ribal, Agnès. I apologize for not writing a special sentence for any of you, but really thanks for all the moments spent together, and for everything I learnt from you.

I want also to thank all the people I met during these years outside the working environment, in Lyon and not only, in particular Fany, Sonia, Diego, Christophe, Julien, Karolina, July, Andrea, Cecilia, Roland, Louis, Marco, Stefano. En particulier, je veux remercier Nadine et la troupe de la Vieille Branche, avec lesquels j'ai partagé le plaisir du théâtre, pour toutes les aventures qu'on a vécu ensemble sur scène, les weekends de répétions intensives, l'émotion et l'adrénaline de la récitation. Vraiment, merci ! Aussi, je veux remercier le Cosy Corner (en particulier Isa et Justine), The Beers, Le Biéristan, le Boston Tavern, pour m'avoir aidé dans les moments de difficulté (finalement, ils devraient aussi me remercier pour mon soutien économique), Ursula et la machine café du labo.

Infine (I am sorry for the reader, but at this point I need to switch to my native language), voglio ringraziare gli amici di una vita e le persone della mia famiglia, per il loro supporto,

per essermi stati accanto durante questi anni di lontananza, per aver tollerato le mie (lunghe) sparizioni, per ogni cosa… Siete in molti, elencarvi tutti sarebbe difficile. Ivan, Nicole, Michele, Sara, Eleonora, Mattia. I miei nonni, zii e cugini. Mia sorella, Virginia. Mio papà. Mia mamma. Non servono parole, e non esisterebbero per ringraziarvi abbastanza.

Abstract

Most of our understanding of metalloproteins derives from atomic or molecular structures obtained from diffraction methods on single crystal samples. However, not all proteins are amenable for diffraction studies, and even when a highly-resolved structure is available, often the nature of the metal ion, its coordination geometry or its oxidation state are not determined.

The aim of the present thesis is the investigation of structural properties of metal sites in paramagnetic metalloproteins by Magic-Angle Spinning Nuclear Magnetic Resonance (MAS NMR). MAS NMR is a powerful technique for the investigation of biological systems, and may represent a direct probe of the structure at the active site of paramagnetic metalloproteins. However, it suffers from limited sensitivity and resolution when applied to nuclei close to a paramagnetic center.

In this thesis, we address these limitations by developing NMR methods based on ultra-fast (60-111 kHz) MAS rates. A "toolkit" of suitably designed pulse sequences is built for the detection and the assignment of nuclei in close proximity of a paramagnetic center. State-of-the-art computational techniques are also employed to convert the experimental data into structural restraints for obtaining atomic-resolution geometries of active sites. We benchmark this approach with the study of Fe, Cu and Co sites in two microcrystalline proteins, and we also provide preliminary data on a non-diffracting divalent metal ion transporter in lipid membranes.

We anticipate that the techniques described here are an essential tool to elucidate many currently unanswered questions about structure and function of metal sites in structural biology.

Résumé

À ce jour, nos connaissances sur les propriétés structurales et fonctionnelles des métalloprotéines sont essentiellement basées sur des structures résolues par des méthodes de diffraction à rayons X appliquées à des échantillons monocristallins. Cependant, certaines protéines ne cristallisent pas ou cristallisent sous une forme qui n'est pas manipulable ou compatible avec des techniques des diffraction, et même si une structure à très haute résolution est disponible, la nature de l'ion métallique, sa géométrie de coordination ou son état d'oxydation restent souvent indéterminés.

La Résonance Magnétique Nucléaire en rotation à l'angle magique (MAS NMR) est une technique très performante pour l'étude de systèmes biologiques et pour la caractérisation de la structure du site actif des métalloprotéines paramagnétiques, mais son application à l'analyse des noyaux proches d'un site paramagnétique est limitée à cause de la résolution et de la sensibilité faibles.

L'objectif de cette thèse a été de développer des méthodes RMN basées sur des hautes fréquences de rotation (60-111 kHz MAS) pour faire face à ces problématiques. Un répertoire de séquences d'impulsion pour la détection et l'attribution des noyaux à proximité d'un centre paramagnétique est proposé, et à l'aide de méthodes de calculs de pointes, les données expérimentales acquises sont converties en contraintes structurales afin de déterminer la géométrie du site actif à l'échelle atomique. Cette approche est validée avec l'analyse de sites actifs de deux protéines microcristallines contenants différents ions paramagnétiques : Fe, Cu et Co. Ensuite, des données préliminaires sur un transporteur membranaire d'ions métalliques divalents non cristalline sont présentées.

Les méthodes analytiques présentées ici constituent un ensemble d'outils indispensable pour l'élucidation de la structure et la fonction des sites métalliques de systèmes macromoléculaires biologiques.

Table of contents

Introduction

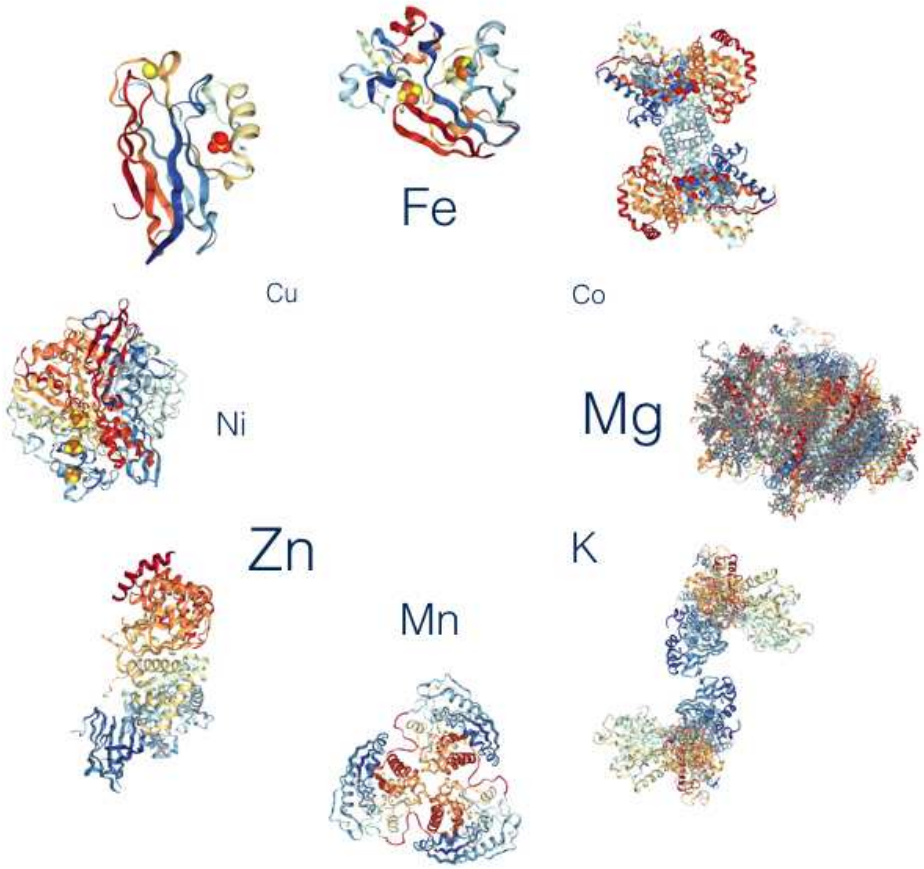

Metal ions play an important role in a large variety of biochemical and cellular events, are present at the active sites of many enzymes that are at the core of cell function, and are the key constituents of complex architectures. As such, they have a tremendous impact on many fields within life sciences, medicine, and industry. It is estimated that one half of the known proteins contain metal ions, and that between one quarter to one third require metal ions to perform their function.[1-3] Making an exhaustive list of all the metal ions and their specific roles in metalloproteins would be impossible, but one should just think at the importance for example of iron, involved among others in oxygen transport in hemoglobin,[4] or copper, which is essential for electron transfer processes mediated by plastocyanins[5] during photosynthesis, or nickel, which plays a pivotal role in catalyzing hydrogen reversible oxidation in many bacteria.[6] Moreover, the importance of metal ions in the cell chemistry requires a fine control of their concentration in the cellular environment, and many proteins are involved in the regulation of metals homeostasis, like to cite one ferritin, which regulates the iron availability and storage in the cell.[7-8] Therefore, the understanding of structure and functioning of metalloproteins is fundamental in order to unveil the mechanisms related to the biological processes they are involved in.

Most of our understanding of chemistry and biology of metal ions in metalloproteins derives from atomic or molecular structures obtained over the past 50 years by diffraction methods on single crystal samples. These atomic level structures are essential to understand the fine details of biochemical processes in cells, and to find efficient drugs. The reactions carried out by these proteins are often much more efficient than industrial processes, and provide synthetic chemists with models for new, improved sites. A precise understanding of the structure of a metal active site thus enables structure-activity relationships to be deduced and allows for the rapid and intelligent development of catalysts with specific properties. However, for many biological systems, single crystals large enough for X-ray diffraction cannot be easily obtained, and the problem of structure elucidation is largely unsolved. For example, although crystallization methods have made progress in the area of membrane proteins, there is still a paucity of solved transmembrane protein structures, which occupy less than one percent of the protein data bank despite their high occurrence in the biological world.

Even when high-resolution structures are available, often the nature of the metal ion, its oxidation state, or its coordination geometry are not determined. Moreover the most

interesting aspects of metallic activity are caused by the electronic structure at the active site, which unfortunately can only be inferred indirectly from the coordinates of the constituent atoms. Today EXAFS, vibrational (IR and Raman), and electronic (UV-Vis) spectroscopies are used to characterize metal centers in crystalline and non-crystalline systems, but the information they provide is indirect or again requires highly crystalline/ordered solids. EPR (often in conjunction with diffraction methods and other spectroscopies) is an elegant technique for the determination of the electronic structure and the validation of the environment of certain meal ions (see for example recent work on nitrate reductase from *E. coli* in native lipid membranes),[9] but lacks site-specific assignment of the electron-nuclear couplings. As a result, the details of many essential biochemical processes are thus still unknown, highlighting a need for a reliable and efficient method for the structure determination of metal centers inside metalloenzymes and transporters. Light in this area will enable a leap forward in the biological understanding, and will simultaneously suggest new solutions to the foremost problems in biological chemistry today.

Magic-angle spinning (MAS) NMR has recently proved to be a new tool for the characterization in microcrystalline, poorly crystalline or disordered protein samples, such as protein aggregates or membrane-embedded systems, complementing liquid-state NMR, X-ray crystallography and electron microscopy. Following seminal work on microcrystalline proteins,[10-11] examples demonstrating the utility of MAS include studies of prion fibrils,[12-17] poly-disperse full-size heat shock complexes,[18] intact viral capsids,[19] bacterial virulence factors,[20-21] membrane channels and membrane-bound drug targets at an atomic level in lipid bilayers.[22-28] Approaches for sample preparation, sequence-specific resonance assignment, and collection of conformational restraints have been designed to calculate three-dimensional structures, and to determine their dynamics.[29-31] However, these procedures are still far from routine, and most proteins for which a complete structure determination has been reported are in the 5-10 kDa range (with notable exceptions[28, 32-33]).

Additionally, and most interestingly, **NMR represents a direct probe of electronic structure at the active site of metal ions, especially in the case of paramagnetic centers originating from unpaired electrons that are intrinsic features of many transition metal ions**.[34]

While the impact of MAS NMR on paramagnetic molecules and materials is hampered by the high occurrence of paramagnetic centers with large magnetic moments and magnetic anisotropies, causing large bulk susceptibility effects and resulting in signals with extremely large shifts and shift anisotropies and very short relaxation rates, a number of pioneering studies have shown that paramagnetic solid-state NMR can disclose unique information in the study of the atomic-level properties of metal complexes, clusters and magnetic frameworks, constituting essential steps for the design of new catalysts and new materials.[34-41] Recently, the field of paramagnetic solid-state NMR has been revolutionized by the development of fast MAS probes (>30 kHz) with large *rf* powers. Under fast MAS, sensitivity and resolution experience a spectacular enhancement as compared to slower rates, allowing efficient detection of previously unobservable nuclei in highly paramagnetic substances.[38, 42-43] This is especially true for the growing area of electrode materials for batteries, and in particular lithium-ion rechargeable batteries,[44-45] where paramagnetic NMR can nowadays be used to determine the metal oxidation state and how it changes on battery cycling (critical to understand the redox processes that occur in these systems), and to elucidate the local environment and the fate of the Li ions (directly involved in battery function).

The object of this PhD thesis is to explore the potential of paramagnetic effects in the field of biomolecular MAS NMR, *particularly to provide a detailed geometric and electronic structure of the active sites* of metalloproteins. In few recent examples, paramagnetic techniques under fast MAS have been used on paramagnetic proteins with success, increasing the amount of achievable information with respect to solution studies,[46] notably because of the absence of Curie relaxation.[47] However, so far these investigations have concerned only portions of the target proteins, and "blind zones" close to the metal center have so far remained elusive in these approaches.

During my PhD, I have worked at removing the main bottlenecks preventing the application of MAS NMR for the characterization of active sites in (large) paramagnetic metalloproteins. This has required a two-fold activity.

On one hand, I have contributed to a novel approach relying on very fast MAS and high magnetic fields, which is today able to increase the size limit of protein targets that can be fully characterized with high resolution and sensitivity by MAS NMR. These progresses allow today for rapid "fingerprinting" of samples and permit extensive, robust and

expeditious assignment of small-to-medium sized proteins in different aggregation states, and the determination of structurally important parameters such as dihedral angles, inter-nuclear proximities, and local dynamics.[32, 48-50]

On the other hand, I have been active in the development of a new methodology to remove the main barriers to spectral acquisition from paramagnetic nuclei and to extend the amount of information that can be extracted from them. This consisted in building a "toolkit" of suitably designed pulse sequences for the detection and the assignment of nuclei in close proximity of a paramagnetic center. State-of-the-art computational techniques were also employed to convert the experimental data into structural restraints for obtaining atomic-resolution geometries of active sites. This approach has been benchmarked with the study of iron, copper, and cobalt sites in two microcrystalline proteins. Moreover, preliminary data on a non-diffracting divalent metal ion transporter in lipid membranes are provided as well.

In order to set the scene for the investigations carried out in this work, **Chapter I** provides an overview of the main aspects related to MAS NMR of paramagnetic systems, pointing out the main differences, advantages and challenges, compared to solution NMR. An overview of the most recent landmark MAS NMR studies of paramagnetic metalloproteins is also provided.

Chapter II describes the recent advances in MAS NMR at ultrafast (60-111 kHz) rates. A set of techniques employing ^{1}H-detection for the backbone and side chain assignment of proteins, as well as for determination of structural restraints, is developed.[51-54] Examples of applicability of these experiments to two paramagnetic microcrystalline metalloproteins are shown.

Chapter III concerns the descriptions of a set of experimental techniques, originally developed for the study of highly paramagnetic materials, for the detection and assignment of nuclei in close proximity of a paramagnetic center in a metalloproteins that are not observable with MAS NMR techniques conventionally employed for the characterization of proteins. A brief description of the theoretical basis for the prediction of paramagnetic NMR (PNMR) shifts is provided as well. The techniques presented in this chapter represent the "toolkit" used in the following chapters.

In **Chapter IV** we show how the techniques presented in Chapter III can be used to detect and characterize resonances from ^{1}H and ^{13}C nuclei experiencing large contact shifts in close proximity of an iron-sulfur cluster in the high potential iron-sulfur protein I from the extremophile *E. halophila*. By targeting this protein in a crystalline environment, we show that MAS NMR can capture two different conformations found in the asymmetric unit.[55]

Chapter V represents the heart of this thesis. Here, the techniques described in Chapter III are used to detect, characterize, and assign resonances from ^{1}H, ^{15}N, and ^{13}C nuclei from the ligands of a cobalt(II) center in the metalloenzyme superoxide-dismutase. We show that at 100 kHz MAS, it is possible to go beyond the detectability limit observed in solution NMR. Large hyperfine NMR shifts can be measured, assigned, and converted into structural restraints for obtaining an ultra-high-resolution geometry of active sites.

In **Chapter VI**, we target a 5x42-kDa metal ion channel, CorA, which is involved in the Mg^{2+} and Co^{2+} homeostasis regulation of the extremophile *T. maritima*. We perform an extensive work in order to optimize the sample preparation for MAS NMR. We show that the experiments described in Chapter II, combined with high fields and MAS rates, allow acquiring high-quality NMR data for backbone assignment of the protein in the Mg^{2+}-loaded form. We also provide first preliminary characterization of the dynamics underlying the gating process of *Tm*CorA.

(1) Thomson, A. J.; Gray, H. B., Bio-inorganic chemistry. *Curr. Opin. Chem. Biol.* **1998,** *2*, 155-158.
(2) *Handbook on metalloproteins*. Bertini, I.; Sigel, A.; Sigel, H. Eds.; Marcel Dekker, Inc.: New York, 2001.
(3) *Handbook of metalloproteins*. Messerschmidt, A. Eds.; Wiley Interscience: New York, 2001.
(4) Perutz, M. F.; Rossmann, M. G.; Cullis, A. F.; Muirhead, H.; Will, G.; North, A. C. T., Structure of hæmoglobin: a three-dimensional fourier synthesis at 5.5-Å. resolution, obtained by x-ray analysis. *Nature* **1960,** *185*, 416.
(5) Colman, P. M.; Freeman, H. C.; Guss, J. M.; Murata, M.; Norris, V. A.; Ramshaw, J. A. M.; Venkatappa, M. P., X-ray crystal structure analysis of plastocyanin at 2.7 Å resolution. *Nature* **1978,** *272*, 319.
(6) Lubitz, W.; Ogata, H.; Rüdiger, O.; Reijerse, E., Hydrogenases. *Chem. Rev.* **2014,** *114*, 4081-4148.
(7) Theil, E. C., Ferritin: structure, gene regulation, and cellular function in animals, plants, and microorganisms. *Annu. Rev. Biochem* **1987,** *56*, 289-315.
(8) Turano, P.; Lalli, D.; Felli, I. C.; Theil, E. C.; Bertini, I., NMR reveals pathway for ferric mineral precursors to the central cavity of ferritin. *Proc. Natl. Acad. Sci. U. S. A.* **2010,** *107*, 545-550.
(9) Arias-Cartin, R.; Grimaldi, S.; Pommier, J.; Lanciano, P.; Schaefer, C.; Arnoux, P.; Giordano, G.; Guigliarelli, B.; Magalon, A., Cardiolipin-based respiratory complex activation in bacteria. *Proc. Natl. Acad. Sci. U.S.A.* **2011,** *108*, 7781-7786.
(10) Castellani, F.; van Rossum, B.; Diehl, A.; Schubert, M.; Rehbein, K.; Oschkinat, H., Structure of a protein determined by solid-state magic-angle-spinning NMR spectroscopy. *Nature* **2002,** *420*, 98-102.
(11) Rienstra, C. M.; Tucker-Kellogg, L.; Jaroniec, C. P.; Hohwy, M.; Reif, B.; McMahon, M. T.; Tidor, B.; Lozano-Perez, T.; Griffin, R. G., De novo determination of peptide structure with solid-state magic-angle spinning NMR spectroscopy. *Proc. Natl. Acad. Sci. U.S.A.* **2002,** *99*, 10260-10265.
(12) Wasmer, C.; Lange, A.; Van Melckebeke, H.; Siemer, A. B.; Riek, R.; Meier, B. H., Amyloid fibrils of the HET-s(218-289) prion form a beta solenoid with a triangular hydrophobic core. *Science* **2008,** *319*, 1523-1526.
(13) Lu, J. X.; Qiang, W.; Yau, W. M.; Schwieters, C. D.; Meredith, S. C.; Tycko, R., Molecular structure of beta-amyloid fibrils in Alzheimer's disease brain tissue. *Cell* **2013,** *154*, 1257-1268.
(14) Xiao, Y. L.; Ma, B. Y.; McElheny, D.; Parthasarathy, S.; Long, F.; Hoshi, M.; Nussinov, R.; Ishii, Y., A beta(1-42) fibril structure illuminates self-recognition and replication of amyloid in Alzheimer's disease. *Nat. Struct. Mol. Biol.* **2015,** *22*, 499-U97.
(15) Walti, M. A.; Ravotti, F.; Arai, H.; Glabe, C. G.; Wall, J. S.; Bockmann, A.; Guntert, P.; Meier, B. H.; Riek, R., Atomic-resolution structure of a disease-relevant A beta(1-42) amyloid fibril. *Proc. Natl. Acad. Sci. U. S. A.* **2016,** *113*, E4976-E4984.
(16) Colvin, M. T.; Silvers, R.; Ni, Q. Z.; Can, T. V.; Sergeyev, I.; Rosay, M.; Donovan, K. J.; Michael, B.; Wall, J.; Linse, S.; Griffin, R. G., Atomic resolution structure of monomorphic A beta(42) amyloid fibrils. *J. Am. Chem. Soc.* **2016,** *138*, 9663-9674.
(17) Gremer, L.; Schölzel, D.; Schenk, C.; Reinartz, E.; Labahn, J.; Ravelli, R. B. G.; Tusche, M.; Lopez-Iglesias, C.; Hoyer, W.; Heise, H.; Willbold, D.; Schröder, G. F., Fibril structure of amyloid-β(1–42) by cryo–electron microscopy. *Science* **2017,** *358*, 116-119.

(18) Jehle, S.; Rajagopal, P.; Bardiaux, B.; Markovic, S.; Kuhne, R.; Stout, J. R.; Higman, V. A.; Klevit, R. E.; van Rossum, B. J.; Oschkinat, H., Solid-state NMR and SAXS studies provide a structural basis for the activation of alphaB-crystallin oligomers. *Nat. Struct. Mol. Biol.* **2010,** *17*, 1037-1042.

(19) Han, Y.; Ahn, J.; Concel, J.; Byeon, I. J. L.; Gronenborn, A. M.; Yang, J.; Polenova, T., Solid-state NMR studies of HIV-1 capsid protein assemblies. *J. Am. Chem. Soc.* **2010,** *132*, 1976-1987.

(20) Shahid, S. A.; Bardiaux, B.; Franks, W. T.; Krabben, L.; Habeck, M.; van Rossum, B. J.; Linke, D., Membrane-protein structure determination by solid-state NMR spectroscopy of microcrystals. *Nat. Methods* **2012,** *9*, 1212-U119.

(21) Loquet, A.; Sgourakis, N. G.; Gupta, R.; Giller, K.; Riedel, D.; Goosmann, C.; Griesinger, C.; Kolbe, M.; Baker, D.; Becker, S.; Lange, A., Atomic model of the type III secretion system needle. *Nature* **2012,** *486*, 276-279.

(22) Lange, A.; Giller, K.; Hornig, S.; Martin-Eauclaire, M. F.; Pongs, O.; Becker, S.; Baldus, M., Toxin-induced conformational changes in a potassium channel revealed by solid-state NMR. *Nature* **2006,** *440*, 959-962.

(23) Sharma, M.; Yi, M.; Dong, H.; Qin, H.; Peterson, E.; Busath, D. D.; Zhou, H. X.; Cross, T. A., Insight into the mechanism of the influenza A proton channel from a structure in a lipid bilayer. *Science* **2010,** *330*, 509-12.

(24) Cady, S. D.; Schmidt-Rohr, K.; Wang, J.; Soto, C. S.; Degrado, W. F.; Hong, M., Structure of the amantadine binding site of influenza M2 proton channels in lipid bilayers. *Nature* **2010,** *463*, 689-692.

(25) Ullrich, S. J.; Glaubitz, C., Perspectives in Enzymology of Membrane Proteins by Solid-State NMR. *Acc. Chem. Res.* **2013,** *46*, 2164-2171.

(26) Tang, M.; Comellas, G.; Rienstra, C. M., Advanced Solid-State NMR Approaches for Structure Determination of Membrane Proteins and Amyloid Fibrils. *Acc. Chem. Res.* **2013**.

(27) Wylie, B. J.; Bhate, M. P.; McDermott, A. E., Transmembrane allosteric coupling of gates in a potassium channel. *Proc. Natl. Acad. Sci. USA* **2014,** *111*, 185-190.

(28) Retel, J. S.; Nieuwkoop, A. J.; Hiller, M.; Higman, V. A.; Barbet-Massin, E.; Stanek, J.; Andreas, L. B.; Franks, W. T.; van Rossum, B. J.; Vinothkumar, K. R.; Handel, L.; de Palma, G. G.; Bardiaux, B.; Pintacuda, G.; Emsley, L.; Kuhlbrandt, W.; Oschkinat, H., Structure of outer membrane protein G in lipid bilayers. *Nat. Commun.* **2017,** *8*, 2073.

(29) Andronesi, O. C.; Becker, S.; Seidel, K.; Heise, H.; Young, H. S.; Baldus, M., Determination of membrane protein structure and dynamics by magic-angle-spinning solid-state NMR spectroscopy. *J. Am. Chem. Soc.* **2005,** *127*, 12965-12974.

(30) Lewandowski, J. R., Advances in solid-state relaxation methodology for probing site-specific protein dynamics. *Acc. Chem. Res.* **2013,** *46*, 2018-2027.

(31) Andreas, L. B.; Le Marchand, T.; Jaudzems, K.; Pintacuda, G., High-resolution proton-detected NMR of proteins at very fast MAS. *J. Magn. Reson.* **2015,** *253*, 36-49.

(32) Marchetti, A.; Jehle, S.; Felletti, M.; Knight, M. J.; Wang, Y.; Xu, Z. Q.; Park, A. Y.; Otting, G.; Lesage, A.; Emsley, L.; Dixon, N. E.; Pintacuda, G., Backbone assignment of fully protonated solid proteins by ^{1}H detection and ultrafast Magic-Angle-Spinning NMR Spectroscopy. *Angew. Chem. Int. Ed.* **2012,** *51*, 10756-10759.

(33) Wang, S.; Munro, R. A.; Shi, L.; Kawamura, I.; Okitsu, T.; Wada, A.; Kim, S.-Y.; Jung, K.-H.; Brown, L. S.; Ladizhansky, V., Solid-state NMR spectroscopy structure determination of a lipid-embedded heptahelical membrane protein. *Nat. Methods* **2013,** *10*, 1007-1012.

(34) Pintacuda, G.; Kervern, G., Paramagnetic solid-state magic-angle spinning NMR spectroscopy. *Modern NMR Methodology* **2013,** *335*, 157-200.
(35) Flambard, A.; Kohler, F. H.; Lescouezec, R., Revisiting Prussian Blue Analogues with Solid-State MAS NMR Spectroscopy: Spin Density and Local Structure in [Cd(3){Fe(CN)(6)}(2)]15 H(2)O. *Angew. Chem. Int. Ed. Engl.* **2009,** *48*, 1673-1676.
(36) Flambard, A.; Kohler, F. H.; Lescouezec, R.; Revel, B., Probing Spin Density and Local Structure in the Prussian Blue Analogues CsCd[Fe/Co(CN)(6)]0.5H(2)O and Cd(3)[Fe/Co(CN)(6)](2) 15H(2)O with Solid-State MAS NMR Spectroscopy. *Chemistry-a European Journal* **2011,** *17*, 11567-11575.
(37) Huang, W.; Schopfer, M.; Zhang, C.; Howell, R. C.; Todaro, L.; Gee, B. A.; Francesconi, L. C.; Polenova, T., ^{31}P magic angle spinning NMR spectroscopy of paramagnetic rare-earth-substituted Keggin and Wells-Dawson solids. *J. Am. Chem. Soc.* **2008,** *130*, 481-490.
(38) Kervern, G.; Pintacuda, G.; Zhang, Y.; Oldfield, E.; Roukoss, C.; Kuntz, E.; Herdtweck, E.; Basset, J. M.; Cadars, S.; Lesage, A.; Coperet, C.; Emsley, L., Solid-state NMR of a paramagnetic DIAD-Fe-II catalyst: Sensitivity, resolution enhancement, and structure-based assignments. *J. Am. Chem. Soc.* **2006,** *128*, 13545-13552.
(39) Heise, H.; Kohler, F. H.; Xie, X. L., Solid-state NMR spectroscopy of paramagnetic metallocenes. *J. Magn. Reson.* **2001,** *150*, 198-206.
(40) Heise, H.; Kohler, F. H.; Mota, F.; Novoa, J. J.; Veciana, J., Determination of the spin distribution in nitronylnitroxides by solid-state H-1, H-2, and C-13 NMR spectroscopy. *J. Am. Chem. Soc.* **1999,** *121*, 9659-9667.
(41) Clayton, A. N.; Dobson, C. M.; Grey, C. P., High-resolution C-13 MAS NMR-spectra of paramagnetic lanthanide complexes. *J. Chem. Soc. - Chem. Commun.* **1990,** 72-74.
(42) Ishii, Y.; Wickramasinghe, N. P.; Chimon, S., A new approach in 1D and 2D C-13 high-resolution solid-state NMR spectroscopy of paramagnetic organometallic complexes by very fast magic-angle spinning. *J. Am. Chem. Soc.* **2003,** *125*, 3438-3439.
(43) Wickramasinghe, N. P.; Shaibat, M.; Ishii, Y., Enhanced sensitivity and resolution in H-1 solid-state NMR spectroscopy of paramagnetic complexes under very fast magic angle spinning. *J. Am. Chem. Soc.* **2005,** *127*, 5796-5797.
(44) Grey, C. P.; Dupre, N., NMR studies of cathode materials for lithium-ion rechargeable batteries. *Chem. Rev.* **2004,** *109*, 4493-4512.
(45) Clement, R. J.; Pell, A. J.; Middlemiss, D. S.; Strobridge, F. C.; Miller, J. K.; Whittingham, M. S.; Emsley, L.; Grey, C. P.; Pintacuda, G., Spin-transfer pathways in paramagnetic lithium transition-metal phosphates from combined broadband isotropic solid-state MAS NMR spectroscopy and DFT calculations. *J. Am. Chem. Soc.* **2012,** *134*, 17178-17185.
(46) Bertini, I.; Emsley, L.; Lelli, M.; Luchinat, C.; Mao, J.; Pintacuda, G., Ultrafast MAS solid-state NMR permits extensive ^{13}C and ^{1}H detection in paramagnetic metalloproteins. *J. Am. Chem. Soc.* **2010,** *132*, 5558-5559.
(47) Kervern, G.; Steuernagel, S.; Engelke, F.; Pintacuda, G.; Emsley, L., Absence of Curie relaxation in paramagnetic solids yields long H-1 coherence lifetimes. *J. Am. Chem. Soc.* **2007,** *129*, 14118-14119.
(48) Knight, M. J.; Webber, A. L.; Pell, A. J.; Guerry, P.; Barbet-Massin, E.; Bertini, I.; Felli, I. C.; Gonnelli, L.; Pierattelli, R.; Emsley, L.; Lesage, A.; Herrmann, T.; Pintacuda, G., Fast resonance assignment and fold determination of human superoxide dismutase by high-resolution proton-detected solid-state MAS NMR spectroscopy. *Angew. Chem. Int. Ed. Engl.* **2011,** *50*, 11697-11701.

(49) Knight, M. J.; Pell, A. J.; Bertini, I.; Felli, I. C.; Gonnelli, L.; Pierattelli, R.; Herrmann, T.; Emsley, L.; Pintacuda, G., Structure and backbone dynamics of a microcrystalline metalloprotein by solid-state NMR. *Proc. Natl. Acad. Sci. U.S.A.* **2012,** *109*, 11095-11100.

(50) Knight, M. J.; Felli, I. C.; Pierattelli, R.; Bertini, I.; Emsley, L.; Herrmann, T.; Pintacuda, G., Rapid measurement of pseudocontact shifts in metalloproteins by proton-detected solid-state NMR spectroscopy. *J. Am. Chem. Soc.* **2012,** *134*, 14730-14733.

(51) Andreas, L. B.; Jaudzems, K.; Stanek, J.; Lalli, D.; Bertarello, A.; Le Marchand, T.; Cala-De Paepe, D.; Kotelovica, S.; Akopjana, I.; Knott, B.; Wegner, S.; Engelke, F.; Lesage, A.; Emsley, L.; Tars, K.; Herrmann, T.; Pintacuda, G., Structure of fully protonated proteins by proton-detected magic-angle spinning NMR. *Proc. Natl. Acad. Sci. U.S.A.* **2016,** *113*, 9187-9192.

(52) Stanek, J.; Andreas, L. B.; Jaudzems, K.; Cala, D.; Lalli, D.; Bertarello, A.; Schubeis, T.; Akopjana, I.; Kotelovica, S.; Tars, K.; Pica, A.; Leone, S.; Picone, D.; Xu, Z. Q.; Dixon, N. E.; Martinez, D.; Berbon, M.; El Mammeri, N.; Noubhani, A.; Saupe, S.; Habenstein, B.; Loquet, A.; Pintacuda, G., NMR spectroscopic assignment of backbone and side-chain protons in fully protonated proteins: microcrystals, sedimented assemblies, and amyloid fibrils. *Angew. Chem. Int. Ed.* **2016,** *55*, 1-6.

(53) Andreas, L. B.; Stanek, J.; Le Marchand, T.; Bertarello, A.; Cala-De Paepe, D.; Lalli, D.; Krejcikova, M.; Doyen, C.; Oster, C.; Knott, B.; Wegner, S.; Engelke, F.; Felli, I. C.; Pierattelli, R.; Dixon, N. E.; Emsley, L.; Herrmann, T.; Pintacuda, G., Protein residue linking in a single spectrum for magic-angle spinning NMR assignment. *J. Biomol. NMR* **2015,** *62*, 253-261.

(54) Barbet-Massin, E.; Pell, A. J.; Retel, J. S.; Andreas, L. B.; Jaudzems, K.; Franks, W. T.; Nieuwkoop, A. J.; Hiller, M.; Higman, V.; Guerry, P.; Bertarello, A.; Knight, M. J.; Felletti, M.; Le Marchand, T.; Kotelovica, S.; Akopjana, I.; Tars, K.; Stoppini, M.; Bellotti, V.; Bolognesi, M.; Ricagno, S.; Chou, J. J.; Griffin, R. G.; Oschkinat, H.; Lesage, A.; Emsley, L.; Herrmann, T.; Pintacuda, G., Rapid proton-detected NMR assignment for proteins with fast magic angle spinning. *J. Am. Chem. Soc.* **2014,** *136*, 12489-12497.

(55) Bertarello, A.; Schubeis, T.; Fuccio, C.; Ravera, E.; Fragai, M.; Parigi, G.; Emsley, L.; Pintacuda, G.; Luchinat, C., Paramagnetic properties of a crystalline iron-sulfur protein by magic-angle spinning NMR spectroscopy. *Inorg. Chem.* **2017,** *56*, 6624-6629.

Chapter I.

Solid-state NMR of paramagnetic proteins: an overview

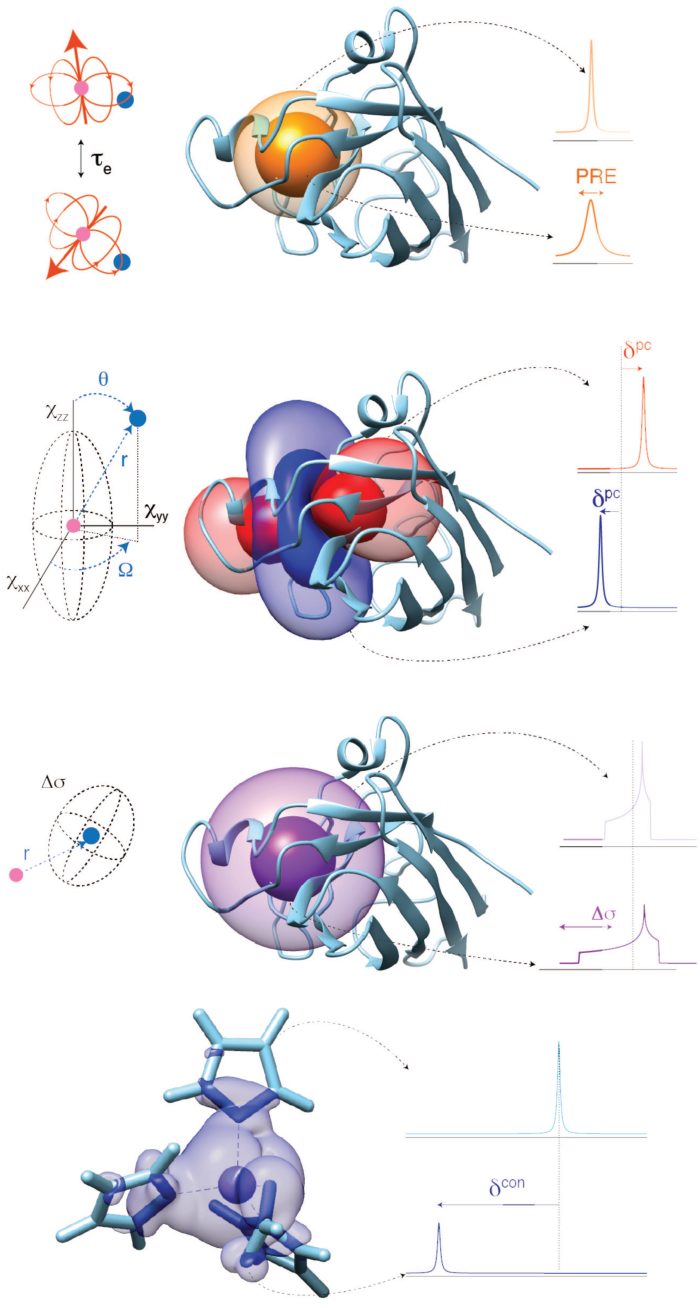

I.1 Introduction

The presence of unpaired electrons in a solid sample perturbs the NMR spectrum of the surrounding nuclei, notably affecting their shift tensors and their relaxation rates. Paramagnetic effects depend in a well-defined manner on the electronic and structural configuration of the metal center, and can provide useful information on the electronic structure of the metal center. Moreover paramagnetic effects can be used as structural restraints and differently from diamagnetic data they provide long-range information. At the same time, these effects can complicate the acquisition and the interpretation of NMR spectra.

In this chapter these effects will be summarized, showing how the presence of paramagnetic ions alters the NMR properties in the solid state, providing in parallel some case studies from the recent literature that highlight the increasing potential of solid-state NMR for the characterization of paramagnetic proteins. While the mechanisms generating these effects are substantially identical to the solution case, some important differences arise from the fact that rotational diffusion is abolished in the solid state.

I.2 Paramagnetic effects and solid-state NMR

I.2.1 Spins and magnetic moments

In quantum mechanics particles possessing a spin are associated with a magnetic dipole moment. In the case of a nucleus its magnetic dipole moment is proportional to its nuclear spin, $\boldsymbol{I}$:

$$\boldsymbol{\mu}_I = \hbar\gamma_I \boldsymbol{I} \tag{I.1}$$

where $\hbar$ is the reduced Planck's constant and γ_I is nuclear gyromagnetic ratio, whose value depends on the nuclear species.

In an analogous way the magnetic dipole moment of an electron can be expressed as:

$$\boldsymbol{\mu}_S = \hbar\gamma_S \boldsymbol{S} \tag{I.2}$$

where in this case γ_S is the electron gyromagnetic ratio and $\boldsymbol{S}$ the electron spin. However it is common practice, especially among the EPR community, to use the alternative, but totally equivalent expression:

$$\boldsymbol{\mu}_S = -\mu_{\mathrm{B}} g_{\mathrm{e}} \boldsymbol{S} \tag{I.3}$$

where g_e is the free-electron *g*-factor and μ_B is the Bohr magneton, which can be calculated from the elementary charge *e* and the rest mass of the electron, m_e:

$$\mu_B = \frac{e\hbar}{2m_e} \tag{I.4}$$

I.2.2 The hyperfine coupling (HFC)

Unpaired electrons interact with nuclear spins, by virtue of their magnetic dipole moments. The hyperfine Hamiltonian, describing this interaction, is given by the following expression:

$$\mathcal{H}^{HF} = \boldsymbol{S} \cdot \boldsymbol{A} \cdot \boldsymbol{I} \tag{I.5}$$

where $\boldsymbol{A}$ is the hyperfine tensor, describing the interaction between the electronic and the nuclear spins. Neglecting relativistic effects, the latter can be separated into two components:

$$\boldsymbol{A} = A^{FC} \cdot \mathbf{1} + \boldsymbol{A}^{SD} \tag{I.6}$$

where the first term represents the Fermi contact (or simply contact) interaction, and the second one the dipolar interaction between the dipole moment of the electronic distribution and the nuclear spins.

The contact term arises from the interaction of the component of the electron spin directly delocalized onto a nuclear spin, the contact constant being directly proportional to the total electron spin density $\rho^{\alpha-\beta}(\mathbf{0})$ at the nucleus of interest:

$$A^{FC} = \frac{\mu_0}{3S}\hbar\gamma_I g_e \mu_B \rho^{\alpha-\beta}(\mathbf{0}) \tag{I.7}$$

where *S* is the electron spin number and μ_0 the vacuum permittivity. The contact term is therefore essentially a through-bond interaction, whose effect is dominant in nuclei that are few bonds apart from the metal center and decreases rapidly moving away from the paramagnetic center.

The dipolar term represents instead a through-space interaction, and it becomes the dominant contribution at larger distances from the metal center. The components of the $\boldsymbol{A}^{SD}$ tensor are given by the following expression, assuming point-dipole approximation (PDA, which can be done at a sufficient distance from the paramagnetic center):

$$A_{ij}^{SD} = \frac{\mu_0 \mu_B g_e \hbar \gamma_I}{4\pi r^3}\left(3u_i u_j - \delta_{ij}\right) \tag{I.8}$$

where *i* and *j* are equal to *x*, *y*, or *z*, u_i and u_j are the unit vectors along *i* and *j*, respectively, δ_{ij} is the Kronecker delta, and r^3 the electron-nucleus distance.

I.2.3 Paramagnetic relaxation enhancement (PRE)

The stochastic variation of the dipolar coupling between the nuclear and the electronic moments induces fluctuating fields at the nuclear sites, providing additional relaxation pathways (the so called Solomon mechanism). In solution this mechanism is dependent on a correlation time, which is a function of both the electronic and the rotational correlation times. As the rotational diffusion is abolished in solids, the Solomon mechanism is mainly determined by electron relaxation, which occurs with correlation times usually in the range 10^{-7} – 10^{-13} s. Assuming PDA and neglecting spin-orbit effects, the paramagnetic contribution to the nuclear longitudinal (R_1^{dip}) and transversal (R_2^{dip}) relaxation rates are thus given by:

$$R_1^{\mathrm{dip}} = \frac{2}{15}\left(\frac{\mu_0}{4\pi}\right)^2 \frac{\gamma_I^2 g_e^2 \mu_B^2 S(S+1)}{r^6}\left(\frac{7\tau_{e2}}{1+\omega_S^2\tau_{e2}^2} + \frac{3\tau_{e1}}{1+\omega_I^2\tau_{e1}^2}\right) \quad \text{(I.9)}$$

$$R_2^{\mathrm{dip}} = \frac{1}{15}\left(\frac{\mu_0}{4\pi}\right)^2 \frac{\gamma_I^2 g_e^2 \mu_B^2 S(S+1)}{r^6}\left(4\tau_{e1} + \frac{13\tau_{e2}}{1+\omega_S^2\tau_{e2}^2} + \frac{3\tau_{e1}}{1+\omega_I^2\tau_{e1}^2}\right) \quad \text{(I.10)}$$

where τ_{e2} and τ_{e1} are the transverse and longitudinal electron correlation times, and ω_I and ω_S the nuclear and the electronic Larmor frequencies, respectively.

On account of the large electron magnetic moment, the PREs occur over larger distances than those characteristic of internuclear interactions (Figure 1A). The inverse 6th power dependence of these effects upon the nucleus-electron distance causes considerable broadening in the NMR lines, especially in the close proximity of the metal center, and shortens coherence lifetimes. Differently from solution, in solids a paramagnetic center also has the consequence of increasing the R_1 rate across the entire sample via a spin-diffusion mechanism, particularly for protons due to their relatively high gyromagnetic ratio. Since the recycle delay in an NMR experiment is predominantly governed by the recovery of ^{1}H magnetization, enhanced ^{1}H R_1 can be used to shorten the recycle delay and thereby allow more scans to be conducted per unit of time without loss of signal intensity due to saturation of the ^{1}H spins.

In the close proximity of the paramagnetic center, also the relaxation due to the contact term becomes relevant (the so called Bloembergen mechanism). The paramagnetic contribution to the nuclear longitudinal (R_1^{con}) and transversal (R_2^{con}) relaxation rates are given by:

$$R_1^{\mathrm{con}} = \frac{2}{3}S(S+1)\left(\frac{A^{\mathrm{FC}}}{\hbar}\right)\frac{\tau_{e2}}{\omega_S^2\tau_{e2}^2} \quad \text{(I.11)}$$

$$R_2^{\mathrm{con}} = \frac{1}{3}S(S+1)\left(\frac{A^{\mathrm{FC}}}{\hbar}\right)\left(\tau_{\mathrm{e1}} + \frac{\tau_{\mathrm{e2}}}{\omega_S^2\tau_{\mathrm{e2}}^2}\right) \qquad \text{(I.12)}$$

Typical values of τ_{e}, R^{con}, and R^{dip} for some selected paramagnetic ions are reported in Table 1.

Ion	Configuration	S	τ_{e} (s^{-1})	R_1^{con} (s^{-1})	R_2^{con} (s^{-1})	R_1^{dip} (s^{-1})	R_2^{dip} (s^{-1})
Mn^{II}	$3d^5$	5/2	10^{-8}	0.002	900000	200	400000
Fe^{III} HS	$3d^5$	5/2	$10^{-9} - 10^{-11}$	0.02 – 2	900 – 90000	500 – 2000	600 – 40000
Fe^{II} HS	$3d^6$ 4 coord.[a]	2	10^{-11}	2	1000	400	400
Co^{II} HS	$3d^7$ 4 coord.[b]	3/2	10^{-11}	2	1000	200	200
Co^{II} HS	$3d^7$ 5-6 coord.[c]	3/2	$10^{-12} - 10^{-13}$	4 – 20	20 – 500	7 – 100	7 – 100
Cu^{II}	$3d^9$	1/2	10^{-9}	0.007-0.04	> 200000	40 – 180	3000 – 15000

Table 1. Typical values of τ_{e}, ^{1}H R^{con} and ^{1}H R^{dip} for some selected paramagnetic ions in rigid solids, assuming $\tau_{\mathrm{e2}} = \tau_{\mathrm{e1}} = \tau_{\mathrm{e}}$, A^{FC} = 4.47 MHz, r = 5 Å, $\omega_I \cdot 2\pi$ = 800 MHz (B_0 = 18.8 T). [a] Found e.g. in tetrahedral and some square planar complexes. [b] For tetrahedral complexes, square-planar complexes are usually low spin. [c] Found e.g. in octahedral, trigonal bipyramidal, square pyramidal complexes. Adapted from reference 1.

I.2.4 The Curie spin and the paramagnetic shift anisotropy

Electronic relaxation times are short on the NMR timescale. As a consequence, the spectral properties of the nuclei are uniquely determined by the coupling to a "relaxed" electronic magnetic moment, thermally averaged over the different Zeeman states, which is referred to as the "Curie spin" $\langle S_z \rangle$. The effects of this static moment upon the NMR spectrum are often conveniently treated by means of the magnetic susceptibility χ, which is the average electronic moment $\langle \boldsymbol{\mu_S} \rangle$ of the electronic spin in a magnetic field B_0:

$$\langle \boldsymbol{\mu_S} \rangle = \frac{\chi}{\mu_0}\boldsymbol{B_0} \qquad \text{(I.13)}$$

In the high temperature approximation (i.e. when the difference between the electron Zeeman states is small compared to kT, where k is the Boltzmann's constant and T the absolute temperature), and in the absence of spin-orbit effects, the magnetic moment $\langle \boldsymbol{\mu_S} \rangle$ associated to the Curie spin is given by:

$$\langle \boldsymbol{\mu_S} \rangle = \frac{g_{\mathrm{e}}^2\mu_{\mathrm{B}}^2 S(S+1)}{3kT}\boldsymbol{B_0} \qquad \text{(I.14)}$$

This yields an average magnetic susceptibility per molecule χ:

$$\chi = \mu_0 \frac{g_{\mathrm{e}}^2\mu_{\mathrm{B}}^2 S(S+1)}{3kT} \qquad \text{(I.15)}$$

The through-space dipolar field of the Curie spin interacts with the surrounding nuclei producing a shielding, $\Delta\sigma^{\mathrm{dip}}$, which is equivalent to a traceless diamagnetic chemical shift anisotropy (CSA), but with an inverse 3rd power distance dependence (Figure 1B). In the absence of spin-orbit effects and assuming PDA this contribution is given by:

$$\Delta\sigma^{\mathrm{dip}} = \frac{\chi}{\hbar\gamma_I r^3} = \frac{\mu_0}{\hbar\gamma_I r^3}\frac{g_e^2\mu_B^2 S(S+1)}{3kT}B_0 \qquad \text{(I.16)}$$

In solution this interaction is averaged in incoherent manner by the rotational diffusion, providing an additional source of relaxation, known as the Curie relaxation.[2] On the contrary, in the solid state, all possible molecular orientations contribute simultaneously to the NMR spectrum. The observed dipolar shift frequency for each single orientation is given by:

$$\omega^{\mathrm{dip}}(\Theta) = \omega_{\mathrm{iso}} - \frac{1}{2}\omega_0\Delta\sigma^{\mathrm{dip}}(3\cos^2\Theta - 1) \qquad \text{(I.17)}$$

where $\omega_{\mathrm{iso}}$is the isotropic chemical shift frequency, $\Delta\sigma^{\mathrm{dip}}$ the shielding anisotropy, and Θ is the polar angle between the orientation of the external magnetic field and the principal axis of the shielding tensor. The signal acquired on a powder sample is the sum of the signals corresponding to all such orientations, leading to a "powder pattern" lineshape (the typical shape of such powder pattern, as well as surfaces of constant $\Delta\sigma$ around a metal center are sketched in Figure 1B).

I.2.5 The hyperfine shift

As in solution, the interaction of the Curie spin with the nuclear spins gives rise to an additional contribution to the observed shift, the hyperfine shift. This is commonly decomposed into the contact shift, arising from the interaction of the nuclear spin with the electron spin density directly delocalized onto the nucleus, and the pseudo-contact shift (PCS), arising from the dipolar interaction between the electron and nuclear spins.

In systems where spin-orbit effects and zero-field splitting are absent or negligible, only the contact term in the hyperfine Hamiltonian contributes to the observed shift (Figure 1D), which is given by the following expression:

$$\delta^{\mathrm{con}} = \frac{A^{\mathrm{FC}}}{\hbar}\frac{g_e\mu_B S(S+1)}{3\gamma_I kT} \qquad \text{(I.18)}$$

The equivalent expression as a function of the magnetic susceptibility is given by

$$\delta^{\mathrm{con}} = \frac{\rho^{\alpha-\beta}(\mathbf{0})}{3S}\chi \qquad \text{(I.19)}$$

When the spin-orbit effects are significant, the magnetic susceptibility becomes orientation dependent, and it is properly described by a tensor with rank-0 and rank-2 components

$$\boldsymbol{\chi} = \chi^{\mathrm{iso}} \cdot \mathbf{1} + \boldsymbol{\Delta\chi} \tag{I.20}$$

In this case, the electron-nucleus dipolar interaction no longer averages to zero over all orientations, but acquires an isotropic component (not removable by MAS) in addition to the anisotropic one described in the previous paragraph. Such isotropic component is the pseudo-contact shift (PCS), which in the principal axis system (PAS) of the χ tensor is given by (Figure 1C):

$$\delta^{\mathrm{pc}} = \frac{1}{12\pi r^3}\left[\Delta\chi_{\mathrm{ax}}(3\cos^2\theta - 1) + \frac{3}{2}\Delta\chi_{\mathrm{rh}}\sin^2\theta\cos 2\Omega\right] \tag{I.21}$$

where θ and Ω are the polar angles connecting the electron-nucleus vector to the PAS of the $\boldsymbol{\chi}$ tensor, r is the electron-nucleus distance, and $\Delta\chi_{ax}$ and $\Delta\chi_{rh}$ are the axial and rhombic component of the $\boldsymbol{\Delta\chi}$ tensor, given by

$$\Delta\chi_{\mathrm{ax}} = \chi_{\mathrm{zz}} - \frac{\chi_{\mathrm{xx}}+\chi_{\mathrm{yy}}}{2} \tag{I.22}$$

$$\Delta\chi_{\mathrm{rh}} = \chi_{\mathrm{xx}} - \chi_{\mathrm{yy}} \tag{I.23}$$

This expression for PCS is derived assuming PDA, while a more complex treatment taking into account the electron delocalization becomes necessary only for nuclei in close proximity of the metal center.[3-4] Note also that the anisotropy of the magnetic susceptibility provides additional components to the observed shift anisotropy.

Contact and pseudo-contact shifts are both contributing to the observed shift of a given nucleus. Contact shifts are predominant for nuclei that are only few bonds away from a paramagnetic center, while the pseudo-contact shifts are active over longer distances, and thus become dominant for nuclei far away from the metal center.

The PCSs observable in solids and described by the equation above are identical to those observable in a paramagnetic molecule in solution. However in solids, as a consequence of the shorter intermolecular distances occurring in microcrystals, sediments or 2D-crystalline lipidic preparations, nuclear spins are simultaneously affected by multiple paramagnetic centers in neighboring proteins, and the observed PCSs are thus usually a superposition of intramolecular and intermolecular effects.[5-6]

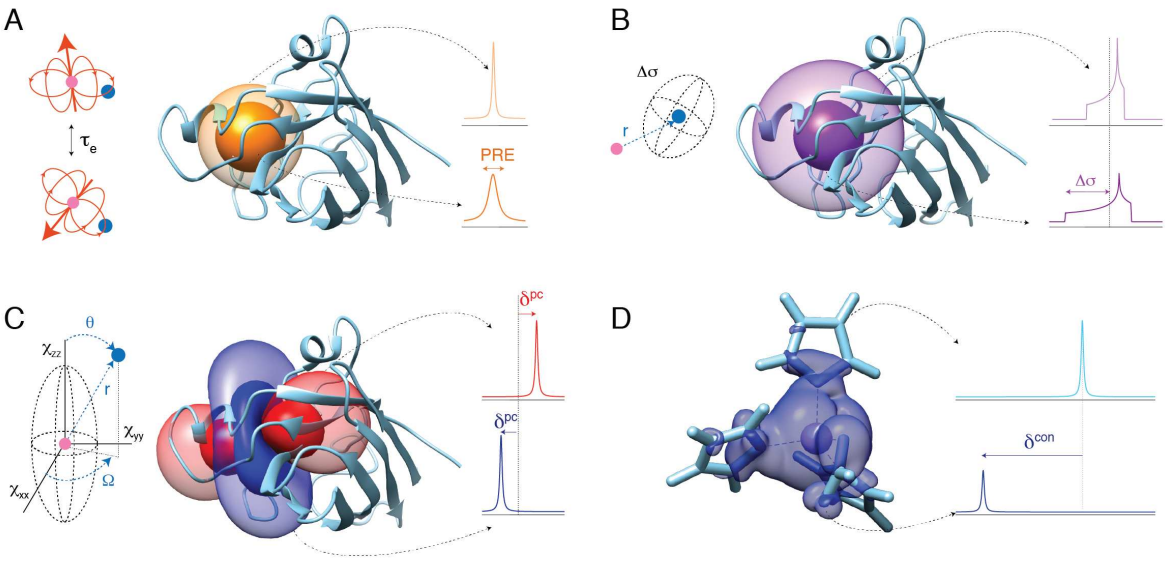

Figure 1. Schematic representation of the paramagnetic effects, and of their spatial dependence, shown on isosurfaces of the protein Co^{II}-SOD,[7-8] containing a paramagnetic Co^{II} ion[7-8]: A) PRE, B) Dipolar shift anisotropy, C) PCS, with the definition of the PAS of the χ tensor. PCS isosurfaces are calculated using the FANTEN software.[9] D) Representation of the distribution of the spin-density around the Co^{II} center in Co^{II}-SOD (present work), and schematic representation of its effect on the contact shift.

I.2.6 Coupled systems

Many systems of interest contain more than one metal ion with unpaired electrons. When the electronic magnetic moments of each metal ion interact with each other, magnetic coupling occurs. The interaction is usually described by the exchange Heisenberg Hamiltonian, which in the case of a dimer is given by:

$$\mathcal{H}^{J} = J\boldsymbol{S_1}\cdot\boldsymbol{S_2} \tag{I.24}$$

where J is a constant, $\boldsymbol{S_1}$ is a spin operator which operates only on the functions of one metal (M_1), and $\boldsymbol{S_2}$ is a spin operator which operates only on the functions of the second metal (M_2). New spin levels are established, with a total spin number S' varying in unitary steps from $S_1 + S_2$ to $|S_1 - S_2|$, and energy levels E_i given by:

$$E_i = \frac{J}{2}\,S_i'(S_i'+1) \tag{I.25}$$

If J is positive (antiferromagnetic coupling), the ground state is given by $|S_1 - S_2|$, while if J is negative (ferromagnetic coupling), the ground state is given by $S_1 + S_2$.

It can be shown that in a magnetically coupled dimer, the contact shift of a nucleus can be expressed by the sum of two contributions $\delta^{\mathrm{con}} = \delta_1^{\mathrm{con}} + \delta_2^{\mathrm{con}}$, with

$$\delta_1^{\mathrm{con}} = \frac{A_1^{\mathrm{FC}}}{\hbar}\frac{g_e\mu_B}{3\gamma_I kT}\frac{\sum_i C_{i1}S_i'(S_i'+1)(2S_i'+1)\exp(-E_i/kT)}{\sum_i(2S_i'+1)\exp(-E_i/kT)} \tag{I.26}$$

$$\delta_2^{\mathrm{con}} = \frac{A_2^{\mathrm{FC}}}{\hbar}\frac{g_e\mu_B}{3\gamma_I kT}\frac{\sum_i C_{i2}S_i'(S_i'+1)(2S_i'+1)\exp(-E_i/kT)}{\sum_i(2S_i'+1)\exp(-E_i/kT)} \quad \text{(I.27)}$$

In this expression A_1^{FC} and A_2^{FC} represent the Fermi-contact coupling constants that would be measured if only M_1 or M_2 were present, respectively, and can be estimated from the monomeric analogs. Therefore the total shift is given by the sum of two contributions associated to the single metal ions. The constants C_{i1} and C_{i2} depend on S_i', S_1 and S_2, and characteristic values from many examples can be found in literature.[10] It can be shown that in the high-temperature limit ($E_i \ll kT$), the two contributions reduce to the expressions given for an isolated ion, therefore in this case the total shift is simply given by the sum of the contact shifts that a nucleus would experience in the presence of only M_1 and M_2, respectively.

In the case of heterodimers, magnetic coupling influences the electronic relaxation rates of each single ion. Qualitatively, three regimes can be identified. Assuming that M_1 is the slower relaxing electronic spin, with an electron correlation time τ_{M1}, in the case of $J/\hbar < \tau_{M1}^{-1}$ no effect on the electron relaxation of the pair will take place. When $\tau_{M1}^{-1} < J/\hbar < \tau_{M2}^{-1}$, τ_{M1} progressively approaches τ_{M2} with increasing J. When $J/\hbar > \tau_{M2}^{-1}$, the Redfield limit is reached, and it is hard to make prediction on τ_{M1} and τ_{M2} values except for their becoming similar and closer to the shorter one.

One interesting aspect of magnetically coupled systems is observed when $|J| \geq kT$, in particular for antiferromagnetic coupling. In this situation, the magnetic moment associated with the larger spin is aligned with the external field, forcing the second spin in the opposite direction. As a result, nuclei coupled to the larger spin experience a stronger local magnetic field and positive shifts, while nuclei coupled to the smaller spin experience a weaker local magnetic field and negative shifts. With increasing temperature, the system tends to the high-temperature limit. Therefore, the shifts of the nuclei coupled to the larger spin decrease (referred as Curie-like behavior), while shifts of the nuclei coupled to the larger spin increase (hyper-Curie or pseudo-Curie behavior), as shown in Figure 2. It might be noticed that, for some range of temperatures, the shifts associated to the smaller spin move downfield and increase with increasing temperatures. This behavior is referred as anti-Curie behavior.

In the case of a polymetallic system, the Heisenberg Hamiltonian is be given by:

$$\mathcal{H}^J = \sum_{j\neq k} J_{jk}\boldsymbol{S_j}\cdot\boldsymbol{S_k} \quad \text{(I.28)}$$

summing all over the possible *j*-*k* pairs. The treatment of this kind of systems for the particular case of a Fe_4S_4 system will be briefly described in Chapter IV.

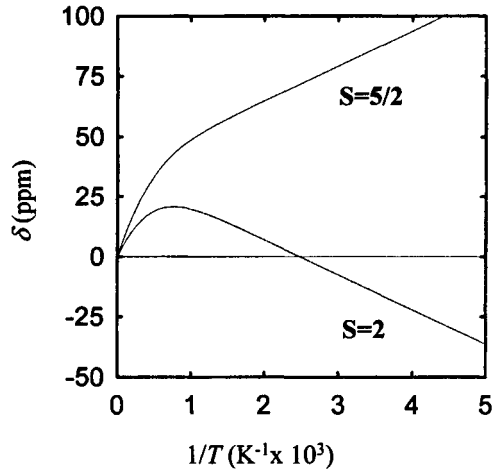

Figure 2. Predicted temperature dependence of the shifts of nuclei sensing either the $\boldsymbol{S} = \frac{5}{2}$ or the $\boldsymbol{S} = \mathbf{2}$ spin of an antiferromagnetically coupled pair with J = 300 cm^{-1}. Reproduced from reference 1.

I.3 Magic-angle spinning

As already mentioned, paramagnetic effects can complicate the NMR analysis of biomolecules in the solid-state. An additional complication arises from the fact that in solid-state NMR we usually deal with powder samples; that is, samples made of different crystallites with random orientations. The nuclear spin interactions affecting solid-state NMR, notably the chemical shielding and the dipole-dipole interaction (and the quadrupole coupling, whenever relevant) are anisotropic. While in solution the anisotropies are averaged out by the rapid molecular tumbling, in static samples this is not the case, and what we observe in a powder sample is an NMR spectrum made of very broad lines, the powder pattern, as all the different molecular orientations have different energies and thus give rise to different spectral frequencies. It is possible to average many of these interactions by the Magic-Angle Spinning (MAS), i.e. by spinning the sample at an angle of 54.7° with respect to the magnetic field. If the spinning frequency is larger (at least 3 or 4 times than the largest anisotropy), the anisotropies are completely averaged and the full isotropic spectrum is recovered. Otherwise the averaging will be incomplete and the spectrum will split in a set of spinning sidebands, set at the spinning rate apart, radiating out from the line at the isotropic chemical shift.[11]

I.3.1 Slow magic-angle spinning

NMR spectra properties are highly dependent on the particular spinning regime used.

In static samples, broadening renders proton and carbon spectra unobservable (Figure 3A).

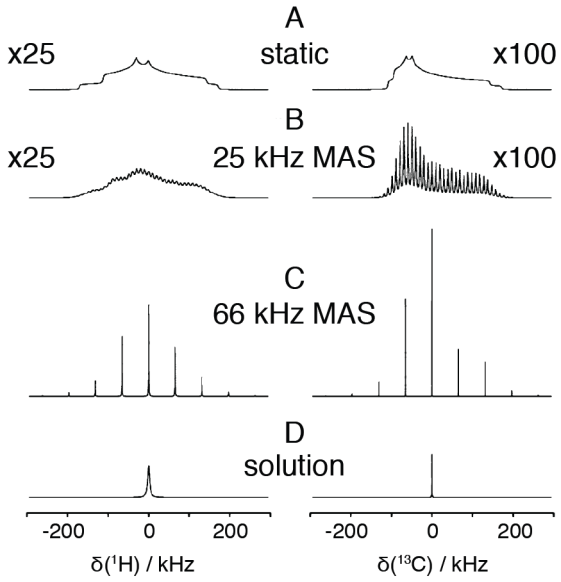

Figure 3. Simulated ^{1}H and ^{13}C spectra for a ^{1}H-^{13}C spins pair at 5 Å from a paramagnetic center (S = 3/2, τ_e = 10^{-11} s, which are typical values for a high-spin Co^{II} ion in a tetrahedral environment) at a different MAS regimes (A-C) and in solution (D). Reproduced from reference 12.

Under magic-angle spinning (MAS), at spinning rates below the powder linewidth, i.e. at rates which are not fast enough to average completely the second-rank paramagnetic interactions, the powder pattern splits in a set of sharp spinning sidebands. This effect is marginal for ^{1}H resonances, which remain severely broadened by the strong homonuclear dipolar interactions, but significantly narrows ^{13}C (or ^{15}N) lines (Figure 3B). Low-γ nuclei such as ^{15}N and ^{13}C are less susceptible to paramagnetic broadening than the ^{1}H nuclei primarily used in solution. Moreover the dipolar-based polarization transfers available in the solid state are more efficient than the scalar-based homonuclear and heteronuclear coherence transfer schemes employed in solution. Experiments based on ^{13}C detection were therefore key to the first extensive resonance assignments of paramagnetic proteins in the solid state, the human superoxide dismutase, containing a Cu^{II} paramagnetic center (Figure 4),[13] and the catalytic domain of the matrix metalloproteinase 12, containing a Co^{II} site.[5]

The superoxide dismutase (SOD) enzyme is a 32-kDa homodimer, which contains two metal sites in the catalytic cavity. In the biologically-relevant form, one site is occupied by Zn^{II}, while the other one is a type II copper center, which contains a Cu ion undergoing a change in oxidation state between Cu^{I} (diamagnetic) and Cu^{II} (paramagnetic) during the catalytic activity, as discussed also in Chapter V.[7, 14-15] The oxidized form is virtually inaccessible to established solution NMR studies due to the long τ_e electronic relaxation times of the Cu^{II} center, where protons closer then 12 Å to the metal center are broadened

beyond detection. ^{13}C-detected solid-state NMR at 15 kHz MAS was applied on microcrystalline Cu^{II},Zn^{II}-SOD. A first set of 2D or 3D heteronuclear ^{15}N-^{13}C correlations was acquired for backbone resonance assignment, connecting the shifts of $^{15}N^{H}$ nuclei with those of the neighboring ^{13}CO, $^{13}C^{\alpha}$ and $^{13}C^{\beta}$ nuclei.[16-18] 2D homonuclear ^{13}C-^{13}C (such as PDSD[19] or DARR[20]) correlations were used in parallel to identify ^{13}C spin-systems and measure internuclear distance restraints in the backbone and the side chains. Overall, resonances as close as 5 Å from the metal center were detected and assigned (Figure 4).[13]

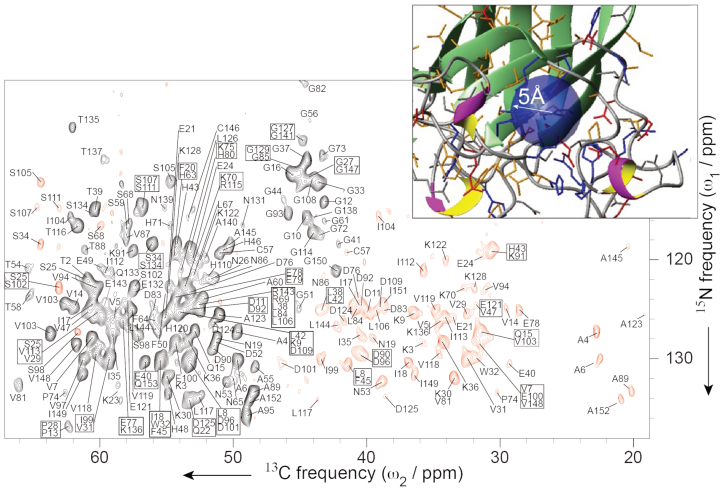

Figure 4. NCACB spectrum of Cu^{II},Zn^{II}-SOD acquired at 15 kHz MAS rate, and a pictorial representation of the NMR inaccessible region around the Cu ion . Reproduced from reference 13.

The catalytic domain of the matrix metalloproteinase 12 (MMP-12)[5, 21] is a 159 residue protein. The catalytic site contains a Zn^{II} ion that can be replaced by Co^{II}.[22] ^{13}C-^{13}C PDSD spectra acquired at 11.5 kHz MAS of both Zn^{II} and Co^{II} containing forms allowed an almost complete assignment of the protein in the two metallation states.[5] While correlations closer than 10 Å to the paramagnetic metal center escaped detection, the comparison of the shifts in the two forms yielded directly a large number of PCSs (Figure 5A). Interestingly, it was observed that most of the PCSs were in good agreement with PCSs measured in solution, but about 10% of them exhibit substantial deviation from the solution values. It appeared that these deviations were to ascribe to the additional contribution arising from the metal centers in surrounding proteins. This intermolecular contribution was estimated using an elegant paramagnetic dilution strategy, using two different schemes.[21] In the first case, paramagnetic ^{13}C, ^{15}N labeled Co^{II}-MMP-12 was diluted with diamagnetic unlabeled Zn^{II}-MMP-12: in this case, the observed PCSs arose only from the intramolecular contribution, the labeled protein being – on average – surrounded only by diamagnetic molecules. In the second scheme, ^{13}C, ^{15}N labeled Zn^{II}-MMP-12 was diluted with unlabeled Co^{II}-MMP-12, and thus the observed

PCSs arose only from intermolecular contribution of neighboring paramagnetic molecules (Figure 5B). It was found that a 33% dilution ratio represented the best compromise to maximize the sensitivity without significantly increasing the probability of having two adjacent labeled proteins.

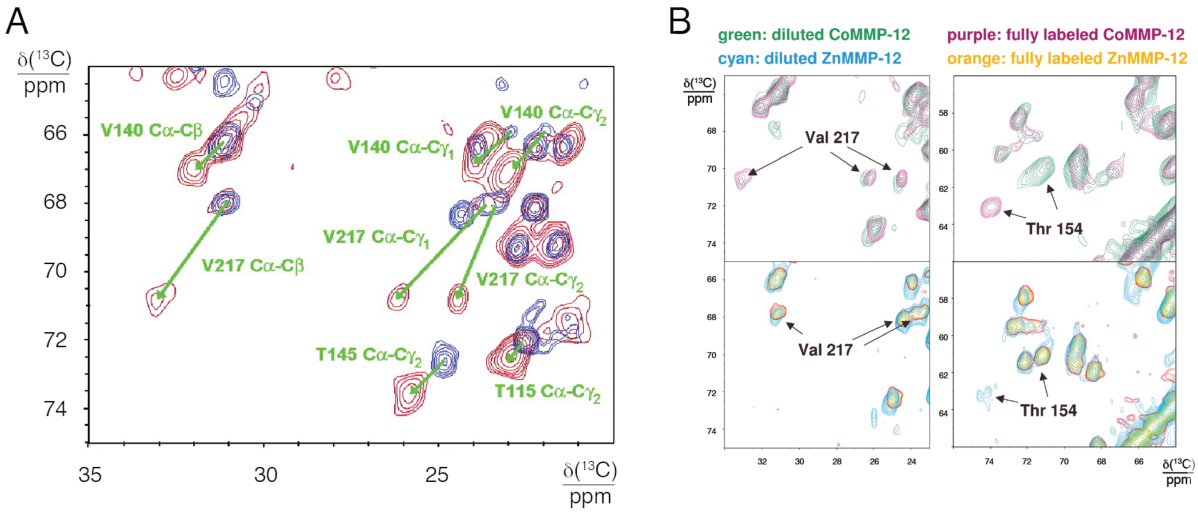

Figure 5. A) Portion of the ^{13}C-^{13}C PDSD spectra of Zn^{II}-MMP-12 (diamagnetic, blue) and of Co^{II}-MMP-112 (paramagnetic, red), acquired at 16.4 T, 11.5 kHz MAS. B) Representative parts of the PDSD spectra of fully labeled Zn^{II}-MMP-12 (orange), fully labeled Co^{II}-MMP-12 (purple), diluted Co^{II}-MMP-12 (green), and diluted Zn^{II}-MMP-12 (cyan). Reproduced from references 5, 21.

I.3.2 Fast magic-angle spinning

At moderate MAS rates, ^{13}C or ^{15}N spectra split into multiple resolved sidebands, but their linewidths are generally still large due to the difficulty to efficiently decouple the strong network of ^{1}H dipolar couplings (Figure 3B). If MAS rates increase above 25 kHz, a gain in resolution, sensitivity and coherence lifetimes of ^{13}C, ^{15}N, and ^{1}H is observed. The effects progressively increase with the spinning speed, and in small diameter probes allowing MAS rates above 50 kHz the effects of large paramagnetic anisotropies are considerably alleviated: the dipolar couplings are more efficiently averaged by the rotation and the signal is concentrated into fewer sidebands, with a consequent dramatic increase in resolution and sensitivity (Figure 3C).[12] If the spinning rate exceeds the magnitude of the anisotropic interaction, complete averaging is eventually achieved, yielding the same isotropic frequencies observed in solution.[11] Differently from solution however, where the Brownian motion imposes a stochastic modulation of the coupling, under MAS the averaging of the dipolar shift anisotropy is performed coherently. As a result, linewidths and coherence lifetimes are minimally affected by the hyperfine dipolar interaction, and narrower intrinsic linewidths are observable in the solid state for paramagnetic proteins of large molecular size and/or at high magnetic fields (Figure 3D).[23] These advantages are larger for metal ions with

rapid electronic correlation times (< 10^{-11} s), such as for example Co^{II}, Fe^{III}, or Ln^{III}, for which transverse relaxation times are dominated by the Curie mechanism in solution, while long coherence lifetimes and efficient coherence transfers between nuclear spins can be observed in solids, similarly to diamagnetic systems.[12, 23]

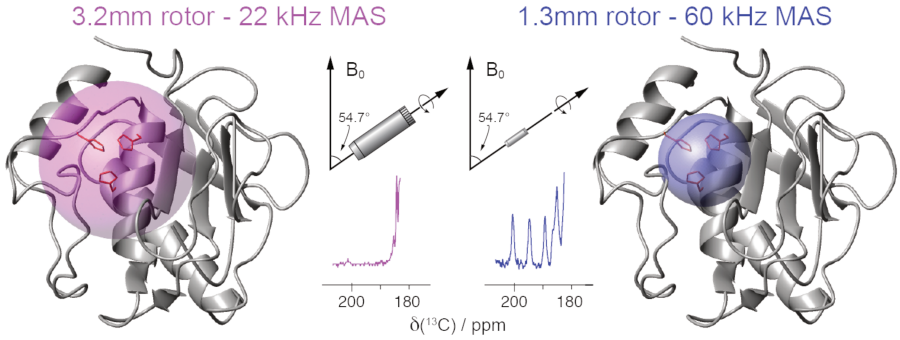

Figure 6. At slow MAS rates (left) a large portion of the Co^{II}-MMP-12 (indicated by the purple sphere centered on the Co^{II} ion) are inaccessible to solid-state NMR. At faster MAS rates (right), this "blind sphere" is narrowed (blue region), and additional peaks are observable in the ^{13}C spectrum (lower inserts). Reproduced from reference 3.

An example where ultra-fast MAS has been applied to a paramagnetic protein is shown in Figure 6, demonstrating the case of Co^{II}-MMP-12. The observation of nuclei closer than 10 Å from the Co^{II} ion was impossible using <25 kHz MAS, due to increasingly large paramagnetic shift anisotropy effects in close proximity to the paramagnetic center. With ultra-fast MAS at 60 kHz, a dramatic increase in resolution and sensitivity was observed, notably enabling the detection of resonances in closer proximity to the Co^{II} ion than before, up to 5.6 Å.[3]

Under ultra-fast MAS, optimal ^{13}C and ^{15}N spectra can be obtained with low-power rf-fields during the whole experiment. This possibility has an important consequence in paramagnetic samples, where PREs from a paramagnetic center increase the R_1 rates across the entire sample via a spin-diffusion mechanism. Coupled with the possibility of low-power rf-irradiation, the recycle delay can be made very short (as short as few tens of ms)[24-26] drastically reducing the experimental times for the acquisition of multidimensional correlations[27-28] and increasing the theoretical sensitivity of solid-state NMR for paramagnetic systems by an order of magnitude with respect to diamagnetic analogs. Similar sensitivity enhancements were shown to be achievable also in diamagnetic protein substrates, by doping of protein crystals with paramagnetic Cu^{II} complexed with EDTA,[29-30] or by incorporating a thiol-specific EDTA-metal reagent loaded with Cu^{II} or Mn^{II} into an otherwise diamagnetic protein.[31] The effect, termed "paramagnetic-relaxation-assisted condensed data collection",[32] raises the possibility of acquiring complex multidimensional experiments on systems of large molecular size, or available only in small amounts.

Faster spinning rates lead to a significant increase in coherence lifetimes,[3] rendering the design and the application of longer and more complex pulse schemes possible. New experiments for sequential assignment, similar to the protonless experiments used in solution,[33] were developed in this context. These experiments correlate the $^{15}N^{H}$ resonance to the ^{13}CO or the $^{13}C^{\alpha}$ resonances in either the same or the preceding residue in a two-dimensional experiment. Heteronuclear transfers are performed using cross-polarization, while thanks to the longer coherence lifetimes, homonuclear ^{13}C-^{13}C transfers are performed through *J*-coupling.[34-35] This has an additional beneficial consequence on both resolution and sensitivity in the ^{13}C dimension, which can be both increased by a spin-state selective block (S^3E) implemented to decouple the ^{13}CO-$^{13}C^{\alpha}$ one bond *J*-coupling.[34]

I.3.3 ^{1}H-detection

The low sensitivity associated with conventional heteronuclear detection methods renders the quantitative measurement of paramagnetic effects in solids very challenging. For example, determining site-specific PREs requires the acquisition of large series of 2D correlation spectra, in order to monitor the relaxation decays, which has been reported only for the model protein GB1 exploiting paramagnetic tags bound to engineered cysteines.[31, 36-37] Analogously, PCSs with ^{13}C-detection were measured only in pioneering studies,[5, 21] being limited by the relatively low resolution of 2D ^{13}C-^{13}C and ^{15}N-^{13}C maps, and the low sensitivity of ^{13}C-detected experiments.

These disadvantages could be overcome using direct acquisition of proton spectra. The availability of faster MAS regimes at 60 kHz provided significant narrowing effects, enabling fast acquisition of ^{13}C and ^{15}N spectra, however ^{1}H linewidths were still too broad in most cases to yield fully resolved two dimensional correlations maps in large fully-protonated systems, posing a problem in the efficient site-specific and quantitative measurement of paramagnetic effects along a protein chain.

These effects can be alleviated if the ^{1}H-^{1}H dipolar network could be weakened. Perdeuteration followed by partial reprotonation of the exchangeable sites was suggested as strategy to obtain well-resolved ^{1}H spectra in diamagnetic biomolecules under moderate MAS rates.[38-39] At higher MAS rates highly resolved spectra could be achieved even in fully H^{N}-reprotonated samples, leading to the acquisition of sensitive and resolved NMR spectra of medium-sized proteins.[40-41] These spectra can be used as 2D fingerprints for the backbone resonance assignment and for the detection of ^{1}H-^{1}H proximities,[41] as discussed in the next chapter. This provides an ideal tool for easy quantitative and site-specific measurement of

paramagnetic effects in solids, as shown in Figure 7, where the possibility of obtaining fast and resolved $^{1}H^{N}$-$^{15}N^{H}$ fingerprint spectra allowed the rapid determination of PREs[42] (Figure 7A-B) and PCSs (Figure 7C) in SOD.[8]

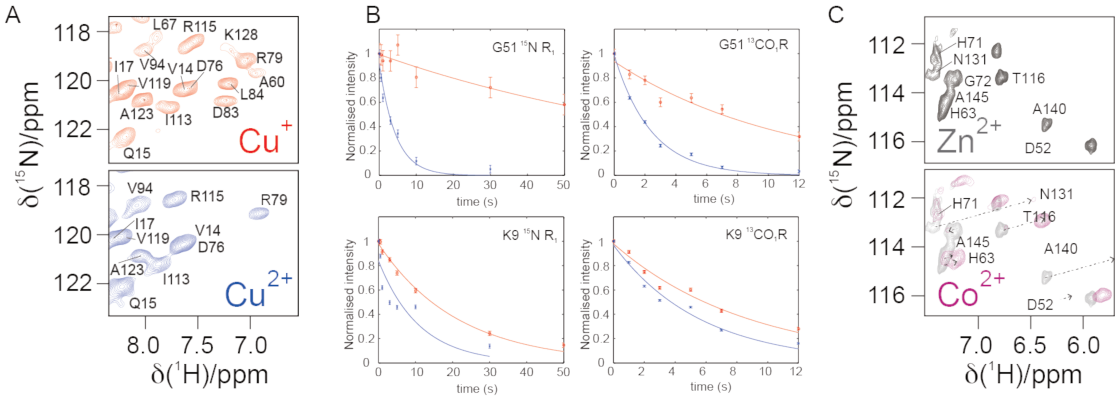

Figure 7. A) Portions of the (H)NH spectra of [U-$^{1}H^{N}$, ^{2}H, ^{13}C, ^{15}N] labeled microcrystalline Cu^{I},Zn^{II}-SOD (red) and Cu^{II},Zn^{II} -SOD (blue), at 800 MHz and 60 kHz MAS. B) Relaxation curves for the determination of $^{15}N^{H}$ and ^{13}CO R_1 in some selected residues from Cu^{I},Zn^{II}-SOD (red) and Cu^{II},Zn^{II} -SOD (blue). C) Portions of the (H)NH spectra of [U-$^{1}H^{N}$, ^{2}H, ^{13}C, ^{15}N] microcrystalline Zn^{II}-SOD (black) and Co^{II}-SOD (magenta), at 800 MHz and 60 kHz MAS. PCSs are identified by the diagonal dashed lines. Reproduced from references 12, 42.

The possibility of performing even faster spinning releases the requirement of proton dilution, and allows the extension of these techniques to fully protonated targets. Figure 8 shows an example of the dramatic improvement of the resolution obtainable in a fingerprint correlation spectrum of the paramagnetic microcrystalline Cu^{II},Co^{II}-SOD at such high MAS rates.

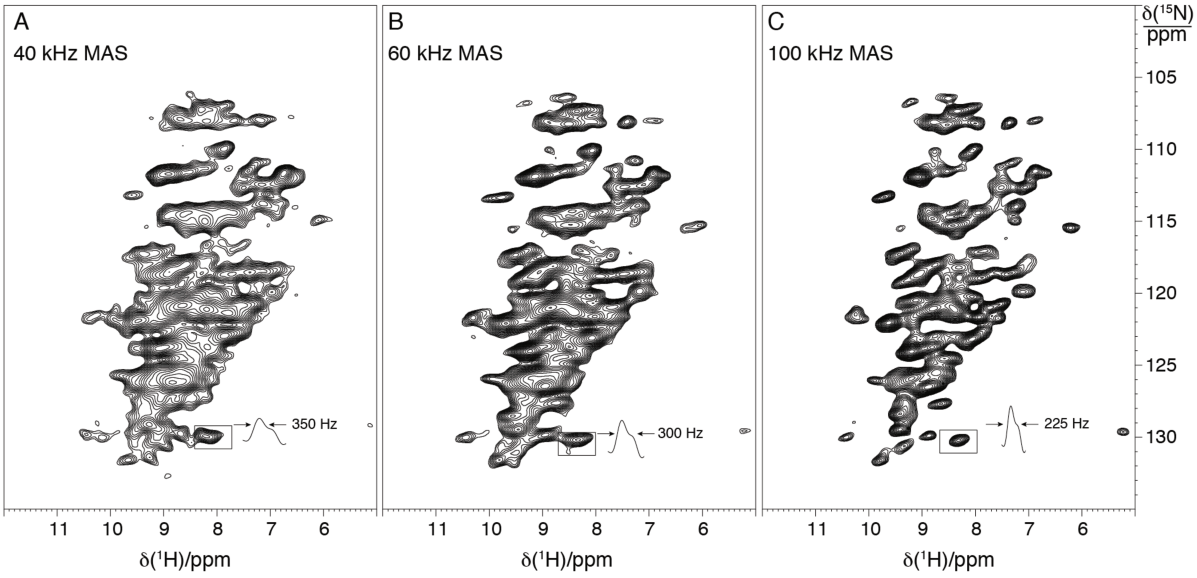

Figure 8. (H)NH spectra of [U-^{13}C, ^{15}N] labeled microcrystalline Cu^{II},Co^{II}-SOD on a 800 MHz (18.8 T) spectrometer and 280 K at A) 40 kHz MAS, B) 60 kHz MAS, and C) 100 kHz MAS, showing the observed linewidth for a selected residue. Spectra acquired by the author.

I.4 Paramagnetic effects as long-range structural restraints

The long-range nature of the PREs and PCSs makes them powerful structural restraints, in particular where long-range information is difficult to obtain otherwise.

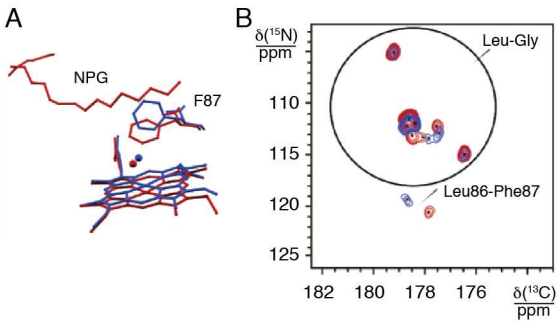

Figure 9. A) Shift in the conformation of the Phe87 residue in cytochrome P450 BM-3 before (blue) and after (red) the substrate binding. B) ^{15}N-^{13}CO correlation spectrum of the ^{13}CO-Leu, ^{15}N-Gly, ^{15}N-Phe labeled cytochrome P450 BM-3 before (blue) and after (red) the substrate binding, acquired at 600 MHz and 13 kHz MAS showing the Leu86-Phe87 correlation which is shifted after substrate binding. Reproduced from reference 43.

Cytochrome P450 BM-3 was the first example where site-specific paramagnetic effects were used in biomolecular solid-state NMR.[43] This protein is a 119-kDa enzyme, paramagnetic by virtue of an heme group containing a Fe^{III} ion. By the use of selective labeling, McDermott and coworkers used paramagnetically perturbed shifts and relaxation rates to monitor conformational rearrangements and iron spin state change from low spin to high spin following the binding of a substrate, N-palmitoylglycine (NPG). In particular, this study highlighted a conformational transition occurring at a particular residue (Phe87) in the proximity of the active site (Figure 9), and allowed the formulation of a control mechanism for its access by the substrate.

I.4.1 Pseudo-contact shifts

The structure determination of microcrystalline Co^{II}-MMP-12 is the first example where PCSs were included in a structural refinement together with diamagnetic restraints (Figure 10A-B). The implementation of PCSs as structure restraints requires the prior determination of the susceptibility χ tensor, which is a function of the particular paramagnetic ion and the coordination environment imposed by the system. The χ tensor is described by eight parameters: the 3 position coordinates of the ion in the protein, the 3 Euler angles specifying the orientation of the PAS of the χ tensor, and its 2 anisotropy parameters. If reference shifts and an approximate structure model are available, it is possible to establish an iterative procedure where the determination of the χ anisotropy and its orientation, the assignment of

PCSs and their translation into structural restraints can be implemented cyclically. In the case of Co^{II}-MMP-12, a RMDS of 3.0 Å within the family and of 3.1 Å with respect to the X-ray structure were obtained, while without the inclusion of PCS restraints the RMDS increased to 5.8 Å within the family and to 5.7 Å with respect to the X-ray structure. Notably, the use of PCSs increased both the precision and the accuracy of the calculated structures. Moreover, intermolecular PCSs could be used to provide a good estimation of the orientation of the two nearest neighboring proteins of MMP-12.[21] Finally, for nuclei closer to the metal center some significant deviation of the PCS values from the predicted ones was observed, highlighting then a non-negligible contribution from the contact interaction.[3]

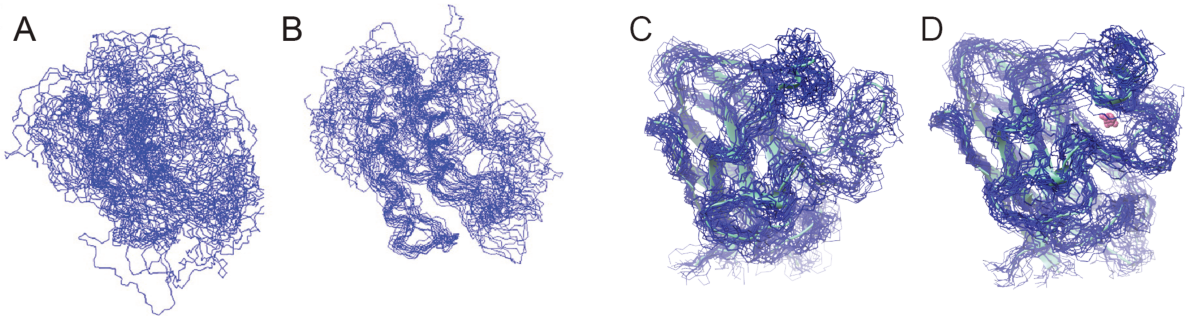

Figure 10. Structures bundles of MMP-12 (A,B) and SOD (C,D) calculated from solid-state NMR data A-C) without paramagnetic restraints, and B-D) with PCSs as paramagnetic restraints. Reproduced from references 12, 21.

Similarly, it was shown that the use of ^{1}H-detected solid-state correlations on perdeuterated samples under ultra-fast MAS enables the measurement of site-specific PCSs, using a mutant of SOD in which the Cu site is empty, and the metallation state of the Zn site is varied between a diamagnetic state (binding Zn^{II}) and a paramagnetic one (binding Co^{II}).[8] This study used 3D (H)CONH and (H)CANH correlations on less than 4 mg (0.5 µmol) sample to obtain several hundred PCSs, including ^{1}H PCS. In contrast to previous studies, PCSs could be obtained for spins up to 5 Å from the Co^{II} ion. From these correlations, PCSs were measured as the difference in chemical shifts relative to the isostructural diamagnetic analogue, binding Zn^{II}, and their assignment was straightforward, exploiting the systematic change in chemical shifts along parallel lines in the spectra characteristic of PCS effects, as shown in Figure 7. PCSs were then incorporated into a structure determination protocol in combination with ^{1}H-^{1}H distance restraints measured from ^{1}H-detected 3D HHN_{RFDR} experiments (totaling 297 ^{1}H-^{1}H pairs), chemical shift-derived dihedral angle restraints and ambiguous H-bond restraints using the program Cyana[44] in the UNIO package. This allowed to reduce the backbone RMSD of the resulting structure ensemble, taking it from 3.1 Å without any paramagnetic restraints down to or 1.7 Å. Notably, in the case of Co^{II}-SOD, due

to the location of the binding site, and to the low anisotropy found for the χ tensor, neighbor effects were found to be negligible.

I.4.2 Paramagnetic relaxation enhancements

The possibility of exploiting enhanced paramagnetic relaxation as an effective source of structural constraints was first explored by Jaroniec and coworkers on microcrystalline samples of a model protein, the B1 immunoglobulin-binding domain of protein G (GB1).[31] There a solvent exposed cysteine residue was used to incorporate a thiol-specific paramagnetic nitroxide (TEMPO) or a thiol-specific EDTA-metal reagent bound to Cu^{II} and Mn^{II} ions. The different effects on the longitudinal (R_1) and the transverse ($R_{1\rho}$) of the protein nuclei induced by paramagnetic moieties with different electron relaxation times and spin quantum numbers could be advantageously exploited to collect structural restraints. In particular, Cu^{II} spin labels cause considerable longitudinal enhancement. R_1 PREs for backbone amide ^{15}N nuclei were found to be highly correlated with the proximity of the Cu^{II} ion to ^{15}N spins, with significant effects observed for nuclei up to 20 Å away. This provided valuable structural information about protein on length scales that are inaccessible to conventional solid-state NMR techniques.

Leveraging all these efforts, Sengupta and coworkers demonstrated that ^{13}C and ^{15}N PREs induced by attaching a paramagnetic chelator to multiple cysteine mutants can be used in addition to dihedral angle restraints to determine the fold of GB1.[45]

PREs were also successfully used to refine the structure of the protein superoxide dismutase (SOD). ^{15}N and ^{13}C R_1 PREs have been measured in human Cu,Zn-SOD (Figure 6)[41] using the ^{15}N-^{1}H CP-HSQC dipolar correlation experiment as a module to build more complex experiments, by the combination with a ^{15}N inversion-recovery block (for ^{15}N R_1 measurement),[46-47] ^{15}N spin-lock (for ^{15}N $R_{1\rho}$ measurement),[48-49] or additional ^{13}C-^{15}N specific transfers and ^{13}C inversion-recovery (for ^{13}C R_1 measurement).[50] The resulting experiments, all based upon the same fingerprint spectrum, were used to determine PREs in SOD as the difference between the longitudinal relaxation values measured in the paramagnetic form of SOD, containing Cu^{II}, and in diamagnetic form, containing Cu^{I}. More than one hundred ^{13}C and ^{15}N PREs were measured between 10 and 24 Å of the Cu ion, which were converted into distance restraints from the metal center using the Solomon equations in the PDA, assuming an upper and a lower limit of 3 Å greater and lower respectively than the calculated values. For those residues whose $^{1}H^{N}$-$^{15}N^{H}$ cross-peaks were

observable only in the diamagnetic form, an upper limit of 10 Å from the metal center was used, with no lower limit. The addition of these paramagnetic restraints significantly reduces the backbone RMSD of the resulting structure ensemble, from to 2.9 Å without PREs to 1.7 Å with PREs. The simultaneous use of PREs from Cu,Zn-SOD and PCS from Co^{II}-SOD further improves the quality of the NMR structure, with a backbone RMSD which drops to 1.4 Å when all constraints are employed (the bundle shown in Figure 11C).

More recently, Lewandowski and coworkers used ^{15}N R_1, ^{15}N $R_{1\rho}$ and ^{1}H R_1 solvent PREs to probe protein-protein interfaces, suggesting the potential existence of an additional binding site in the GB1:IgG complex.[51]

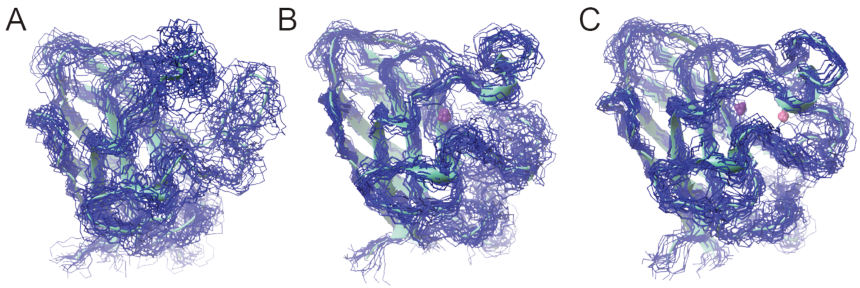

Figure 11. Solid-state NMR structure bundles for SOD, with different types of paramagnetic restraints: A) no paramagnetic restraints, B) with PREs, C) with both PCS and PREs. Pink is used to represent the Co^{II} ion, purple for the Cu^{II} ion, and the aquamarine ribbon diagram is the mean NMR structure for each case. Reproduced from reference 12.

I.5 Conclusions

Paramagnetic effects in NMR provide precious information on structure of proteins containing paramagnetic centers. Their potential is well exploited in solution NMR, but still of limited application in solid-state NMR. However, the examples reported in this chapter demonstrate that, following the impressive development experienced by solid-state NMR in the recent years, this technique has become mature for the analysis of proteins containing paramagnetic centers.

In the next chapter an overview of the recent developments of the NMR ^{1}H-detected methods for protein assignment and structure determination will be provided. These methods, which are originally developed on diamagnetic systems, can be successfully applied for the NMR characterization of paramagnetic proteins, as it will be demonstrated on two benchmark microcrystalline metalloenzymes.

I.6 References

(1) Bertini, I.; Luchinat, C.; Parigi, G.; Ravera, E., *NMR of paramagnetic molecules. Applications to metallobiomolecules and models*. Elsevier: Boston, 2017.

(2) Vega, A. J.; Fiat, D., Nuclear relaxation processes of paramagnetic complexes. The slow-motion case. *Mol. Phys.* **1976,** *31*, 347-355.

(3) Bertini, I.; Emsley, L.; Lelli, M.; Luchinat, C.; Mao, J.; Pintacuda, G., Ultrafast MAS solid-state NMR permits extensive ^{13}C and ^{1}H detection in paramagnetic metalloproteins. *J. Am. Chem. Soc.* **2010,** *132*, 5558-5559.

(4) Benda, L.; Mareš, J.; Ravera, E.; Parigi, G.; Luchinat, C.; Kaupp, M.; Vaara, J., Pseudo-contact NMR shifts over the paramagnetic metalloprotein CoMMP-12 from first principles. *Angew. Chem. Int. Ed.* **2016,** *55*, 14713-14717.

(5) Balayssac, S.; Bertini, I.; Lelli, M.; Luchinat, C.; Maletta, M., Paramagnetic ions provide structural restraints in solid-state NMR of proteins. *J. Am. Chem. Soc.* **2007,** *129*, 2218-2219.

(6) Kervern, G.; D'Aleo, A.; Toupet, L.; Maury, O.; Emsley, L.; Pintacuda, G., Crystal-structure determination of powdered aramagnetic lanthanide complexes by proton NMR Spectroscopy. *Angew. Chem. Int. Ed.* **2009,** *48*, 3082-3086.

(7) Parge, H. E.; Hallewell, R. A.; Tainer, J. A., Atomic structures of wild-type and thermostable mutant recombinant human Cu,Zn superoxide dismutase. *Proc. Natl. Acad. Sci. U.S.A.* **1992,** *89*, 6109-6113.

(8) Knight, M. J.; Felli, I. C.; Pierattelli, R.; Bertini, I.; Emsley, L.; Herrmann, T.; Pintacuda, G., Rapid measurement of pseudocontact shifts in metalloproteins by proton-detected solid-state NMR spectroscopy. *J. Am. Chem. Soc.* **2012,** *134*, 14730-14733.

(9) Rinaldelli, M.; Carlon, A.; Ravera, E.; Parigi, G.; Luchinat, C., FANTEN: a new web-based interface for the analysis of magnetic anisotropy-induced NMR data. *J. Biomol. NMR* **2015,** *61*, 21-34.

(10) Banci, L.; Bertini, I.; Luchinat, C., The ^{1}H NMR parameters of magnetically coupled dimers—The Fe_2S_2 proteins as an example. *Struct. Bond.* **1990,** *72*, 113-136.

(11) Maricq, M. M.; Waugh, J. S., NMR in rotating solids. *J. Chem. Phys.* **1979,** *70*, 3300-3316.

(12) Knight, M. J.; Felli, I. C.; Pierattelli, R.; Emsley, L.; Pintacuda, G., Magic angle spinning NMR of paramagnetic proteins. *Acc. Chem. Res.* **2013,** *46*, 2108-2116.

(13) Pintacuda, G.; Giraud, N.; Pierattelli, R.; Bockmann, A.; Bertini, I.; Emsley, L., Solid-state NMR spectroscopy of a paramagnetic protein: assignment and study of human dimeric oxidized Cu^{II}-Zn^{II} superoxide dismutase (SOD). *Angew. Chem. Int. Ed. Engl.* **2007,** *46*, 1079-1082.

(14) McCord, J. M.; Fridovich, I., Superoxide dismutase. An enzymic function for erythrocuprein (hemocuprein). *J. Biol. Chem.* **1969,** *244*, 6049-6055.

(15) Bertini, I.; Luchinat, C.; Piccioli, M., Copper-zinc superoxide dismutase: a paramagnetic protein that provides a unique frame for the NMR investigation. *Prog. Nucl. Magn. Reson. Spectrosc.* **1994,** *26*, 91-139.

(16) Pauli, J.; Baldus, M.; van Rossum, B.; de Groot, H.; Oschkinat, H., Backbone and side-chain ^{13}C and ^{15}N signal assignments of the alpha-spectrin SH3 domain by magic angle spinning solid-state NMR at 17.6 Tesla. *ChemBioChem* **2001,** *2*, 272-281.

(17) Li, Y.; Berthold, D. A.; Frericks, H. L.; Gennis, R. B.; Rienstra, C. M., Partial ^{13}C and ^{15}N chemical-shift assignments of the disulfide-bond-forming enzyme DsbB by 3D magic-angle spinning NMR spectroscopy. *ChemBioChem* **2007,** *8*, 434-442.

(18) Franks, W. T.; Kloepper, K. D.; Wylie, B. J.; Rienstra, C. M., Four-dimensional heteronuclear correlation experiments for chemical shift assignment of solid proteins. *J. Biomol. NMR* **2007,** *39*, 107-131.
(19) Eden, M.; Levitt, M. H., Pulse sequence symmetries in the nuclear magnetic resonance of spinning solids: Application to heteronuclear decoupling. *J. Chem. Phys.* **1999,** *111*, 1511-1519.
(20) Szeverenyi, N. M.; Sullivan, M. J.; Maciel, G. E., Observation of spin exchange by two-dimensional Fourier-transform C-13 cross polarization-magic-angle spinning. *J. Magn. Reson.* **1982,** *47*, 462-475.
(21) Balayssac, S.; Bertini, I.; Bhaumik, A.; Lelli, M.; Luchinat, C., Paramagnetic shifts in solid-state NMR of proteins to elicit structural information. *Proc. Natl. Acad. Sci. U.S.A.* **2008,** *105*, 17284-9.
(22) Bertini, I.; Fragai, M.; Lee, Y. M.; Luchinat, C.; Terni, B., Paramagnetic metal ions in ligand screening: the Co(II) matrix metalloproteinase 12. *Angew. Chem. Int. Ed.* **2004,** *43*, 2254-6.
(23) Kervern, G.; Steuernagel, S.; Engelke, F.; Pintacuda, G.; Emsley, L., Absence of Curie relaxation in paramagnetic solids yields long H-1 coherence lifetimes. *J. Am. Chem. Soc.* **2007,** *129*, 14118-14119.
(24) Ishii, Y.; Wickramasinghe, N. P.; Chimon, S., A new approach in 1D and 2D C-13 high-resolution solid-state NMR spectroscopy of paramagnetic organometallic complexes by very fast magic-angle spinning. *J. Am. Chem. Soc.* **2003,** *125*, 3438-3439.
(25) Wickramasinghe, N. P.; Shaibat, M.; Ishii, Y., Enhanced sensitivity and resolution in H-1 solid-state NMR spectroscopy of paramagnetic complexes under very fast magic angle spinning. *J. Am. Chem. Soc.* **2005,** *127*, 5796-5797.
(26) Kervern, G.; Pintacuda, G.; Zhang, Y.; Oldfield, E.; Roukoss, C.; Kuntz, E.; Herdtweck, E.; Basset, J. M.; Cadars, S.; Lesage, A.; Coperet, C.; Emsley, L., Solid-state NMR of a paramagnetic DIAD-Fe-II catalyst: Sensitivity, resolution enhancement, and structure-based assignments. *J. Am. Chem. Soc.* **2006,** *128*, 13545-13552.
(27) Laage, S.; Marchetti, A.; Sein, J.; Pierattelli, R.; Sass, H. J.; Grzesiek, S.; Lesage, A.; Pintacuda, G.; Emsley, L., Band-selective 1H-13C cross-polarization in fast magic angle spinning solid-state NMR spectroscopy. *J. Am. Chem. Soc.* **2008,** *130*, 17216-17217.
(28) Laage, S.; Sachleben, J. R.; Steuernagel, S.; Pierattelli, R.; Pintacuda, G.; Emsley, L., Fast acquisition of multi-dimensional spectra in solid-state NMR enabled by ultra-fast MAS. *J. Magn. Reson.* **2009,** *196*, 133-41.
(29) Wickramasinghe, N. P.; Shaibat, M. A.; Ishii, Y., Elucidating connectivity and metal-binding structures of unlabeled paramagnetic complexes by C-13 and H-1 solid-state NMR under fast magic angle spinning. *J. Phys. Chem. B* **2007,** *111*, 9693-9696.
(30) Wickramasinghe, N. P.; Parthasarathy, S.; Jones, C. R.; Bhardwaj, C.; Long, F.; Kotecha, M.; Mehboob, S.; Fung, L. W.; Past, J.; Samoson, A.; Ishii, Y., Nanomole-scale protein solid-state NMR by breaking intrinsic 1HT1 boundaries. *Nature methods* **2009,** *6*, 215-8.
(31) Nadaud, P. S.; Helmus, J. J.; Kall, S. L.; Jaroniec, C. P., Paramagnetic Ions Enable Tuning of Nuclear Relaxation Rates and Provide Long-Range Structural Restraints in Solid-State NMR of Proteins. *J. Am. Chem. Soc.* **2009,** *131*, 8108-8120.
(32) Nadaud, P. S.; Helmus, J. J.; Sengupta, I.; Jaroniec, C. P., Rapid acquisition of multidimensional solid-state NMR spectra of proteins facilitated by covalently bound paramagnetic tags. *J. Am. Chem. Soc.* **2010,** *132*, 9561-3.

(33) Bermel, W.; Bertini, I.; Duma, L.; Felli, I. C.; Emsley, L.; Pierattelli, R.; Vasos, P. R., Complete assignment of heteronuclear protein resonances by protonless NMR spectroscopy. *Angew. Chem. Int. Ed.* **2005,** *44*, 3089-92.

(34) Laage, S.; Lesage, A.; Emsley, L.; Bertini, I.; Felli, I. C.; Pierattelli, R.; Pintacuda, G., Transverse-dephasing optimized homonuclear J-decoupling in solid-state NMR spectroscopy of uniformly C-13-labeled proteins. *J. Am. Chem. Soc.* **2009,** *131*, 10816-10817.

(35) Barbet-Massin, E.; Pell, A. J.; Knight, M. J.; Webber, A. L.; Felli, I. C.; Pierattelli, R.; Emsley, L.; Lesage, A.; Pintacuda, G., ^{13}C-detected through-bond correlation experiments for protein resonance assignment by ultra-fast MAS solid-state NMR. *ChemPhysChem* **2013,** *14*, 3131-7.

(36) Nadaud, P. S.; Helmus, J. J.; Hofer, N.; Jaroniec, C. P., Long-range structural restraints in spin-labeled proteins probed by solid-state nuclear magnetic resonance spectroscopy. *J. Am. Chem. Soc.* **2007,** *129*, 7502-3.

(37) Nadaud, P. S.; Helmus, J. J.; Jaroniec, C. P., 13C and 15N chemical shift assignments and secondary structure of the B3 immunoglobulin-binding domain of streptococcal protein G by magic-angle spinning solid-state NMR spectroscopy. *Biomol. NMR Assign.* **2007,** *1*, 117-20.

(38) Reif, B.; Jaroniec, C. P.; Rienstra, C. M.; Hohwy, M.; Griffin, R. G., 1H-1H MAS correlation spectroscopy and distance measurements in a deuterated peptide. *J. Magn. Reson.* **2001,** *151*, 320-327.

(39) Chevelkov, V.; Rehbein, K.; Diehl, A.; Reif, B., Ultrahigh resolution in proton solid-state NMR spectroscopy at high levels of deuteration. *Angew. Chem. Int. Ed.* **2006,** *45*, 3878-3881.

(40) Lewandowski, J. R.; Dumez, J. N.; Akbey, U.; Lange, S.; Emsley, L.; Oschkinat, H., Enhanced Resolution and Coherence Lifetimes in the Solid-State NMR Spectroscopy of Perdeuterated Proteins under Ultrafast Magic-Angle Spinning. *J. Phys. Chem. Lett.* **2011,** *2*, 2205-2211.

(41) Knight, M. J.; Webber, A. L.; Pell, A. J.; Guerry, P.; Barbet-Massin, E.; Bertini, I.; Felli, I. C.; Gonnelli, L.; Pierattelli, R.; Emsley, L.; Lesage, A.; Herrmann, T.; Pintacuda, G., Fast resonance assignment and fold determination of human superoxide dismutase by high-resolution proton-detected solid-state MAS NMR spectroscopy. *Angew. Chem. Int. Ed. Engl.* **2011,** *50*, 11697-11701.

(42) Knight, M. J.; Pell, A. J.; Bertini, I.; Felli, I. C.; Gonnelli, L.; Pierattelli, R.; Herrmann, T.; Emsley, L.; Pintacuda, G., Structure and backbone dynamics of a microcrystalline metalloprotein by solid-state NMR. *Proc. Natl. Acad. Sci. U.S.A.* **2012,** *109*, 11095-11100.

(43) Jovanovic, T.; McDermott, A. E., Observation of ligand binding to cytochrome P450 BM-3 by means of solid-state NMR spectroscopy. *J. Am. Chem. Soc.* **2005,** *127*, 13816-13821.

(44) Herrmann, T.; Guntert, P.; Wuthrich, K., Protein NMR structure determination with automated NOE-identification in the NOESY spectra using the new software ATNOS. *J. Biomol. NMR* **2002,** *24*, 171-189.

(45) Sengupta, I.; Nadaud, P. S.; Helmus, J. J.; Schwieters, C. D.; Jaroniec, C. P., Protein fold determined by paramagnetic magic-angle spinning solid-state NMR spectroscopy. *Nat. Chem.* **2012,** *4*, 410-417.

(46) Giraud, N.; Blackledge, M.; Goldman, M.; Böckmann, A.; Lesage, A.; Penin, F.; Emsley, L., Quantitative analysis of backbone dynamics in a crystalline protein from nitrogen-15 spin-lattice relaxation. *J. Am. Chem. Soc.* **2005,** *127*, 18190-201.

(47) Schanda, P.; Meier, B. H.; Ernst, M., Quantitative analysis of protein backbone dynamics in microcrystalline ubiquitin by solid-state NMR spectroscopy. *J. Am. Chem. Soc.* **2010,** *132*, 15957-67.
(48) Krushelnitsky, A.; Zinkevich, T.; Reichert, D.; Chevelkov, V.; Reif, B., Microsecond time scale mobility in a solid protein as studied by the 15N R(1rho) site-specific NMR relaxation rates. *J. Am. Chem. Soc.* **2010,** *132*, 11850-3.
(49) Lewandowski, J. R.; Sass, H. J.; Grzesiek, S.; Blackledge, M.; Emsley, L., Site-specific measurement of slow motions in proteins. *J. Am. Chem. Soc.* **2011,** *133*, 16762-16765.
(50) Lewandowski, J. R.; Sein, J.; Sass, H. J.; Grzesiek, S.; Blackledge, M.; Emsley, L., Measurement of site-specific 13C spin-lattice relaxation in a crystalline protein. *J. Am. Chem. Soc.* **2010,** *132*, 8252-4.
(51) Öster, C.; Kosol, S.; Hartlmüller, C.; Lamley, J. M.; Iuga, D.; Oss, A.; Org, M.-L.; Vanatalu, K.; Samoson, A.; Madl, T.; Lewandowski, J. R., Characterization of protein–protein interfaces in large complexes by solid-state NMR solvent paramagnetic relaxation enhancements. *J. Am. Chem. Soc.* **2017,** *139*, 12165-12174.

Chapter II.

Proton-detected NMR methods for proteins under ultrafast MAS

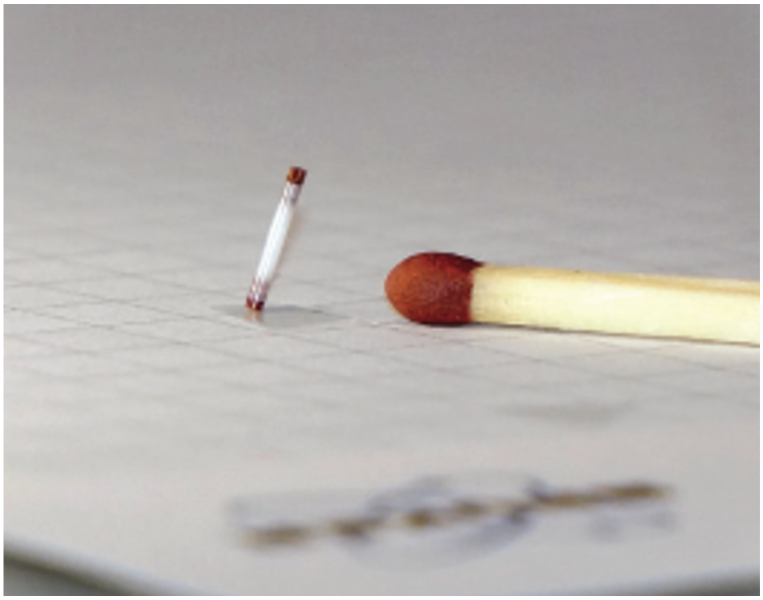

II.1 Introduction

In the previous chapter an overview of the recent achievements of the NMR technique for the study of paramagnetic proteins has been provided. It was mentioned that the experimental approach adopted differs depending on the dominant paramagnetic effects affecting the nuclei of interest. When dealing with long-range effects, one can usually successfully employ "conventional" experiments that are used for the NMR analysis of diamagnetic proteins. This approach allows accessing information of the majority of resonances and thus accelerating the investigation of a paramagnetic protein.

In the brief historical excursus provided in the previous section it was quickly mentioned how, with the advent of ultra-fast MAS probes (capable of spinning at the frequencies of at least 60 kHz), a revolutionary breakthrough in the NMR technique has been achieved, and opened the way to proton detection in solid-state NMR of proteins. Our laboratory has been among the leading ones in driving this revolution, and during my PhD I have been able to personally witness and contribute to this fascinating recent progress in solid-state NMR.

In this chapter a description of the ^{1}H-detected NMR techniques developed in our laboratory will be provided. It consists of literature review of the ^{1}H-detected methods proposed prior to my PhD studies, as well as of those introduced later (sections 4 and 5), in development of which I have been involved.

After a brief overview of the state of the art prior to the advent of 60 kHz and faster MAS probes, the third and fourth sections will describe in detail a set of 2D and 3D ^{1}H -detected experiments for sequential backbone assignment. These experiments allow the extensive assignment of $^{1}H^{N}$, $^{15}N^{H}$, $^{13}C^{\alpha}$, and $^{13}C^{\beta}$ resonances in uniformly ^{13}C, ^{15}N-labeled proteins, in a way analogous to the one adapted in solution NMR, optionally with the help of perdeuteration followed by reprotonation at the exchangeable sites.[1-2]

The fifth section will describe the breakthrough that occurred with the advent of 0.7 mm probes, attaining the 100-111 kHz MAS regime. In this MAS regime the ^{1}H dipolar coupling network is sufficiently weakened to allow the detection of well-resolved proton-detected spectra in fully protonated systems. The main breakthrough in this regime is given by the fact that side chains protons become finally accessible, which represents a precious source of information for structure calculation. Moreover, this opens the way to the possibility of developing new pulse schemes for backbone and side chains assignment that rely on the $^{1}H^{\alpha}$-$^{13}C^{\alpha}$ pairs as anchors for the third dimension of the spectrum, instead of the $^{1}H^{N}$-$^{15}N^{H}$ pairs used previously. This increases the level of redundancy obtainable, which can be precious for

the assignment of complex systems, where extensive signal overlap can occur even in multidimensional experiments.[3-4]

The extent of the applicability for the methods described, originally developed for diamagnetic proteins, will be demonstrated on two original examples with paramagnetic proteins showing that extensive backbone and side chain assignment can be achieved with the aforementioned experiments in such systems. This part is an original contribution of the author.

II.2 MAS NMR of proteins in the last two decades

II.2.1 The ^{13}C-detection approach

In the last twenty years, Magic-Angle Spinning (MAS) NMR emerged as a generally applicable structural biology technique, complementing solution NMR, X-ray crystallography and electron microscopy. Following seminal work on microcrystalline proteins,[5-6] examples demonstrating the utility of MAS include studies of prion fibrils,[7-12] poly-disperse full-size heat shock complexes,[13] intact viral capsids,[14] membrane-bound drug targets,[15-17] and bacterial virulence factors[18-19] at an atomic level.

Most of these works were performed in the moderate MAS regime (less than 20 kHz). At these spinning rates, the ^{1}H-^{1}H dipolar couplings are not sufficiently averaged by the sample rotation, and ^{1}H linewidths are considerably broadened. For this reason ^{13}C-detection is employed, and the assignment procedures are based on double and triple resonance spectra, primarily making use of correlations between ^{13}C and ^{15}N signals, unveiling the connectivity between the $^{15}N^{H}$ nuclei with the ^{13}CO, $^{13}C^{\alpha}$, and $^{13}C^{\beta}$ nuclei.[20-24] They make use of spin-diffusion (such as proton-driven spin-diffusion, PDSD,[25] or dipolar assisted rotational resonance, DARR[26]) to record ^{13}C-^{13}C correlations and distance restraints between the backbone and the side chain spins. In order to obtain narrow ^{13}C lines, high-power ^{1}H dipolar decoupling was used, such as the TPPM (two-pulse phase-modulated)[27] or the SPINAL-64 (small phase incremental alternation),[28] with decoupling field amplitudes of the order of 80-100 kHz.

Due to the inherent low sensitivity of detected low-γ nuclei, this approach requires long acquisition times (weeks to months), large amount (~1 mg/kD) of ^{13}C/^{15}N labeled samples,

and expert manual analysis of the spectra. Moreover, the use of strong decoupling powers could be detrimental to the sample, particularly affecting its hydration level.

The advent of the new generation of probes, allowing faster spinning rates (between 40 and 60 kHz) and low-power decoupling schemes, lead to the increase in resolution and coherence lifetimes,[29] and triggered the development of more complex pulse schemes with longer coherence pathways. New experiments for sequential assignment, similarly to the protonless experiments used in solution,[30] were proposed, as described in the previous chapter.

Despite these improvements, MAS NMR still did not constitute a widespread tool in structural biology. This is in contrast to the standard solution NMR acquisition and analysis protocols, where established triple-resonance pulse schemes correlating backbone and side-chain ^{1}H, ^{13}C, and ^{15}N resonances are used for sequential assignment.[31] These experiments have been used serially in solution NMR, and for small to medium-sized soluble proteins they provide high-quality data that allow the use of computational analysis protocols with minimal human intervention.[32]

II.2.2 Moving to ^{1}H-detection: the first attempts

The sensitivity of detecting a polarization scales with $\gamma^{3/2}$, where γ represents the gyromagnetic ratio of the detected nucleus.[33] ^{1}H-detection thus represents an attractive remedy to the intrinsic sensitivity problem of ^{13}C-detection, however, to obtain resolved signals the homogeneous broadening characteristic of this network[34] needs to be overcome. One strategy relies on the dilution of the proton content in a sample.[35-36] In proteins this can be easily achieved by expression in deuterated media followed by partial or complete reprotonation at the exchangeable sites, [37-38] or in alternative by expression in partially protonated media like in the RAP (Reduced Adjoining Protonation) strategy.[39] Resolved spectra were demonstrated on a deuterated protein sample with full protonation of the amide sites at MAS of 20 kHz,[40] but usually partial (10-40 %) reprotonation was needed in order to obtain sufficient resolution.[35, 41-45] Obviously, the latter approach trades sensitivity for resolution, which somehow contradicts the original rationale of the use of protons for detection.

The other strategy relies rather on increasing the spinning speed.[33, 46-47] First studies at 40 kHz MAS demonstrated that a dramatic increase in resolution can be obtained in model systems, and that ^{1}H-detection can be successfully combined with assignment protocols based on dipolar-based ^{15}N-^{13}C and ^{13}C-^{13}C correlations.[48-51]

II.2.3 ^{1}H-detection at 60 kHz MAS

The advent of new 1.3 mm probes that could attain spinning frequencies of 60 kHz represented a milestone in the NMR field. In this regime the suppression of coherent effects is sufficiently strong to allow complete reprotonation at amide sites,[52-54] thus with a significant gain in sensitivity. Moreover, above 40 kHz MAS, heteronuclear decoupling can be efficiently performed with low-power ^{1}H irradiation.[55-56] This avoids the risk of sample damage, and allows a two- to three-fold reduction of the interscan delay, which yields an increase in sensitivity by acquisition of a higher number of transients per unit of time.

The increased spinning rate entails a reduction of the rotor size, and thus of the sample volume. This can appear as a limitation, however, the sensitivity of a typical-sized NMR coil scales with the inverse of its diameter,[57] partially compensating the signal loss compared to a larger rotor. Taking into account the intrinsic advantage of ^{1}H-detection, the sensitivity of a 1.3 mm coil is still nearly twice as sensitive as ^{13}C-detection in a 3.2 mm coil.[58]

In this spinning regime proton-detected cross-polarization-based ^{15}N-^{1}H correlations (named "CP-HSQC" in analogy to the solution *J*-based counterpart, or (H)NH in a more concise way, Figure 12) that maintain simultaneously high sensitivity and high resolution can be obtained for fully back-protonated at amide sites, and otherwise deuterated samples.[40, 52, 54]

Moreover, extremely long ^{13}C and ^{15}N coherence lifetimes are observed,[55, 59-60] and scalar couplings can be used for efficient transfer of coherences between ^{13}C spins, similarly to solution NMR. This has opened the way to new, expeditious backbone resonance assignment strategies for significantly larger proteins (up to ~35 kDa), and to the rapid detection of structurally relevant parameters such as $^{1}H^{N}$-$^{1}H^{N}$ proximities, PREs and PCSs.[61-63]

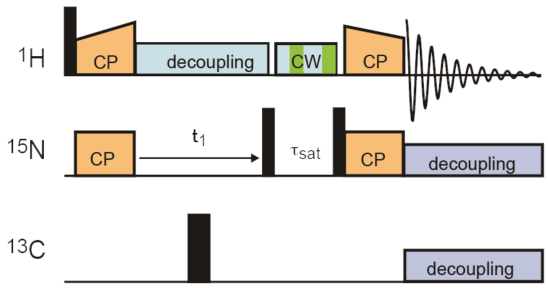

Figure 12. Pulse scheme for the (H)NH. Narrow and broad black rectangles indicate 90˚and 180˚ pulses, respectively. Orange boxes indicate CP steps, while gray and azure boxes indicate heteronuclear decoupling. The water suppression block is indicated by the striped box and labeled "CW". Reproduced from reference 1.

II.2.4 (H)NH provides a rapid protein fingerprint

The (H)NH spectrum[40, 52, 54] provides a protein fingerprint similar to the ^{15}N-^{1}H HSQC in solution NMR. The (H)NH pulse scheme, (Figure 12) includes a first 90°pulse on the ^{1}H-channel to generate transverse magnetization, which is transferred to ^{15}N spins through CP. ^{15}N evolution proceeds under ^{1}H low-power decoupling, encoding for ^{15}N chemical shift during the t_1, and transferred back to the ^{1}H with a second CP step (with a typical global efficiency of 70 %). Importantly, the water signal can be efficiently suppressed with low-power schemes, such as the MISSISSIPPI sequence.[64]

At 60 kHz MAS this spectrum can be acquired with adequate signal-to-noise ratio in 5-30 minutes for a perdeuterated, fully back $^{1}H^{N}$-exchanged protein, depending on the complexity of the system analyzed, and packing factor, using only 2-3 mg of sample. Linewidths of approximately 50-100 Hz for ^{1}H and 20-60 Hz for ^{15}N are usually observed. As an example, Figure 13 shows the (H)NH spectrum of microcrystalline His6-tagged ubiquitin[65] at 60 kHz MAS on a 800 MHz (18.8 T) spectrometer (details about sample preparation and NMR experiments are reported in Appendix).

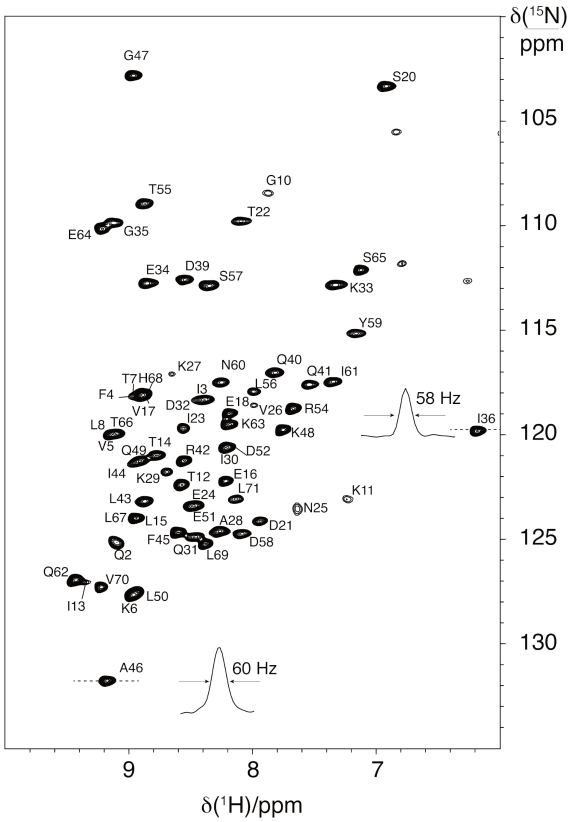

Figure 13. (H)NH spectrum of [U-$^{1}H^{N}$,^{2}H,^{13}C,^{15}N]-labeled microcrystalline His6-tagged ubiquitin recorded by the author at 60 kHz MAS on a 800 MHz (18.8 T) spectrometer. ^{1}H cross-sections for cross-peaks of Ile36 and Ala46 residues are shown with the respective linewidths.

II.3 A suite of 3D experiments for sequential assignment

II.3.1 (H)NH as a building block for 3D experiments: (H)CANH and (H)CONH sequences

The (H)NH experiment can be used as an efficient detection module to build 3D triple-resonance experiments. In the simplest implementation, $^{1}H^{N}$-$^{15}N^{H}$ pairs can be correlated to the neighboring (intraresidue) $^{13}C^{\alpha}$ in the (H)CANH sequence (Figure 14C):[52] after the excitation of ^{1}H spins with the first 90˚pulse, magnetization is transferred through CP to $^{13}C^{\alpha}$. ^{13}C evolution proceeds under low-power ^{1}H decoupling. In the middle of the $^{13}C^{\alpha}$ evolution period, a selective 180˚pulse is applied to the ^{13}CO to refocus the evolution due to the scalar coupling between ^{13}CO and $^{13}C^{\alpha}$ and thus to maximize resolution. Magnetization is then transferred to the neighboring $^{15}N^{H}$ nucleus through CP, and the pulse sequence continues in exactly the same way as (H)NH, yielding a correlation of the $^{13}C^{\alpha}$ spin to the $^{1}H^{N}$-$^{15}N^{H}$ pair.

In an analogous way $^{1}H^{N}$-$^{15}N^{H}$ pairs can be correlated to the neighboring ^{13}CO of the preceding residue in the (H)CONH sequence (Figure 14A).[48, 52]

Typical acquisition times required for sufficient signal-to-noise ratio and resolution for these two experiments range between 1 hour and 1 day, depending on the sample. The relative sensitivity with respect to the (H)NH (evaluated from the integral of the first increment FID) in a fully back-protonated, deuterated sample for both experiments ranges usually between 20 and 35%.

II.3.2 Transferring coherences using scalar ^{13}C-^{13}C coupling: (H)(CO)CA(CO)NH and (H)CO(CA)NH sequences

At MAS rates of 60 kHz and above, coherences lifetimes are long enough (> 15-20 ms) to allow the exploitation of scalar couplings for homonuclear ^{13}C-^{13}C magnetization transfers.[66-67] The principal advantage of this kind of magnetization transfer is high selectivity. In contrast to previously used methods based on spin-diffusion, this allows to establish correlations only among the species of interest, thus greatly reducing the ambiguity of the assignment. *J*-based transfer is exploited in the (H)(CO)CA(CO)NH[68] and (H)CO(CA)NH[52] experiments, which establish correlations between the $^{1}H^{N}$-$^{15}N^{H}$ pairs and the $^{13}C^{\alpha}$ of the preceding residue and the ^{13}CO of the same residue, respectively, complementing the information available from (H)CONH and (H)CANH.

The (H)CO(CA)NH sequence (Figure 14B) begins exactly as the (H)CONH sequence. After the ^{13}CO evolution period, an INEPT step is performed, which transfers the magnetization to the neighboring $^{13}C^{\alpha}$ spin. After having refocused the antiphase term with respect to ^{13}CO to a pure in-phase $^{13}C^{\alpha}$ term, the magnetization is transferred to ^{15}N with CP, and then to ^{1}H for detection, as in the previously described experiments.

The (H)(CO)CA(CO)NH (Figure 14D) adopts a quite different approach, and does *not* start with ^{1}H-$^{13}C^{\alpha}$ CP. Instead, after the first ^{1}H-^{13}CO CP, a first INEPT step is used to transfer magnetization to the neighboring $^{13}C^{\alpha}$ spin, and after the evolution in the t_1 dimension, a second INEPT step transfers the magnetization back to the ^{13}CO spin. In this way (a.k.a. "out-and-back"), a typically longer ^{13}CO coherence lifetime is exploited. Next, the pulse sequence proceeds as in the (H)CONH experiment.

Typical acquisition times in order to obtain sufficient signal-to-noise ratio and resolution for these two experiments range between few hours and few days, depending mostly on the ^{13}CO and $^{13}C^{\alpha}$ coherence lifetimes. Typically, the sensitivity with respect to the (H)NH ranges between 5 and 12% for the (H)CO(CA)NH sequence, and between 10 and 20% for the (H)(CO)CA(CO)NH one.

II.3.3 Extending the connectivity to the $^{13}C^{\beta}$: (H)(CA)CB(CA)NH and (H)(CA)CB(CA)(CO)NH sequences

The strategy described above can be developed to establish connectivity between $^{1}H^{N}$-$^{15}N^{H}$ pairs and the $^{13}C^{\beta}$ of the same or the preceding residue in the (H)(CA)CB(CA)NH[68] and (H)(CA)CB(CA)(CO)NH sequences, respectively.

The (H)(CA)CB(CA)NH (Figure 14E) adapts the same strategy as the previously described (H)(CO)CA(CO)NH: after the first ^{1}H-$^{13}C^{\alpha}$ CP the magnetization is transferred from the $^{13}C^{\alpha}$ to the $^{13}C^{\beta}$ spins, $^{13}C^{\beta}$ chemical shift-encoded in t_1, and then transferred back to $^{13}C^{\alpha}$. A *z*-filter is introduced to dephase any undesired transverse ^{13}C magnetization prior to the transfer to ^{15}N.

The (H)(CA)CB(CA)(CO)NH experiment (Figure 14F) employs nearly the same pulse scheme, except the fact that after that the magnetization is transferred back to the $^{13}C^{\alpha}$ spin, a second INEPT step is introduced to transfer the magnetization to the neighboring ^{13}CO spin, from which is transferred to ^{15}N through CP.

Typical acquisition times in order to obtain adequate signal-to-noise ratio and resolution for these two experiments range between several hours and few days. Typical sensitivity, compared to the (H)NH experiment, is approximately 5-15% for the (H)(CA)CB(CA)NH

sequence and below 10% for the (H)(CA)CB(CA)(CO)NH, which is the least sensitive one among the six 3D pulse sequences described here. Recently, an improvement of the latter experiment has been proposed in our group (*unpublished results*), which greatly reduces magnetization losses by concatenation of INEPT transfers, and thus nearly equalizes the performance of both $^{13}C^{\beta}$-correlating pulse schemes.

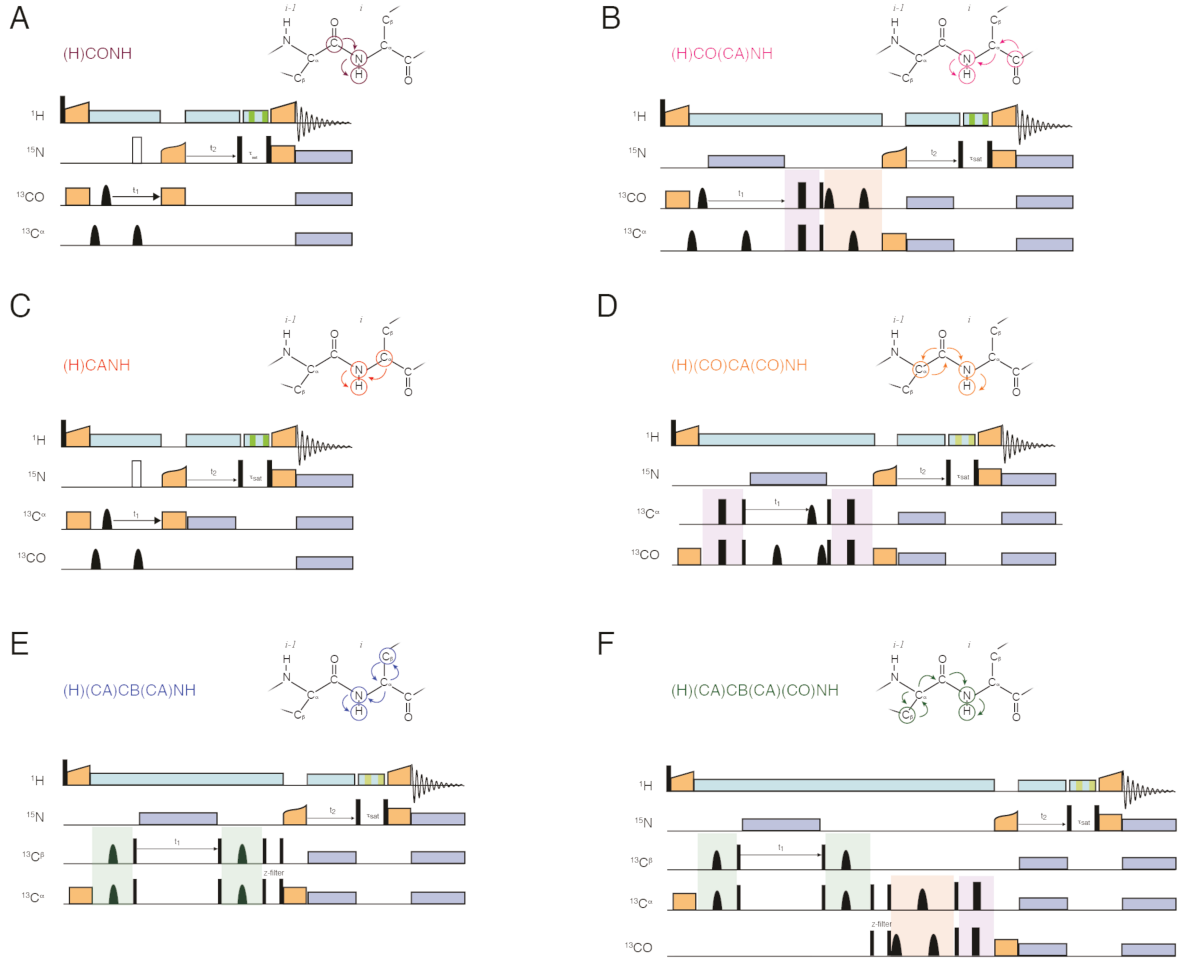

Figure 14. Pulse schemes for the six sequential backbone assignment experiments, with an illustration of the coherence transfers and spins involved (the first ^{1}H-^{13}C CP is omitted in the coherence transfers illustration). A) (H)CONH experiment, for inter-residue ^{13}CO correlation. B) (H)CO(CA)NH, for intraresidue ^{13}CO correlation. C) (H)CANH, for intraresidue $^{13}C^{\alpha}$ correlation. D) (H)(CO)CA(CO)NH, for inter-residue $^{13}C^{\alpha}$ correlation. E) (H)(CA)CB(CA)NH experiment, for intraresidue $^{13}C^{\beta}$ correlation. F) (H)(CA)CB(CA)(CO)NH experiment, for inter-residue $^{13}C^{\beta}$ correlation. Narrow and broad black rectangles indicate 90˚and 180˚ non-selective pulses, bell shapes represent selective inversion pulses, orange boxes indicate cross-polarization steps, and gray and azure boxes denote a heteronuclear decoupling. The water suppression block is indicated by the striped box. Spin echoes involved in the transfer between ^{13}CO and $^{13}C^{\alpha}$ are indicated in purple and red, while those involved in the transfer between $^{13}C^{\beta}$ and $^{13}C^{\alpha}$ are indicated in green. Reproduced and adapted from reference 1.

II.3.4 Sequence-specific resonance assignment with ^{1}H-detection

The joint analysis of the set of the six spectra allows sequence-specific resonance assignments. The simultaneous matching of three ^{13}C chemical shifts (^{13}CO, $^{13}C^{\alpha}$, $^{13}C^{\beta}$) yields a high level of redundancy for establishing sequential connectivity, in a similar way to

the assignment protocols used in solution NMR. In a manual approach, this is realized stepwise as follows: firstly, $^{13}C^{\alpha}$ and $^{13}C^{\beta}$ chemical shifts of each spin system allow for a crude classification of the residue type, secondly, a sequential matching of spin systems is established. Fragments of three and more sequentially connected spin systems can then usually be unambiguously aligned with the protein sequence.

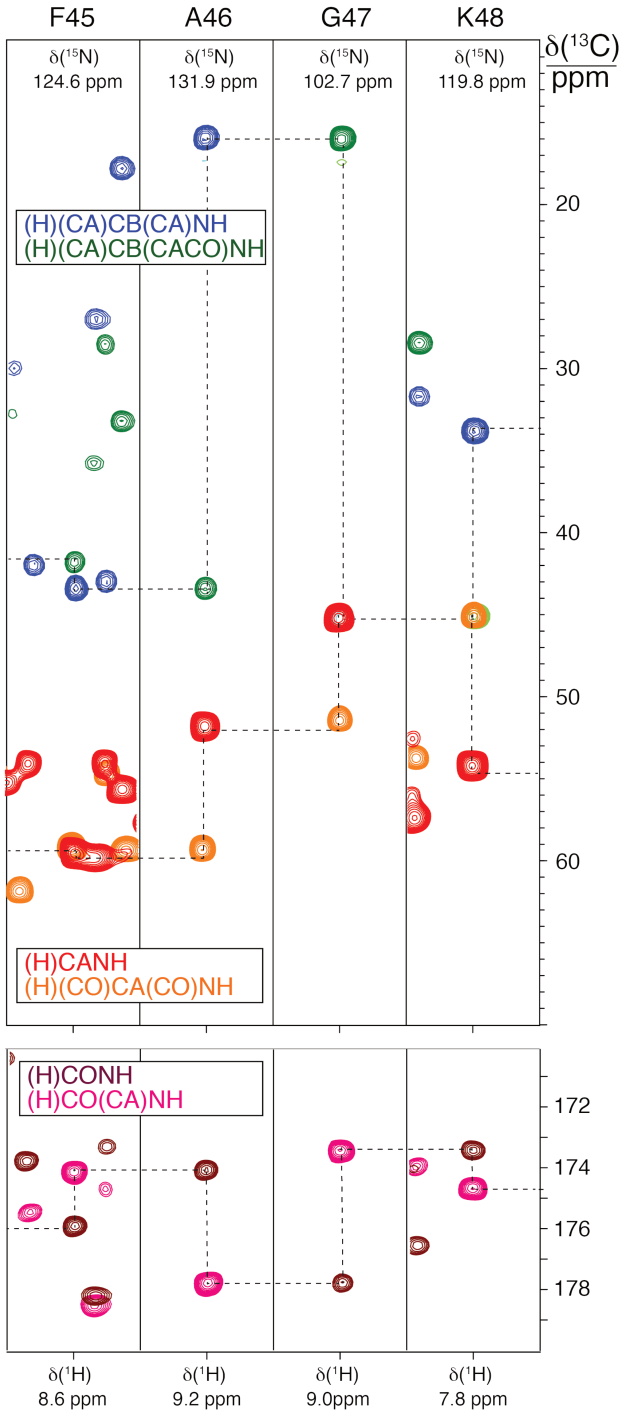

Figure 15. Strip plots of inter- and intraresidue ^{13}CO, $^{13}C^{\alpha}$ and $^{13}C^{\beta}$ correlations for selected $^{1}H^{N}$-$^{15}N^{H}$ pairs in microcrystalline ubiquitin recorded at 60 kHz MAS and on a 800 MHz spectrometer.

This is illustrated in Figure 15 for microcrystalline His6-tagged ubiquitin (whose ^{1}H assignment in the solid-state, albeit in the absence of the His6-tag, was first reported by Meier and coworkers),[69] where the ^{13}C strips for $^{1}H^{N}$-$^{15}N^{H}$ pairs from four consecutive residues are shown. From the analysis of the $^{13}C^{\alpha}$ and $^{13}C^{\beta}$ chemical shifts it is possible to unambiguously classify two of the four residues as a glycine and an alanine, respectively (note that the negative strong peaks appearing at the glycine $^{13}C^{\alpha}$ position in the (H)(CA)CB(CA)NH and (H)(CA)CB(CA)(CO)NH spectra additionally confirms for the identification of glycine residues). By exploiting the connectivity between different spin systems, the fragment can be matched to the sequence.

For relatively small systems, displaying sufficiently resolved triple-resonance 3D spectra, the application of computational backbone assignment algorithms automated analysis appeared to be possible. Notably, it was demonstrated[1] that automatic assignment can be obtained by manually assembling six peak lists of NMR resonance signals from the NMR experiments and subjecting them together with the six correlation patterns and the protein sequence to a modified version of the program UNIO-MATCH.[70] The automation represents an attractive feature that is essential to accelerate and render more unbiased both the data analysis and the assignment procedure.

In this work, I was involved in the inspection of spectra of the membrane-embedded conductance domain from influenza A M2, and verification of peaklists.

II.3.5 Case study I: backbone assignment of a paramagnetic protein, Cu^{II},Co^{II}-SOD

In this section the application of the aforementioned techniques is illustrated in the backbone assignment of a paramagnetic mutant of the human superoxide dismutase 1 (SOD1).

SOD is 16x2 kDa homodimer,[71-72] and each monomer is comprised of 153 residues and contains two binding sites for metal cations, whose metallation state can be experimentally controlled allowing to obtain different NMR effects with minimal structural perturbation.[73] The structural investigation of this protein will be the object of Chapter V, therefore a more detailed description of the system will be provided there.

In the present analysis a sample containing Cu^{II} in one site and Co^{II} in the second one is used. As it will be discussed in Chapter V, in this metallation state both metal ions possess very short electronic correlation times (~10^{-11} s for Cu^{II} and ~$5\cdot10^{-11}$ s for Co^{II}),[73] with minimal PRE effect on the surrounding nuclei, according to the equations provided in Chapter I.

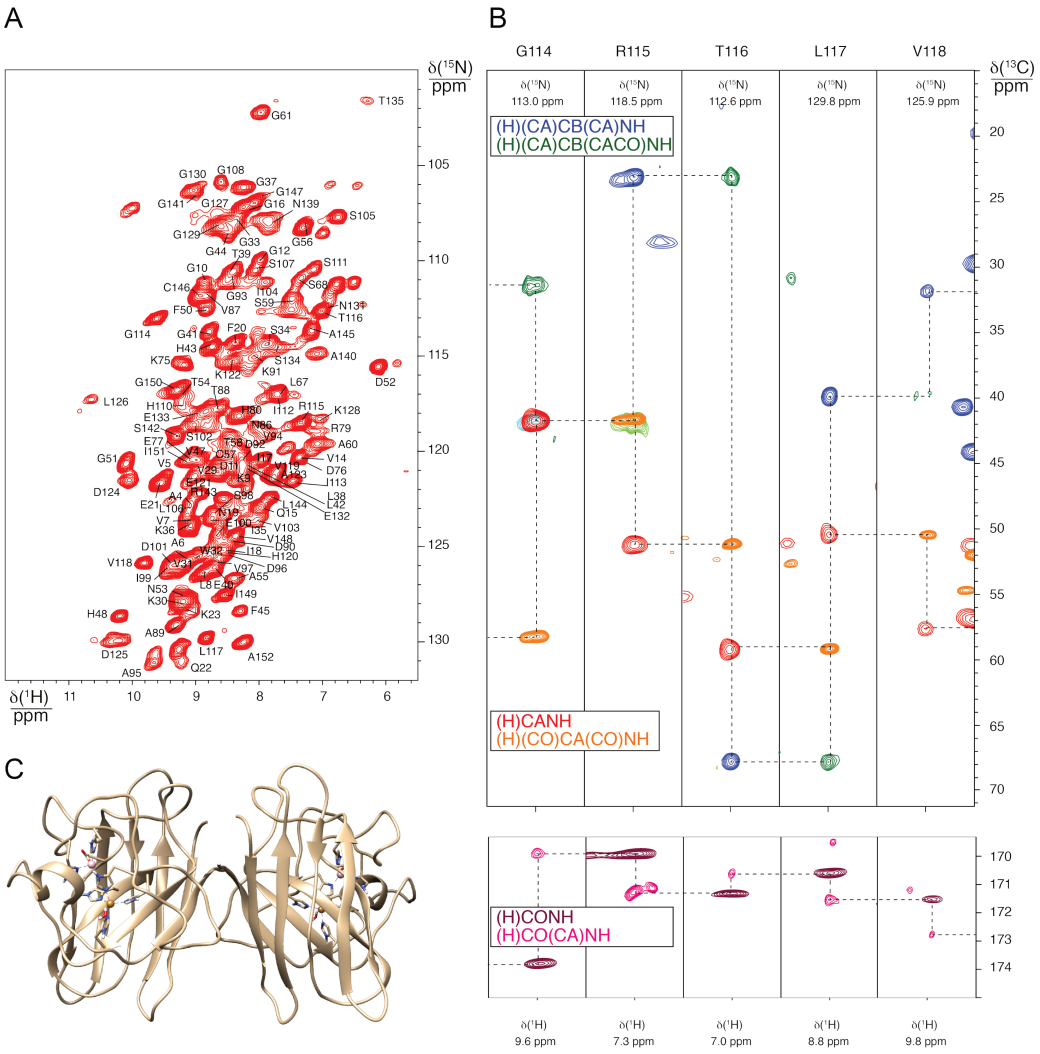

Figure 16. A) (H)NH spectrum of [U-$^{1}H^{N}$,^{2}H,^{13}C,^{15}N]-labeled microcrystalline Cu^{II},Co^{II}-SOD acquired at 60 kHz MAS on a 800 MHz (18.8 T) spectrometer. B) Strip plots of inter- and intraresidue ^{13}CO, $^{13}C^{\alpha}$ and $^{13}C^{\beta}$ correlations to $^{1}H^{N}$-$^{15}N^{H}$ pairs of Cu^{II},Co^{II}-SOD. C) Structure of the homodimer of SOD (PDB code: 1SOS).

Under this favorable circumstances coherence lifetimes are sufficiently long to allow the acquisition of well-resolved fingerprint spectra. Figure 16A shows the (H)NH spectrum of perdeuterated fully back exchanged Cu^{II},Co^{II}-SOD acquired at 60 kHz MAS. Approximately 90 well-resolved site-specific resonances are identified. Linewidths of approximately 90-120 Hz for ^{1}H and 30-70 Hz for ^{15}N are observed.

In these conditions all the 3D experiments for backbone assignment were acquired with good resolution and sensitivity, as shown in a representative strip-plot in Figure 16B. The obtained assignment is reported in Appendix, as well as details about sample preparation and NMR experiments. A total of 123 out of 148 amide ^{1}H and ^{15}N of non-proline residues (85 %) were assigned, and 125 out of 153 $^{13}C^{\alpha}$ spins (81 %) could be assigned as well. The assignment for ^{13}CO and $^{13}C^{\beta}$ is less complete (67 % and 69 % respectively), due to extensive signal overlap in some regions of the spectra and lower sensitivity of the respective

experiments. Notably, it was possible to partially assign the backbone shifts of some of the histidines coordinating the two metal ions (His48, His80, His120). For His48 and His120 the assignment could be extended to the $^{13}C^{\beta}$ spins, whose chemical shifts (61.8 and 56.2 ppm, respectively) is quite large compared to average values for histidine (30.3 ppm according to the Biological Magnetic Resonance Data Bank), which is a clear indication of a non-negligible hyperfine contribution. The unassigned residues are mostly located in unstructured parts of the protein, or spatially close to one of the metal ions.

II.4 Protein backbone assignment in a single spectrum

II.4.1 Direct matching of amide resonances as an additional strategy

The approach described in Section II.3 relies on establishing intra- and inter-residue correlations in six spectra correlating ^{15}N-^{1}H groups to ^{13}CO, $^{13}C^{\alpha}$ and $^{13}C^{\beta}$ resonances. This typically ensures sufficient data to resolve degeneracies for sequential connectivity.

As an additional strategy for sequential resonance assignment, direct matching of amide resonances can be used. In solution, introduction of multiple ^{15}N frequencies has been shown to greatly reduce the ambiguity in crowded spectra of disordered proteins,[74-76] an approach that built upon other amide matching strategies.[77-80] These pulse sequences rely on weak $^{3}J_{C\alpha\text{-}C\alpha}$ scalar couplings, or require many scalar transfer steps. The efficiency is high for small molecules, but generally prohibitively low for larger molecules. For proteins in the solid state, ^{15}N-^{15}N correlations schemes based on through-space magnetization transfers have been proposed at both slow[81] and fast MAS,[82] but the resulting spectra contain both sequential and long-range cross-peaks and are therefore of limited use for assignment.

II.4.2 The (H)N(CO)(CA)NH and (H)N(CA)(CO)NH sequences

We developed two new 3D pulse sequences, (H)N(CO)(CA)NH and (H)N(CA)(CO)NH, that correlate the amide $^{1}H^{N}$-$^{15}N^{H}$ pair of a residue *i* with the amide ^{15}N of residue *i*+1 and *i*-1, respectively. The efficiency of the pulse sequence leans on long ^{13}C coherence lifetimes under fast MAS and low power ^{1}H decoupling. These conditions also favor fast recycle times with low risk of sample degradation. Five coherence transfers are employed: one ^{13}C-^{13}C scalar based transfer, and 4 cross polarization (CP) transfers between ^{1}H and ^{15}N and between ^{13}C and ^{15}N (Figure 17).

Within the same transfer pathway, three additional chemical shifts can be evolved, namely of a starting $^{1}H^{N}$ and of the bridging ^{13}CO and $^{13}C^{\alpha}$ nuclei enabling acquisition of high dimensional spectra.

The new sequences result in spectra that are diagonal free, which decreases spectral crowding: they correlate the chemical shifts of a residue (*i*) and the $^{15}N^{H}$ shift of *only* the preceding (*i*-1) or the following (*i*+1) residue.

The applicability of the proposed experiment was verified on five proteins, including microcrystalline and sedimented ones. In particular, my contribution was represented by sample preparation of microcrystalline ubiquitin, deuterated and fully back-protonated at labile amide sites. I also performed data acquisition and spectral analysis on the same sample.

One concern in this approach is the sensitivity as five coherence transfers are employed. When referred to the (H)NH (evaluated from the integral of first increment), (H)N(CO/CA)(CA/CO)NH show comparable signal-to-noise as (H)(CA)CB(CA)(CO)NH experiment. For the sample of ubiquitin, we found a sensitivity of 7% for the (H)N(CA)(CO)NH experiment, and of 6% for the (H)N(CO)(CA)NH experiment, respectively. Typical acquisition times in order to obtain adequate signal-to-noise ratio and resolution for these two experiments range between several hours and a few days (36 hours in the case of ubiquitin).

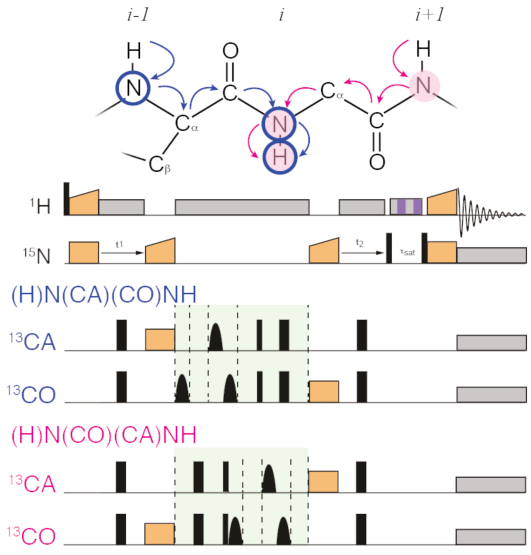

Figure 17. Schematic magnetization pathway (*top*) and pulse schemes for the (H)N(CA)(CO)NH (blue) and the (H)N(CO)(CA)NH (magenta) experiments. Heteronuclear transfers via cross polarization are shown in orange, while the homonuclear scalar $^{13}C^{\alpha}$-^{13}CO transfer is highlighted in green. Bell shapes represent selective inversion pulses. Excitation and inversion pulses are shown as narrow and broad black rectangles, respectively. Gray rectangles represent heteronuclear decoupling. The water suppression block is indicated by the striped box. Reproduced and adapted from reference 2.

II.4.3 The (H)N(CO)(CA)NH and (H)N(CA)(CO)NH allow fast sequential assignment

In contrast to ^{13}C matching approaches, here each individual signal encodes a pair of nitrogen shifts, and, in principle, a single spectrum is thus sufficient for linking amide resonances along the protein backbone.

A more robust approach is however obtained when both 3D datasets are recorded. The simultaneous analysis of signals from the pair builds triplets of $^{15}N^{H}$ chemical shifts. As illustrated in Figure 18, the simultaneous matching of these triplets establishes connections spanning three residues. The alignment of stretches relies on two $^{15}N^{H}$ frequencies that are directly correlated in each spectrum. Comparable reliability of sequential assignment would require two pairs of ^{13}C-based spectra. Additionally, matching $^{15}N^{H}$ shifts results in low peak overlap due to the excellent resolution of $^{15}N^{H}$.

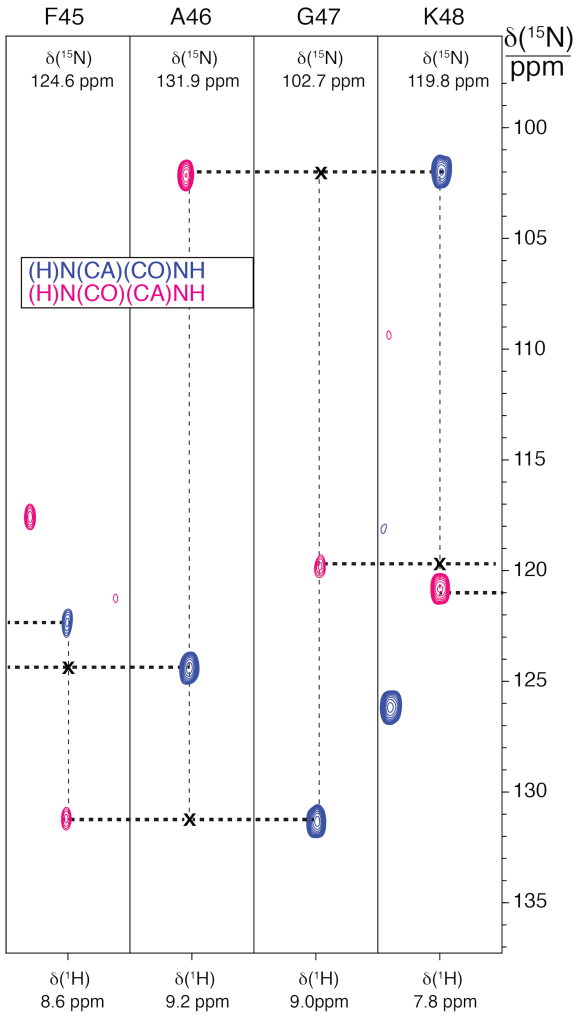

Figure 18. Strip plots of N^{H} (i+1) and N^{H} (i-1) resonances for H^{N}-N^{H} pairs observed in (H)N(CO)(CA)NH and (H)N(CA)(CO)NH spectra for ubiquitin, for the same residues used in **Figure 15**. The position of the hypothetical diagonal peak (not observed in the spectra) in the second indirect ^{15}N dimension is indicated with a bold cross ('x'). The spectra are obtained at 60 kHz MAS and on an 800 MHz (18.8 T) spectrometer.

Once the signals are identified, the sequence-specific assignment of resonances can be quickly obtained with automated protocols, such as those developed for solution NMR data, and implemented in UNIO-MATCH.[70,83] In the case of microcrystalline His6-tagged ubiquitin (76 amino acids),[65] 41 and 43 peaks were identified in the (H)N(CA)(CO)NH and (H)N(CO)(CA)NH spectra, respectively. Inter-residue linking was determined by UNIO-MATCH for 38 $^{15}N^{H}$-$^{1}H^{N}$ pairs. The resulting assignment shows little deviations with respect to that of non His6-tagged microcrystals.[69]

We showed that a bidirectional amide ^{15}N matching results in the unambiguous identification of sequential stretches of residues for proteins in different aggregation states. For long stretches and highly complete data, correct assignment is possible, while with less complete data (as for the sample of ubiquitin), both correct residue placement and sequential linking can be done with the addition of datasets encoding $^{13}C^{\alpha}$ or $^{13}C^{\beta}$ shifts (e.g. (H)CANH or (H)(CA)CB(CA)NH spectra previously described) because these shifts are particularly sensitive to residue type and secondary structure. This is particularly relevant when large portions of the protein (often flexible loops or tails) are not observed in the MAS spectra.

In conclusion, this method simplifies protein resonance assignment, providing spectra that can be rapidly and automatically assigned using UNIO-MATCH. Amide signals provide particularly unambiguous sequential connectivity and can be applied generally to microcrystalline and sedimented deuterated proteins. This method is expected to be useful for a wide range of insoluble crystalline or non-crystalline samples.

II.5 Structure of fully protonated proteins by proton-detected MAS NMR

II.5.1 Spinning faster: MAS NMR in the 100-111 kHz regime

The advent of 1.3 mm MAS probes capable of spinning at 60 kHz represented a major breakthrough in the biomolecular solid-state NMR community. However, proton resonances remain significantly dipolar broadened at 40-60 kHz, and extensive deuteration is still required for most proteins in order to obtain sufficiently resolved spectra, and to allow the acquisition of multidimensional spectra.[62, 83-86]

This severely limits observation of side chain signals, which are essential for the determination of a protein structure at high resolution. The redundancy of information intrinsic to spectra of proteins protonated in side chains, leads to a mutually supportive network of distance restraints, and thus is crucial to an unbiased and robust spectral analysis by unsupervised algorithms.[32, 87-89] Moreover, complete amide reprotonation in the interior of the protein can be problematic for systems that lack a refolding protocol, and deuterated media can reduce or even eliminate protein expression.[90] Even if different approaches to selective reintroduction of protons in side-chains exist, such as fractional ^{2}H labeling,[39, 91-92] ILV methyl labeling[17, 93-94] or Stereo-Array Isotope Labeled (SAIL),[95] they are not widely applicable, considering that they still require to deal with deuterated media, or due to their high cost.

All these drawbacks are overcome if resolved side chain proton resonances are available from a fully protonated sample. Fully-protonated samples are by far the simplest to produce, and their effective use could be applied to a much wider array of molecules including biomolecules labeled in mammalian systems.[96]

The need for narrow proton resonances without such extreme levels of deuteration has motivated a continuous technological development resulting in a dramatic increase in the available spinning frequency.[47, 58, 82, 94, 97-100] With the availability of the first probes reaching 100 kHz MAS,[101] it has been demonstrated that in this regime resonance assignment,[100] structure determination, and interaction studies,[97] are possible on perdeuterated fully back-exchanged model proteins with as little as 0.5 mg of sample.[94]

In our laboratory, we had the possibility to test the first prototype of a Bruker 0.7 mm probe operating on a 1 GHz (23.5 T) spectrometer and reaching spinning frequencies of 100-111 kHz. Equipped with this probe, we demonstrated for the first time the feasibility of the *de novo* structure determination of two fully protonated proteins (notably a 28-kDa protein dimer in 2.5-MDa viral capsid assembly) with ^{1}H-detected MAS NMR, which opens the avenue to the NMR study of systems of increasing complexity.[3]

In this work I mainly contributed in the acquisition and analysis of NMR data for the GB1 protein. Therefore in this section only the results concerning this protein are presented.

II.5.2 Resolution and sensitivity of ^{1}H-detected spectra at 111 kHz MAS

When MAS rates increase from 60 to 100 kHz and above, a dramatic improvement in resolution and sensitivity is observed for fully protonated proteins, which allows the acquisition of resolve ^{1}H-detected 2D and 3D correlation spectra without the need of

deuteration. This is illustrated in Figure 19, where the (H)NH and subregions of (H)CH spectra of the protonated microcrystalline beta 1 immunoglobulin binding domain of protein G (GB1) are shown (details about NMR experiments are reported in Appendix). GB1 is a 6.2-kDa model protein known for its high spectral quality in solid-state NMR.[102] Typical $^{1}H^{N}$ linewidths decrease from about 250 Hz at 60 kHz MAS to 120 Hz at 111 kHz MAS. Most notably, full protonation allows access to side chains protons with well resolved ^{1}H-^{13}C correlation spectra ((H)CH, which pulse sequence is equivalent to the (H)NH one where the ^{13}C and ^{15}N channel are swapped). Typical linewidths for aliphatic ^{1}Hs range between 120 and 200 Hz, depending mostly on the multiplicity of CH_n group.

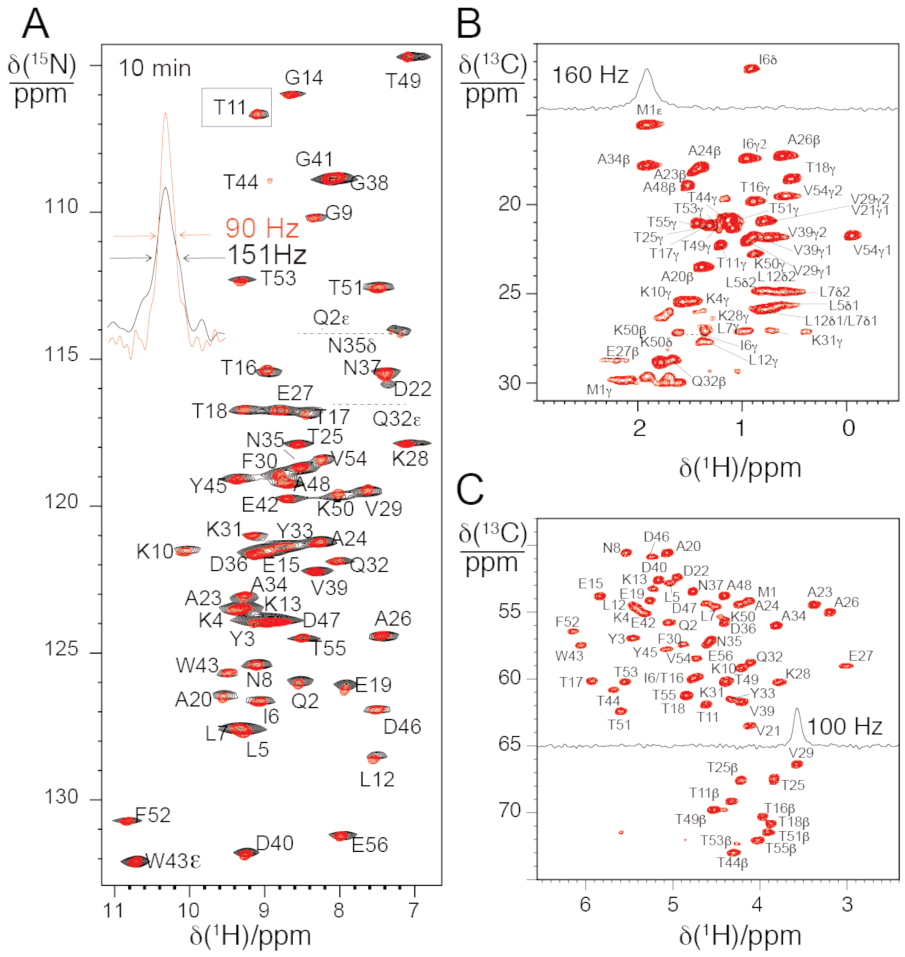

Figure 19. A) (H)NH spectra of microcrystalline [U- ^{13}C, ^{15}N]-labeled GB1 acquired at 60 (black) and 111 (red) kHz MAS in a 1 GHz (23.5 T) spectrometer. A representative ^{1}H cross-section and linewidth are shown for residue Thr11. B) Methyl and, C) $^{1}H^{\alpha}$-$^{13}C^{\alpha}$ regions of the (H)CH spectrum of the same protein acquired at 111 kHz MAS on a 1 GHz spectrometer. Reproduced from reference 3.

Increased spinning rate and resolution come at the expense of the total sample volume. However, this loss is partially compensated by the increased inductive coupling of smaller coils, and especially by the increased coherences lifetimes. For GB1, bulk $^{1}H^{N}$ transverse coherence lifetimes (T_2'), increased to 4.6 ms at 111 kHz MAS compared to 1.8 ms at 60 kHz

MAS, which translated into narrower lines and thus higher sensitivity of detection. T_2' increased as well for ^{13}CO (from 14 to 46 ms), $^{13}C^{\alpha}$ (from 42 to 77 ms), and $^{15}N^{H}$ (from 60 to 120 ms). This is reflected in an overall improvement of the efficiency of multidimensional experiments involving multiple coherence transfers schemes, notably *J*-based transfers.

II.5.3 Backbone and side chain resonance assignment

Backbone assignment of GB1 can be easily accomplished with the set of six $^{1}H^{N}$-detected experiments developed for deuterated samples at 60 kHz. In alternative, the pair of experiments described in the previous section also provides sequential linking based on amide matching.[2]

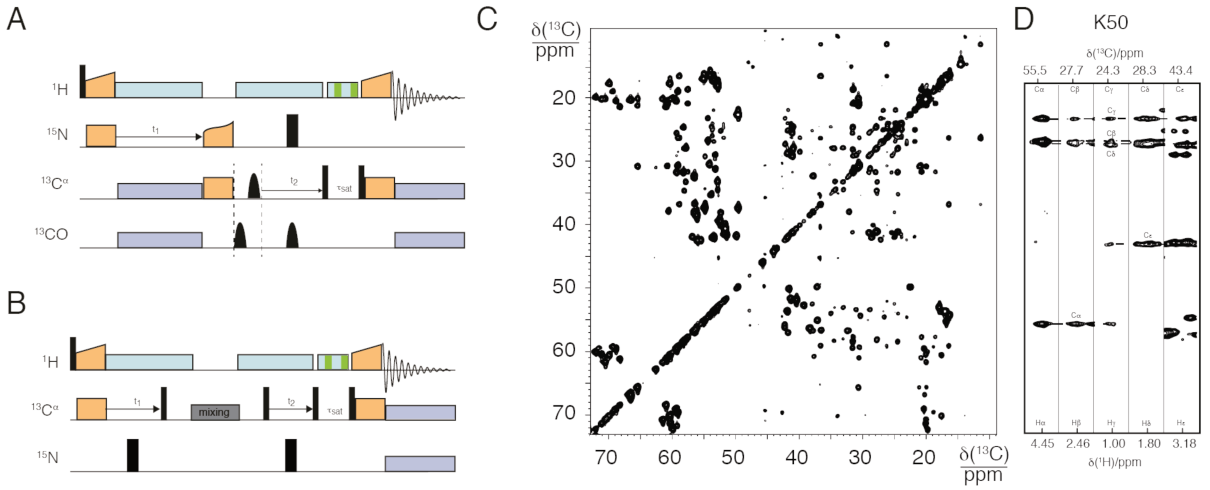

Figure 20. A) Pulse sequence for the (H)NCAHA experiment. B) Pulse sequence for the (H)CCH experiment. C) ^{13}C-^{13}C projection and D) selected strips of the (H)CCH spectrum of GB1 acquired at 111 kHz MAS on a 1 GHz (23.5 T) spectrometer. Reproduced and adapted from reference 3.

Most importantly, resolution and sensitivity are suitable to extend assignment to side chain protons. To perform this, we designed a new procedure in two steps. First, the backbone assignment can be extended to the $^{1}H^{\alpha}$ spins, with the acquisition of an (H)NCAHA spectrum (Figure 20A).[49] This experiment correlates $^{15}N^{H}$-$^{13}C^{\alpha}$ pairs of one residue with the corresponding H^{α} resonance. Then, $^{1}H^{\alpha}$ and $^{13}C^{\alpha}$ chemical shifts are used as anchors to propagate the resonance assignment from backbone to side chains with an (H)CCH spectrum (Figure 20B).[103] This is implemented with a CP-based sequence and WALTZ-16 mixing,[104] applied at a nutation frequency of one quarter of the rotor frequency (to avoid recoupling of dipolar or CSA interactions during 90° pulse elements of which WALTZ-16 is composed), to induce isotropic mixing of ^{13}C magnetization based exclusively on scalar couplings. This spectrum correlates every ^{1}H and ^{13}C pair in an aliphatic side chain to every ^{1}H or ^{13}C resonance within its side chain, resulting in the robust identification of all side chains ^{1}H and

^{13}C shifts. This is in contrast e.g. with ILV labeled samples, in which it is difficult to unambiguously connect a single methyl proton at the end of a side-chain to an amide ^{1}H resonance (in a ^{1}H-detected approach) or to a backbone ^{13}C resonance (in a ^{13}C-detected approach).

Overall, for GB1 the completeness of assignment of proton resonances was 94.4%, and the all atom completeness was 85.9%, with the missing resonances being primarily aromatics. The acquisition and the analysis of the (H)CCH spectrum leading to extensive assignment of side-chains in GB1 was a particular contribution of the author in the work described.

II.5.4 ^{1}H-^{1}H contacts and structure calculation

For the protein fold determination, 3D RFDR (H)NHH and (H)CHH spectra[105] (Figure 21C) were recorded to directly probe ^{1}H-^{1}H proximities (Figure 21A-B). These spectra, acquired in 72 hours for GB1, contain two ^{1}H dimensions, and therefore benefit doubly from the line narrowing of backbone and side-chain proton resonances. In the experiments employed, ^{1}H-^{1}H contacts were resolved with the chemical shift of ^{15}N, aliphatic ^{13}C, or aromatic ^{13}C.

Observed correlations were manually identified, and converted into unassigned peak lists, containing the frequency coordinates and the intensity of each signal. For GB1, the NMR structure was calculated with the UNIO software package using as inputs these unrefined peak lists, the assigned backbone and side-chain chemical shifts, and backbone dihedral angles predicted from the chemical shifts using TALOS+.[106] The standard unsupervised protocol of iterative cross-peak assignment, conversion into distance restraints and structure calculation was applied as implemented in the program UNIO-CANDID.[107] The chemical-shift based assignment tolerances were set to the corresponding experimental linewidths, namely 0.15 and 0.4 ppm (on a 1 GHz spectrometer) for proton and heavy atom dimensions, respectively. Due to the high quality of the input data (in terms of redundancy and mutual support of cross-peaks), an efficient network-anchored assignment of the contacts resulted in a well-defined fold of the protein already in the first cycle of the iterative protocol. This is a crucial criterion certifying the reliability of a result in an unsupervised data analysis run.[88]

The calculated bundle of NMR conformers (Figure 21D) has a backbone heavy atom RMSD of 0.48 Å, an all heavy atom RMSD of 1.04 Å, and deviates from the X-ray structure (PDB code: 2QMT) in the backbone atom positions by 1.45 Å. The structure is held together by a dense network of long-range (between residues i and j, $|i-j|>4$) ^{1}H-^{1}H contacts, which encode distances up to about 5.5 Å (see e.g. Figure 21A). This amounts to 236 meaningful

long-range contacts. The total information content is described by approximately 13.7 meaningful, non-redundant distance restraints per residue, approaching the criteria established for solution NMR determinations at high resolution.[108]

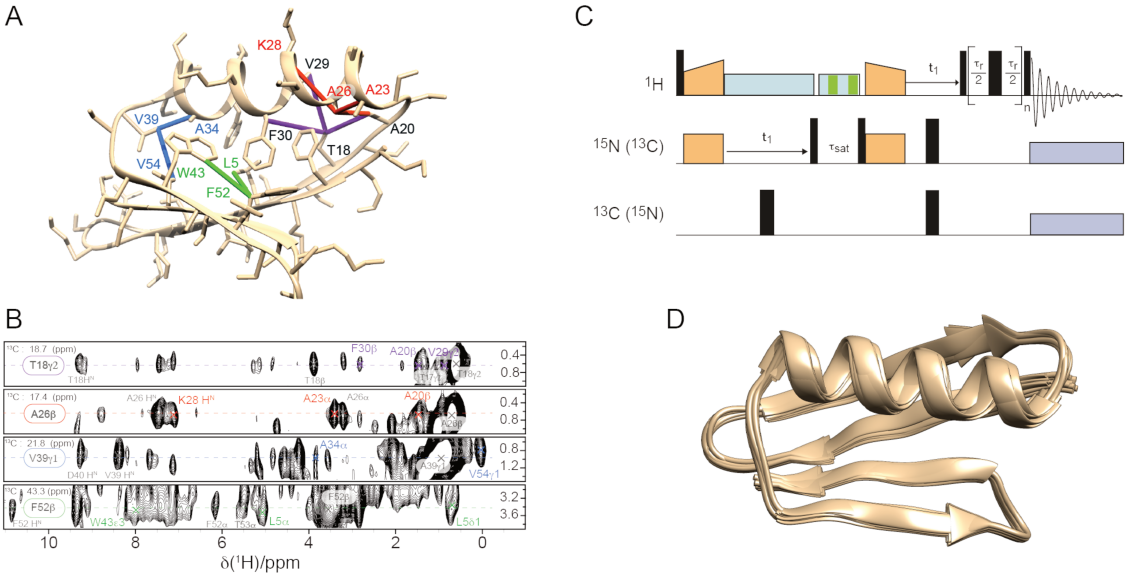

Figure 21. A-B) Representative restraints from the (H)CHH-RFDR spectra displayed on the lowest-energy NMR structure of GB1. The color of these restraints indicates the corresponding strip from the spectra shown in B). C) Pulse sequence for the (H)NHH and (H)CHH RFDR experiments used. Narrow and broad black rectangles indicate 90˚and 180˚ non-selective pulses, orange boxes cross-polarization, gray and azure boxes heteronuclear decoupling. The water suppression block is indicated by the striped box. D) Ribbon diagram of the 10 lowest-energy conformers for GB1. Reproduced and adapted from reference 3.

Previous structural approaches in ^{1}H-detected MAS NMR relied on extensive deuteration, which resulted in the observation of contacts only among amide protons and ILV methyl sites.[43, 52, 93-94, 109] However, amide-amide contacts, or even contacts between ILV methyl and amide protons, represent a small number of the total, the large majority of which involve side-chain protons. While in principle a small set of long-range restraints could define a high quality structure, a large set indicates a high quality determination in the presence of limited precision and assignment ambiguity, which are typical of many systems of interest. The key for obtaining these sets of distance constraints lies in the possibility of directly recording and assigning resolved resonances for proton sites throughout the backbone and side-chains of protein, as described above.

II.5.5 $^{1}H^{\alpha}$-$^{13}C^{\alpha}$ pairs as additional detection probes for protein backbone assignment

The possibility to work with fully protonated proteins paved the way to additional experimental schemes for protein resonance assignment.[4] $^{1}H^{\alpha}$-$^{13}C^{\alpha}$ pairs, which, in contrast to extensively deuterated proteins, are accessible at 100% abundance, can also be used as starting point for propagation of assignment from backbone to side chains.

This complementary assignment strategy exploits the $^{1}H^{\alpha}$-$^{13}C^{\alpha}$ region of the (H)CH spectrum (Figure 19C) as site-specific protein fingerprint, similarly to the (H)NH spectrum. The chemical shift dispersion for proton and heteronuclei is similar to that observed for the (H)NH spectrum, and additionally prolines can be detected.

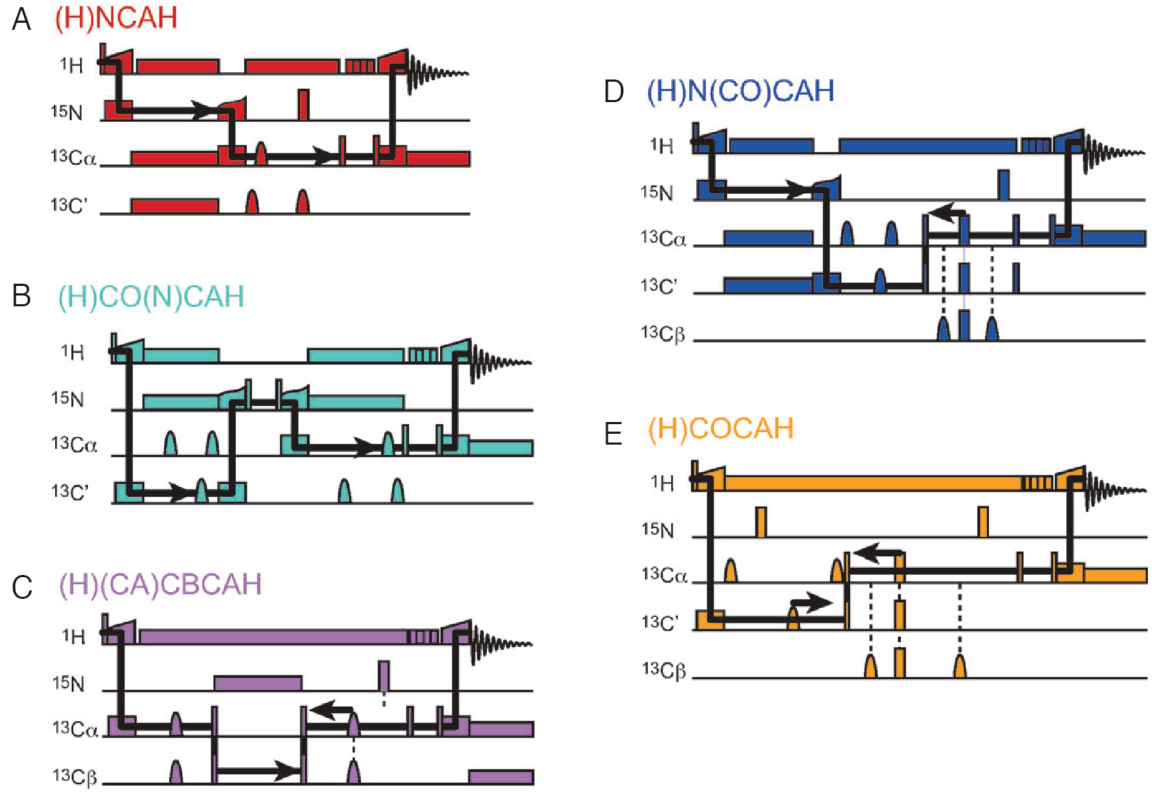

Figure 22. Simplified pulse sequence schemes for the $^{1}H^{\alpha}$-detected experiments described in the text. The indirect ^{13}C or ^{15}N chemical shift evolution periods are denoted with arrows. Reproduced and adapted from reference 4.

We exploited the favorable resolution and sensitivity of the $^{1}H^{\alpha}$ resonances to develop a suite of 3D experiments for sequential backbone and side-chain assignment that employ $^{1}H^{\alpha}$-$^{13}C^{\alpha}$ as the detection scheme. Two complementary pulse sequences, (H)N(CO)CAHA and (H)NCAHA[49] allow to record inter and intra-residue correlations, respectively, which sequentially link $^{1}H^{\alpha}$-$^{13}C^{\alpha}$ pairs by matching a common $^{15}N^{H}$ chemical shift (Figure 22A, D).

An additional pair of spectra, (H)CO(N)CAHA and (H)COCAHA link sequential $^{1}H^{\alpha}$-$^{13}C^{\alpha}$ pairs based on correlations to a common ^{13}CO chemical shift. Simultaneous matching of $^{15}N^{H}$ and ^{13}CO chemical shifts resolves ambiguities and ensures high reliability of sequential assignment (Figure 22B, E). A fifth sequence, (H)CBCAHA provides access to $^{13}C^{\beta}$ chemical shifts, which are of high importance for residue typing, which in turn is essential for the alignment of the linked stretches of pairs with the primary sequence (Figure 22C).

The $^{1}H^{\alpha}$-detected sequences show other advantages compared to $^{1}H^{N}$-detected ones. Notably, ^{13}CO and $^{13}C^{\beta}$ chemical shifts are accessible with higher sensitivity compared to $^{1}H^{N}$-detection, as a result of the shorter coherence transfer pathways. Moreover, $^{1}H^{\alpha}$-detected experiments enable the detection of proline resonances and thus improve the reliability sequential assignment for proline-rich proteins.

Most importantly, the approach based on $^{1}H^{\alpha}$-detection opens the way to assign side chain protons with high sensitivity through TOCSY-based techniques. These protons are sensitive probes of the protein environment, intermolecular interactions, internal dynamics, and three-dimensional structure as previously shown.

II.5.6 Case study II: backbone and side chains assignment of a paramagnetic protein, *Eh*HiPIP I

As a second example of the applicability of the methods discussed above to a paramagnetic protein, we illustrate here the backbone and side chain assignment of a small microcrystalline protein, the high potential iron sulfur protein I, from *Ectothiorhodospira halophila* (*Eh*HiPIP I). This is a 8-kDa, 73-residues long protein which binds a paramagnetic Fe_4S_4 cluster through four cysteine ligands (Cys33, Cys36, Cys50 and Cys66), as discussed in detail in Chapter IV. This example is qualitatively different from SOD in "case study I", since *Eh*HiPIP is investigated without deuteration, and therefore required the use of the ultrafast MAS (> 100 kHz). Indeed, bulk transverse coherences lifetimes $^{1}H^{N}$ increased from 1.3 ms at 60 kHz to 2.3 ms at 111 kHz MAS, while for $^{15}N^{H}$ they increased from 21 to 31 ms, with an undoubted benefit in terms of sensitivity. Data collection and analysis of spectra for *Eh*HIPIP was performed predominantly by the author.

With a set of six 3D experiments ((H)CANH, (H)(CO)CA(CO)NH, (H)CONH, (H)CO(CA)NH, (H)NCAHA and (H)CCH), together with the two 2D fingerprint (H)NH and (H)CH spectra (Figure 23), acquired at 111 kHz on a 1 GHz (23.5 T) spectrometer, it was possible to assign 53 (73%) out of 73 residues. Partial side chains assignment was also obtained. The resonance frequencies are reported in Appendix 7.

Notably, for some residues two sets of resonances for the same nucleus were identified. The significant line broadening observed for many other resonances suggests the presence of unresolved peak splitting also for other nuclei. This is compatible with two backbone conformations observed by X-ray crystallography for molecules in the asymmetric unit of the protein crystal structure (PDB code: 2HIP),[110] as discussed in Chapter IV.

Interestingly, it was possible to detect and assign nuclei experiencing strong hyperfine shifts, e.g. Thr51 or Ala37, whose $^{15}N^{H}$ chemical shift is outside the usually observed region for $^{15}N^{H}$ nuclei, similarly as in solution,[111-112] and to partially assign one of the coordinating cysteine (Cys33). However, the remaining ligand cysteines, as well as the side chain of Cys33, remain inaccessible with the techniques described in the present chapter.

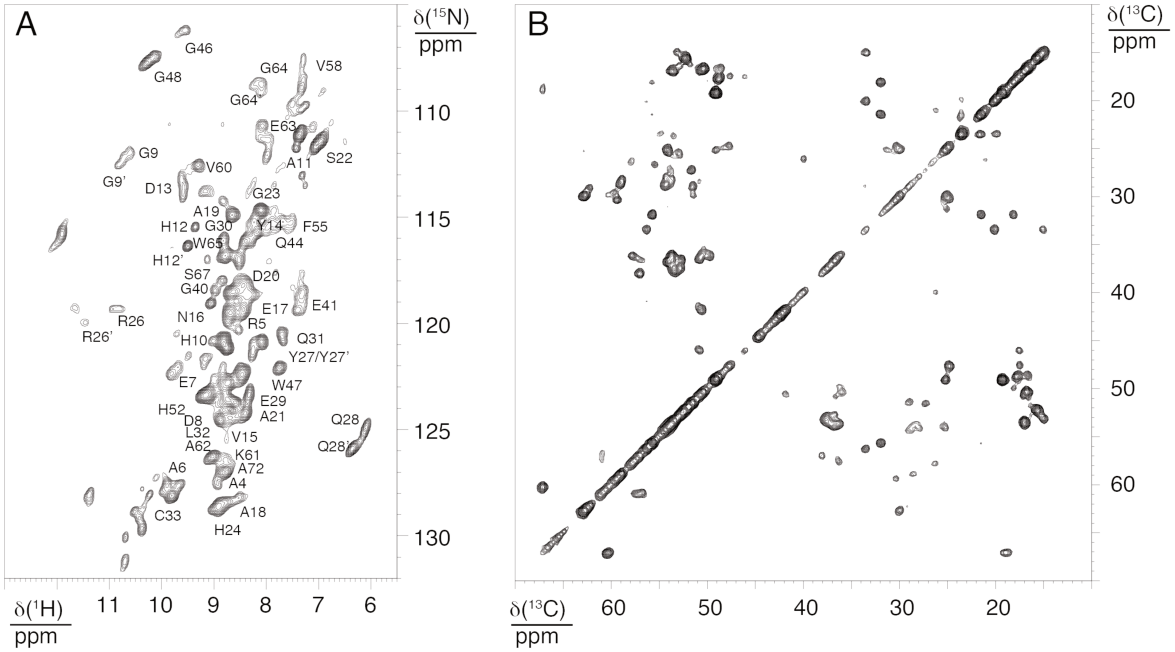

Figure 23. A) (H)NH spectrum of [U-^{13}C,^{15}N]-labeled microcrystalline *Eh*HiPIP acquired at 111 kHz MAS on a 1 GHz (23.5 T) spectrometer. Some of the assigned peaks resonate outside of the displayed region. B) ^{13}C-^{13}C projection of the (H)CCH-TOCSY spectrum of *Eh*HiPIP I acquired at 111 kHz MAS on a 1 GHz (23.5 T) spectrometer.

II.6 Conclusions

In summary, in this chapter the potential of ^{1}H-detection and fast MAS for the structural characterization of proteins is demonstrated. In MAS regimes above 60 kHz, ^{1}H-detected experiments allow the robust assignment of backbone nuclei, in extensively or completely protonated proteins. In many systems, this can be performed with automated algorithms, thus reducing the time required for analysis and rendering the assignment procedure more impartial. This represents a step towards the applicability of MAS NMR to a wide variety of systems that are nowadays still hardly accessible to other experimental techniques.

The techniques described in this chapter can be successfully employed for backbone and side chain assignment of paramagnetic proteins. However, they are not suitable to investigate

nuclei that are very close to the paramagnetic centers. A different approach is therefore needed to accomplish this task, which will be described in the following three chapters.

II.7 References

(1) Barbet-Massin, E.; Pell, A. J.; Retel, J. S.; Andreas, L. B.; Jaudzems, K.; Franks, W. T.; Nieuwkoop, A. J.; Hiller, M.; Higman, V.; Guerry, P.; Bertarello, A.; Knight, M. J.; Felletti, M.; Le Marchand, T.; Kotelovica, S.; Akopjana, I.; Tars, K.; Stoppini, M.; Bellotti, V.; Bolognesi, M.; Ricagno, S.; Chou, J. J.; Griffin, R. G.; Oschkinat, H.; Lesage, A.; Emsley, L.; Herrmann, T.; Pintacuda, G., Rapid proton-detected NMR assignment for proteins with fast magic angle spinning. *J. Am. Chem. Soc.* **2014,** *136*, 12489-12497.

(2) Andreas, L. B.; Stanek, J.; Le Marchand, T.; Bertarello, A.; Cala-De Paepe, D.; Lalli, D.; Krejcikova, M.; Doyen, C.; Oster, C.; Knott, B.; Wegner, S.; Engelke, F.; Felli, I. C.; Pierattelli, R.; Dixon, N. E.; Emsley, L.; Herrmann, T.; Pintacuda, G., Protein residue linking in a single spectrum for magic-angle spinning NMR assignment. *J. Biomol. NMR* **2015,** *62*, 253-261.

(3) Andreas, L. B.; Jaudzems, K.; Stanek, J.; Lalli, D.; Bertarello, A.; Le Marchand, T.; Cala-De Paepe, D.; Kotelovica, S.; Akopjana, I.; Knott, B.; Wegner, S.; Engelke, F.; Lesage, A.; Emsley, L.; Tars, K.; Herrmann, T.; Pintacuda, G., Structure of fully protonated proteins by proton-detected magic-angle spinning NMR. *Proc. Natl. Acad. Sci. U.S.A.* **2016,** *113*, 9187-9192.

(4) Stanek, J.; Andreas, L. B.; Jaudzems, K.; Cala, D.; Lalli, D.; Bertarello, A.; Schubeis, T.; Akopjana, I.; Kotelovica, S.; Tars, K.; Pica, A.; Leone, S.; Picone, D.; Xu, Z. Q.; Dixon, N. E.; Martinez, D.; Berbon, M.; El Mammeri, N.; Noubhani, A.; Saupe, S.; Habenstein, B.; Loquet, A.; Pintacuda, G., NMR spectroscopic assignment of backbone and side-chain protons in fully protonated proteins: microcrystals, sedimented assemblies, and amyloid fibrils. *Angew. Chem. Int. Ed.* **2016,** *55*, 1-6.

(5) Castellani, F.; van Rossum, B.; Diehl, A.; Schubert, M.; Rehbein, K.; Oschkinat, H., Structure of a protein determined by solid-state magic-angle-spinning NMR spectroscopy. *Nature* **2002,** *420*, 98-102.

(6) Rienstra, C. M.; Tucker-Kellogg, L.; Jaroniec, C. P.; Hohwy, M.; Reif, B.; McMahon, M. T.; Tidor, B.; Lozano-Perez, T.; Griffin, R. G., De novo determination of peptide structure with solid-state magic-angle spinning NMR spectroscopy. *Proc. Natl. Acad. Sci. U.S.A.* **2002,** *99*, 10260-10265.

(7) Wasmer, C.; Lange, A.; Van Melckebeke, H.; Siemer, A. B.; Riek, R.; Meier, B. H., Amyloid fibrils of the HET-s(218-289) prion form a beta solenoid with a triangular hydrophobic core. *Science* **2008,** *319*, 1523-1526.

(8) Lu, J. X.; Qiang, W.; Yau, W. M.; Schwieters, C. D.; Meredith, S. C.; Tycko, R., Molecular structure of beta-amyloid fibrils in Alzheimer's disease brain tissue. *Cell* **2013,** *154*, 1257-1268.

(9) Xiao, Y. L.; Ma, B. Y.; McElheny, D.; Parthasarathy, S.; Long, F.; Hoshi, M.; Nussinov, R.; Ishii, Y., A beta(1-42) fibril structure illuminates self-recognition and replication of amyloid in Alzheimer's disease. *Nat. Struct. Mol. Biol.* **2015,** *22*, 499-U97.

(10) Walti, M. A.; Ravotti, F.; Arai, H.; Glabe, C. G.; Wall, J. S.; Bockmann, A.; Guntert, P.; Meier, B. H.; Riek, R., Atomic-resolution structure of a disease-relevant A beta(1-42) amyloid fibril. *Proc. Natl. Acad. Sci. U. S. A.* **2016,** *113*, E4976-E4984.

(11) Colvin, M. T.; Silvers, R.; Ni, Q. Z.; Can, T. V.; Sergeyev, I.; Rosay, M.; Donovan, K. J.; Michael, B.; Wall, J.; Linse, S.; Griffin, R. G., Atomic resolution structure of monomorphic A beta(42) amyloid fibrils. *J. Am. Chem. Soc.* **2016,** *138*, 9663-9674.

(12) Gremer, L.; Schölzel, D.; Schenk, C.; Reinartz, E.; Labahn, J.; Ravelli, R. B. G.; Tusche, M.; Lopez-Iglesias, C.; Hoyer, W.; Heise, H.; Willbold, D.; Schröder, G. F., Fibril structure of amyloid-β(1–42) by cryo–electron microscopy. *Science* **2017,** *358*, 116-119.

(13) Jehle, S.; Rajagopal, P.; Bardiaux, B.; Markovic, S.; Kuhne, R.; Stout, J. R.; Higman, V. A.; Klevit, R. E.; van Rossum, B. J.; Oschkinat, H., Solid-state NMR and SAXS studies provide a structural basis for the activation of alphaB-crystallin oligomers. *Nat. Struct. Mol. Biol.* **2010,** *17*, 1037-1042.

(14) Han, Y.; Ahn, J.; Concel, J.; Byeon, I. J. L.; Gronenborn, A. M.; Yang, J.; Polenova, T., Solid-state NMR studies of HIV-1 capsid protein assemblies. *J. Am. Chem. Soc.* **2010,** *132*, 1976-1987.

(15) Lange, A.; Giller, K.; Hornig, S.; Martin-Eauclaire, M. F.; Pongs, O.; Becker, S.; Baldus, M., Toxin-induced conformational changes in a potassium channel revealed by solid-state NMR. *Nature* **2006,** *440*, 959-962.

(16) Cady, S. D.; Schmidt-Rohr, K.; Wang, J.; Soto, C. S.; Degrado, W. F.; Hong, M., Structure of the amantadine binding site of influenza M2 proton channels in lipid bilayers. *Nature* **2010,** *463*, 689-692.

(17) Andreas, L. B.; Reese, M.; Eddy, M. T.; Gelev, V.; Ni, Q. Z.; Miller, E. A.; Emsley, L.; Pintacuda, G.; Chou, J. J.; Griffin, R. G., Structure and mechanism of the Influenza A M218–60 dimer of dimers. *J. Am. Chem. Soc.* **2015,** *137*, 14877-14886.

(18) Shahid, S. A.; Bardiaux, B.; Franks, W. T.; Krabben, L.; Habeck, M.; van Rossum, B. J.; Linke, D., Membrane-protein structure determination by solid-state NMR spectroscopy of microcrystals. *Nat. Methods* **2012,** *9*, 1212-U119.

(19) Loquet, A.; Sgourakis, N. G.; Gupta, R.; Giller, K.; Riedel, D.; Goosmann, C.; Griesinger, C.; Kolbe, M.; Baker, D.; Becker, S.; Lange, A., Atomic model of the type III secretion system needle. *Nature* **2012,** *486*, 276-279.

(20) Pauli, J.; Baldus, M.; van Rossum, B.; de Groot, H.; Oschkinat, H., Backbone and side-chain ^{13}C and ^{15}N signal assignments of the alpha-spectrin SH3 domain by magic angle spinning solid-state NMR at 17.6 Tesla. *ChemBioChem* **2001,** *2*, 272-281.

(21) Li, Y.; Berthold, D. A.; Frericks, H. L.; Gennis, R. B.; Rienstra, C. M., Partial ^{13}C and ^{15}N chemical-shift assignments of the disulfide-bond-forming enzyme DsbB by 3D magic-angle spinning NMR spectroscopy. *ChemBioChem* **2007,** *8*, 434-442.

(22) Franks, W. T.; Kloepper, K. D.; Wylie, B. J.; Rienstra, C. M., Four-dimensional heteronuclear correlation experiments for chemical shift assignment of solid proteins. *J. Biomol. NMR* **2007,** *39*, 107-131.

(23) Rienstra, C. M.; Hohwy, M.; Hong, M.; Griffin, R. G., 2D and 3D ^{15}N^{13}C^{13}C NMR chemical shift correlation spectroscopy of solids: assignment of MAS spectra of peptides. *J. Am. Chem. Soc.* **2000,** *122*, 10979 - 10990.

(24) Böckmann, A.; Lange, A.; Galinier, A.; Luca, S.; Giraud, N.; Juy, M.; Heise, H.; Montserret, R.; Penin, F.; Baldus, M., Solid state NMR sequential resonance assignments and conformational analysis of the 2 x 10.4 kDa dimeric form of the Bacillus subtilis protein Crh. *J. Biomol. NMR* **2003,** *27*, 323-339.

(25) Eden, M.; Levitt, M. H., Pulse sequence symmetries in the nuclear magnetic resonance of spinning solids: Application to heteronuclear decoupling. *J. Chem. Phys.* **1999,** *111*, 1511-1519.

(26) Takegoshi, K.; Nakamura, S.; Terao, T., ^{13}C–^{1}H dipolar-assisted rotational resonance in magic-angle spinning NMR. *Chem. Phys. Lett.* **2001,** *344*, 631-637.

(27) Bennett, A. E.; Rienstra, C. M.; Auger, M.; Lakshmi, K. V.; Griffin, R. G., Heteronuclear decoupling in rotating solids. *J. Chem. Phys.* **1995,** *103*, 6951-6958.

(28) Fung, B. M.; Khitrin, A. K.; Ermolaev, K., An improved broadband decoupling sequence for liquid crystals and solids. *J. Magn. Reson.* **2000,** *142*, 97-101.
(29) Bertini, I.; Emsley, L.; Lelli, M.; Luchinat, C.; Mao, J.; Pintacuda, G., Ultrafast MAS solid-state NMR permits extensive ^{13}C and ^{1}H detection in paramagnetic metalloproteins. *J. Am. Chem. Soc.* **2010,** *132*, 5558-5559.
(30) Bermel, W.; Bertini, I.; Duma, L.; Felli, I. C.; Emsley, L.; Pierattelli, R.; Vasos, P. R., Complete assignment of heteronuclear protein resonances by protonless NMR spectroscopy. *Angew. Chem. Int. Ed.* **2005,** *44*, 3089-92.
(31) Sattler, M.; Schleucher, J.; Griesinger, C., Heteronuclear multidimensional NMR experiments for the structure determination of proteins in solution employing pulsed field gradients. *Prog. Nucl. Magn. Reson. Spectrosc.* **1999,** *34*, 93-158.
(32) Guerry, P.; Herrmann, T., Advances in automated NMR protein structure determination. *Q. Rev. Biophys.* **2011,** *44*, 257-309.
(33) Ishii, Y.; Yesinowski, J. P.; Tycko, R., Sensitivity Enhancement in Solid-State ^{13}C NMR of Synthetic Polymers and Biopolymers by ^{1}H NMR Detection with High-Speed Magic Angle Spinning. *J. Am. Chem. Soc.* **2001,** *123*, 2921-2922.
(34) Maricq, M. M.; Waugh, J. S., NMR in rotating solids. *J. Chem. Phys.* **1979,** *70*, 3300-3316.
(35) Zheng, L.; Fishbein, K. W.; Griffin, R. G.; Herzfeld, J., Two-dimensional solid-state proton NMR and proton exchange. *J. Am. Chem. Soc.* **1993,** *115*, 6254-6261.
(36) Liu, K.; Ryan, D.; Nakanishi, K.; McDermott, A., Solid-state NMR-studies of paramagnetic coordination-complexes - a comparison of protons and deuterons in detection and decoupling. *J. Am. Chem. Soc.* **1995,** *117*, 6897-6906.
(37) Zheng, L.; Fishbein, K. W.; Griffin, R. G.; Herzfeld, J., 2-dimensional solid-state H-1-NMR and proton-exchange. *J. Am. Chem. Soc.* **1993,** *115*, 6254-6261.
(38) Reif, B.; Jaroniec, C. P.; Rienstra, C. M.; Hohwy, M.; Griffin, R. G., 1H-1H MAS correlation spectroscopy and distance measurements in a deuterated peptide. *J. Magn. Reson.* **2001,** *151*, 320-327.
(39) Asami, S.; Schmieder, P.; Reif, B., High resolution ^{1}H-detected solid-state NMR spectroscopy of protein aliphatic resonances: access to tertiary structure information. *J. Am. Chem. Soc.* **2010,** *132*, 15133-5.
(40) Paulson, E. K.; Morcombe, C. R.; Gaponenko, V.; Dancheck, B.; Byrd, R. A.; Zilm, K. W., Sensitive high resolution inverse detection NMR spectroscopy of proteins in the solid state. *J. Am. Chem. Soc.* **2003,** *125*, 15831-15836.
(41) Akbey, U.; Lange, S.; Trent Franks, W.; Linser, R.; Rehbein, K.; Diehl, A.; van Rossum, B. J.; Reif, B.; Oschkinat, H., Optimum levels of exchangeable protons in perdeuterated proteins for proton detection in MAS solid-state NMR spectroscopy. *J. Biomol. NMR* **2010,** *46*, 67-73.
(42) Chevelkov, V.; Rehbein, K.; Diehl, A.; Reif, B., Ultrahigh resolution in proton solid-state NMR spectroscopy at high levels of deuteration. *Angew. Chem. Int. Ed.* **2006,** *45*, 3878-3881.
(43) Linser, R.; Bardiaux, B.; Higman, V.; Fink, U.; Reif, B., Structure calculation from unambiguous long-range amide and methyl ^{1}H-^{1}H distance restraints for a microcrystalline protein with MAS solid-state NMR spectroscopy. *J. Am. Chem. Soc.* **2011,** *133*, 5905-5912.
(44) Linser, R.; Dasari, M.; Hiller, M.; Higman, V.; Fink, U.; del Amo, J. M. L.; Markovic, S.; Handel, L.; Kessler, B.; Schmieder, P.; Oesterhelt, D.; Oschkinat, H.; Reif, B., Proton-detected solid-state NMR spectroscopy of fibrillar and membrane proteins. *Angew. Chem. Int. Ed.* **2011,** *50*, 4508-4512.

(45) Akbey, U.; Lange, S.; Franks, W. T.; Linser, R.; Rehbein, K.; Diehl, A.; van Rossum, B. J.; Reif, B.; Oschkinat, H., Optimum levels of exchangeable protons in perdeuterated proteins for proton detection in MAS solid-state NMR spectroscopy. *J. Biomol. NMR* **2012,** *46*, 67-73.

(46) Samoson, A.; Tuherm, T.; Gan, Z., High-field high-speed MAS resolution enhancement in ^{1}H NMR spectroscopy of solids. *Solid State Nucl. Magn. Reson.* **2001,** *20*, 130-6.

(47) Kobayashi, T.; Mao, K.; Paluch, P.; Nowak-Krol, A.; Sniechowska, J.; Nishiyama, Y.; Gryko, D. T.; Potrzebowski, M. J.; Pruski, M., Study of intermolecular interactions in the corrole matrix by solid-state NMR under 100 kHz MAS and theoretical calculations. *Angew. Chem. Int. Ed.* **2013,** *52*, 14108-14111.

(48) Zhou, D. H.; Shea, J. J.; Nieuwkoop, A. J.; Franks, W. T.; Wylie, B. J.; Mullen, C.; Sandoz, D.; Rienstra, C. M., Solid-state protein-structure determination with proton-detected triple-resonance 3D magic-angle-spinning NMR spectroscopy. *Angew. Chem. Int. Ed. Engl.* **2007,** *46*, 8380-3.

(49) Zhou, D. H.; Shah, G.; Cormos, M.; Mullen, C.; Sandoz, D.; Rienstra, C. M., Proton-detected solid-state NMR Spectroscopy of fully protonated proteins at 40 kHz magic-angle spinning. *J. Am. Chem. Soc.* **2007,** *129*, 11791-11801.

(50) Ward, M. E.; Shi, L.; Lake, E.; Krishnamurthy, S.; Hutchins, H.; Brown, L. S.; Ladizhansky, V., Proton-detected solid-state nmr reveals intramembrane polar networks in a seven-helical transmembrane protein proteorhodopsin. *J. Am. Chem. Soc.* **2011,** *133*, 17434-17443.

(51) Zhou, D. H.; Nieuwkoop, A. J.; Berthold, D. A.; Comellas, G.; Sperling, L. J.; Tang, M.; Shah, G. J.; Brea, E. J.; Lemkau, L. R.; Rienstra, C. M., Solid-state NMR analysis of membrane proteins and protein aggregates by proton detected spectroscopy. *J. Biomol. NMR* **2012,** *54*, 291-305.

(52) Knight, M. J.; Webber, A. L.; Pell, A. J.; Guerry, P.; Barbet-Massin, E.; Bertini, I.; Felli, I. C.; Gonnelli, L.; Pierattelli, R.; Emsley, L.; Lesage, A.; Herrmann, T.; Pintacuda, G., Fast resonance assignment and fold determination of human superoxide dismutase by high-resolution proton-detected solid-state MAS NMR spectroscopy. *Angew. Chem. Int. Ed. Engl.* **2011,** *50*, 11697-11701.

(53) Nieuwkoop, A. J.; Franks, W. T.; Rehbein, K.; Diehl, A.; Akbey, Ü.; Engelke, F.; Emsley, L.; Pintacuda, G.; Oschkinat, H., Sensitivity and resolution of proton detected spectra of a deuterated protein at 40 and 60 kHz magic-angle-spinning. *J. Biomol. NMR* **2015,** *61*, 161-171.

(54) Lewandowski, J. R.; Dumez, J. N.; Akbey, U.; Lange, S.; Emsley, L.; Oschkinat, H., Enhanced resolution and coherence lifetimes in the solid-state NMR spectroscopy of perdeuterated proteins under ultrafast Magic-Angle Spinning. *J. Chem. Phys. Lett.* **2011,** *2*, 2205-2211.

(55) Laage, S.; Sachleben, J. R.; Steuernagel, S.; Pierattelli, R.; Pintacuda, G.; Emsley, L., Fast acquisition of multi-dimensional spectra in solid-state NMR enabled by ultra-fast MAS. *J. Magn. Reson.* **2009,** *196*, 133-141.

(56) Laage, S.; Marchetti, A.; Sein, J.; Pierattelli, R.; Sass, H. J.; Grzesiek, S.; Lesage, A.; Pintacuda, G.; Emsley, L., Band-selective ^{1}H-^{13}C cross-polarization in fast magic angle spinning solid-state NMR spectroscopy. *J. Am. Chem. Soc.* **2008,** *130*, 17216-7.

(57) Peck, T. L.; Magin, R. L.; Lauterbur, P. C., Design and analysis of microcoils for NMR microscopy. *J Magn Reson B* **1995,** *108*, 114-124.

(58) Andreas, L. B.; Le Marchand, T.; Jaudzems, K.; Pintacuda, G., High-resolution proton-detected NMR of proteins at very fast MAS. *J. Magn. Reson.* **2015,** *253*, 36-49.

(59) Wickramasinghe, N. P.; Parthasarathy, S.; Jones, C. R.; Bhardwaj, C.; Long, F.; Kotecha, M.; Mehboob, S.; Fung, L. W. M.; Past, J.; Samoson, A.; Ishii, Y., Nanomole-scale protein solid-state NMR by breaking intrinsic H-1 T-1 boundaries. *Nat Methods* **2009,** *6*, 215-218.

(60) Lewandowski, J. R.; De Paëpe, G.; Eddy, M. T.; Struppe, J.; Maas, W.; Griffin, R. G., Proton assisted recoupling at high spinning frequencies. *J. Phys. Chem. B* **2009,** *113*, 9062-9069.

(61) Knight, M. J.; Pell, A. J.; Bertini, I.; Felli, I. C.; Gonnelli, L.; Pierattelli, R.; Herrmann, T.; Emsley, L.; Pintacuda, G., Structure and backbone dynamics of a microcrystalline metalloprotein by solid-state NMR. *Proc. Natl. Acad. Sci. U.S.A.* **2012,** *109*, 11095-11100.

(62) Marchetti, A.; Jehle, S.; Felletti, M.; Knight, M. J.; Wang, Y.; Xu, Z. Q.; Park, A. Y.; Otting, G.; Lesage, A.; Emsley, L.; Dixon, N. E.; Pintacuda, G., Backbone assignment of fully protonated solid proteins by ^{1}H detection and ultrafast Magic-Angle-Spinning NMR Spectroscopy. *Angew. Chem. Int. Ed.* **2012,** *51*, 10756-10759.

(63) Knight, M. J.; Felli, I. C.; Pierattelli, R.; Bertini, I.; Emsley, L.; Herrmann, T.; Pintacuda, G., Rapid measurement of pseudocontact shifts in metalloproteins by proton-detected solid-state NMR spectroscopy. *J. Am. Chem. Soc.* **2012,** *134*, 14730-14733.

(64) Zhou, D. H.; Rienstra, C. M., High-performance solvent suppression for proton detected solid-state NMR. *J. Magn. Reson.* **2008,** *192*, 167-72.

(65) Igumenova, T. I.; Wand, A. J.; McDermott, A. E., Assignment of the backbone resonances for microcrystalline ubiquitin. *J. Am. Chem. Soc.* **2004,** *126*, 5323-5331.

(66) Laage, S.; Lesage, A.; Emsley, L.; Bertini, I.; Felli, I. C.; Pierattelli, R.; Pintacuda, G., Transverse-dephasing optimized homonuclear J-decoupling in solid-state NMR spectroscopy of uniformly C-13-labeled proteins. *J. Am. Chem. Soc.* **2009,** *131*, 10816-10817.

(67) Barbet-Massin, E.; Pell, A. J.; Knight, M. J.; Webber, A. L.; Felli, I. C.; Pierattelli, R.; Emsley, L.; Lesage, A.; Pintacuda, G., ^{13}C-detected through-bond correlation experiments for protein resonance assignment by ultra-fast MAS solid-state NMR. *ChemPhysChem* **2013,** *14*, 3131-7.

(68) Barbet-Massin, E.; Pell, A. J.; Jaudzems, K.; Franks, W. T.; Retel, J. S.; Kotelovica, S.; Akopjana, I.; Tars, K.; Emsley, L.; Oschkinat, H.; Lesage, A.; Pintacuda, G., Out-and-back ^{13}C-^{13}C scalar transfers in protein resonance assignment by proton-detected solid-state NMR under ultra-fast MAS. *J. Biomol. NMR* **2013,** *56*, 379-86.

(69) Schanda, P.; Meier, B. H.; Ernst, M., Quantitative analysis of protein backbone dynamics in microcrystalline ubiquitin by solid-state NMR spectroscopy. *J. Am. Chem. Soc.* **2010,** *132*, 15957-67.

(70) Volk, J.; Herrmann, T.; Wuthrich, K., Automated sequence-specific protein NMR assignment using the memetic algorithm MATCH. *J. Biomol. NMR* **2008,** *41*, 127-138.

(71) McCord, J. M.; Fridovich, I., Superoxide dismutase. An enzymic function for erythrocuprein (hemocuprein). *J. Biol. Chem.* **1969,** *244*, 6049-6055.

(72) Parge, H. E.; Hallewell, R. A.; Tainer, J. A., Atomic structures of wild-type and thermostable mutant recombinant human Cu,Zn superoxide dismutase. *Proc. Natl. Acad. Sci. U.S.A.* **1992,** *89*, 6109-6113.

(73) Bertini, I.; Luchinat, C.; Piccioli, M., Copper-zinc superoxide dismutase: a paramagnetic protein that provides a unique frame for the NMR investigation. *Prog. Nucl. Magn. Reson. Spectrosc.* **1994,** *26*, 91-139.

(74) Panchal, S. C.; Bhavesh, N. S.; Hosur, R. V., Improved 3D triple resonance experiments, HNN and HN(C)N, for H^N and ^{15}N sequential correlations in (^{13}C, ^{15}N) labeled proteins: application to unfolded proteins. *J. Biomol. NMR* **2001,** *20*, 135-47.

(75) Yoshimura, Y.; Kulminskaya, N. V.; Mulder, F. A., Easy and unambiguous sequential assignments of intrinsically disordered proteins by correlating the backbone ^{15}N or ^{13}C' chemical shifts of multiple contiguous residues in highly resolved 3D spectra. *J. Biomol. NMR* **2015,** *61*, 109-121.

(76) Liu, A.; Riek, R.; Wider, G.; von Schroetter, C.; Zahn, R.; Wuthrich, K., NMR experiments for resonance assignments of ^{13}C, ^{15}N doubly-labeled flexible polypeptides: application to the human prion protein hPrP(23-230). *J. Biomol. NMR* **2000,** *16*, 127-138.

(77) Frueh, D. P.; Sun, Z. Y.; Vosburg, D. A.; Walsh, C. T.; Hoch, J. C.; Wagner, G., Non-uniformly sampled double-TROSY hNcaNH experiments for NMR sequential assignments of large proteins. *J. Am. Chem. Soc.* **2006,** *128*, 5757-5763.

(78) Bracken, C.; Palmer, A. G., 3rd; Cavanagh, J., (H)N(COCA)NH and HN(COCA)NH experiments for ^{1}H-^{15}N backbone assignments in ^{13}C/^{15}N-labeled proteins. *J. Biomol. NMR* **1997,** *9*, 94-100.

(79) Weisemann, R.; Ruterjans, H.; Bermel, W., 3D triple-resonance NMR techniques for the sequential assignment of ^{N}H and ^{15}N resonances in ^{15}N- and ^{13}C-labelled proteins. *J Biomol NMR* **1993,** *3*, 113-20.

(80) Matsuo, H.; Kupce, E.; Li, H.; Wagner, G., Use of selective C alpha pulses for improvement of HN(CA)CO-D and HN(COCA)NH-D experiments. *J. Magn. Reson. B* **1996,** *111*, 194-198.

(81) van Rossum, B. J.; Castellani, F.; Pauli, J.; Rehbein, K.; Hollander, J.; de Groot, H. J.; Oschkinat, H., Assignment of amide proton signals by combined evaluation of HN, NN and HNCA MAS-NMR correlation spectra. *J. Biomol. NMR* **2003,** *25*, 217-23.

(82) Nishiyama, Y.; Malon, M.; Ishii, Y.; Ramamoorthy, A., 3D ^{15}N/^{15}N/1H chemical shift correlation experiment utilizing an RFDR-based ^{1}H/^{1}H mixing period at 100 kHz MAS. *J. Magn. Reson.* **2014,** *244*, 1-5.

(83) Sinnige, T.; Daniëls, M.; Baldus, M.; Weingarth, M., Proton Clouds to measure long-range contacts between nonexchangeable side chain protons in solid-state NMR. *J. Am. Chem. Soc.* **2014,** *136*, 4452-4455.

(84) Barbet-Massin, E.; Felletti, M.; Schneider, R.; Jehle, S.; Communie, G.; Martinez, N.; Jensen, M. R.; Ruigrok, R. W.; Emsley, L.; Lesage, A.; Blackledge, M.; Pintacuda, G., Insights into the structure and dynamics of measles virus nucleocapsids by ^{1}H-detected solid-state NMR. *Biophys. J.* **2014,** *107*, 941-6.

(85) Vasa, S. K.; Rovo, P.; Giller, K.; Becker, S.; Linser, R., Access to aliphatic protons as reporters in non-deuterated proteins by solid-state NMR. *Phys. Chem. Chem. Phys.* **2016,** *18*, 8359-8363.

(86) Xiang, S. Q.; Biernat, J.; Mandelkow, E.; Becker, S.; Linser, R., Backbone assignment for minimal protein amounts of low structural homogeneity in the absence of deuteration. *Chem. Commun.* **2016,** *52*, 4002-4005.

(87) Rosato, A.; Aramini, J. M.; Arrowsmith, C.; Bagaria, A.; Baker, D.; Cavalli, A.; Doreleijers, J. F.; Eletsky, A.; Giachetti, A.; Guerry, P.; Gutmanas, A.; Guntert, P.; He, Y.; Herrmann, T.; Huang, Y. J.; Jaravine, V.; Jonker, H. R.; Kennedy, M. A.; Lange, O. F.; Liu, G.; Malliavin, T. E.; Mani, R.; Mao, B.; Montelione, G. T.; Nilges, M.; Rossi, P.; van der Schot, G.; Schwalbe, H.; Szyperski, T. A.; Vendruscolo, M.; Vernon, R.; Vranken, W. F.; Vries, S.; Vuister, G. W.; Wu, B.; Yang, Y.; Bonvin, A. M., Blind testing of routine, fully automated determination of protein structures from NMR data. *Structure* **2012,** *20*, 227-36.

(88) Guerry, P.; Duong, V. D.; Herrmann, T., CASD-NMR 2: robust and accurate unsupervised analysis of raw NOESY spectra and protein structure determination with UNIO. *J. Biomol. NMR* **2015,** *62*, 473-480.
(89) Buchner, L.; Guntert, P., Systematic evaluation of combined automated NOE assignment and structure calculation with CYANA. *J. Biomol. NMR* **2015,** *62*, 81-95.
(90) Lian, L. Y.; Middleton, D. A., Labelling approaches for protein structural studies by solution-state and solid-state NMR. *Progr. NMR Spectrosc.* **2001,** *39*, 171-190.
(91) Asami, S.; Szekely, K.; Schanda, P.; Meier, B. H.; Reif, B., Optimal degree of protonation for ^{1}H detection of aliphatic sites in randomly deuterated proteins as a function of the MAS frequency. *J. Biomol. NMR* **2012,** *54*, 155-68.
(92) Mance, D.; Sinnige, T.; Kaplan, M.; Narasimhan, S.; Daniels, M.; Houben, K.; Baldus, M.; Weingarth, M., An efficient labelling approach to harness backbone and side-chain protons in 1H-detected solid-state NMR spectroscopy. *Angew. Chem. Int. Ed. Engl.* **2015,** *54*, 15799-15803.
(93) Huber, M.; Hiller, S.; Schanda, P.; Ernst, M.; Bockmann, A.; Verel, R.; Meier, B. H., A proton-detected 4D solid-state NMR experiment for protein structure determination. *ChemPhysChem* **2011,** *12*, 915-918.
(94) Agarwal, V.; Penzel, S.; Szekely, K.; Cadalbert, R.; Testori, E.; Oss, A.; Past, J.; Samoson, A.; Ernst, M.; Bockmann, A.; Meier, B. H., De novo 3D structure determination from sub-milligram protein samples by solid-state 100 kHz MAS NMR spectroscopy. *Angew. Chem. Int. Ed.* **2014,** *53*, 12253-12256.
(95) Wang, S.; Parthasarathy, S.; Nishiyama, Y.; Endo, Y.; Nemoto, T.; Yamauchi, K.; Asakura, T.; Takeda, M.; Terauchi, T.; Kainosho, M.; Ishii, Y., Nano-mole scale side-chain signal assignment by ^{1}H-detected protein solid-state NMR by ultra-fast magic-angle spinning and stereo-array isotope labeling. *PloS One* **2015,** *10*, e0122714.
(96) Chow, W. Y.; Rajan, R.; Muller, K. H.; Reid, D. G.; Skepper, J. N.; Wong, W. C.; Brooks, R. A.; Green, M.; Bihan, D.; Farndale, R. W.; Slatter, D. A.; Shanahan, C. M.; Duer, M. J., NMR spectroscopy of native and in vitro tissues implicates polyADP ribose in biomineralization. *Science* **2014,** *344*, 742-746.
(97) Lamley, J. M.; Iuga, D.; Öster, C.; Sass, H.-J.; Rogowski, M.; Oss, A.; Past, J.; Reinhold, A.; Grzesiek, S.; Samoson, A.; Lewandowski, J. R., Solid-state NMR of a protein in a precipitated complex with a full-length antibody. *J. Am. Chem. Soc.* **2014,** *136*, 16800-16806.
(98) Zhang, R.; Pandey, M. K.; Nishiyama, Y.; Ramamoorthy, A., A novel high-resolution and sensitivity-enhanced three-dimensional solid-state nmr experiment under ultrafast magic angle spinning conditions. *Sci. Rep.* **2015,** *5*, 11810.
(99) Bockmann, A.; Ernst, M.; Meier, B. H., Spinning proteins, the faster, the better? *J. Magn. Reson.* **2015,** *253*, 71-9.
(100) Penzel, S.; Smith, A. A.; Agarwal, V.; Hunkeler, A.; Org, M. L.; Samoson, A.; Bockmann, A.; Ernst, M.; Meier, B. H., Protein resonance assignment at MAS frequencies approaching 100 kHz: a quantitative comparison of J-coupling and dipolar-coupling-based transfer methods. *J. Biomol. NMR.* **2015,** *63*, 165-186.
(101) Nishiyama, Y.; Malon, M.; Gan, Z.; Endo, Y.; Nemoto, T., Proton–nitrogen-14 overtone two-dimensional correlation NMR spectroscopy of solid-sample at very fast magic angle sample spinning. *J. Magn. Reson.* **2013,** *230*, 160-164.
(102) Franks, W. T.; Zhou, D. H.; Wylie, B. J.; Money, B. G.; Graesser, D. T.; Frericks, H. L.; Sahota, G.; Rienstra, C. M., Magic-angle spinning solid-state NMR spectroscopy of the beta1 immunoglobulin binding domain of protein G (GB1): ^{15}N and ^{13}C chemical shift assignments and conformational analysis. *J. Am. Chem. Soc.* **2005,** *127*, 12291-12305.

(103) Agarwal, V.; Reif, B., Residual methyl protonation in perdeuterated proteins for multi-dimensional correlation experiments in MAS solid-state NMR spectroscopy. *J. Magn. Reson.* **2008,** *194*, 16-24.
(104) Shaka, A. J.; Frenkiel, T.; Freeman, R., NMR broadband decoupling with low radiofrequency power. *J. Magn. Reson.* **1983,** *52*, 159-163.
(105) Paulson, E. K.; Morcombe, C. R.; Gaponenko, V.; Dancheck, B.; Byrd, R. A.; Zilm, K. W., High-sensitivity observation of dipolar exchange and NOEs between exchangeable protons in proteins by 3D solid-state NMR spectroscopy. *J. Am. Chem. Soc.* **2003,** *125*, 14222-14223.
(106) Shen, Y.; Delaglio, F.; Cornilescu, G.; Bax, A., TALOS plus : a hybrid method for predicting protein backbone torsion angles from NMR chemical shifts. *J. Biomol. NMR* **2009,** *44*, 213-223.
(107) Herrmann, T.; Guntert, P.; Wuthrich, K., Protein NMR structure determination with automated NOE assignment using the new software CANDID and the torsion angle dynamics algorithm DYANA. *J. Mol. Biol.* **2002,** *319*, 209-227.
(108) Montelione, G. T.; Nilges, M.; Bax, A.; Guntert, P.; Herrmann, T.; Richardson, J. S.; Schwieters, C. D.; Vranken, W. F.; Vuister, G. W.; Wishart, D. S.; Berman, H. M.; Kleywegt, G. J.; Markley, J. L., Recommendations of the wwPDB NMR Validation Task Force. *Structure* **2013,** *21*, 1563-1570.
(109) Linser, R.; Bardiaux, B.; Andreas, L. B.; Hyberts, S. G.; Morris, V. K.; Pintacuda, G.; Sunde, M.; Kwan, A. H.; Wagner, G., Solid-state NMR structure determination from diagonal-compensated, sparsely nonuniform-sampled 4D proton-proton restraints. *J. Am. Chem. Soc.* **2014,** *136*, 11002-11010.
(110) Breiter, D. R.; Meyer, T. E.; Rayment, I.; Holden, H. M., The molecular-structure of the High-Potential Iron-Sulfur protein isolated from *Ectothiorhodospira-halophila* determined at 2.5-Å resolution. *J. Biol. Chem.* **1991,** *266*, 18660-18667.
(111) Bertini, I.; Eltis, L. D.; Felli, I. C.; Kastrau, D. H. W.; Luchinat, C.; Piccioli, M., The solution structure of oxidized HiPIPI from *Ectothiorhodospira halophila*; Can NMR spectroscopy be used to probe rearrangements associated with electron transfer processes? *Chem. Eur. J.* **1995,** *1*, 598-607.
(112) Felli, I.; Banci, L.; Bertini, I.; Eitis, L. D.; Kastrau, D. H. W.; Luchinat, C.; Piccioli, M.; Pierattelli, R.; Smith, M., Solution Structure Of The Recombinant Iron-Sulfur Protein Iso-I (Hipip-I) From E-Halophila, In Both Oxidation-States. *J. Cell. Biochem.* **1995,** 45-45.

Chapter III.

Breaking into the blind sphere:

the “toolkit”

III.1 Introduction

The techniques described in the previous chapter, initially designed for the NMR characterization of diamagnetic proteins, can be also successfully employed for the detection and assignment of nuclei that experience long-range paramagnetic effects, as shown in the case of Cu^{II},Co^{II}-SOD and *Eh*HiPIP I.

However, in the close proximities of a paramagnetic metal ion, the large isotropic and anisotropic shifts and the short relaxation times prevent the standard manipulation of nuclear coherences and the feasibility of the multidimensional experiments as described in the previous chapter. It is common to refer to this region as a "blind sphere" in a metalloprotein.[1] Nevertheless, this does not mean that this region is completely inaccessible to NMR. On the contrary, if the experimental approach is suitably tuned, resonances from nuclear spins may still be detected and characterized. Some of these tools have been previously developed for the analysis of highly paramagnetic materials or small inorganic complexes, and are reviewed in the present chapter.

Another challenging aspect of NMR in the close proximities of a paramagnetic metal ion is related to the assignment of the observed resonances in proteins and the interpretation of their spectral properties. Indeed, it is impossible to establish sequential connectivity over long stretches of the protein, and the observed shifts do not usually directly relate to residue types, nuclei positions, chain topology or local environments like in diamagnetic systems. For a full understanding of the observed properties, experimental spectra need therefore to be complemented with structure-based calculation. In this respect, extensive effort has been made in order to calculate with sufficient accuracy paramagnetic NMR (PNMR) shifts, and some recent advances in this field are reviewed as well at the end of the chapter.

III.2 The experimental toolkit

III.2.1 Spin-echoed acquisitions

The simplest pulse sequence for obtaining a one-dimensional spectrum is a one-pulse sequence. However the application of this simple sequence suffers from a problem imposed by the limitation of the instrumentation. In order to switch from excitation to observation mode, and avoid saturation of the receiver, a dead time of few microseconds is needed after

the pulse and prior to the acquisition. The inclusion of this dead time means that the initial points of the FID are missed, and the initial evolution of the signal is not acquired. This becomes a problem when large spectral windows are needed such as in paramagnetic systems. Since the sampling rate is inversely proportional to the spectral width, in these cases the spectrum acquires large frequency-dependent phase errors, which severely degrade its quality. A solution for this problem consists in a rotor-synchronized spin-echo (Figure 24).[2] In this module, an excitation pulse is followed by an 180° pulse, sandwiched by two identical delays, equal to an integer multiple of the rotor period. In this way, the dead time is absorbed into the second delay, and if the 180° pulse is sufficiently broadband, both the isotropic and anisotropic shifts are refocused by the echo, allowing the acquisition of the full FID evolution.

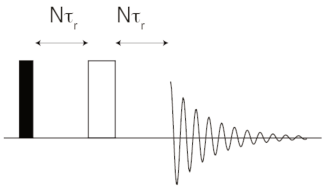

Figure 24. The spin-echo pulse scheme. Black and white rectangles represent 90° and 180° hard pulses, respectively, while τ_r indicate the rotor period and N is an integer number.

III.2.2 Adiabatic inversion and refocusing pulses

Depending on the nature of the paramagnetic center, paramagnetic shifts and shift anisotropies induced on the surrounding nuclei can be on the order of 100-1000 ppm, values that are larger than the practicable rf-amplitudes. Under these conditions, square pulses do not provide the necessary bandwidth, and alternative pulse schemes have to be used to ensure broadband inversion or refocusing. Adiabatic pulses offer a solution to this problem, featuring an impressive ratio between the rf-power used and the achieved bandwidth, and providing a performance that is virtually independent from the resonance offsets.[3]

In an adiabatic pulse the transmitter offset is swept through the spectrum, rather than being fixed at a given frequency. The pulse is defined by a pulse length τ_p, a time-dependent rf-field amplitude $\omega_1(t)$, and a time dependent phase $\phi_p(t)$, which induces a time-dependent irradiation frequency, $\omega_{\mathrm{rf}}(t) = d\phi_p(t)/\mathrm{d}t$, sweeping through a range of frequencies $\Delta\omega$. The rf-amplitude increases smoothly from zero at the beginning of the pulse to a maximum value of $\omega_1^{\max}$ and then decreases back to zero at the end of the pulse. In the frequency modulated frame, the rf-field and the resonance offset (the instantaneous frequency offset between the shift and the irradiation frequency) combine into an effective field, ω_{eff}, inclined at an angle

Θ with respect to the *z*-axis. For suitably chosen $\omega_{\mathrm{rf}}(t)$ and $\Delta\omega$, the rate of change of Θ becomes negligible with respect to the ω_{eff} (adiabaticity condition). The magnetization vector remains then "locked" along the effective field throughout the pulse, and can for example be inverted from $+z$ to $-z$, if the sweep is arranged so that Θ varies from +90° to -90°. Classical adiabatic pulses in solution are based on long low-power irradiations, while in paramagnetic solids under MAS efficient inversion is best achieved with the so-called Short High-power Adiabatic Pulse (SHAPs).[4] These elements are endowed with high power, which induces a larger effective field overcoming the modulation associated to the shift anisotropy, a wide and fast frequency sweep, which provides a uniform amplitude modulation for all the crystallites, and a short duration, which minimizes signal losses due to the PRE.

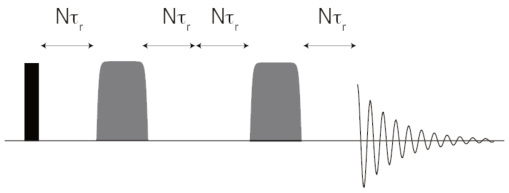

Figure 25. The double-adiabatic spin echo pulse scheme. The black rectangle represents 90° hard pulse, while τ_r indicate the rotor period and *N* is an integer number. The gray shapes represent the adiabatic pulses.

One the most successful scheme employed in solids is the tanh/tan scheme[5]. The amplitude $\omega_1(t)$, phase $\phi_p(t)$ and frequency-sweep $\omega_{\mathrm{rf}}(t)$ profiles of the tanh/tan scheme are given by the following expressions:

$$\omega_1(t) = \begin{cases} \omega_1^{\max} \tanh\left(\frac{2\xi t}{\tau_p}\right) & \left(0 \le t \le \tau_p/2\right) \\ \omega_1^{\max} \tanh\left(2\xi\left(1-\frac{t}{\tau_p}\right)\right) & \left(\tau_p/2 < t \le \tau_p\right) \end{cases} \quad \text{(III.1)}$$

$$\phi_p(t) = \frac{\Delta\omega\tau_p}{4\kappa\tan(\kappa)} \ln\left(\cos\left(\kappa\left(1-2t/\tau_p\right)\right)\right) \quad \text{(III.2)}$$

$$\omega_{\mathrm{rf}}(t) = -\frac{1}{2}\,\Delta\omega\,\frac{\tan\left(\kappa\left(1-2t/\tau_p\right)\right)}{\tan(\kappa)} \quad \text{(III.3)}$$

where ξ and κ are dimensionless parameters (usually $\xi = 10$ and $\kappa = \tan^{-1} 20$).

The adiabaticity condition for a tanh/tan pulse is fulfilled when:[4]

$$\omega_1^{\max} > \sqrt{1.41\Delta\sigma\omega_0\omega_r} \quad \text{(III.4)}$$

$$\frac{2\Delta\omega}{\tan(\kappa)} \ge \Delta\sigma\omega_0 \quad \text{(III.5)}$$

$$\tau_p > \frac{2\Delta\omega}{\Delta\sigma\omega_0\omega_r}\frac{\kappa}{\tan(\kappa)} \qquad \text{(III.6)}$$

where $\Delta\sigma$ is the shift anisotropy, ω_0 the angular Larmor frequency and ω_r the angular spinning frequency.

Once optimized, the SHAPs can be incorporated as inversion elements in more complex pulse sequences, or used for refocusing through a double spin echo (Figure 25B), where a second SHAP compensates the frequency-dependent phase errors on the coherences induced by the first SHAP and leading to a dephasing of the signal in the powder.[4, 6] An example of the beneficial effect of employing adiabatic pulses is shown in Figure 26, where the incorporation of SHAPs into the double-echo sequence allows to increase the global intensity and recover a wider anisotropy pattern in a paramagnetic complex.[4]

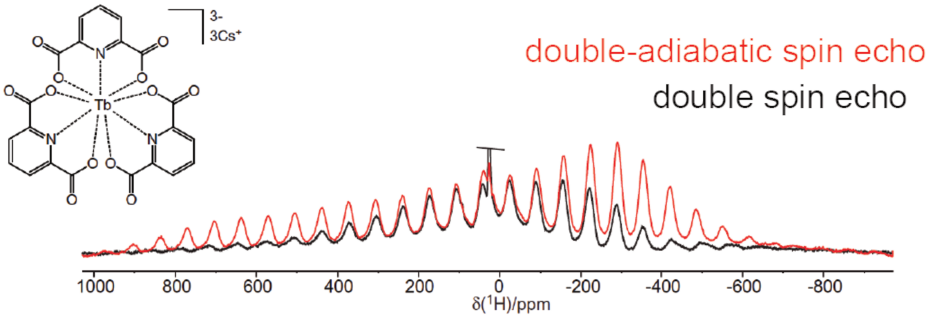

Figure 26. Double spin echo (black) and double-adiabatic spin echo (red) of the paramagnetic compound shown in the figure, acquired at 33 kHz MAS on a 500 MHz (11.7 T) spectrometer. For the double-adiabatic spin echo tanh/tan SHAPs are used (τ_p= 50 µs, $\omega_1^{max}/2\pi$ = 200 kHz, $\Delta\omega/2\pi$ = 500 MHz). Reproduced and adapted from reference 4.

III.2.3 Heteronuclear correlations

The pulse sequences described in the previous chapters mainly use CP to perform magnetization transfer between two different spins. CP is the most commonly used scheme for coherence transfer between two heteronuclear dipolar-coupled nuclei. For nuclei experiencing strong paramagnetic effects, the efficiency of the CP transfer is reduced considerably compared to diamagnetic systems, because of the magnetization loss during the spin-lock pulses due to PRE, and to the difficulty of efficiently spin-lock nuclear spin resonances with large shift anisotropies under MAS with practicable rf-field amplitudes.[7] An improvement in the heteronuclear coherence transfer can be obtained by the use of the Transferred-Echo DOuble-Resonance (TEDOR).[7-8] In this sequence (Figure 27A), ^{1}H coherences excited by a first pulse evolve during a spin echo. A train of 180° pulses applied to the *X*-spin (^{13}C or ^{15}N) during each half of the echo results in the recoupling of the

heteronuclear dipolar coupling and generation of anti-phase coherences. A pair of 90° pulses then transfers the coherences to the *X*-spin, and a second recoupling scheme converts them into observable in-phase coherences. A *z*-filter is used to remove any unwanted signal not suppressed by the phase cycling.

The sequence can also be implemented in a ^{1}H-detected version (Figure 27B),[9-10] enhancing the sensitivity compared to the previous case thanks to the higher gyromagnetic ration of protons. In this case after the first pulse ^{1}H coherences evolve during an spin-echo and anti-phase coherences are generated, like in the previous case, by a train of 180° pulses applied to the *X*-spin (^{13}C or ^{15}N) during each half of the of the echo. A pair of 90° pulses then transfers the coherences to the *X*-spin, whose chemical shift is encoded during the t_1 period. A second pair of 90° pulses is used to transfer the coherences back to ^{1}H and a second recoupling scheme converts them into observable in-phase coherences.

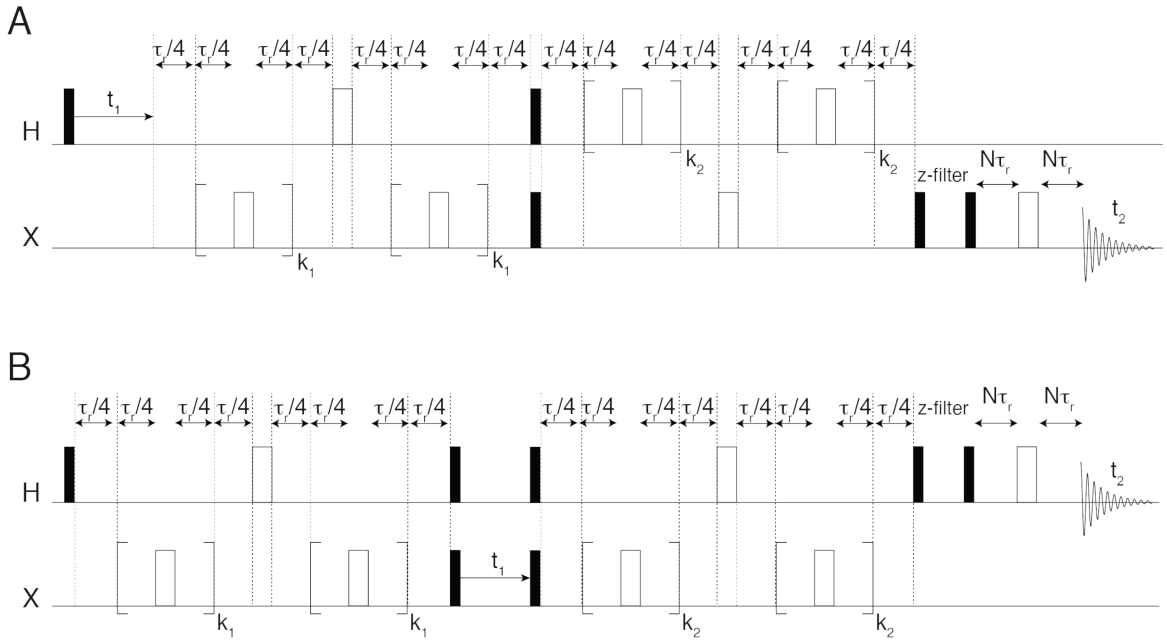

Figure 27. A) The HX TEDOR and B) the (H)XH TEDOR pulse schemes. Black and white rectangles represent 90°and 180° hard pulses, respectively. τ_r indicate the rotor period, while k_1 and k_2 are odd integer numbers.

Differently from CP, these sequences employ only short, high-power pulses, which allows the use of higher rf-field amplitudes, and avoids the need to spin-lock the large anisotropic resonances. As an example, Figure 28 shows the comparison between the ^{13}C spectrum of a paramagnetic DIAD-Fe^{II} catalyst acquired using CP (blue) or TEDOR (red, here implemented in a 1D version). Clearly the TEDOR spectrum displays an increased sensitivity, and highly hyperfine-shifted peaks, invisible in the CP spectrum, become observable.

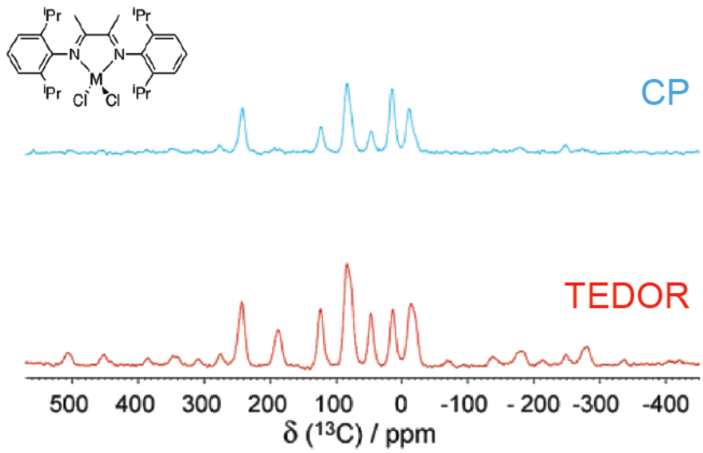

Figure 28. Comparison of the ^{13}C spectra obtained for the compound in the figure (where M = Fe^{II}) with CP (blue, contact time 0.5 ms) and TEDOR (red, recoupling period 60 μs) at 33 kHz MAS on a 500 MHz (11.7 T) spectrometer. Reproduced from reference 7.

III.2.4 Homonuclear correlations

In solids spin diffusion is an important mechanism that can be exploited for obtaining homonuclear through space correlations, like it is done in the PDSD sequence mentioned above.[11] However, magnetization loss occurs during the mixing time due to longitudinal PRE, which can dramatically affect the final sensitivity. The drop in sensitivity might be too severe under fast MAS conditions (>40 kHz), where the spin diffusion rates are considerably reduced, and longer mixing times are required.

The rate of transfers can be enhanced by the use of a homonuclear dipolar sequence during the mixing time. One advantageous scheme, already mentioned in Chapter II, is the Radio-Frequency Driven Recoupling (RFDR) scheme[12] (Figure 29). In this scheme, the mixing time comprises several rotor periods, and each rotor period is divided in two by the application of an 180° pulse.

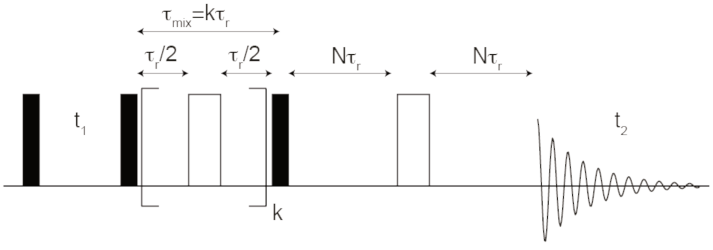

Figure 29. The RFDR pulse scheme. Black and white rectangles represent 90° and 180° hard pulses, respectively. τ_r indicate the rotor period, while *k* and *N* are odd integer numbers.

III.2.5 Infinite-speed MAS spectra

Nuclei close to a paramagnetic center experience large isotropic and anisotropic shifts, and their signal is split over multiple sidebands, even at the largest MAS rates available. In a

paramagnetic protein, the NMR spectrum of each nucleus contains multiple spinning-sideband manifolds that, in general, overlap. An experiment design removing the overlap of isotropic and anisotropic signals in MAS is the Magic Angle Turning (MAT) technique (Figure 30A).[13] In this experiment, after the generation of transverse coherence on the nucleus of interest, five 180° pulses are applied with fixed timings over a period *T* that is constant and equal to an integer multiple of the rotor period. In particular, the second and fourth pulse are applied at fixed times $T/3$ and $2T/3$ respectively, while the first, the third and fifth pulse are applied at times $T/6-\tau$, $T/2-\tau$, $5\,T/6-\tau$, respectively, where τ is the evolution variable and is restricted to the range $-T/6<\tau<T/6$. The sequence yields a spectrum consisting in a series of spinning sidebands manifolds in the direct dimension, correlating to the corresponding pure isotropic shifts in the indirect dimension. In this way, both the shift anisotropy and the isotropic shifts can be measured accurately.

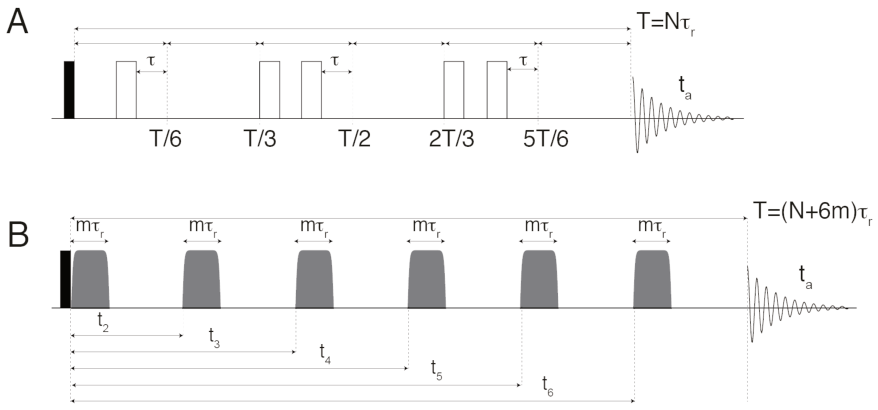

Figure 30. Pulse schemes for the A) MAT and B) aMAT experiments. Black and white rectangles represent 90°and 180° hard pulses, respectively, while τ_r indicates the rotor period, τ a variable delay comprised between *T/6* and *-T/6*, t_a the direct acquisition time, and *N* and *m* are integer numbers. The gray shapes represent the adiabatic pulses.

The scheme can be extended into an adiabatic version (aMAT), with the incorporation of SHAPs which increase its efficiency over larger bandwidths.[14] In this version (Figure 30B), one additional sixth fixed pulse is placed at the beginning the sequence in order to refocus the phase errors from the other five SHAPs. In particular, the timing of the *k*th pulse t_k is given by the following expressions:[14]

$$t_k=(k-1)(m+N/6)\tau_r \qquad \text{(III.7)}$$

$$t_k=(k-1)(m+N/6)\tau_r \pm (j-1)N\tau_r/(6n) \qquad \text{(III.8)}$$

where the former expression applies if *k* is odd, the latter if *k* is even, and *N* is an integer that is not a multiple of three, m is an integer, $m\tau_r$ is the duration of the SHAP, *n* is the total

number of points in the indirect dimension, and *j* represents the *j*th point acquired in the indirect dimension. Note that, despite the different notations used, the timing of the pulses is the same for the two sequences.

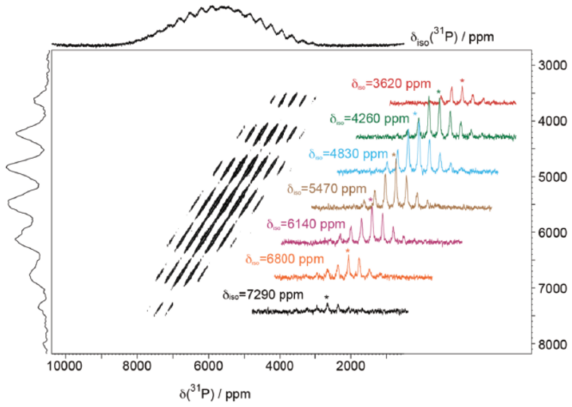

Figure 31. ^{13}P aMAT spectrum of $LiFe_{0.5}Mn_{0.5}PO_4$, acquired at 60 kHz MAS on a 500 MHz (11.7 T) spectrometer using τ_p= 50 µs, $\omega_1^{max}/2\pi$ = 417 kHz, $\Delta\omega/2\pi$ = 5 MHz tanh/tan SHAPs. The projection along the indirect dimension contains just the isotropic shifts. Reproduced from reference 14.

The example in Figure 31 shows one interesting application of the aMAT sequence to a paramagnetic lithium transition-metal phosphate. The use of aMAT allowed the complete separation of the isotropic chemical shifts of this complex paramagnetic material.[14]

III.2.6 ^{1}H-decoupling and paramagnetism

Another relevant aspect of NMR in the solid state is represented by the fact that the incomplete averaging of the dipolar interaction shortens the nuclear coherence lifetimes. In particular, even at high MAS rates (< 60 kHz), the extensive network of homonuclear ^{1}H-^{1}H couplings produces severe ^{1}H line broadening, as already mentioned in the previous chapters, and severely broadens ^{13}C or ^{15}N signals. In diamagnetic samples, this effect can be alleviated by the use of opportune decoupling sequences. Extensive work has been done in the past in this field, and nowadays a wide variety of decoupling schemes are available.[15-20] However in paramagnetic systems the situation is more complex, notably for nuclei in very close proximity to the metal center, which experience large anisotropies. It was recognized early that heteronuclear ^{1}H decoupling is ineffective for increasing the resolution in NMR spectra of paramagnetic complexes: the large anisotropies and the dispersion of isotropic chemical shifts prevents the possibility to efficiently irradiate over the required spectral window.[21] A part from few cases where heteronuclear decoupling provided some minor improvement in sensitivity and increasing of ^{13}C coherence lifetimes,[22] the general observation is that heteronuclear decoupling is at best ineffective and at worse has a deleterious effect on the spectrum. In addition to that, when high-power decoupling is used, long recycle delays are

required in order to prevent probe damages, thus preventing the exploitation of short T_1 for accelerated acquisition. At the same time, the large ^{1}H shifts weaken the ^{1}H bath, and allow MAS to better average the heteronuclear interaction. In this situation, it was recognized that it might be more convenient to completely remove decoupling, and rely on fast MAS to average the dipolar couplings, with the additional advantage of accelerating the acquistion.[23-25]

As an example, slices from the ^{13}C aMAT spectra of the Co^{II}-SOD protein acquired with and without decoupling at different spinning rates are shown in Figure 32. As it can be seen, while for the aliphatic region of the spectrum (right panels) the use of decoupling is beneficial for the sensitivity of the spectrum, for the selected contact-shifted resonance at ~450 ppm the use of decoupling is even deleterious.

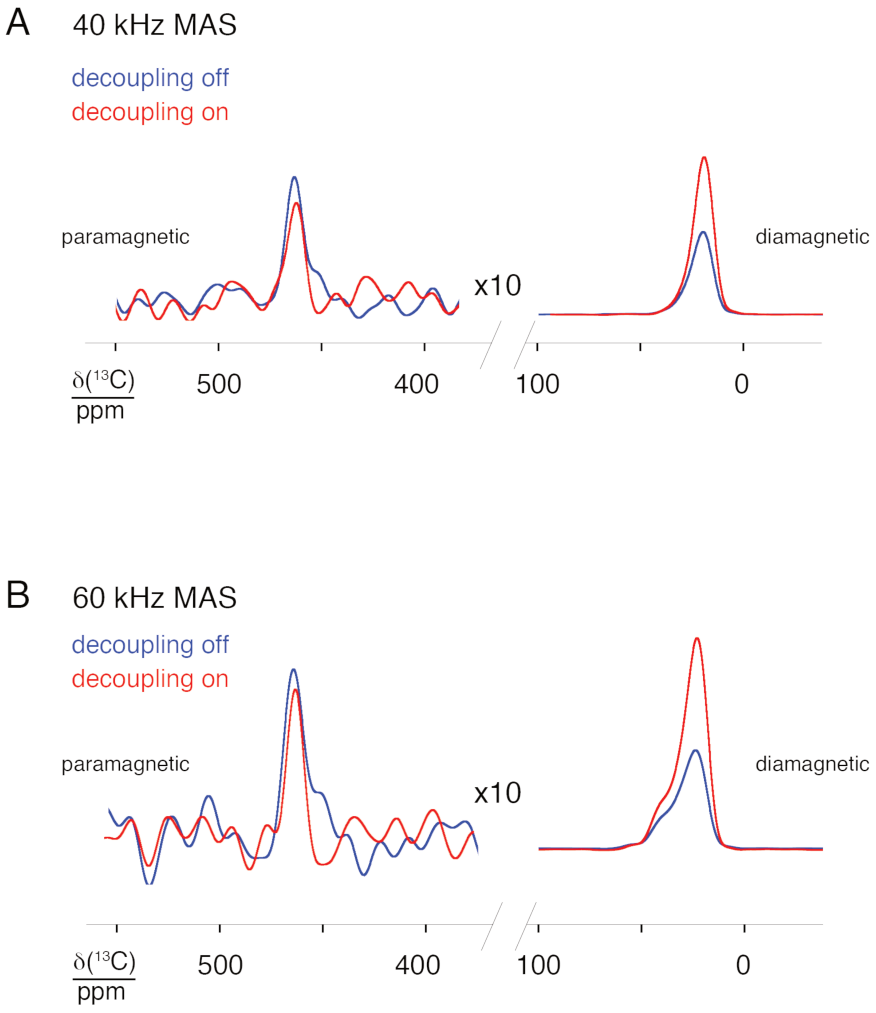

Figure 32. Slices from the ^{13}C aMAT spectra of Co^{II}-SOD acquired on a 500 MHz (11.7 T) spectrometer at 280 K, and at 40 kHz MAS (A) and at 60 kHz MAS (B), respectively, with (red) and without (blue) decoupling, using τ_p= 50 µs, $\omega_1^{max}/2\pi$ = 150 kHz, $\Delta\omega/2\pi$ = 5 MHz tanh/tan SHAPs. The right panels correspond to the aliphatic region of the protein, while the left ones to the contact-shifted His80 $^{13}C^{\delta 2}$ resonance. In both cases, XiX decoupling was used,[17, 22] using a ^{1}H rf-field of 350 kHz, and a $\tau_p = 1.88\tau_r$ at 40 kHz MAS, and $\tau_p = 1.84\tau_r$ at 60 kHz MAS. Spectra acquired by the author.

III.3 The theoretical toolkit

The experimental techniques described in the previous section can be successfully employed to detect NMR signals from nuclei in the close proximity of a paramagnetic metal ion, and to assess internuclear connectivity. However, assignment of the observed resonances might be a challenging task, for the reasons described in the introduction of this chapter. In this regard, the possibility of predicting PNMR shifts with sufficiently high reliability represents an attractive tool. The possibility to unravel the close relationship between PNMR shifts and structure can eventually provide structural information on the system under examination,[26] as will be shown in Chapter V.

III.3.1 Brief theoretical overview

The first efforts to predict PNMR shifts date back to the early times of NMR with the seminal works of McConnell and coworkers in the 50s,[27-28] followed by the developments made by Kurland and McGarvey in the 70s.[29]

Their theory has been recently translated into a modern quantum-chemical language by Vaara and coworkers.[30] In this implementation the PNMR shift tensor is derived from the EPR spin Hamiltonian parameters, i.e. the hyperfine coupling (HFC) tensor, the *g*-tensor, and the zero-field splitting (ZFS) tensor, for a system with arbitrary spin multiplicity.[30] Starting point is the EPR Hamiltonian of the system, which for a given nucleus is:

$$\mathcal{H}^{\mathrm{EPR}} = -\hbar\gamma \boldsymbol{B_0} \cdot \left(\mathbf{1} - \boldsymbol{\sigma}^{\mathrm{orb}}\right) \cdot \boldsymbol{I} + \mu_{\mathrm{B}} \boldsymbol{B_0} \cdot \boldsymbol{g} \cdot \boldsymbol{S} + \boldsymbol{S} \cdot \boldsymbol{A} \cdot \boldsymbol{I} + \boldsymbol{S} \cdot \boldsymbol{D} \cdot \boldsymbol{S} \qquad \text{(III.9)}$$

where the first term represent the nuclear Zeeman interaction and the nuclear orbital shielding, the second term the electron Zeeman interaction, the third term the HFC, and the last term the ZFS interaction. In Vaara's implementation, the paramagnetic (hyperfine) contribution to the chemical shift tensor of the nucleus, $\boldsymbol{\delta}^{\mathrm{HF}}$, is given by

$$\boldsymbol{\delta}^{\mathrm{HF}} = \frac{\mu_{\mathrm{B}}}{\hbar\gamma_I kT} \boldsymbol{g} \cdot \langle \boldsymbol{SS} \rangle \cdot \boldsymbol{A} \qquad \text{(III.10)}$$

where $\boldsymbol{g}$ is the *g*-tensor, $\boldsymbol{A}$ is the HFC tensor of the nucleus, and $\langle \boldsymbol{SS} \rangle$ is the "spin dyadic", which represents a thermal average of the two electron spin operators over the eigenstates of the ZFS Hamiltonian with the inclusion of magnetic couplings between these states.[30] As can be seen in this formulation, the hyperfine shift can be estimated once the EPR parameters are known.

Note that equation (III.10) reduces to equation (I.18) in the absence of relativistic effects. Indeed in this case $\boldsymbol{g} = g_{\mathrm{e}} \cdot \mathbf{1}$, $\langle \boldsymbol{SS} \rangle = \frac{S(S+1)}{3}$ and equation (I.6) applies. For the isotropic part we obtain:

$$\boldsymbol{\delta}^{\mathrm{HF}} = \frac{g_{\mathrm{e}}\mu_{\mathrm{B}}S(S+1)}{3\hbar\gamma_I kT} A^{\mathrm{FC}} = \delta^{\mathrm{con}} \qquad \text{(III.11)}$$

III.3.2 Practical aspects of quantum chemistry modeling

The calculation of PNMR shifts by first-principle quantum-chemical methods is computationally expensive, considering that it requires the evaluation of the HFC tensor for each nucleus in the molecule. This is prohibitive for a system of the size of a protein, and the full treatment is possible only for a limited number of atoms (<200) in the coordination sphere of the paramagnetic ion.

In practice, a structural model of the coordination sphere of the paramagnetic ion is built, which comprises the metal ion, the first coordination sphere, and eventually other residues or atoms relevant for defining the local environment (e.g. residues involved in H-bonding with atoms in the first coordination sphere). This model can be obtained from previously available structures (e.g. crystallographic data), or in principle built *ex nihilo*. Usually a geometry optimization step is required in order to reliably compute the EPR parameters. This is performed by DFT, keeping the C^{α} position fixed during the optimization step. The choice of the DFT functional has been proven to be determinant in this regard.[31]

The computation of *g* and *D* tensor requires an *ab initio* treatment, DFT methods being usually insufficiently accurate for this purpose.[32-33] This is performed on a smaller model, built from the previously optimized one (the dimension of the latter would be prohibitive for an *ab initio* treatment), which comprises only a limited number of suitably chosen atoms of the first coordination sphere.

The evaluation of the HFC tensor would require as well an *ab initio* treatment in order to obtain a sufficient level of accuracy, but unfortunately contemporary HFC calculations are lacking a benchmark *ab initio* level applicable to systems of biologically relevant sizes. Resorting to density functional theory (DFT) methods, there is currently no universally preferred functional for HFCs.[34] In such a situation, the HFC tensors need to be calculated with a set of DFT functionals in order to provide a reliable range of values, as will be shown in detail in Chapter V.

Once all the EPR parameters are evaluated, $\boldsymbol{\delta}^{\mathrm{HF}}$ can be obtained from equation (III.10).

Even if not relevant for the present work, it should be mentioned that for nuclei not included in the structural model used for the calculation of the PNMR shifts it is not possible to evaluate the full hyperfine shift. However for these nuclei it is usually possible to neglect the contact interaction and in many cases the PDA can be applied. In this case, the hyperfine contribution to the chemical shift can be approximated by

$$\boldsymbol{\delta}^{\mathrm{HF}} \approx \frac{\mu_0 \mu_{\mathrm{B}}^2 g_{\mathrm{e}}}{4\pi r^3 kT}\, \boldsymbol{g} \cdot \langle \boldsymbol{SS} \rangle \cdot \left(\frac{3\boldsymbol{rr}}{r^2} - \mathbf{1} \right) \qquad \text{(III.12)}$$

where $\boldsymbol{r}$ is the vector connecting the positions of the nuclear and electron spin. Under this approximation then, only the calculation of the *g* and the *D* tensor is required, and the $\boldsymbol{\delta}^{\mathrm{HF}}$ (which in this case reduces to the PCS) can be evaluated provided that a structural model of the protein is available.[31]

The advantage of performing accurate prediction of the PNMR shifts is twofold: on one side, if the structure of the system under examination is known with sufficiently high accuracy, then the prediction of the NMR shifts can support the assignment of the observed resonances; on the other, if the assignment is known, it is then possible to provide structural information on the analyzed system.[26] This will be shown in Chapter V, where with the combined use of experimental NMR data and predicted PNMR shifts it is possible to provide structural information on the coordination sphere of a paramagnetic ion in a metalloenzyme.

III.4 Conclusions

The techniques described in this chapter provide a precious tool for the MAS NMR investigation of nuclei in close proximity of a paramagnetic metal ion in a metalloprotein, which would be inaccessible with conventional MAS NMR techniques. In the following two chapters this "toolkit" is successfully used for the characterization of nuclei in the "blind sphere" in two microcrystalline metalloenzymes binding an iron-sulfur cluster and a Co^{II} ion, respectively.

III.5 References

(1) Bertini, I.; Luchinat, C.; Parigi, G.; Ravera, E., *NMR of paramagnetic molecules. Applications to metallobiomolecules and models*. Elsevier: Boston, 2017.

(2) Hahn, E. L., Spin echoes. *Phys. Rev.* **1950,** *80*, 580-594.

(3) Garwood, M.; DelaBarre, L., The return of the frequency sweep: designing adiabatic pulses for contemporary NMR. *J. Magn. Reson.* **2001,** *153*, 155-177.

(4) Kervern, G.; Pintacuda, G.; Emsley, L., Fast adiabatic pulses for solid-state nmr of paramagnetic systems. *Chem. Phys. Lett.* **2007,** *435*, 157-162.

(5) Hwang, T. L.; van Zijl, P. C.; Garwood, M., Fast broadband inversion by adiabatic pulses. *J. Magn. Reson.* **1998,** *133*, 200-203.

(6) Pell, A. J.; Pintacuda, G., Broadband solid-state MAS NMR of paramagnetic systems. *Prog. Nucl. Magn. Reson. Spectrosc.* **2015,** *84-85*, 33-72.

(7) Kervern, G.; Pintacuda, G.; Zhang, Y.; Oldfield, E.; Roukoss, C.; Kuntz, E.; Herdtweck, E.; Basset, J. M.; Cadars, S.; Lesage, A.; Coperet, C.; Emsley, L., Solid-state NMR of a paramagnetic DIAD-Fe-II catalyst: Sensitivity, resolution enhancement, and structure-based assignments. *J. Am. Chem. Soc.* **2006,** *128*, 13545-13552.

(8) Hing, A. W.; Vega, S.; Schaefer, J., Transferred-echo double-resonance NMR. *J. Magn. Reson.* **1992,** *96*, 205-209.

(9) Schnell, I.; Langer, B.; Sontjens, S. H.; van Genderen, M. H.; Sijbesma, R. P.; Spiess, H. W., Inverse detection and heteronuclear editing in ^{1}H-^{15}N correlation and ^{1}H-^{1}H double-quantum NMR spectroscopy in the solid state under fast MAS. *J. Magn. Reson.* **2001,** *150*, 57-70.

(10) Saalwachter, K.; Graf, R.; Demco, D. E.; Spiess, H. W., Heteronuclear double-quantum MAS NMR spectroscopy in dipolar solids. *J. Magn. Reson.* **1999,** *139*, 287-301.

(11) Eden, M.; Levitt, M. H., Pulse sequence symmetries in the nuclear magnetic resonance of spinning solids: Application to heteronuclear decoupling. *J. Chem. Phys.* **1999,** *111*, 1511-1519.

(12) Bennett, A. E.; Griffin, R. G.; Ok, J. H.; Vega, S., Chemical shift correlation spectroscopy in rotating solids: Radio frequency ‐ driven dipolar recoupling and longitudinal exchange. *J. Chem. Phys.* **1992,** *96*, 8624-8627.

(13) J.Z. Hu, D. W. A., C.H. Ye, R.J. Pugmire, D.M. Grant, An isotropic chemical shift-chemical shift anisotropy magic-angle slow-spinning 2D NMR experiment. *J. Magn. Reson., Ser A* **1993,** *105*, 82-87.

(14) Clement, R. J.; Pell, A. J.; Middlemiss, D. S.; Strobridge, F. C.; Miller, J. K.; Whittingham, M. S.; Emsley, L.; Grey, C. P.; Pintacuda, G., Spin-transfer pathways in paramagnetic lithium transition-metal phosphates from combined broadband isotropic solid-state MAS NMR spectroscopy and DFT calculations. *J. Am. Chem. Soc.* **2012,** *134*, 17178-17185.

(15) Bennett, A. E.; Rienstra, C. M.; Auger, M.; Lakshmi, K. V.; Griffin, R. G., Heteronuclear decoupling in rotating solids. *J. Chem. Phys.* **1995,** *103*, 6951-6958.

(16) Fung, B. M.; Khitrin, A. K.; Ermolaev, K., An improved broadband decoupling sequence for liquid crystals and solids. *J. Magn. Reson.* **2000,** *142*, 97-101.

(17) Detken, A.; Hardy, E. H.; Ernst, M.; Meier, B. H., Simple and efficient decoupling in magic-angle spinning solid-state NMR: the XiX scheme. *Chem. Phys. Lett.* **2002,** *356*, 298-304.

(18) Hodgkinson, P., Heteronuclear decoupling in the NMR of solids. *Prog. Nucl. Magn. Reson. Spectrosc.* **2005,** *46*, 197-222.
(19) Thakur, R. S.; Kurur, N. D.; Madhu, P. K., "Swept-frequency two-pulse phase modulation for heteronuclear dipolar decoupling in solid-state NMR". *Chem. Phys. Lett.* **2006,** *426*, 459-463.
(20) Mote, K. R.; Agarwal, V.; Madhu, P. K., Five decades of homonuclear dipolar decoupling in solid-state NMR: Status and outlook. *Prog. Nucl. Magn. Reson. Spectrosc.* **2016,** *97*, 1-39.
(21) Clayton, A. N.; Dobson, C. M.; Grey, C. P., High-resolution C-13 MAS NMR-spectra of paramagnetic lanthanide complexes. *J. Chem. Soc. - Chem. Commun.* **1990,** 72-74.
(22) Willans, M. J.; Sears, D. N.; Wasylishen, R. E., The effectiveness of ^{1}H decoupling in the ^{13}C MAS NMR of paramagnetic solids: An experimental case study incorporating copper(II) amino acid complexes. *J. Magn. Reson.* **2008,** *191*, 31-46.
(23) Ishii, Y.; Wickramasinghe, N. P.; Chimon, S., A new approach in 1D and 2D C-13 high-resolution solid-state NMR spectroscopy of paramagnetic organometallic complexes by very fast magic-angle spinning. *J. Am. Chem. Soc.* **2003,** *125*, 3438-3439.
(24) Wickramasinghe, N. P.; Shaibat, M.; Ishii, Y., Enhanced sensitivity and resolution in H-1 solid-state NMR spectroscopy of paramagnetic complexes under very fast magic angle spinning. *J. Am. Chem. Soc.* **2005,** *127*, 5796-5797.
(25) Wickramasinghe, N. P.; Ishii, Y., Sensitivity enhancement, assignment, and distance measurement in C-13 solid-state NMR spectroscopy for paramagnetic systems under fast magic angle spinning. *J. Magn. Reson.* **2006,** *181*, 233-243.
(26) *Calculation of NMR and EPR parameters. Theory and applications.* Kaupp, M.; Bühl, M.; Malkin, V. G. Eds.; Wiley-VCH: Weinheim, 2004.
(27) McConnell, H. M.; Robertson, R. E., Isotropic nuclear resonance shifts. *J. Chem. Phys.* **1958,** *29*, 1361-1365.
(28) McConnell, H. M.; Chesnut, D. B., Theory of isotropic hyperfine interactions in π - electron radicals. *J. Chem. Phys.* **1958,** *28*, 107-117.
(29) Kurland, R. J.; McGarvey, B. R., Isotropic NMR shifts in transition metal complexes: The calculation of the fermi contact and pseudocontact terms. *J. Magn. Reson.* **1970,** *2*, 286-301.
(30) Vaara, J.; Rouf, S. A.; Mareš, J., Magnetic couplings in the chemical shift of paramagnetic NMR. *J. Chem. Theory Comput.* **2015,** *11*, 4840-4849.
(31) Benda, L.; Mareš, J.; Ravera, E.; Parigi, G.; Luchinat, C.; Kaupp, M.; Vaara, J., Pseudo-contact NMR shifts over the paramagnetic metalloprotein CoMMP-12 from first principles. *Angew. Chem. Int. Ed.* **2016,** *55*, 14713-14717.
(32) Maganas, D.; Sottini, S.; Kyritsis, P.; Groenen, E. J. J.; Neese, F., Theoretical analysis of the spin hamiltonian parameters in Co(ii)S4 complexes, using density functional theory and correlated *ab initio* methods. *Inorg. Chem.* **2011,** *50*, 8741-8754.
(33) Kubica, A.; Kowalewski, J.; Kruk, D.; Odelius, M., Zero-field splitting in nickel(II) complexes: A comparison of DFT and multi-configurational wavefunction calculations. *J. Chem. Phys.* **2013,** *138*, 064304.
(34) Munzarová, M.; Kaupp, M., A critical validation of density functional and coupled-cluster approaches for the calculation of EPR hyperfine coupling constants in transition metal complexes. *J. Phys. Chem. A* **1999,** *103*, 9966-9983.

Chapter IV.

Paramagnetic properties of a crystalline iron-sulfur protein

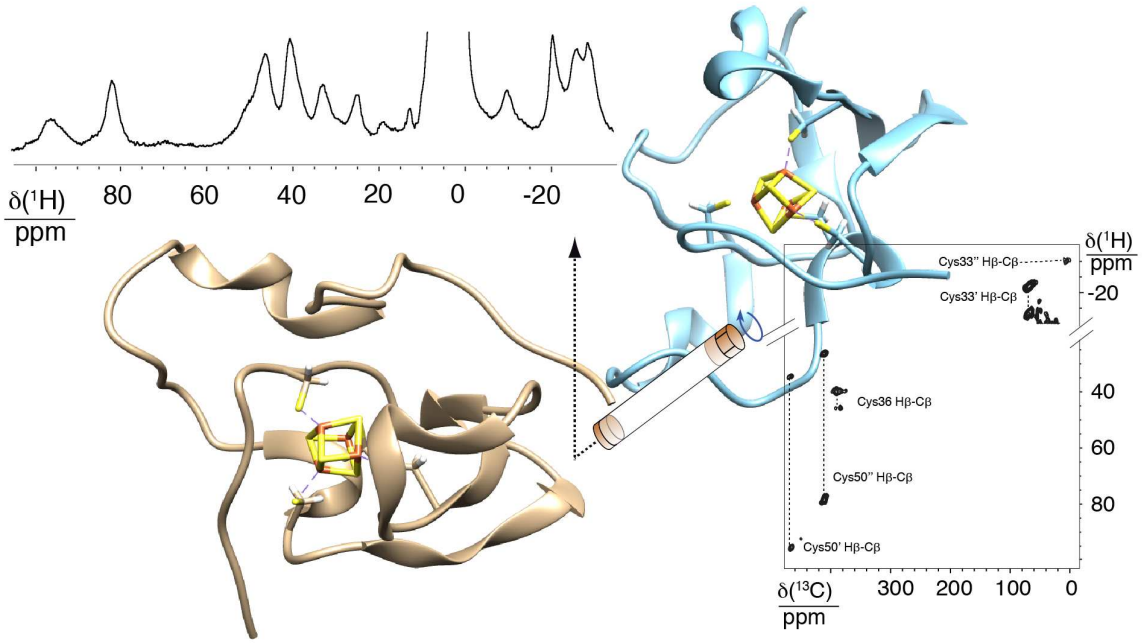

IV.1 Introduction

Despite the tremendous progress experienced by biomolecular MAS NMR in the last years, only few high-resolution studies were performed on paramagnetic metalloproteins up to now, as illustrated in Chapter I. Moreover, these studies mostly dealt with long-range paramagnetic effects, like PCSs and PREs, which are accessible with conventional techniques used for diamagnetic proteins.

Expanding the repertoire of solid-state NMR accessible paramagnetic systems is however not necessarily a trivial task, because of the different properties of the different metals in the different coordination environments that are encountered in metalloproteins. An example of this is represented by trivalent lanthanide ions, where the quality of the spectra is extremely dependent on the properties of the metal ligands: whereas small inorganic complexes[1-2] or rigid binding sites in proteins[3] yield substantially sharp lines, a more flexible environment reorients the magnetic susceptibility tensor,[4] producing significant inhomogeneous broadening, or possibly reintroducing Curie relaxation.[5]

In this chapter the first solid-state NMR data on a protein containing an iron-sulfur Fe_4S_4 cluster is reported.[6] By the combined use of very fast (60 kHz) MAS and tailored rf-irradiation schemes, it was possible to detect and assign most of ^{1}H and ^{13}C resonances from the side chains of the residues coordinating the Fe_4S_4 cluster in the oxidized high-potential iron-sulfur protein I from *E. halophila* (*Eh*HiPIP I). For these residues, contact shifts as large as 100 ppm and 400 ppm for ^{1}H and ^{13}C resonances, respectively, were observed. Moreover, by targeting *Eh*HiPIP I in a crystalline environment, it was possible to capture distinct paramagnetic signatures from the two conformations present in the asymmetric unit of the crystal. The magnetic properties of the system were also verified by following the temperature dependence of the contact-shifted cysteine resonances.

IV.2 HiPIPs and their magnetic properties

Iron-sulfur clusters (ISCs) are ubiquitous prosthetic groups of many metalloenzymes,[7-10] often associated to membranes, and they have a variety of functions in diverse cellular processes in almost all life-forms, with the large majority of them being involved in electron uptake, storage, donation, and exchange.[11] Within ISCs, each iron ion is almost always in a tetrahedral coordination, provided by two or three inorganic sulfides groups and two or one

thiolate sulfur centers from cysteine coordinating residues (with the exception of the Rieske's proteins, where histidines as well coordinate the cluster). The most common ISCs are represented by Fe_2S_2, Fe_3S_4 and Fe_4S_4 clusters, each of them displaying at least two different oxidation states (Figure 33).[11-12]

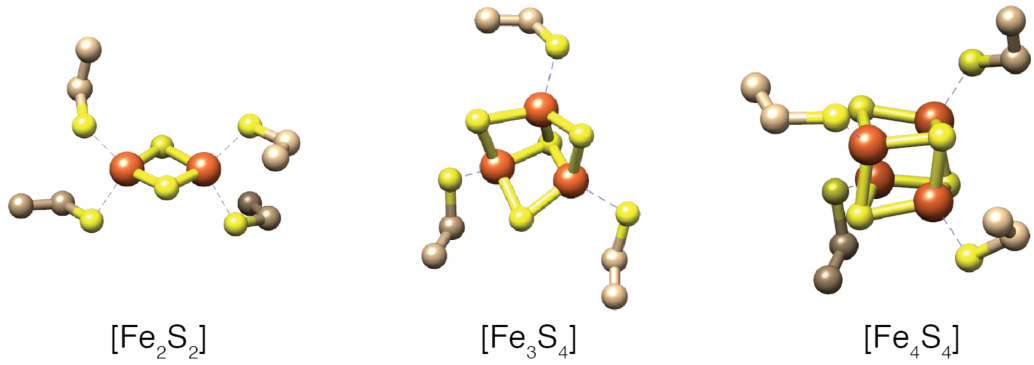

Figure 33. Representation of the three most common forms of ISCs clusters found in iron-sulfur proteins. Iron ions are reported in orange, sulfur atoms in yellow, carbon atom in brown. Hydrogen atoms are omitted.

In a first seminal work,[13] MAS NMR was used to elucidate the fine details of the electronic structure of model Fe_4S_4 cluster compounds by studying the dependence of their isotropic and anisotropic ^{13}C shifts over a very large (180 – 300 K) temperature range, but no characterization was attempted yet for such systems in a protein environment. Here, by the use of NMR at very fast MAS, together with some of the spectroscopic tools described in Chapter III, it has been possible to characterize the oxidized form of fully protonated *Eh*HiPIP I in a microcrystalline preparation.[14]

High-potential iron-sulfur proteins (HiPIPs) are a class of iron-sulfur proteins found in photosynthetic bacteria.[11] These proteins contain a Fe_4S_4 cluster, which can switch between a reduced state, $[Fe_4S_4]^{2+}$, containing formally two Fe^{3+} ions and two Fe^{2+} ions, and an oxidized state, $[Fe_4S_4]^{3+}$, containing formally three Fe^{3+} ions and one Fe^{2+} ion. However in both forms extensive charge delocalization is observed. Indeed, in the reduced state, these systems display a completely delocalized valence, in which each iron ion is formally $Fe^{2.5+}$. The two ions are pairwise coupled, giving two S=9/2 subspins, which are antiferromagnetically coupled obtaining a diamagnetic S=0 ground state.[15] However, at room temperature, also the S=1 state is populated, providing a paramagnetic contribution to the observed shifts and relaxation rates.[16-17] In the oxidized state one electron is formally removed, and the system contains a ferric ion pair and a mixed-valence pair,[18] as described in detail later for the oxidized *Eh*HiPIP I.

*Eh*HiPIP I is an 8.1-kDa protein of 73 residues containing a cubane Fe_4S_4 cluster that is coordinated by the side chains of four cysteine residues (Cys33, Cys36, Cys50, and Cys66, Figure 35B). Over the last twenty years, *Eh*HiPIP I has become a model system for biophysical applications, and has been extensively characterized by X-ray crystallography,[19] EPR and Mössbauer measurements at very low temperatures,[20] Raman spectroscopy,[20] and solution NMR,[21-22] where the electronic properties of the Fe_4S_4 cluster give distinctive features in the ^1H and ^{13}C spectra.[21-23] As mentioned before, in its oxidized form, the cluster formally contains one Fe^{2+} ion and three Fe^{3+} ions, but experimental data are consistent with the cluster being formed by one mixed valence pair (with S=9/2), containing two $Fe^{2.5+}$ ions and one pair containing two Fe^{3+} ions (forced by exchange coupling to S=4). The two pairs are antiferromagnetically coupled, resulting in an overall spin $S'$of the cluster equal to 1/2.[14, 22] This can be represented pictorially by the scheme in Figure 34, where the subspin S'_{12} corresponds to the ferric pair, and the S'_{34} subspin to the mixed valence pair. Different models can be used to interpret the system, which in principle should be described by Hamiltonian (I.28). The analysis of temperature dependence of the cysteine ^1H chemical shifts observed for different HiPIPs performed in solution NMR is well described by a simplified expression of Hamiltonian (I.28), where $J_{jk} = J$, except for $J_{12} = J + \Delta J_{12}$ and $J_{34} = J + \Delta J_{34}$, which is the situation represented in Figure 34.[24-25] In this case the energy levels are given by:

$$E(S', S'_{12}, S'_{34}) = \frac{1}{2}\left[JS'(S'+1) + \Delta J_{12} S'_{12}(S'_{12}+1) + \Delta J_{34} S'_{34}(S'_{34}+1)\right] \qquad \text{(IV.1)}$$

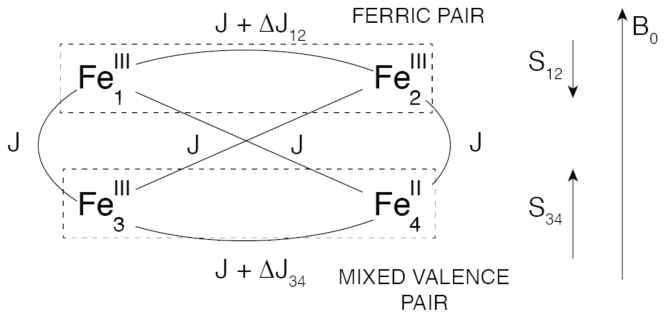

Figure 34. Heisenberg exchange coupling scheme for the Fe_4S_4 cluster in HiPIPs (left). Typical values for J, ΔJ_{12}, and ΔJ_{34}, in HiPIPs are 300, 100, -100 cm^{-1}, respectively.[24] The magnetic spin moment of the mixed valence pair, with larger spin, is aligned with the external field, while the ferric pair magnetic spin moment is aligned in the opposite direction (right).

The electronic properties of Fe_4S_4 clusters are made extremely complex by the presence of the highly asymmetric protein matrix that induces equilibria between different charge distributions among the iron ions. In particular, *Eh*HiPIP I has two EPR isomers: while one iron ion always has an oxidation state of 2.5+ and another of 3+, two other irons exchange

2.5+ and 3+ oxidation states with 80 – 20% probability (Figure 35B).[14] This is actually rather common among the different HiPIPs.[14]

The mixed valence pair (S'_{34}in Figure 34) usually assumes the higher spin state and forces the ferric pair (S'_{12}in Figure 34) to have a lower spin state with opposed spin, due to exchange coupling, yielding as mentioned above a ground state$|S'_{34}, S'_{12}, S'\rangle$ of the type |9/2, 4, 1/2⟩. To further complicate the picture, it is found that the ground state is not a pure |9/2, 4, 1/2⟩ state, but rather a superposition of different states.[26] However, since the behavior of HiPIPs has remarkable similarities, one can expect the exchange coupling parameters to be similar to what has been estimated with a quantum mechanical formalism for *Eh*HiPIP II, which has a single EPR isomer.[27]

Besides benchmarking MAS NMR with a new target paramagnetic system, the present investigation on microcrystalline *Eh*HiPIP I represents an important complement to the literature data, by providing a link between the characterizations of the molecule in solutions and in crystals. Most notably here, the unit cell of crystalline *Eh*HiPIP I (PDB ID: 2HIP) contains two molecules, featuring an overall backbone RMSD of 0.67 Å (Figure 35A).[19] Considering that paramagnetic NMR shifts are highly sensitive to the local geometry,[28-29] solid-state NMR could be able to capture distinct signatures from the two conformations present in the asymmetric unit.

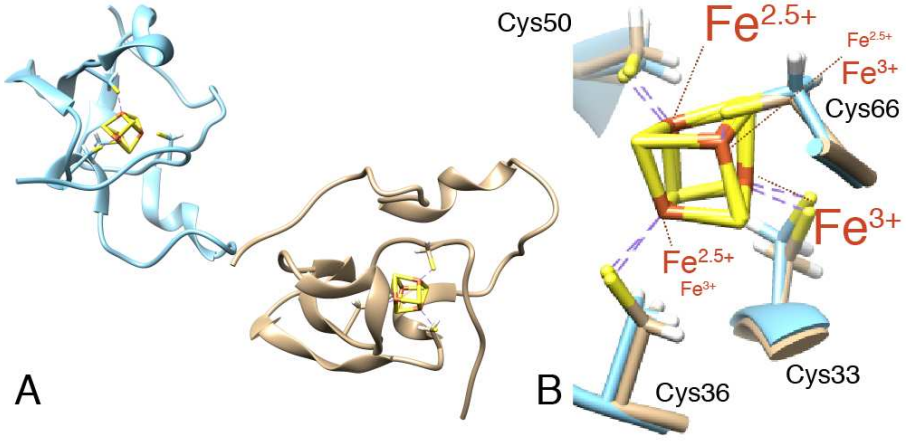

Figure 35. A) Asymmetric unit of *Eh*HiPIP I showing the two molecules. B) Superposition of the two molecules showing the cluster and the coordinating cysteines. Reproduced from reference 6.

IV.3 MAS NMR of *Eh*HiPIP I

IV.3.1 The first MAS NMR detection of contact-shifted signals in an protein

With the techniques described in Chapter II it was possible to perform a partial assignment of the NMR resonances of the less paramagnetic portion of protein. However, nuclei in the side chain of the cysteine ligands could not be detected with that experimental setup. Indeed, these nuclei are expected to experience strong hyperfine effects, and suitably tailored pulse sequences are needed in order to successfully detect and assign their signals. In particular, CP-based methods are expected to be ineffective for this purpose, due to the difficulty of locking the magnetization over the large required spectral windows (above 100 ppm), and to the magnetization losses during the contact times (which are usually on the order of 0.5 – 2 ms).

Here, for the first time, we successfully apply the set of experiments described in Chapter III, to characterize signals in the blind sphere in a paramagnetic microcrystalline metalloprotein. A doubly ^{13}C, ^{15}N labeled sample of *Eh*HiPIP I was microcrystallized and packed in a 1.3 mm rotor. The 1D ^{1}H and ^{13}C spectra of oxidized *Eh*HiPIP I acquired on a 500 MHz (11.7 T) spectrometer at a MAS rate of 60 kHz are shown in Figure 36A-B. These spectra are acquired with the double spin-echo sequence, using two adiabatic SHAP pulses,[30] allowing broadband excitation without phase distortions (details on the acquisition of NMR experiments are reported in the Appendix). Contact shifted resonances, up to 100 ppm in the ^{1}H case and up to 400 ppm for ^{13}C are observed, associated to the nuclei in β and α positions of the cysteines coordinating the Fe_4S_4 cluster. These resonances represented the most hyperfine-shifted NMR signals observed for a metalloprotein in the solid-state at the time of this study.

The interpretation of these spectra was supported with the acquisition of two 2D maps: a ^{1}H-^{1}H RFDR spectrum (Figure 36C),[31] which correlates protons close in space, and a ^{1}H-^{13}C TEDOR spectrum (Figure 36D),[32-33] which correlates pairs of nearby protons and carbons. As already mentioned, the short relaxation times of these strongly paramagnetic signals (^{1}H T_2' of ~0.5 ms for the hyperfine shifted peaks are observed in *Eh*HiPIP I) and their large shifts obliterate spin diffusion and prevent heteronuclear coherence transfers by cross-polarization, while the pulsed methods used here provide a broadband, offset-insensitive route to efficient 2D correlations.[34]

The pattern of the ^{1}H and ^{13}C contact-shifted resonances is characteristic of the electronic distribution in the oxidized Fe_4S_4 cluster, and is analogous to what already reported in solution (Table 2).[14, 22-23] As mentioned above, in solution the behavior of the cluster is well described by assuming that the iron ions are pairwise coupled into a mixed-valence pair and a ferric pair, with the presence of an equilibrium between two different distributions. The two pairs are antiferromagnetically coupled to each other, and the mixed valence pair dominates the pattern.[14, 35] Therefore, as also discussed in Chapter I and shown in Figure 34, the iron ion in the mixed-valence state induces a strong downfield shift on the coordinating cysteine proton and carbons signals (Cys50). The Fe ion in the ferric state induces an upfield shift on the protons and carbons of the attached cysteine (Cys33). The ion with large (80%) ferric character induces a small downfield shift on the coordinating cysteine signals (Cys66), while the one with transient (20%) ferric character induces a downfield shift on the attached cysteine (Cys36) which is smaller than that induced by a 100% mixed-valence iron ion.

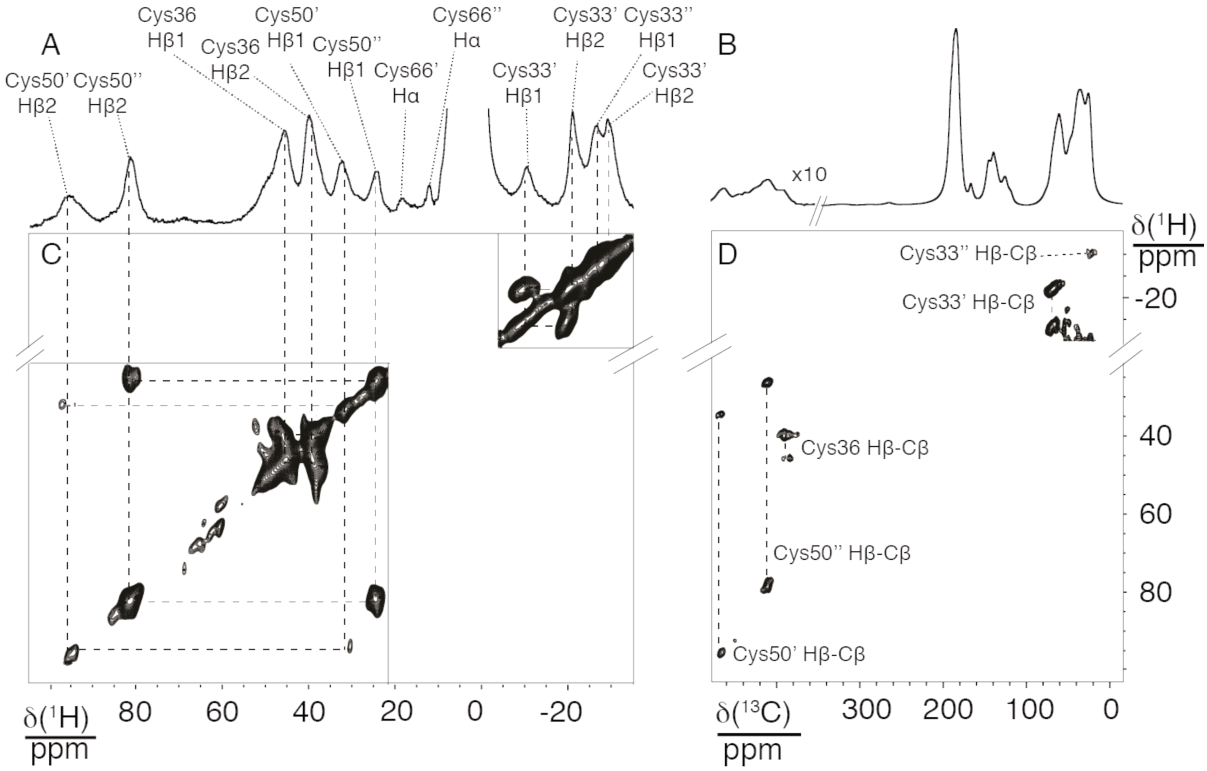

Figure 36. A) 1D ^{1}H and B) 1D ^{13}C double-adiabatic echo spectra. C) Selected regions of the ^{1}H-^{1}H RDFR spectrum. D) Selected regions of the ^{1}H-^{13}C TEDOR spectrum. (‘) and (“) denote the two different forms observed for that residue. Reproduced from reference 6.

IV.3.2 MAS NMR captures the two different conformations in the asymmetric unit

Interestingly, it is apparent that for three cysteines out of four, the contact-shifted resonances show a doubling in the MAS NMR spectra of crystalline *Eh*HiPIP I as compared

to the solution case, whikle the pattern is clearly maintained, allowing for direct transfer of the solution assignment. Similarly, in the 2D maps of Figure 2C and 2D, the correlation patterns expected on the basis of the solution NMR shifts are doubled. In particular, it appears that two forms are observable for Cys50 and Cys33, for which each $^{1}H^{\beta}$ and $^{13}C^{\beta}$ nucleus displays two different chemical shift values. Differently from the case of the $^{1}H^{N}$-$^{15}N^{H}$ correlations discussed in Chapter II, here the shift difference between equivalent proton signals is more than 10 ppm. Only one set of resonances is observable for Cys36, but the considerable broadening of these two peaks suggests that two species with very close chemical shift values may be associated to this residue as well. For Cys66 $^{1}H^{\beta}$ and $^{13}C^{\beta}$ resonances are not observable, being probably buried in the diamagnetic region of the spectrum, but from the $^{1}H^{\alpha}$ and $^{13}C^{\alpha}$ resonances it is clear that this residue features two forms as well.

Nucleus	δ (ppm)	Averaged δ (ppm)	δ_{sol} (ppm)	Difference (ppm)
		Cys33 (Fe^{3+} 100 %)		
$C^{\beta\prime}$/ $C^{\beta\prime\prime}$	68/7	37.5	41.1*	3.6
$H^{\beta1\prime}$/ $H^{\beta1\prime\prime}$	-10.5/-26.5	-18.5	-16.3	2.2
$H^{\beta2\prime}$/ $H^{\beta2\prime\prime}$	-21.0/-29.0	-25.0	-24.1	0.9
		Cys36 ($Fe^{2.5+}$ 80 %)		
C^{β}	390		390*	0
$H^{\beta1}$	44.7		45.2	0.5
$H^{\beta2}$	39.1		41.1	2.0
		Cys50 ($Fe^{2.5+}$ 100 %)		
$C^{\beta\prime}$/ $C^{\beta\prime\prime}$	465/410	437.5	440*	2.5
$H^{\beta1\prime}$/ $H^{\beta1\prime\prime}$	31.7/23.9	27.8	27.0	0.8
$H^{\beta2\prime}$/ $H^{\beta2\prime\prime}$	93.8/79.9	86.8	88.1	1.3
		Cys66 (Fe^{3+} 80 %)		
$C^{\alpha\prime}$/ $C^{\alpha\prime\prime}$	130/11.5	70.7	129*	58.3
$H^{\alpha\prime}$/ $H^{\alpha\prime\prime}$	17.9/11.7	14.8	16*	1.2

Table 2. ^{1}H and ^{13}C chemical shifts of the cysteine residues coordinating the Fe_4S_4 cluster at 298 K. Signals belonging to the two forms in solid are denoted with (') and (''), while data from solution NMR[22] are labeled with ($_{sol}$). (*) data acquired at 288 K.

^{1}H and ^{13}C chemical shifts and their assignment are reported in Table 2. It is interesting to observe how in all the cases the chemical shift values in solution are very close to the average

of the values observed in the solid state. This may indicate that the conformation of the cluster-coordinating cysteines in solution is intermediate or exchanges between two extreme conformations represented by the two different molecules found in the crystal.

IV.3.3 Temperature dependence of the hyperfine-shifted signals

The possibility to detect strongly contact shifted ^{1}H signals in microcrystalline *Eh*HIPIP I allows to measure their temperature dependence, which in turn is a direct reporter of the magnetic properties of the system. Under MAS, the temperature dependence of the proton chemical shifts could be probed in the range between 293 K and 305 K.

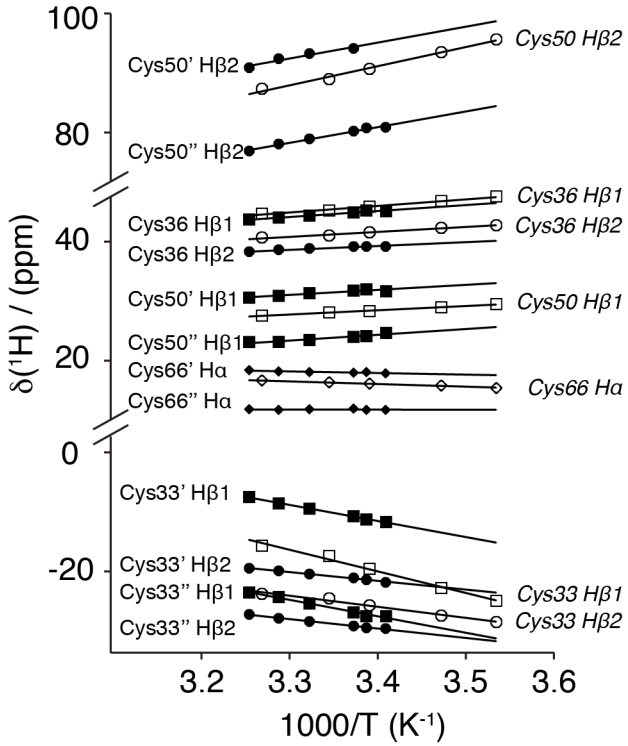

Figure 37. Curie plot of *Eh*HiPIP I in solution[23] (open symbols) and in the solid state (solid symbols). Reproduced from reference 6.

Figure 37 shows the Curie plot obtained from these measurements, and linearly fitted slopes and intercepts are reported in Table 3. Cys50 and Cys36 $^{1}H^{\beta}$ resonances, which are both bound to a mostly mixed-valence iron ion, follow a Curie-like temperature dependence (see Chapter I), while Cys33 $^{1}H^{\beta}$ resonances, bound to an iron ion belonging to the ferric pair, follow a hyper-Curie dependence,[36] extrapolating quite far downfield in the limit of infinite temperature. Cys66 $^{1}H^{\alpha}$ resonances follow instead an anti-Curie behavior, extrapolating far downfield at infinite temperature too.[16, 35-36]

Nucleus	Slope (SD) (ppm·K)	Intercept (SD) (ppm)
	Cys33 (Fe^{3+} 100 %)	
$H^{\beta1}$,	-27.06 (0.64)	80.5 (2.2)
$H^{\beta2}$,	-14.72 (0.32)	28.5 (1.1)
$H^{\beta1}$,,	-27.7 (1.8)	66.6 (5.9)
$H^{\beta2}$,,	-15.85 (0.67)	24.3 (2.3)
$H^{\beta1}{}_{sol}$	-36.4 (2.0)	103.6 (6.9)
$H^{\beta2}{}_{sol}$	-18.7 (1.3)	37.4 (4.4)
	Cys36 ($Fe^{2.5+}$ 80 %)	
$H^{\beta1}$	10.0 (1.0)	11.0 (3.3)
$H^{\beta2}$	6.49 (0.72)	17.2 (2.4)
$H^{\beta1}{}_{sol}$	11.02 (0.61)	8.6 (2.1)
$H^{\beta2}{}_{sol}$	8.56 (0.59)	13.2 (2.0)
	Cys50 ($Fe^{2.5+}$ 100 %)	
$H^{\beta1}$,	8.5 (1.7)	3.1 (5.7)
$H^{\beta2}$,	26.8 (4.5)	4 (15)
$H^{\beta1}$,,	9.7 (1.4)	-8.8 (4.6)
$H^{\beta2}$,,	26.4 (1.5)	-8.9 (5.2)
$H^{\beta1}{}_{sol}$	7.16 (0.14)	4.10 (0.48)
$H^{\beta2}{}_{sol}$	32.2 (1.7)	-18.5 (5.9)
	Cys66 (Fe^{3+} 80 %)	
H^{α},	-2.69 (0.73)	27.0 (2.5)
H^{α},,	-0.13 (0.49)	12.2 (1.7)
$H^{\alpha}{}_{sol}$	-4.41 (0.12)	31.04 (0.39)

Table 3. Fitting parameters for the Curie plots of *Eh*HiPIP I. Signals belonging to the two forms in solid are denoted with (') and (''), while data from solution NMR[22] are labeled with ($_{sol}$).

The data reveal that a similar behavior is generally observed in solution and in the solid state, and that no appreciable differences between the trends of the two sets of resonances associated to the two different forms can be observed in the solid state. This confirms that the spin distributions of the iron ions is preserved in the solid state, and the model used to interpret solution data can thus be still considered valid. This is particularly useful to confirm the performed assignment, especially where the little difference in chemical shifts makes it difficult to discriminate between $^1H^{\beta1}$ and $^1H^{\beta2}$ protons, as in the case of Cys33. Interestingly,

the Curie plots of Cys50 and Cys33 in solution have somewhat different slopes from those observed in the solid state for the two forms. This may suggest that upon temperature changes a modest structural change could occur in solution, in such a way that the conformation passes from being closer to one to being closer to the other of the two forms present in the solid state. However the analyzed temperature range is too narrow to perform a quantitative analysis, and no further investigation in this direction has been attempted.

IV.4 Conclusions

In this chapter, we have shown that solid-state NMR with very fast MAS rates and tailored rf-irradiation schemes allows for the extensive characterization of a highly paramagnetic metalloprotein containing an oxidized ISC in a microcrystalline state. Notably, resolved resonances from nuclei that experience considerable ^{1}H and ^{13}C hyperfine shifts were detected and assigned to two inequivalent conformations of the cubane cluster present in the asymmetric unit. The magnetic properties of the system were finally verified by following the variable temperature changes of the contact shifts. ISCs are common in biochemistry and are present in many membrane-bound systems, which cannot be easily accessed by atomic-resolution diffraction techniques or solution NMR. We expect therefore that the methods described above will be very broadly applicable to such important class of targets. More generally, this work represents an important proof of principle of how the experimental "toolkit" described in Chapter III can be successfully used for the detection and characterization of hyperfine-shifted resonances in a paramagnetic metalloprotein.

In the next chapter a similar approach will be used to study another paramagnetic microcrystalline protein, the human superoxide-dismutase. There, even more impressive results are obtained with the use of 100 kHz MAS rates. Moreover, the combination of the aforementioned experimental setup with state-of-the art computational tools will provide structural information on the first-coordination sphere of the paramagnetic metal ion.

IV.5 References

(1) Huang, W.; Schopfer, M.; Zhang, C.; Howell, R. C.; Todaro, L.; Gee, B. A.; Francesconi, L. C.; Polenova, T., ^{31}P magic angle spinning NMR spectroscopy of paramagnetic rare-earth-substituted Keggin and Wells-Dawson solids. *J. Am. Chem. Soc.* **2008,** *130*, 481-490.

(2) Kervern, G.; D'Aleo, A.; Toupet, L.; Maury, O.; Emsley, L.; Pintacuda, G., Crystal-structure determination of powdered aramagnetic lanthanide complexes by proton NMR Spectroscopy. *Angew. Chem. Int. Ed.* **2009,** *48*, 3082-3086.

(3) Li, J.; Pilla, K. B.; Li, Q.; Zhang, Z.; Su, X.; Huber, T.; Yang, J., Magic angle spinning nmr structure determination of proteins from pseudocontact shifts. *J. Am. Chem. Soc.* **2013,** *135*, 8294-8303.

(4) Boulon, M.-E.; Cucinotta, G.; Luzon, J.; Degl'Innocenti, C.; Perfetti, M.; Bernot, K.; Calvez, G.; Caneschi, A.; Sessoli, R., Magnetic anisotropy and spin-parity effect along the series of lanthanide complexes with DOTA. *Angew. Chem. Int. Ed.* **2013,** *52*, 350-354.

(5) Bhaumik, A.; Luchinat, C.; Parigi, G.; Ravera, E.; Rinaldelli, M., NMR crystallography on paramagnetic systems: solved and open issues. *CrystEngComm* **2013,** *15*, 8639-8656.

(6) Bertarello, A.; Schubeis, T.; Fuccio, C.; Ravera, E.; Fragai, M.; Parigi, G.; Emsley, L.; Pintacuda, G.; Luchinat, C., Paramagnetic properties of a crystalline iron-sulfur protein by magic-angle spinning NMR spectroscopy. *Inorg. Chem.* **2017,** *56*, 6624-6629.

(7) Brancaccio, D.; Gallo, A.; Mikolajczyk, M.; Zovo, K.; Palumaa, P.; Novellino, E.; Piccioli, M.; Ciofi-Baffoni, S.; Banci, L., Formation of [4Fe-4S] clusters in the mitochondrial iron-sulfur cluster assembly machinery. *J. Am. Chem. Soc.* **2014,** *136*, 16240-16250.

(8) Banci, L.; Brancaccio, D.; Ciofi-Baffoni, S.; Del Conte, R.; Gadepalli, R.; Mikolajczyk, M.; Neri, S.; Piccioli, M.; Winkelmann, J., [2Fe-2S] cluster transfer in iron-sulfur protein biogenesis. *Proc. Natl. Acad. Sci. USA* **2014,** *111*, 6203-8.

(9) Cai, K.; Tonelli, M.; Frederick, R. O.; Markley, J. L., Human mitochondrial ferredoxin 1 (fdx1) and ferredoxin 2 (fdx2) both bind cysteine desulfurase and donate electrons for iron-sulfur cluster biosynthesis. *Biochemistry* **2017,** *56*, 487-499.

(10) Andreini, C.; Bertini, I.; Cavallaro, G.; Najmanovich, R. J.; Thornton, J. M., Structural analysis of metal sites in proteins: non-heme iron sites as a case study. *J. Mol. Biol.* **2009,** *388*, 356-80.

(11) *Handbook on metalloproteins*. Bertini, I.; Sigel, A.; Sigel, H. Eds.; Marcel Dekker, Inc.: New York, 2001.

(12) *Handbook of metalloproteins*. Messerschmidt, A. Eds.; Wiley Interscience: New York, 2001.

(13) Crozet, M.; Chaussade, M.; Bardet, M.; Emsley, L.; Lamotte, B.; Mouesca, J.-M., Carbon-13 solid-state NMR studies on synthetic model compounds of [4Fe−4S] clusters in the 2+ state. *J. Phys. Chem. A* **2000,** *104*, 9990-10000.

(14) Bertini, I.; Capozzi, F.; Eltis, L. D.; Felli, I. C.; Luchinat, C.; Piccioli, M., Sequence-specific assignment of ligand cysteine protons of oxidized, recombinant HiPIP-I from Ectothiorhodospira-halophila. *Inorg. Chem.* **1995,** *34*, 2516-2523.

(15) Piccioli, M.; Turano, P., Transient iron coordination sites in proteins: Exploiting the dual nature of paramagnetic NMR. *Coord. Chem. Rev.* **2015,** *284*, 313-328.

(16) Bertini, I.; Briganti, F.; Luchinat, C.; Scozzafava, A.; Sola, M., Proton NMR spectroscopy and the electronic structure of the high potential iron-sulfur protein from *Chromatium vinosum*. *J. Am. Chem. Soc.* **1991,** *113*, 1237-1245.

(17) Banci, L.; Bertini, I.; Eltis, L. D.; Felli, I. C.; Kastrau, D. H.; Luchinat, C.; Piccioli, M.; Pierattelli, R.; Smith, M., The three-dimensional structure in solution of the paramagnetic high-potential iron-sulfur protein I from *Ectothiorhodospira halophila* through nuclear magnetic resonance. *Eur. J. Biochem.* **1994,** *225*, 715-725.

(18) Bertini, I.; Briganti, F.; Luchinat, C.; Messori, L.; Monnanni, R.; Scozzafava, A.; Vallini, G., 2D ^{1}H NMR studies of oxidized 2(Fe_4S_4) ferredoxin from *Clostridium pasteurianum*. *FEBS Lett.* **1991,** *289*, 253-6.

(19) Breiter, D. R.; Meyer, T. E.; Rayment, I.; Holden, H. M., The molecular-structure of the High-Potential Iron-Sulfur protein isolated from *Ectothiorhodospira-halophila* determined at 2.5-Å resolution. *J. Biol. Chem.* **1991,** *266*, 18660-18667.

(20) Bertini, I.; Campos, A. P.; Luchinat, C.; Teixeira, M., A Mössbauer investigation of oxidized Fe_4S_4 Hipip-II from *Ectothiorohodospira-halophila*. *J. Inorg. Biochem.* **1993,** *52*, 227-234.

(21) Bertini, I.; Eltis, L. D.; Felli, I. C.; Kastrau, D. H. W.; Luchinat, C.; Piccioli, M., The solution structure of oxidized HiPIPI from *Ectothiorhodospira halophila*; Can NMR spectroscopy be used to probe rearrangements associated with electron transfer processes? *Chem. Eur. J.* **1995,** *1*, 598-607.

(22) Bertini, I.; Donaire, A.; Felli, I. C.; Luchinat, C.; Rosato, A., ^{1}H and ^{13}C NMR studies of an oxidized HiPIP. *Inorg. Chem.* **1997,** *36*, 4798-4803.

(23) Krishnamoorthi, R.; Markley, J. L.; Cusanovich, M. A.; Przysiecki, C. T.; Meyer, T. E., Hydrogen-1 nuclear magnetic resonance investigation of high-potential iron-sulfur proteins from *Ectothiorhodospira halophila* and *Ectothiorhodospira vacuolata*: a comparative study of hyperfine-shifted resonances. *Biochemistry* **1986,** *25*, 60-67.

(24) Banci, L.; Bertini, I.; Ciurli, S.; Ferretti, S.; Luchinat, C.; Piccioli, M., The electronic structure of $Fe_4S_4^{3+}$ clusters in proteins - an investigation of the oxidized High-Potential Iron-Sulfur Protein-II from *Ectothiorhodospira-Vacuolata*. *Biochemistry* **1993,** *32*, 9387-9397.

(25) Banci, L.; Bertini, I.; Luchinat, C., The ^{1}H NMR parameters of magnetically coupled dimers—The Fe_2S_2 proteins as an example. *Struct. Bond.* **1990,** *72*, 113-136.

(26) Dilg, A. W.; Mincione, G.; Achterhold, K.; Iakovleva, O.; Mentler, M.; Luchinat, C.; Bertini, I.; Parak, F. G., Simultaneous interpretation of Mossbauer, EPR and ^{57}Fe ENDOR spectra of the [Fe_4S_4] cluster in the high-potential iron protein I from *Ectothiorhodospira halophila*. *J. Biol. Inorg. Chem.* **1999,** *4*, 727-741.

(27) Belinskiy, M.; Bertini, I.; Galas, O.; Luchinat, C., An exchange coupling model for the $Fe_4S_4^{3+}$ polymetallic center present in high potential iron-sulfur proteins. *Inorg. Chim. Acta* **1996,** *243*, 91-99.

(28) Bertini, I.; Capozzi, F.; Luchinat, C.; Piccioli, M., ^{1}H-NMR investigation of oxidized and reduced high-potential iron-sulfur protein from *Rhodopseudomonas globiformis*. *Eur. J. Biochem.* **1993,** *212*, 69-78.

(29) Westler, W. M.; Lin, I. J.; Perczel, A.; Weinhold, F.; Markley, J. L., Hyperfine-shifted ^{13}C resonance assignments in an iron-sulfur protein with quantum chemical verification: aliphatic C-H...S 3-center-4-electron interactions. *J. Am. Chem. Soc.* **2011,** *133*, 1310-1316.

(30) Kervern, G.; Pintacuda, G.; Emsley, L., Fast adiabatic pulses for solid-state nmr of paramagnetic systems. *Chem. Phys. Lett.* **2007,** *435*, 157-162.

(31) Griffiths, J. M.; Griffin, R. G., Nuclear magnetic resonance methods for measuring dipolar couplings in rotating solids. *Anal. Chim. Acta* **1993,** *283*, 1081-1101.

(32) Holl, S. M.; Marshall, G. R.; Beusen, D. D.; Kociolek, K.; Redlinski, A. S.; Leplawy, M. T.; McKay, R. A.; Vega, S.; Schaefer, J., Determination of an 8-Angstrom interatomic distance in a helical peptide by solid-state NMR-spectroscopy. *J. Am. Chem. Soc.* **1992,** *114*, 4830-4833.

(33) Saalwachter, K.; Graf, R.; Demco, D. E.; Spiess, H. W., Heteronuclear double-quantum MAS NMR spectroscopy in dipolar solids. *J. Magn. Reson.* **1999,** *139*, 287-301.

(34) Kervern, G.; Pintacuda, G.; Zhang, Y.; Oldfield, E.; Roukoss, C.; Kuntz, E.; Herdtweck, E.; Basset, J. M.; Cadars, S.; Lesage, A.; Coperet, C.; Emsley, L., Solid-state NMR of a paramagnetic DIAD-Fe-II catalyst: Sensitivity, resolution enhancement, and structure-based assignments. *J. Am. Chem. Soc.* **2006,** *128*, 13545-13552.

(35) Capozzi, F.; Ciurli, S.; Luchinat, C., Coordination sphere versus protein environment as determinants of electronic and functional properties of iron-sulfur proteins. In *Metal Sites in Proteins and Models Redox Centres*, Hill, H. A. O.; Sadler, P. J.; Thomson, A. J., Eds. Springer Berlin Heidelberg: Berlin, Heidelberg, 1998; pp 127-160.

(36) Banci, L.; Bertini, I.; Luchinat, C.; Pierattelli, R.; Shokhirev, N. V.; Walker, F. A., Analysis of the temperature dependence of the ^{1}H and ^{13}C isotropic shifts of horse heart ferricytochrome c: explanation of Curie and anti-Curie temperature dependence and nonlinear pseudocontact shifts in a common two-level framework. *J. Am. Chem. Soc.* **1998,** *120*, 8472-8479.

Chapter V.

Experiments and theory meet at the active site of a metalloprotein

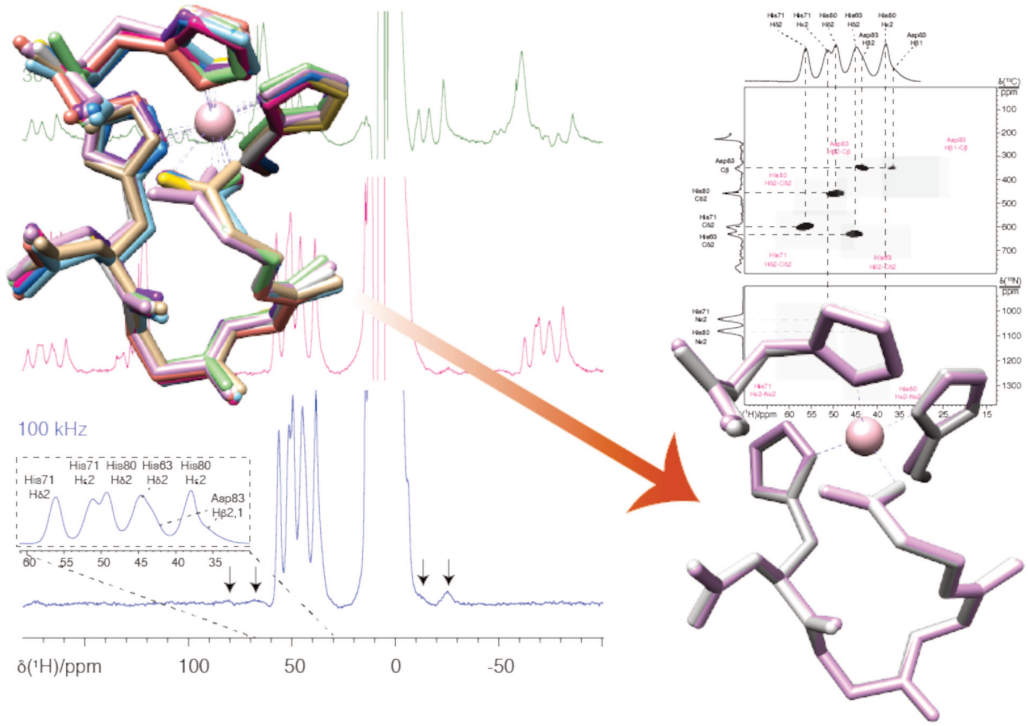

V.1 Introduction

In the previous chapter the combined use of fast MAS and suitably tailored radiofrequency irradiation schemes allowed detection and characterization of nuclei in the coordination sphere of a paramagnetic cluster in a metalloprotein experiencing large contact shifts. It was also shown how MAS NMR is a sensitive probe of the geometric environment of the active site of a metalloprotein.

In this chapter, we will try to move one step further, and investigate the possibility to exploit PNMR effects to provide atomic level structural information on the metal binding site of a metalloprotein. Accurate determination of three-dimensional molecular structures at atomic resolution is a tremendous task. Most of our understanding of chemistry and biology of metalloproteins derives from molecular structures obtained with X-ray diffraction (XRD) crystallography.[1] The resolution of XRD structures is limited by a number of factors such as the need of highly ordered crystalline samples and the X-ray-induced radiation damage, due to which the data usually need to be acquired at cryogenic temperatures. Moreover, even when high-resolution XRD structures are available, often the structure of the metal site and its coordination geometry are not well determined.[2] Metal coordination distances can be refined with X-ray absorption techniques[3] which, however, share many of the limitations of XRD.

In this respect, we would like to exploit the sensitivity of NMR to the electronic structure and coordination geometry of paramagnetic metal ions at the active site in a new perspective. Long-range effects such as pseudo-contact shifts and NMR relaxation enhancements in systems containing paramagnetic metal ions are already available and largely exploited both in solution and in the solid state, as discussed in Chapter I. However, these NMR parameters are not used for determining the structure of the metal center itself.

In this chapter, MAS NMR combined with quantum chemistry modeling is proposed as a robust approach for obtaining structural restraints on the coordination sphere of a paramagnetic metal at the core of a metalloprotein. The method relies on the measurement, calculation, assignment, and structural interpretation of PNMR shifts in the Fermi-contact regime. This leverages the recent experimental advances, already highlighted in the previous chapter, and the recent development of theory of PNMR shift tensors (see Chapter III), which has enabled their rigorous modeling from first principles of quantum mechanics[4] providing a direct access to the structural interpretation of measured PNMR shifts.

The method is demonstrated on a metalloenzyme, the human superoxide dismutase 1, in its copper-free form containing a paramagnetic Co^{II} ion (Co^{II}-SOD). The method allows

refinement of the coordination structure of the paramagnetic Co^{II} complex and yields fine structural details of the metal coordination sphere with sub-atomic resolution at room temperature.

V.2 Superoxide dismutase: a benchmark system for PNMR

Superoxide dismutases (SODs) are a class of metalloenzymes that catalyze the dismutation of superoxide radicals into hydrogen peroxide and oxygen using transition metal ions as cofactors. As such, they represent an important antioxidant defense in almost all living cells exposed to oxygen.[5] Different types of SODs have been identified in all living organisms, displaying variable oligomerization degrees and binding different metal ions.[5-6]

In this chapter the thermostable C6A, C111S mutant of human SOD1 is analyzed.[7] This protein is a 32-kDa non-covalent homodimer, which has two high-affinity binding sites for metal cations in its catalytic cavity. One site is occupied by Cu, which switches between Cu^{I} and Cu^{II} oxidation states during the enzymatic activity, and the other one is occupied by Zn^{II}. In the oxidized form the Cu^{II} ion is coordinated to four histidines through their $N^{\varepsilon 2}$ atom (His48, His63, His120) or $N^{\delta 1}$ atom (His46), and to a distant water molecule. The Zn^{II} ion is in a distorted tetrahedral coordination, being coordinated to three histidines through their $N^{\delta 1}$ atom (His63, which bridges the two ions, His71, and His80) and to the carboxylate group of Asp83 (Figure 38).

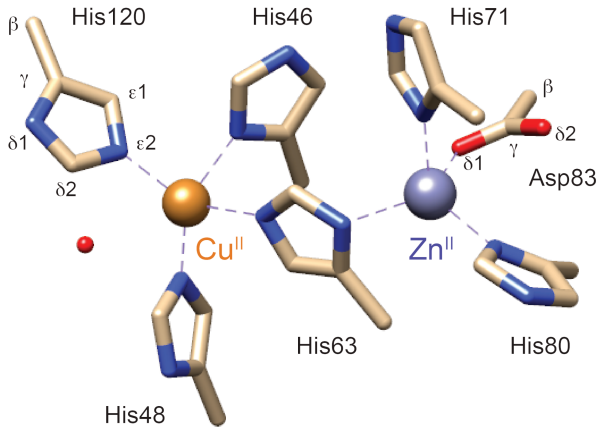

Figure 38. Schematic representation of the active site of human Cu^{II},Zn^{II}-SOD with labeling of histidine and aspartate positions (PDB code: 1SOS). Hydrogen atoms are omitted.

Cu^{II} is a paramagnetic ion with S=1/2 and a long electronic correlation time, τ_e, usually between 10^{-8} and 10^{-9} s. This leads to very fast paramagnetic relaxation of the NMR signals of

the nuclei in the coordination sphere of the metal (see Chapter I), which are broadened beyond detection. In order to recover these NMR signals it would be necessary to shorten the electron relaxation time of Cu^{II}.

Interestingly, the metallation state of the protein can be experimentally changed with minimal structural and functional changes.[8-9] This was exploited in the past to selectively tune the paramagnetic behavior of the sample, so that different positions of the molecule could be characterized by solution NMR.[8] Notably, the substitution of Zn^{II} with Co^{II} allowed the spectroscopic characterization of the Zn site in native SOD,[8] as well as to perform high-resolution ^{1}H-NMR of the Zn site in the copper-free form.[10] High-spin Co^{II} is an ion with S=3/2 and short electronic relaxation time (10^{-11} – 10^{-12} s in a tetrahedral environment), which is suitable for investigation by NMR.[11] Resolved hyperfine-shifted peaks arising from nuclei in the Co^{II} coordination sphere can then be observed, providing a probe of the local environment.

Moreover, when Zn^{II} is substituted with Co^{II} in the protein binding Cu^{II} (Cu^{II},Co^{II}-SOD), the weak antiferromagnetic coupling ($J \cong 16.5$ cm^{-1})[12] between Cu^{II} and Co^{II} trough the histidine ring dramatically shortens the electron relaxation time for Cu^{II}, which approaches those of high-spin Co^{II}.[13] As a consequence high-resolution NMR characterization of the Cu site is possible.[13-14] Cu^{II},Co^{II}-SOD has a catalytic activity comparable to that of the native enzyme and, therefore, can be used as a model of the latter.[15]

Following the impressive work done in the past on SOD by solution NMR,[13] we decided to target it as an attractive benchmark system for solid-state NMR. In a first step we focused on the microcrystalline fully protonated copper-free form of SOD where Zn^{II} is substituted with Co^{II} (Co^{II}-SOD). We show how the combined use of state of the art MAS NMR technology and PNMR theory not only reproduces the results obtained in solution, but also complements the available data with the observation and assignment of new resonances, previously invisible. In addition to that, NMR data can be interpreted with the aid of novel theoretical and computational tools to provide structural information on the coordination sphere of the metal ion. Notably, the XRD structure of human SOD[7] describes the metal site with a substantial uncertainity. The deposited structure corresponds to an ensemble of ten conformers, whose RSMD at the active site is of 0.20 Å. With the methodology proposed in this chapter, it is possible to narrow the bundle of structures of the Co^{II} complex to those that well correspond to the measured ^{1}H, ^{13}C, and ^{15}N PNMR shift pattern, thereby reducing the structural disorder at this site.

As a future perspective, we show preliminary results on Cu^{II},Co^{II}-SOD as well. In this case, the theoretical framework for calculation of PNMR shifts from first principle still misses the formalism for the inclusion of ZFS effects; therefore a structural interpretation of the experimental data is not available at the time of writing. Still, the results obtained for Co^{II}-SOD can be used for a qualitative interpretation of the Cu^{II},Co^{II} -SOD case.

V.3 Exploring the metal center of Co^{II}-SOD

V.3.1 MAS NMR of Co^{II}-SOD

By using the experimental toolkit provided in Chapter III it is possible to acquire the NMR spectra of nuclei in the coordination sphere of the metal ion. ^{1}H and ^{13}C spin-echo spectra are shown in Figure 39A-B. Contact-shifted resonances were observed between -26–82 ppm in the ^{1}H spectrum and up to 1210 ppm in the ^{13}C spectrum. From the ^{1}H spectra it is evident how the large shift anisotropies (SAs) caused by the presence of the paramagnetic ion induce spreading of the signals over more spinning sidebands, affecting both sensitivity and resolution of the spectra. In this respect, the use of the fastest MAS rates available is highly beneficial in order to concentrate the signal into fewer sidebands, as observed in the ^{1}H spectrum in Figure 39A. Using 100 kHz MAS actually allowed for the complete removal of the overlap with the spinning-sideband manifold. The region between 35–60 ppm shows the same pattern of PNMR shifts as observed in solution, and then can be easily assigned.[10, 13] Notably, at state-of-the-art 100 kHz MAS several very broad ^{1}H resonances become observable above 60 ppm and below -8 ppm, which were escaping detection at lower MAS rates and in solution (marked with an arrow in Figure 39A).

In the ^{13}C spin-echo spectrum the overlap with the spinning-sideband manifold was not removed even at 100 kHz MAS, potentially hindering the observation of some resonances. In order to recover the isotropic spectrum a ^{13}C aMAT spectrum has been acquired,[16] allowing to correlate the spinning-sideband manifold of each ^{13}C nucleus with its isotropic shift. The isotropic spectrum was recovered as a projection along the indirect dimension (Figure 39B). The aMAT experiment was also used to evaluate the ^{1}H and ^{13}C SAs by extracting rows in the spectrum corresponding to individual isotropic shifts and fitting thus obtained spinning-sideband manifold, as shown for the proton case in Figure 39E.

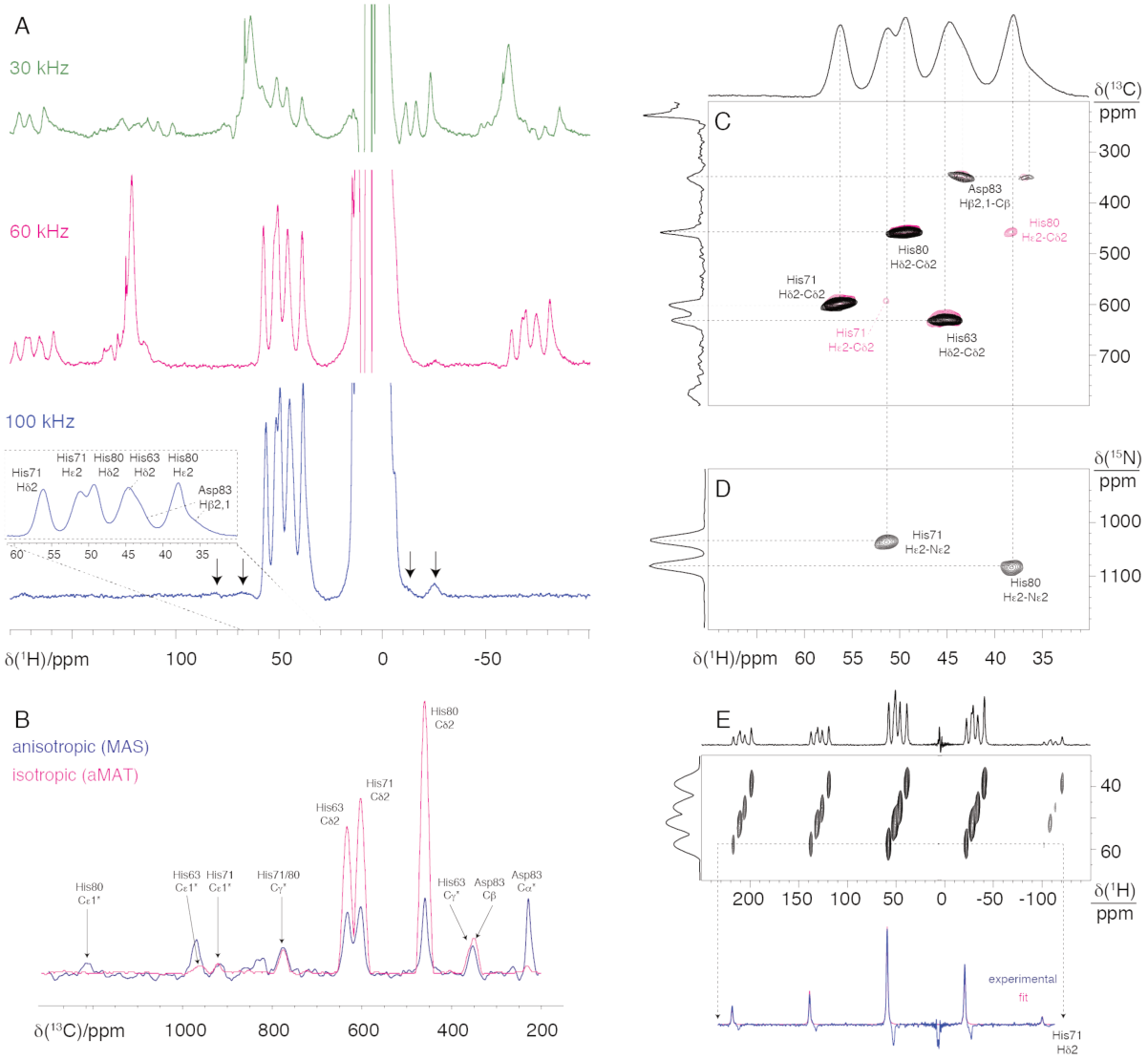

Figure 39. A) ^{1}H spin-echo spectra of [U-^{13}C, ^{15}N]-labeled Co^{II}-SOD acquired at different MAS rates, with assignment of the 35–60 ppm region in the close-up box. Vertical arrows in the 100 kHz MAS spectrum label the newly observed ^{1}H signals. B) ^{13}C spin-echo spectrum (blue) and projection from the ^{13}C aMAT spectrum (magenta), acquired at 100 and 50 kHz MAS, respectively, with assignment of observable peaks (* assigned based on calculations). C) (H)CH TEDOR spectrum (black) and (H)C(H)H TEDOR spectrum (magenta). D) (H)NH TEDOR spectrum. E) ^{1}H aMAT spectrum, with the row corresponding to His71 ^{1}H$^{\delta 2}$ spinning-sideband manifold and the relative fit. All spectra were acquired at 280 K in a 500 MHz (11.7 T) spectrometer.

Detection of the paramagnetically shifted signals is not all. (H)CH and (H)NH TEDOR[17-18] experiments allowed to correlate pairs of spatially nearby protons and carbons or nitrogens (Figure 39C-D), which represents a main hint towards resonance assignment. Differently from what done in Chapter IV, we used here a ^{1}H-detected version of the experiments, which displays increased sensitivity compared to the ^{13}C (or ^{15}N) detected one. The (H)CH TEDOR was also used as a building block in the (H)C(H)H TEDOR experiment, where a radio-frequency driven recoupling (RFDR) scheme[19] was added at the end of the sequence, allowing mixing between protons close in space. The resulting spectrum shows, in addition to the peaks observed in the (H)CH TEDOR, correlations to protons that are not directly bonded

to a given carbon nucleus, thus providing additional information for the resonance assignment (Figure 39C, magenta). The possibility to extend the assignment to ^{13}C and ^{15}N nuclei represents a complement to the data obtained in solution NMR, where no information on heteronuclear connectivity could be assessed. This represents a main fundamentals advantage of the MAS NMR approach.

Overall, the application of this experimental toolkit combined with fast MAS has the effect of almost completely removing the blind sphere.

V.3.2 PNMR calculations for the metal site

Once the PNMR shifts and SAs are acquired, a reliable assignment protocol is needed. For diamagnetic proteins this is a well-established procedure relying on the fact that different types of nuclei in different residues and structural environments display well-defined ranges of chemical shifts. However, this is not the case for paramagnetic systems, especially in the presence of strong contact interactions, which alter the observed shifts in a non-empirically predictable way. For this reason, the assignment based solely on experimental data is often not possible[11] and the use of theoretical modeling is of fundamental importance.

We performed a series of DFT and *ab initio* calculations in order to predict the NMR shifts of the nuclei of interest and to connect the experimental data to the electronic and three-dimensional structure of the Co^{II}-binding complex of Co^{II}-SOD. Accordingly to the employed theory of PNMR shifts discussed in Chapter III,[4] we calculated the EPR parameters of the Co^{II} complex, in particular the *g*-tensor, the zero-field splitting (ZFS) tensor and the hyperfine coupling (HFC) tensors of the NMR nuclei. This requires a structural model of the metal coordination sphere. In this case as a starting model we used the XRD structure of human Cu^{II},Zn^{II}-SOD containing ten protein chains (five dimers) in the crystallographic asymmetric unit.[7] From these protein chains, we built models A–J of the Co^{II}-binding site of Co^{II}-SOD. These models included the side chains of residues directly coordinating the metal ion (His63, His71, His80 and Asp83) as well as portions of other residues (Gly72, Arg79, Val81, Gly82) that are involved in H-bonding with the ligands, which are fundamental in determining the correct coordination geometry. Partial geometry optimization with C^{α} atoms fixed in space was used to adjust the Co^{II} binding geometry, while at the same time keeping the overall molecular fold intact. This step was necessary to refine the Co^{II} coordination sphere to a degree required for obtaining reliable EPR property tensors while maintaining the structural variation associated with the uncertainty of the XRD data (Figure 41A). We note that the DFT optimization of the models A–J should not be viewed by itself as a structure refinement of the

crystallographic data. This can be reliably achieved only by comparing calculated and experimental values of spectroscopic parameters, here the PNMR shifts.

The calculations revealed that the isotropic *g*-value had a rather stable value of 2.22–2.23 among all models (Table 4), comparing perfectly with the experimental value of 2.24.[12] The absolute value of the zero-field splitting $|D|$ varied between 5.1–7.5 cm^{-1} in the calculations which is somewhat lower than the previously measured value of 10.8 cm^{-1}.[12] This difference is likely caused by a combination of factors. We cannot exclude effects beyond our computational approach. Furthermore, the experimental *D*-value is likely inaccurate since it had been obtained by fitting of temperature dependent paramagnetic susceptibility assuming a simplified Hamiltonian with isotropic *g*-tensor and axial ZFS.

EPR parameter	1SOS.A	1SOS.B	1SOS.C	1SOS.D	1SOS.E	1SOS.F	1SOS.G	1SOS.H	1SOS.I	1SOS.J	EXP [a]
g_{iso}	2.231	2.222	2.222	2.229	2.223	2.221	2.224	2.231	2.227	2.226	2.24
g_{11}	2.183	2.178	2.196	2.180	2.183	2.192	2.179	2.185	2.180	2.196	
g_{22}	2.236	2.232	2.219	2.229	2.229	2.223	2.235	2.231	2.230	2.216	
g_{33}	2.274	2.257	2.251	2.277	2.256	2.247	2.258	2.276	2.269	2.265	
g_{aniso}	0.064	0.052	0.043	0.072	0.050	0.039	0.051	0.068	0.064	0.059	
D_{11} [b]	4.676	4.618	3.275	4.980	4.483	3.523	4.624	4.817	4.916	3.538	
D_{22} [b]	-0.509	-1.287	0.140	-0.161	-0.743	-0.398	-1.721	-0.069	-1.105	0.985	
D_{33} [b]	-4.168	-3.331	-3.415	-4.819	-3.740	-3.125	-2.903	-4.749	-3.811	-4.524	
$\|D\|$ [b]	7.01	6.93	5.12	7.47	6.72	5.28	6.94	7.23	7.37	6.79	10.8
E/D	0.261	0.148	0.306	0.312	0.223	0.258	0.085	0.324	0.184	0.188	

Table 4. Summary of EPR parameters of the Co^{II} center of Co^{II}-SOD calculated at NEVPT2 level and comparison to the available experimental data. [a] Taken from reference 12. [b] In cm^{-1}. Principal values of the traceless *D*-tensor (D_{ii}, ii = 11, 22, 33) sorted in mutual correspondence with the principal values of the *g*-tensor (g_{ii}) such that the principal axes of the two tensors with the same label approximately coincide.

Nevertheless, the geometry dependence of the PNMR shifts (see Tables 17-18 in Appendix) was to a large extent dominated by that of the EPR hyperfine couplings. Contemporary HFC calculations are lacking a benchmark *ab initio* level applicable to systems of biologically relevant sizes. Resorting to DFT methods, there is currently no universally preferred functional for HFCs.[20] In such a situation, the HFC tensors need to be calculated with a set of DFT functionals in order to provide a reliable range of values. Previous calculations on a different Co^{II}-binding complex[21] showed that the range given by PBE0 and PBE50 hybrid DFT functionals defines a reliable confidence interval.

V.3.3 Structural interpretation of PNMR shifts

The calculated PNMR shifts and SAs should be viewed in the following way: when the experimental PNMR data lie within the calculated bounds, this establishes the resonance assignment and confirms the validity of the employed structural model. Conversely, when a significant portion of experimental data lies far outside of the calculated bounds the underlying structural model can be excluded. This principle may be exploited to refine the structure of the metal binding complex by selecting a subset of models that satisfy the agreement with the experiment.

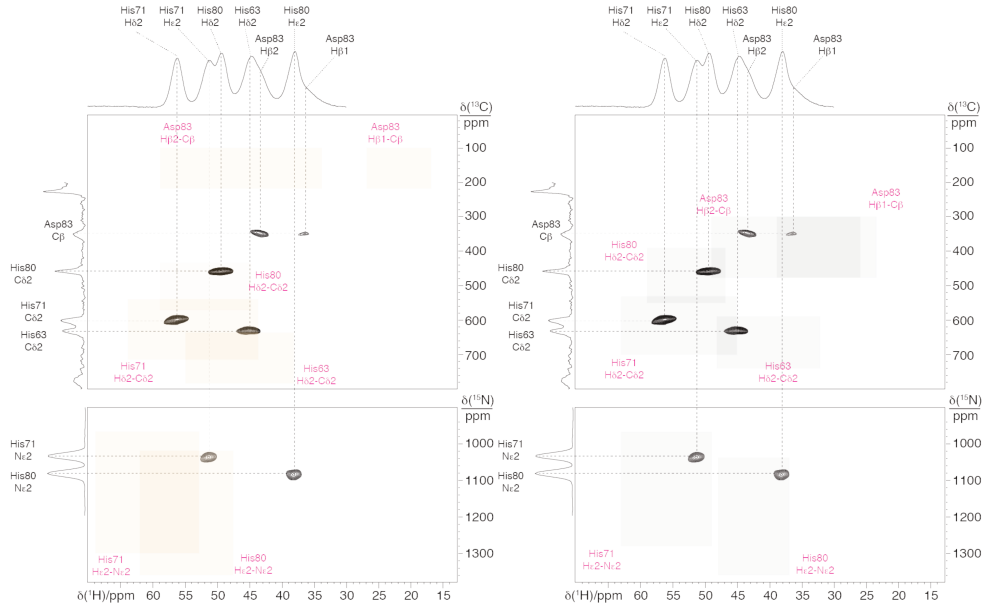

Figure 40. Experimental (H)CH TEDOR (top) and (H)NH TEDOR (bottom) spectra and the calculated correlations for model A (left, orange boxes) and model F (right, gray boxes).

Figure 40 illustrates a good (right panel) and an unsatisfactory (left panel) agreement between experimental resonances and calculated intervals (shaded boxes) as obtained for models F and A, respectively. Note that despite the large uncertainty associated with the calculations, the even larger dispersion of paramagnetic shifts guarantees to this procedure a strong structural discriminating power. At the same time, as the computational methods evolve, the accuracy of the calculated PNMR shifts bounds is guaranteed to improve in the future.

Out of the ten models A–J, only models C and F fully satisfy the agreement criteria with the (H)CH and (H)NH correlation spectra. At the same time, these models define a structural ensemble with a significantly better resolution at the metal site than the original XRD-based ensemble (Figure 41B), lowering the RMSD from 0.20 Å of the initial ensemble to 0.09 Å. Additionally, using the calculations for model F it was possible to achieve a complete

assignment of all ^{1}H, ^{13}C, and ^{15}N observed resonances. This substantially enhances the so far limited set of available assignments for the contact-shifted resonances in Co^{II}-SOD,[13] as discussed later.

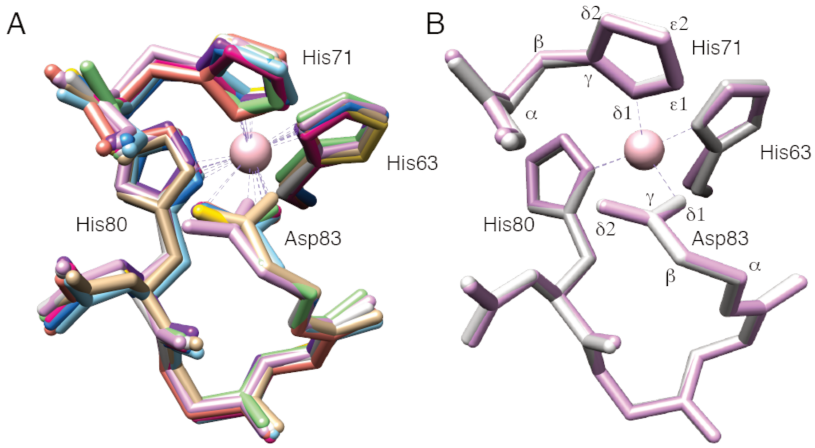

Figure 41. Ensemble of Co^{II} site models built from the ten protein chains of the XRD structure of human superoxide dismutase 1 (PDB code: 1SOS), illustrating the crystallographic uncertainty in the metal coordination geometry (A) and the refined ensemble of structures of the Co^{II} complex of Co^{II}-SOD (B). The labeling of the histidine and aspartate atoms is also shown. The resolution at the metal site, evaluated as root mean square deviation (RMSD) of non-hydrogen atoms of metal-binding amino-acid side chains, improved from 0.20 Å for the XRD structural ensemble to 0.09 Å for the refined ensemble.

With a reliable structure of the Co^{II}-binding complex at hand it is possible to interpret the measured PNMR shift pattern in terms of local geometry parameters of the metal site. The most important structure descriptors of the Co^{II} site are the symmetry of the coordination sphere and the metal-ligand distances (Table 5). The Co^{II} site has a distorted tetrahedral coordination geometry, binding to His63 $N^{\delta1}$, His71 $N^{\delta1}$, His80 $N^{\delta1}$, and Asp83 $O^{\delta1}$, with an admixture of penta-coordination given by the inclination of Asp83 $O^{\delta2}$ to the metal. A closer look at the optimized models A–J reveals that a longer Co–$O^{\delta2}$ distance is accompanied by a slightly shorter Co–$O^{\delta1}$ coordination bond and vice versa.

	A	B	C	D	E	F	G	H	I	J
r(Co–Asp83 Oδ1) (r_1) [a]	1.991	1.935	1.947	1.966	1.939	1.945	1.940	1.973	1.924	1.974
r(Co–Asp83 Oδ2) (r_2) [a]	2.508	2.833	2.777	2.631	2.828	2.762	2.814	2.598	2.871	2.663
Δr(Co–Oδ) [a]	0.517	0.898	0.831	0.665	0.889	0.816	0.874	0.624	0.947	0.688
θ(His63 Nδ1–Co–His71 Nδ1) ($\theta_{63\text{-}71}$) [b]	99.2	101.3	103.8	100.2	102.0	102.8	102.0	98.6	101.2	103.3
θ(His80 Nδ1–Co–Asp83 Oδ1) ($\theta_{80\text{-}83}$) [b]	123.0	124.2	119.4	123.3	108.1	120.1	124.3	123.2	121.0	119.3
PDB structures:										
r(Zn–His63 Nδ1) [a]	2.102	2.121	2.079	2.125	2.124	2.088	2.071	2.109	2.106	2.078
r(Zn–His71 Nδ1) [a]	2.058	2.076	2.062	2.081	2.097	2.050	2.070	2.051	2.053	2.068
r(Zn–His80 Nδ1) [a]	2.044	2.055	2.046	2.093	2.079	2.063	2.053	2.085	2.042	2.061
r(Zn–Asp83 Oδ1) [a]	1.923	1.966	1.943	1.955	1.964	1.951	1.948	1.919	1.947	1.934
r(Zn–Asp83 Oδ2) [a]	3.038	2.937	3.742	2.890	2.512	3.160	2.692	3.191	2.817	2.999
Δr(Zn–Oδ) [a]	0.772	0.701	1.115	0.972	1.799	0.935	0.548	1.209	0.745	1.272

Table 5. Selected geometry parameters of the metal center of SOD. [a] Distance in Å. [b] Angle in deg.

We found that certain PNMR shifts are particularly sensitive to the mode of Asp83 binding to the metal, most notably the Asp83 $^{13}C^{\beta}$ shift observed at 350 ppm. The Asp83 $^{13}C^{\beta}$ shift values calculated for the optimized models A–J span a wide range and there is a clear structural correlation to both r(Co–$O^{\delta1}$) and r(Co–$O^{\delta2}$) (r_1 and r_2 respectively in Figure 42A-B). Hence, the experimental Asp83 $^{13}C^{\beta}$ shift constrains the distances r(Co–$O^{\delta1}$) and r(Co–$O^{\delta2}$) according to the calculated structural dependences to 1.95 ± 0.01 Å and 2.75 ± 0.08 Å, respectively. This determines the mode of Co^{II} coordination in Co^{II}-SOD: the relatively long r(Co–$O^{\delta2}$) distance implies that Co^{II} is distinctly tetra-coordinated. We note that, despite the uncertainty, the Co–O^{δ} coordination distances are determined with a substantially better resolution than was available in the original XRD ensemble (Table 5).

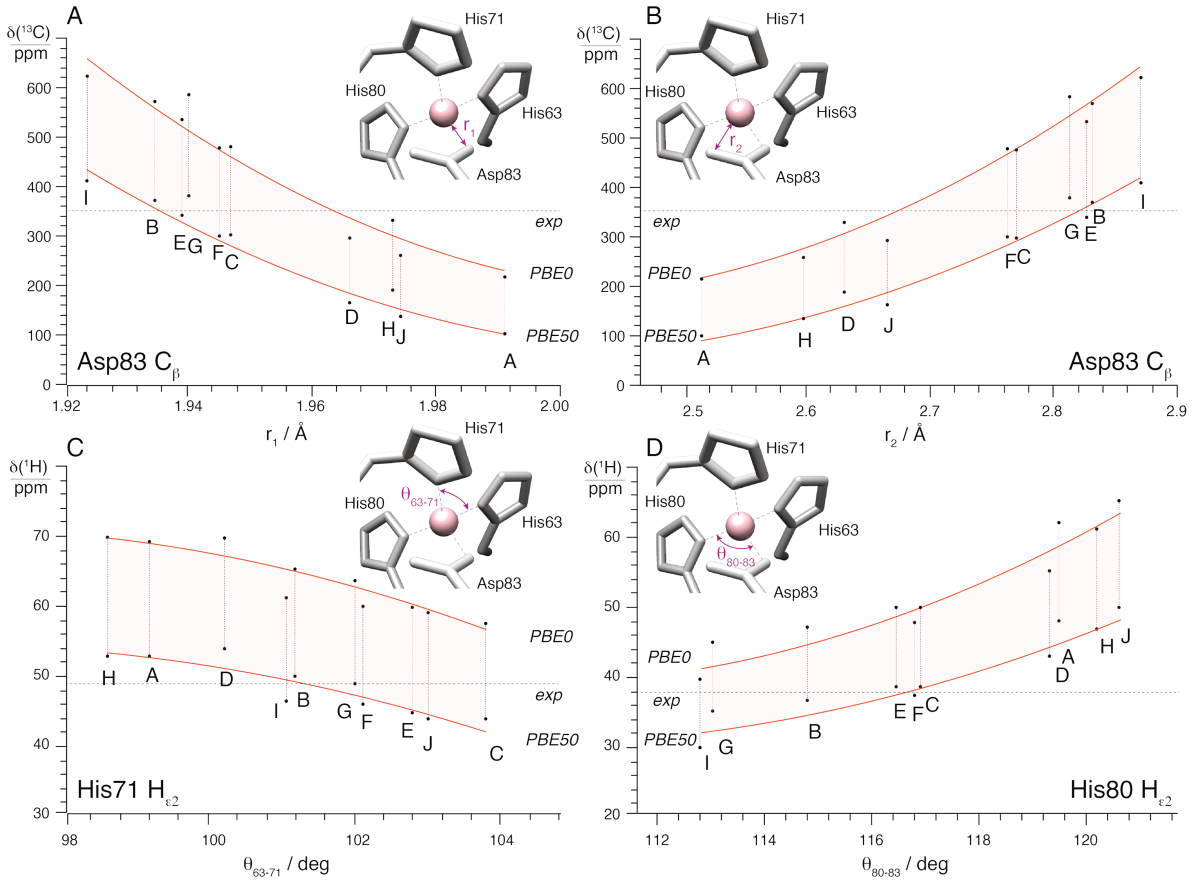

Figure 42. Calculated shifts for the ten models A-J using PBE0-PBE50 functionals for the hyperfine coupling, compared to the experimentally observed shifts: Asp83 $^{13}C^{\beta}$ shift plotted as a function of the r_1 (A) and r_2 (B) distances; His71 $^{1}H^{\varepsilon2}$ shift plotted as a function of the $\theta_{63\text{-}71}$ angle (C); His80 $^{1}H^{\varepsilon2}$ shift plotted as a function of the $\theta_{80\text{-}83}$ angle (D).

The Asp83 $^{13}C^{\beta}$ shift is not the only parameter that can be used as probe of the structural environment of the Co^{II} complex of Co^{II}-SOD. We observed that certain PNMR shifts are sensitive to the angles defined by two donor atoms and the metal ion, which as the Asp83 binding mode are intimately related to geometry of the Co^{II} complex. In particular, His71 $^{1}H^{\varepsilon2}$

shift puts a lower bound of 101° on the (His63 $N^{\delta1}$–Co–His71 $N^{\delta1}$) angle ($\theta_{63\text{-}71}$ in Figure 42C), and His80 $^1H^{\varepsilon2}$ shift constrains the (His80 $N^{\delta1}$–Co–Asp83 $O^{\delta1}$) angle ($\theta_{80\text{-}83}$ in Figure 42D) below 117°.

These values could be in principle directly applied as constrains on the metal coordination geometry in the XRD data refinement procedure, improving the resolution of the generated structure.

V.3.4 NMR assignment strategy

The full assignment of ^1H, ^{13}C, and ^{15}N NMR signals is reported in Table 6. The general assignment strategy is based on the comparison between experimental and calculated isotropic chemical shifts (Table 6) and SAs (Table 7) for model F, which among the ten models the best reproduces the experimental values. Depending on the quality of the experimental data for a given atom, an unambiguous or just a tentative assignment can be provided. It should be noted that, even if the previously published solution NMR ^1H assignment was initially used to validate our method, the combined use of the experimental and calculated data would have allowed the complete assignment without any prior knowledge.

Unambiguously assigned resonances. From the comparison of the ^1H spin-echo spectrum with the previously published ^1H solution spectrum[10, 13] it is evident that the pattern of the observed shifts is preserved, and thus the available solution assignment can be easily transferred. In particular, His71 $^1H^{\varepsilon2}$ and $^1H^{\delta2}$, His80 $^1H^{\varepsilon2}$ and $^1H^{\delta2}$, His63 $^1H^{\delta2}$, and Asp83 $^1H^{\beta1}$ and $^1H^{\beta1}$ can be assigned. His63 $^1H^{\varepsilon2}$ resonance is not observed. This might be due to chemical exchange phenomena occurring at this site, which is solvent exposed, as was already noticed in solution.[13] All these nuclei can then be correlated with the directly attached ^{13}C or ^{15}N nuclei through the (H)CH and (H)NH TEDOR spectra, and thus His63, His71, and His80 $^{13}C^{\delta2}$, His71 and His80 $^{15}N^{\varepsilon2}$, and Asp83 $^{13}C^{\beta}$, can be assigned. The (H)C(H)H TEDOR spectrum provides additional confirmation of the assignment, displaying correlations between $^1H^{\delta2}$ and $^1H^{\varepsilon2}$ nuclei in the same residue.

The assignment made is then used to validate our computational approach. The model F was chosen as the best representative structure since all the observed resonances in the TEDOR spectra lie in the corresponding calculated intervals.

Tentatively assigned resonances. Once the computational approach is validated, the calculated data can be used to assign all the other observed resonances in the ^1H and ^{13}C 1D spectra to the corresponding nuclei.

Two very broadened resonances appear in the ^{1}H spin-echo spectrum at 82 and 68 ppm, both characterized by very large SAs. Based on calculations the peak observed at 82 ppm might be assigned to $^{1}H^{\varepsilon 1}$ of either His71 or His80, while the peak observed at 68 ppm might be assigned either to $^{1}H^{\varepsilon 1}$ of His71 or $^{1}H^{\varepsilon 2}$ of His63 that is, however, subject to chemical exchange. It is also possible that both resonances are overlapped in the ^{1}H spin-echo spectrum. This might be the reason why the fitted experimental SA of 795 ppm is considerably smaller compared to the calculations for His71 $^{1}H^{\varepsilon 1}$, while the calculations suggest a much smaller SA just below 300 ppm for His63 $^{1}H^{\varepsilon 2}$. If the two signals overlapped, the SA fitting would be giving an approximate averaged value. The experimental uncertainty of this SA value is thus larger than for other resonances. We note that, in principle, $^{1}H^{\varepsilon 1}$-$^{13}C^{\varepsilon 1}$ correlations should be observable in the (H)CH TEDOR spectrum. However, strong PREs, due the metal proximity, prevent the observation of these correlations. His63 $^{1}H^{\varepsilon 1}$ is not observed even in the ^{1}H spin-echo spectrum but it is expected to be very broadened and based on calculations this signal is probably overlapped with stronger ^{1}H signals around 50 ppm.

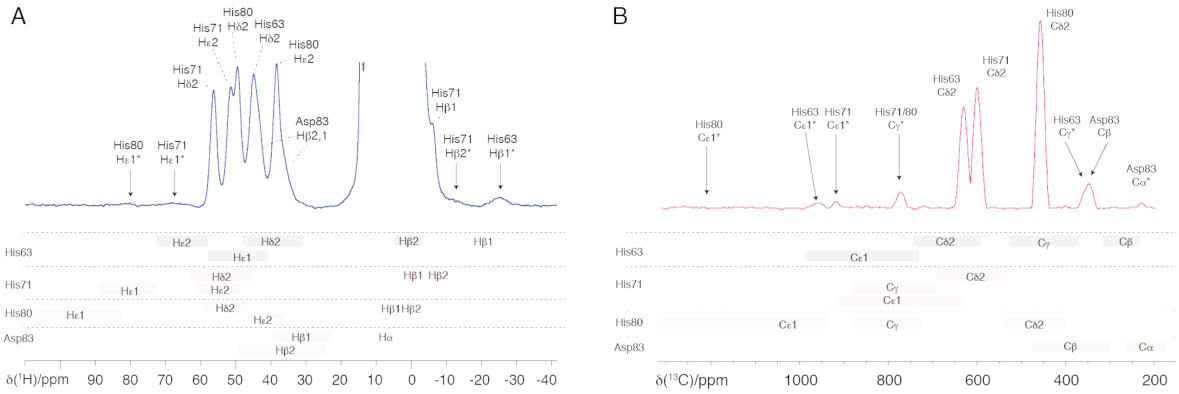

Figure 43. A) ^{1}H spin-echo spectrum, acquired at 100 kHz MAS, with assignment of observable peaks and comparison with the calculated ^{1}H shift ranges for model F. B) ^{13}C aMAT spectrum, acquired at 100 kHz MAS, with assignment of observable peaks and comparison with the calculated ^{13}C shift ranges for model F.

Broad resonances appearing at -26, -13, and -8 ppm in the ^{1}H spin-echo spectrum can be tentatively assigned to His63 $^{1}H^{\beta 1}$, His71 $^{1}H^{\beta 2}$, and His71 $^{1}H^{\beta 1}$ nuclei, respectively (Figure 43A). Note that the SAs calculated for $^{1}H^{\beta 2}$ and $^{1}H^{\beta 1}$ of a given residue strongly differ, and thus they can be used to stereospecifically distinguish between the $^{1}H^{\beta}$ nuclei. Moreover, His71 $^{1}H^{\beta 2}$ at -13 ppm correlates in the TEDOR spectrum with a ^{13}C nucleus resonating at 119 ppm (not shown), which is then assigned to His71 $^{13}C^{\beta}$. No TEDOR correlations are observed for the other two negatively shifted ^{1}H resonances, probably again because of strong relaxation effects. The calculations indicate that His80 $^{1}H^{\beta 1}$, $^{1}H^{\beta 2}$, His63 $^{1}H^{\beta 2}$, and Asp83 $^{1}H^{\alpha}$ are probably buried in the diamagnetic bulk.

In the ^{13}C spin-echo and aMAT spectra unassigned resonances show up at 1210, 960, 915, 775, 358, and 220 ppm. Based on calculations (see also Figure 43A), the resonance at 1210 ppm can be assigned to His80 $^{1}C^{\varepsilon 1}$, while the resonances at 960 and 915 ppm likely belong to His63 and His71 $^{1}H^{\varepsilon 1}$, respectively, although the reversed assignment cannot be completely excluded given the proximity of the two peaks and the computational uncertainty. The calculated ranges for $^{13}C^{\gamma}$ of His71 and His80 almost coincide, and also the calculated SAs are very similar. The broad signal at 775 ppm can be then assigned to either of the two or both of them. When not considering the SA, the resonance at 775 ppm could also be assigned to His71 $^{13}C^{\varepsilon 1}$ (also Figure 43B), however such an assignment is disfavored by a worse agreement with the measured SA. The peak at 358 ppm is most likely assignable to His63 $^{13}C^{\gamma}$, although in the absence of the experimental SA value the assignment to His63 $^{13}C^{\beta}$ cannot be completely excluded. Finally, the signal observed in ^{13}C aMAT at 220 ppm coincides with the calculated chemical shift ranges of His63 $^{13}C^{\beta}$ and Asp83 $^{13}C^{\alpha}$ but only Asp83 $^{13}C^{\alpha}$ gives acceptable agreement with between the experimental and calculated CSA values. Unassigned remain His80 $^{13}C^{\beta}$, and Asp83 $^{13}C^{\gamma}$, all of which are according to the calculations likely to be buried in the diamagnetic bulk, and His63 $^{13}C^{\beta}$.

In summary, the metal center of SOD contains eighteen ^{1}H, fifteen ^{13}C, and six ^{15}N atoms in the contact-shift regime. It was possible to observe and at least tentatively assign twelve ^{1}H, twelve ^{13}C, and two ^{15}N resonances and based on calculations predicted the likely positions of all remaining signals.

		Experiment (solution NMR)[13]	**Experiment** (MAS NMR)		**Calculation**			
					PBE0 [a]		PBE50 [a]	
Residue	Atom type	^{1}H	^{1}H	^{13}C/^{15}N	^{1}H	^{13}C/^{15}N	^{1}H	^{13}C/^{15}N
His63	β1	-	*-26*	-	-17	308	-17	236
	β2	-	-		2		-3	
	γ			*358*		525		373
	δ1			-		16210		13759
	δ2	46	45	631	48	741	32	586
	ε1	-	-	*960*	58	979	42	741
	ε2	-	*68*	-	72	1265	58	934
His71	β1	-	*-8*	*119*	0	184	-1	141
	β2	-	*-13*		-8		-6	
	γ			*775*		879		692
	δ1			-		15363		12830
	δ2	56	56	600	63	695	45	527
	ε1	-	*82 (68)*	*915*	89	898	73	613
	ε2	49	51	1034	63	1276	49	969
His80	β1	-	-	-	5	126	5	104
	β2	-	-		0		2	
	γ			*775*		872		714
	δ1			-		11778		9742
	δ2	49	50	458	59	545	47	399
	ε1	-	*82*	*1210*	107	1327	83	938
	ε2	39	38	1095	48	1357	37	1041
Asp83	α	-	-	*220*	8	262	8	174
	β1	36 (43)	36	350	39	477	24	299
	β2	43 (36)	43		49		26	
	γ			-		-44		23

Table 6. Assignment of the paramagnetically shifted experimental ^{1}H, ^{13}C, and ^{15}N resonances (in ppm) and comparison with the calculated data for the model F for Co^{II}-SOD. Numbers in italics indicate tentative assignment. [a] Method for hyperfine coupling. (-) Atom unassigned.

		Experiment		Calculation			
				PBE0 [a]		PBE50 [a]	
Residue	Atom type	^{1}H	^{13}C/^{15}N	^{1}H	^{13}C/^{15}N	^{1}H	^{13}C/^{15}N
His63	β1	*618* [b]	-	743	874	729	860
	β2	-		1307		1288	
	γ		-		1387		1331
	δ1		-		6359		5481
	δ2	188	381	272	502	262	487
	ε1	-	-	1087	1186	1070	1183
	ε2	-	-	307	471	295	458
His71	β1	*232*	-	359	725	350	713
	β2	*780* [b]		925		911	
	γ		*1019*		1286		1216
	δ1		-		6355		5403
	δ2	184	381	256	568	247	534
	ε1	*795* [b]	-	1252	1560	1233	1537
	ε2	223	-	306	624	295	584
His80	β1	-	-	502	842	491	828
	β2	-		1435		1414	
	γ		*1019*		1368		1287
	δ1		-		6611		5719
	δ2	199	405	258	567	248	543
	ε1	*994* [b]	-	1176	1484	1155	1439
	ε2	257	-	310	748	297	704
Asp83	α	-	*309*	498	414	470	384
	β1	201	-	416	745	398	632
	β2	211		370		351	
	γ		-		1742		1712

Table 7. Experimental shift anisotropies (SAs, in Haeberlen convention[22]) for the paramagnetically shifted ^{1}H, ^{13}C, and ^{15}N nuclei (in ppm) and comparison with the calculated data for the model F for Co^{II}-SOD. Numbers in italics indicate tentative assignment. [a] Method for hyperfine coupling. [b] Estimated from ^{1}H spin echo. (-) Atom unassigned or SA not measurable.

V.4 Moving further: Cu^{II},Co^{II}-SOD

V.4.1 MAS NMR of Cu^{II},Co^{II}-SOD

Following an approach similar to that adopted in solution NMR, once the Zn site is characterized following its substitution with Co^{II}, it is possible to provide a full description of the active site when also Cu^{II} is present. As already mentioned, when Zn^{II} is substituted with Co^{II}, the magnetic coupling between the Co^{II} and the Cu^{II} ion trough the bridging histidine allows the reduction of the electron relaxation time of Cu^{II} ion, $\tau_{e,Cu}$. While for the native form $\tau_{e,Cu}$has been estimated to be ~$1.8 \cdot 10^{-9}$ s,[13] when Zn^{II} is substituted with Co^{II} $\tau_{e,Cu}$ shortens to ~$1.7 \cdot 10^{-11}$ s,[23-24] allowing high-resolution NMR characterization of the Cu site.

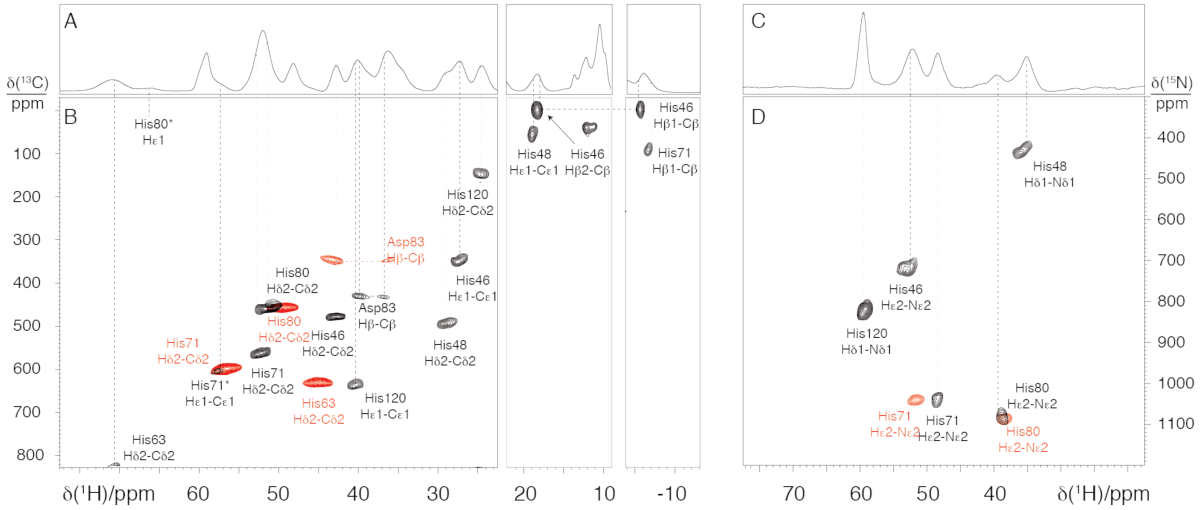

Figure 44. A) Portions of the ^{1}H spin-echo spectrum, and B) of the (H)CH TEDOR, of microcrystalline [U-^{13}C,^{15}N] Cu^{II},Co^{II}-SOD acquired at 100 kHz MAS in a 500 MHz (11.7 T) spectrometer. *Tentative assignment, based on comparison with the calculation obtained for Co^{II}-SOD. C) ^{1}H spin-echo spectrum, and D) (H)NH TEDOR of microcrystalline [U-$^{1}H^{N}$,^{2}H,^{13}C,^{15}N] Cu^{II},Co^{II}-SOD acquired at 100 kHz MAS in a 500 MHz (11.7 T) spectrometer. In red the (H)CH and (H)NH TEDOR spectra of Co^{II}-SOD are shown for comparison.

Figure 44.A shows the ^{1}H spin-echo spectrum acquired on a microcrystalline fully protonated Cu^{II},Co^{II}-SOD sample at 100 kHz on a 500 MHz spectrometer. Well-resolved contact-shifted resonances between -30 – 83 ppm are observable. The spectrum shows the same pattern of PNMR shifts as observed in solution, and can be easily assigned by comparison to the solution NMR data.[13-14] The assignment procedure is assisted by the comparison with the ^{1}H spin-echo spectrum of the perdeuterated fully back-exchanged sample, in which only the exchangeable contact-shifted protons, i.e. $^{1}H^{\varepsilon 2}$ and $^{1}H^{\delta 1}$ spins, are observed (Figure 44.C). Also in this case, very broadened resonances that were undetectable in solution are observable. In particular, the two very broadened peaks observed at 66 and 58

ppm can be tentatively assigned to $^{1}H^{\varepsilon 1}$ of His80 and His71, respectively, in analogy to Co^{II}-SOD.

Same as for Co^{II}-SOD, the assignment can then be extended to ^{13}C and ^{15}N nuclei with the aid of (H)CH and (H)NH TEDOR spectra (Figure 44.B-D). It was possible to identify all the ^{15}N atoms of the histidine rings that do not directly bind to the metals, contrary to what was previously observed in solution, where only the $^{15}N^{\delta 1}$ nuclei of His120 and His48 could be identified.[25] Extended assignment of the ^{13}C spins was also possible: all the $^{13}C^{\delta 2}$ nuclei could be identified, as well as the $^{13}C^{\beta}$ of His46, His71, and Asp83, and $^{13}C^{\varepsilon 1}$ of His46, His48, His71, and His120.

V.4.2 A comparative analysis of Co^{II}-SOD and Cu^{II},Co^{II}-SOD

It is interesting at this point to compare the observed resonances for Co^{II}-SOD and Cu^{II},Co^{II}-SOD. As previously mentioned, the Cu^{II} and Co^{II} ion are weakly antiferromagnetically coupled at room temperature ($J \cong 16.5$ cm^{-1}).[12] Under these circumstances the shifts of the nuclei are to a good approximation expected to be given by the sum of the shifts that would be observed in the presence of only one paramagnetic ion, as discussed in Chapter I.[11] In particular, for His71, His80 and Asp83, which are closer the Co^{II} ion, we would expect to observe the same pattern of shifts observed for Co^{II}-SOD, while for His46, His48 and His120 the same pattern that we would observe in Cu^{II},Zn^{II}-SOD. For His63, which experiences extensive electron delocalization from both metal ions, we would expect significant deviations of the observed shifts compared to the Co^{II}-SOD case.

Indeed, the general pattern observed in Co^{II}-SOD is preserved in Cu^{II},Co^{II}-SOD, except for His63, whose $^{1}H^{\delta 2}$ and $^{13}C^{\delta 2}$ shifts are significantly changed in Cu^{II},Co^{II}-SOD. Interestingly, while for His80 the correlations observed in (H)CH and (H)NH TEDOR spectra are almost identical between the two samples, more significant deviations are observed for His71 and Asp83. With the available information, it is difficult to determine whether the changes are due to a modification of the spin density pattern or to a structural difference of the Co^{II} coordination sphere, or to both effects. However, it is quite tempting to interpret the differences in the light of the calculated variation of the chemical shifts as a function of the different structural parameters in Figure 42. In particular, the increased value of Asp83 $^{13}C^{\beta}$ shift in Cu^{II},Co^{II}-SOD could arise from an increase in r_2 and a decrease in r_1 values, indicating a slight variation of the coordination mode of Asp83. Analogously, the variation of His71 $^{1}H^{\varepsilon 2}$ shift could be explained with a variation of the $\theta_{63\text{-}71}$ angle.

Unfortunately the current PNMR theory lacks a formalism for the calculation of PNMR shifts from first-principle including ZFS effects.[26] Inclusion of ZFS in the PNMR formalism for coupled systems is currently under development in our group, and once developed, a rigorous treatment, analogously to the one provided for Co^{II}-SOD, will be possible.

		Atom type						
Residue		β1	β2	γ	δ1	δ2	ε1	ε2
His 46	solution NMR $^{1}H/^{15}N$	18.7	-6.2			40.6	25.3	50.3
	MAS NMR ^{1}H	-6	19			43	27	53
	$^{13}C/^{15}N$	24				491	358	713
His 48	solution NMR $^{1}H/^{15}N$	-	12.5		34.5/460	28.4	19.6	
	MAS NMR ^{1}H	13			36	29	20	
	$^{13}C/^{15}N$	69			424	510	77	
His 63	solution NMR $^{1}H/^{15}N$					66.2		
	MAS NMR ^{1}H					70		
	$^{13}C/^{15}N$					826		
His 71	solution NMR $^{1}H/^{15}N$		-6.2			49.4		35.4**
	MAS NMR ^{1}H	-7				52	58*	49
	$^{13}C/^{15}N$	115				577	614*	1052
His 80	solution NMR $^{1}H/^{15}N$					48.8		46.7**
	MAS NMR ^{1}H					51	66*	37
	$^{13}C/^{15}N$					470		1091
Asp 83	solution NMR $^{1}H/^{15}N$	37.4	35.6					
	MAS NMR ^{1}H	37	40					
	$^{13}C/^{15}N$	440						
His 120	solution NMR $^{1}H/^{15}N$	18.7	-6.2		56.5/820	24.1	39.0	
	MAS NMR ^{1}H	12.7			60	25	40	
	$^{13}C/^{15}N$	72			821	157	648	

Table 8. Assignment of the paramagnetically shifted experimental ^{1}H, ^{13}C, and ^{15}N resonances (in ppm) for Cu^{II},Co^{II}-SOD.(-) Atom unassigned. *Tentative assignment. **In solution the assignment for His80 $^{1}H^{\varepsilon 2}$ and His71 $^{1}H^{\varepsilon 2}$ are reversed between Co^{II}-SOD and Cu^{II},Co^{II}-SOD. We propose to reassign them on the basis of the (H)NH TEDOR of Co^{II}-SOD. This assignment will be confirmed once more experimental data and dedicated calculations will be available.

V.5 Conclusions

In this chapter, we show that with the experimental toolkit used it is possible to remove the blind sphere around a paramagnetic ion in a metalloprotein, and detect and assign resonances that are invisible in solution. Moreover, a generally applicable method was introduced to determine at sub-atomic resolution the structure of the coordination sphere of a paramagnetic metal via measurement and calculation of paramagnetic NMR shifts in the Fermi-contact regime. Detection and assignment of contact-shifted resonances required the application of state-of-the-art methodology including 100 kHz MAS, tailored radiofrequency irradiation schemes, and advanced quantum chemistry modeling. The method was applied to the Co^{II}-SOD metalloprotein, where it resulted in key structural constrains on the Co^{II} coordination sphere. We expect that this method will be generally applicable to metalloenzymes coordinating paramagnetic metals.

In the next chapter the preliminary NMR characterization of a metal ion transporter will be illustrated. This system is involved in the regulation of intracellular Mg^{2+} concentration, but it has been shown that it can bind Co^{2+} as well, with biological relevance. The data shown in the next chapter will concern mostly the enzyme bound with Mg^{2+}. However, we wish to characterize in the future the same enzyme complexed with Co^{2+}. In this regard, the "toolkit" described in this chapter should provide precious structural information.

V.6 References

(1) Bowman, S. E. J.; Bridwell-Rabb, J.; Drennan, C. L., Metalloprotein crystallography: more than a structure. *Acc. Chem. Res.* **2016,** *49*, 695-702.

(2) Volbeda, A., X-ray crystallographic studies of metalloproteins. *Methods in molecular biology (Clifton, N.J.)* **2014,** *1122*, 189-206.

(3) Arcovito, A.; Benfatto, M.; Cianci, M.; Hasnain, S. S.; Nienhaus, K.; Nienhaus, G. U.; Savino, C.; Strange, R. W.; Vallone, B.; Della Longa, S., X-ray structure analysis of a metalloprotein with enhanced active-site resolution using in situ x-ray absorption near edge structure spectroscopy. *Proc. Natl. Acad. Sci. U.S.A.* **2007,** *104*, 6211-6216.

(4) Vaara, J.; Rouf, S. A.; Mareš, J., Magnetic couplings in the chemical shift of paramagnetic NMR. *J. Chem. Theory Comput.* **2015,** *11*, 4840-4849.

(5) *Handbook on metalloproteins*. Bertini, I.; Sigel, A.; Sigel, H. Eds.; Marcel Dekker, Inc.: New York, 2001.

(6) *Handbook of metalloproteins*. Messerschmidt, A. Eds.; Wiley Interscience: New York, 2001.

(7) Parge, H. E.; Hallewell, R. A.; Tainer, J. A., Atomic structures of wild-type and thermostable mutant recombinant human Cu,Zn superoxide dismutase. *Proc. Natl. Acad. Sci. U.S.A.* **1992,** *89*, 6109-6113.

(8) Fee, J. A., Studies on the reconstitution of bovine erythrocyte superoxide dismutase I. The presence of four divalent metal-binding sites on the apo protein which are different from the native sites. *Biochim. Biophys. Acta* **1973,** *295*, 87-95.

(9) McCord, J. M.; Fridovich, I., Superoxide dismutase. An enzymic function for erythrocuprein (hemocuprein). *J. Biol. Chem.* **1969,** *244*, 6049-6055.

(10) Banci, L.; Bertini, I.; Luchinat, C.; Viezzoli, M. S., A comment on the proton NMR spectra of cobalt(II)-substituted superoxide dismutases with histidines deuteriated in the ε1-position. *Inorg. Chem.* **1990,** *29*, 1438-1440.

(11) Bertini, I.; Luchinat, C.; Parigi, G.; Ravera, E., *NMR of paramagnetic molecules. Applications to metallobiomolecules and models*. Elsevier: Boston, 2017.

(12) Morgenstern-Badarau, I.; Cocco, D.; Desideri, A.; Rotilio, G.; Jordanov, J.; Dupre, N., Magnetic susceptibility studies of the native cupro-zinc superoxide dismutase and its cobalt-substituted derivatives. Antiferromagnetic coupling in the imidazolate-bridged copper(II)-cobalt(II) pair. *J. Am. Chem. Soc.* **1986,** *108*, 300-302.

(13) Bertini, I.; Luchinat, C.; Piccioli, M., Copper-zinc superoxide dismutase: a paramagnetic protein that provides a unique frame for the NMR investigation. *Prog. Nucl. Magn. Reson. Spectrosc.* **1994,** *26*, 91-139.

(14) Bertini, I.; Lanini, G.; Luchinat, C.; Messori, L.; Monnanni, R.; Scozzafava, A., Investigation of Cu_2Co_2SOD and its anion derivatives. Proton NMR and electronic spectra. *J. Am. Chem. Soc.* **1985,** *107*, 4391-4396.

(15) Fee, J. A., Studies on the reconstitution of bovine erythrocyte superoxide dismutase. IV. Preparation and some properties of the enzyme in which Co(II) is substituted for Zn(II). *J. Biol. Chem.* **1973,** *248*, 4229-34.

(16) Clement, R. J.; Pell, A. J.; Middlemiss, D. S.; Strobridge, F. C.; Miller, J. K.; Whittingham, M. S.; Emsley, L.; Grey, C. P.; Pintacuda, G., Spin-transfer pathways in paramagnetic lithium transition-metal phosphates from combined broadband isotropic solid-state MAS NMR spectroscopy and DFT calculations. *J. Am. Chem. Soc.* **2012,** *134*, 17178-17185.

(17) Hing, A. W.; Vega, S.; Schaefer, J., Transferred-echo double-resonance NMR. *J. Magn. Reson.* **1992,** *96*, 205-209.

(18) Saalwachter, K.; Graf, R.; Demco, D. E.; Spiess, H. W., Heteronuclear double-quantum MAS NMR spectroscopy in dipolar solids. *J. Magn. Reson.* **1999,** *139*, 287-301.
(19) Bennett, A. E.; Griffin, R. G.; Ok, J. H.; Vega, S., Chemical shift correlation spectroscopy in rotating solids: Radio frequency ‐ driven dipolar recoupling and longitudinal exchange. *J. Chem. Phys.* **1992,** *96*, 8624-8627.
(20) Munzarová, M.; Kaupp, M., A critical validation of density functional and coupled-cluster approaches for the calculation of EPR hyperfine coupling constants in transition metal complexes. *J. Phys. Chem. A* **1999,** *103*, 9966-9983.
(21) Benda, L.; Mareš, J.; Ravera, E.; Parigi, G.; Luchinat, C.; Kaupp, M.; Vaara, J., Pseudo-contact NMR shifts over the paramagnetic metalloprotein CoMMP-12 from first principles. *Angew. Chem. Int. Ed.* **2016,** *55*, 14713-14717.
(22) Harris, R. K.; Becker, E. D.; Cabral De Menezes, S. M.; Granger, P.; Hoffman, R. E.; Zilm, K. W., Further conventions for NMR shielding and chemical shifts IUPAC recommendations 2008. *Solid State Nucl. Magn. Reson.* **2008,** *33*, 41-56.
(23) Banci, L.; Bertini, I.; Luchinat, C.; Scozzafava, A., Nuclear relaxation in the magnetic coupled system Cu_2Co_2SOD. Histidine-44 is detached upon anion binding. *J. Am. Chem. Soc.* **1987,** *109*, 2328-2334.
(24) Banci, L.; Bertini, I.; Luchinat, C.; Piccioli, M.; Scozzafava, A.; Turano, P., Proton NOE studies on dicopper(II) dicobalt(II) superoxide dismutase. *Inorg. Chem.* **1989,** *28*, 4650-4656.
(25) Bertini, I.; Luchinat, C.; Macinai, R.; Piccioli, M.; Scozzafava, A.; Viezzoli, M. S., Paramagnetic metal centers in proteins investigated through heterocorrelated NMR spectroscopy. *J. Magn. Reson. B* **1994,** *104*, 95-98.
(26) Banci, L.; Bertini, I.; Luchinat, C., The ^{1}H NMR parameters of magnetically coupled dimers—The Fe_2S_2 proteins as an example. *Struct. Bond.* **1990,** *72*, 113-136.

Chapter VI.

MAS NMR characterization of a membrane metal ion channel

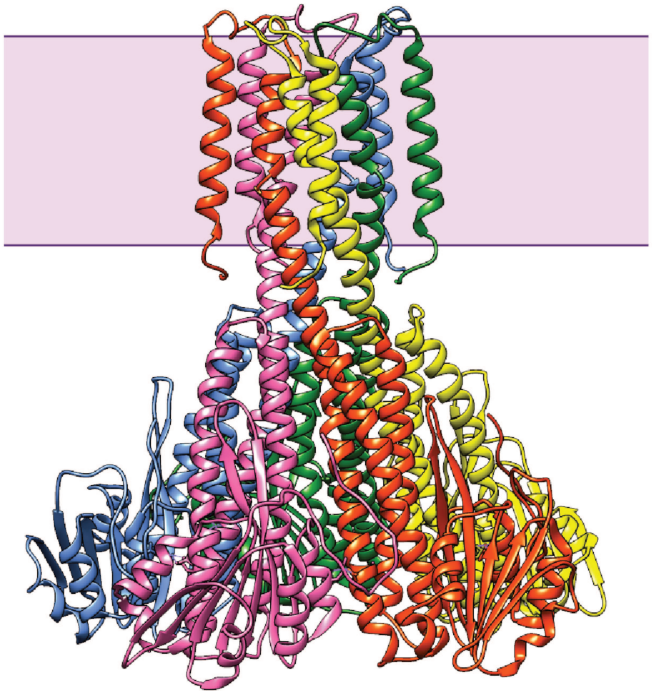

VI.1 Introduction

In the previous chapters we showed that solid-state NMR can be successfully used for the characterization of proteins containing paramagnetic centers. From one side, with the experimental toolkit presented in Chapter II, extensive backbone and side chains assignment can be obtained for nuclei experiencing long-range paramagnetic effects. On the other, the tools described in Chapter III can be employed, as shown in Chapter IV and V, to detect and assign nuclei in close proximity of a paramagnetic ion or a paramagnetic ions cluster, and their shifts can be converted, under the guidance of state-of-the-art computational tools, into structural parameters.

The results described in Chapter II, IV and V are obtained on benchmark microcrystalline paramagnetic proteins, for which extensive characterization was already available. This allowed establishing and validating our methodological approach, which can be now used to investigate more complex systems, for those important biological questions still remain unsolved. Membrane proteins represent with this regard an attractive target for solid-state NMR.

One important class of membrane-related proteins is represented by channels and transporters, which are essential in regulating the flux of ions, nutrients, toxins and other molecules across the cell membrane. In particular, regulation of metal ions concentrations is of crucial importance for the proper functioning of the cell, and living organisms evolved a large variety of transporters and channels, which play different roles in the regulation of the metal ions homeostasis.

In this chapter, we target CorA, a divalent metal ion channel that has received an increasing attention from the scientific community over the last years, as the major Mg^{2+} uptake system in prokaryotes. As discussed later, this protein undergoes a conformational change from a closed state, which does not allow Mg^{2+} to flow across the membrane, to an open state, which allows Mg^{2+} to enter the cell. Different X-ray and one cryo-EM structures of the closed state, as well as two low-resolution cryo-EM structures of the open state have been presented/published. However, the mechanism which triggers the conformational change, the basis of the gating process, as well as the dynamics of the entire conformational rearrangement, remain unclear, and no consensus has been found yet on the events that accompany the Mg^{2+} uptake process. Interestingly here, it has been found that the protein can also bind and transport Co^{2+} and other divalent cations. This represents an attractive aspect for the introduction of a paramagnetic probe in the protein, which will allow the use of

paramagnetic effects for the structural studies, in particular with the methodology developed in the previous chapters.

This is an ongoing project in our laboratory, and only preliminary results are available at the time of writing. Considering the excellent quality of the NMR data obtained up to now, we expect that in the near future it will be possible to apply the methodologies described in the previous chapters and to provide important structural information on this protein, and hopefully to give additional insights into the mechanism of the metal uptake.

VI.2 The CorA channel

Mg^{2+} is the most abundant intracellular divalent cation and is involved in a wide variety of biochemical processes.[1] Nature has evolved a large number of structural scaffolds to selectively transport Mg^{2+}, but up to now only for few of these systems the complete structures have been determined.[2]

Among these, the CorA system represents one the most investigated class of bacterial Mg^{2+} transport proteins. CorA was named from the cobalt-resistant mutants in which it was first identified.[3-4] A relationship between protein concentration and Mg^{2+} concentration in prokaryotic cells was established, highlighting the importance of the protein in the regulation of Mg^{2+} homeostasis, which was further confirmed by the evidence that this protein is required for the virulence of different pathogens.[5-6]

The protein is found in half of the sequenced prokaryotic genomes, for which it is presumed to function as the primary cellular Mg^{2+} transport system.[2] It has been found that the protein can transport also other divalent cations, in particular Co^{2+}.[7] For most of prokaryotes this has been considered of non-physiological relevance, because of the low affinity of Co^{2+} for CorA. However, it has been observed that in the hyperthermophilic organism *Thermotoga maritima (Tm),* CorA selects Co^{2+} over Mg^{2+} at 100 times lower concentrations and that *Tm*CorA displays higher thermostability in the presence of Co^{2+}, rather than of Mg^{2+}.[8-9] Considered that in the natural environment of *T. maritima* Co^{2+} concentration is relatively high, while those of Mg^{2+} relatively low,[10] it has been proposed that *Tm*CorA works actually as a Co^{2+} channel *in vivo*, but there is still no consensus on this aspect among the scientific community.[2]

Three groups almost simultaneously reported the first crystal structures of *Tm*CorA in the presence of divalent cations, at 2.9, 3.9 and 3.7 Å resolution, respectively, in 2006.[11-13] Other

X-ray structures were determined in the following years[9, 14] and, recently, a cryo-EM structure at 3.8 Å resolution was obtained.[15] All these structures were solved in the presence of Mg^{2+} and are very similar, with the major differences located at the flexible parts of the protein.

*Tm*CorA is, in the presence of divalent cations, a 5x42 kDa symmetric pentamer with the shape of a cone (Figure 45A-B), whose tip is formed by two transmembrane (TM) helices from each monomer, located at the C-terminal part of the protein. The basis of the cone is represented by the N-terminal cytosolic region of the protein (Figure 45C). Each monomer consists of 354 residues and is formed by an N-terminal α/β domain with a central seven-stranded mixed β sheet lined by three small helixes (helixes α1, α2, α3). Two longer helixes (α5, α6) cover one face of this domain and are bundled with a very long (70 residues) helix (α7), whose C-terminal part constitutes the first TM domain. A second helix (α8) follows, which forms the second TM domain, and packs in a ring-shape around the helix α7. Helixes α7 and α8 are connected by a short extracellular loop. Two highly conserved motifs are found in the TM regions: a YGMNF motif (residues 311-315), located at the end of the TM1 region, and a KKKKWL motif, at the end of the TM2 region. The TM domains in the X-ray structures form a narrow pore that displays a hydrophobic stretch (residues 291 and 294) making it too narrow to permit the passage of even a single water molecule, suggesting that these structures represent closed, non-conductive forms of the channel.[2, 12]

Two regulatory metal-binding sites were identified in almost all of the available structures, which are usually indicated as the M1 and M2 sites (Figure 45F). In the M1 site, the metal is closely coordinated by the side chains of Asp89 and Glu88 from one monomer, and Asp253 from a second monomer, thus bridging two different subunits. Water molecules are supposed to complete the coordination sphere of the ion, probably in an octahedral geometry.[9] The M2 site is found in the proximity of the M1 site, in a cavity surrounded by the main chain of Leu12, and side chains of Asp175 and Asp253, also in this case bridging two different subunits. The distance to the potential protein ligands is too large for a direct binding, and the ion is probably in a fully hydrated form.[11]

Other potential metal binding sites are found in some of the structures. One is found at the entrance of the pore, which can accommodate a fully hydrated cation distantly bound to the side chain of Asn314 of the YGMNF motif (Figure 45D), which is believed to represent a selectivity filter.[2, 15] Others are found along the pore, in particular at the Asp277 position (Figure 45E), which is located at the intracellular extremity of the pore, and at the Ser284 position.[14]

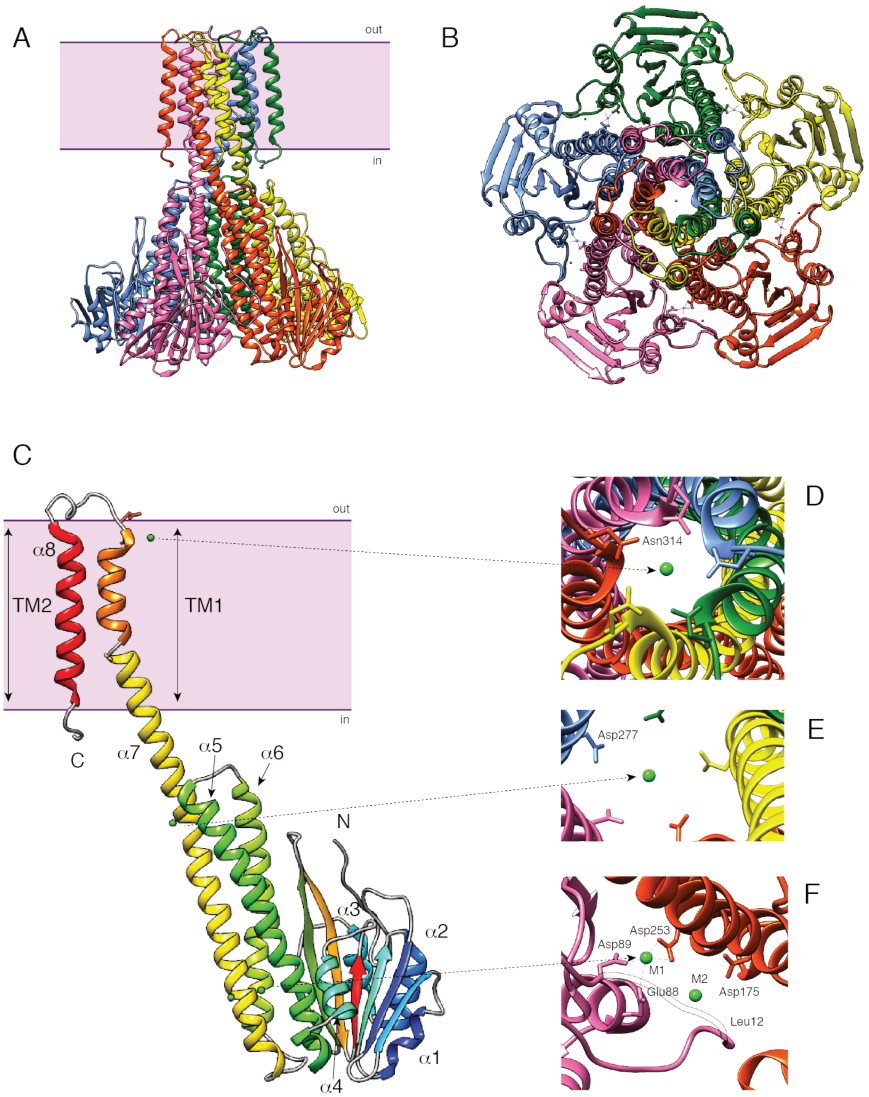

Figure 45. Section (A) and top view (B) of the *Tm*CorA pentamer in the closed form. Each monomer has a different color. C) Structure of the *Tm*CorA monomer, highlighting the different elements of the secondary structure, Mg^{2+} ions are in green. D) Putative metal binding site at the entrance of the pore. E) Putative metal binding site at the exit of the pore. F) M1 and M2 metal binding sites at the interface of two monomers. All the pictures refer to the cryo-EM structure[15] (PDB code: 3JCF).

Despite different efforts, no crystal structures of the protein in the absence of divalent cations could be solved, with the exception of an N-truncated coiled-coil mutant.[14] The first structures of the wild-type protein in the absence of divalent cations were obtained by cryo-EM, at a resolution of ~ 7.1 Å.[15] Two distinct conformations could be observed (Figure 46A-B), in which the 5-fold symmetry is lost: in both states the cytoplasmic domain of one subunit (subunit A) displays a considerable outward translation, while a second one (subunit B), is translated towards the inner part of the channel. Smaller reorientations affect the other three subunits, while the TM region retains an approximate 5-fold symmetry. This was in agreement with previous double electron-electron resonance (DEER) measurements.[15-16]

These structures suggest a peculiar mechanism for ligand-driven gating. It has been proposed that inter-subunit forces, mediated by the divalent cations in sites M1 and M2, stabilize the 5-fold symmetric close state, but that a reduction in intracellular divalent cations leads to their release from the interfacial sites, inducing large rearrangements of the cytoplasmic domain. In particular, the release of the divalent cation driven would destabilize one of the subunit (subunit A in Figure 46C), leading to a local increase in dynamics that sequentially destabilizes its complementary interface (subunit B in Figure 46C), allowing large excursions of the cytoplasmic domain of this subunit from the symmetry axis (Figure 46B-C). The subsequent release of other divalent cations from the related interfaces would trigger a cascade of similar events, leading to an increase in dynamics and flexibility of all the five subunits (Figure 46C), especially at the TM regions, and causing the opening of the hydrophobic gate. This proposed mechanism is in contrast with previously suggested ones assuming a concerted movement of the five subunits, leading to a symmetric open state.[9, 16]

Still undefined, however, is the mechanism by which the large rearrangements of the cytoplasmic domains are propagated to the TM domains, triggering the Mg^{2+} uptake.[15]

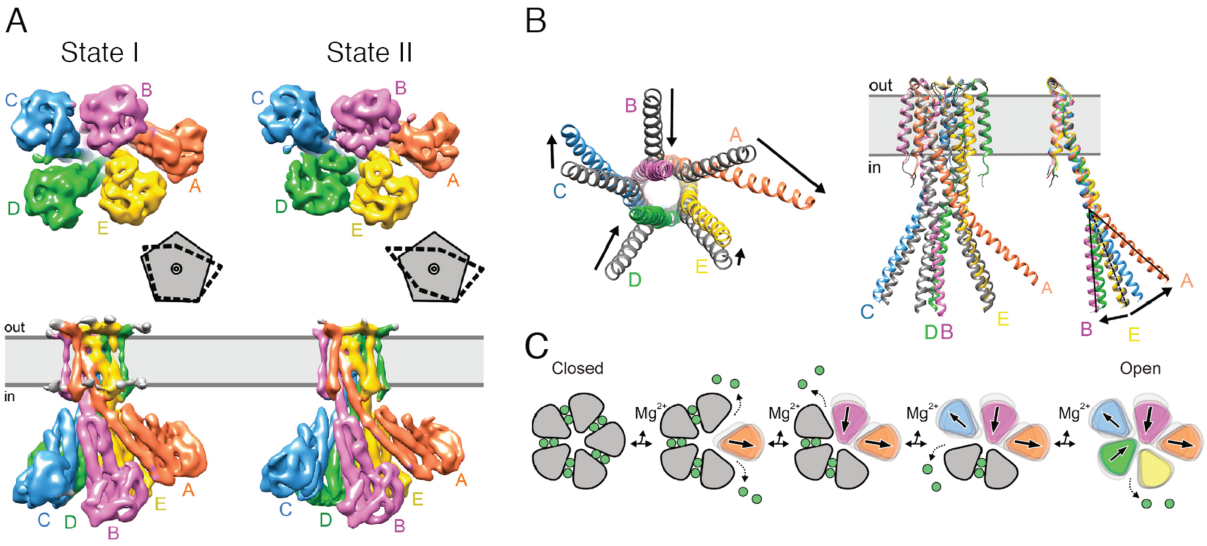

Figure 46. A) Bottom and side views of the two opens states of *Tm*CorA obtained by cryo-EM, showing a simplified representation of the subunits movements (dashed line) compared to the closed state (filled-line pentagon). B) Bottom and side-view of the closed state (gray) and open state II (colored), highlighting the relative movements of different subunits between the open and the closed state. C) Proposed mechanism for the asymmetric opening of the channel. When Mg^{2+} (or Co^{2+}) is bound, neighboring subunits are stabilized in the closed state (left). When the cation concentration drops, Mg^{2+} (or Co^{2+}) between subunits are progressively released, leading to an ensemble of open states. Reproduced from reference 15.

MAS NMR could provide precious information, which would complement the available information obtained from the crystallographic and cryo-EM structures. In particular, sequence specific chemical shift information could give insight into local secondary structure, eventually highlighting site-specific structural rearrangements. Moreover, NMR can be a

powerful tool for elucidating the global and local dynamics of a protein,[17-18] which will be very useful in the present case considered that important changes in the protein dynamics probably accompany the channel gating, as just discussed. In addition to this, the fact that the protein can bind and transport Co^{2+} makes it an attractive aspect for the acquisition of long-range paramagnetic effects, notably PCSs, and for the application of the methods described in the previous chapters, which could provide additional insights into the local structure of the metal binding sites, as well on the transport of metal ions through the channel.

VI.3 MAS NMR characterization of *Tm*CorA

The study of *Tm*CorA represented a completely new project for our group, therefore an extensive work for the preparation of an NMR suitable sample had to do performed. Firstly, we optimized the expression and purification protocols. After this, we targeted the protein in two different environments, either by reconstitution in lipid bilayers, which represent a good mimic of the cellular membrane environment,[19] or in a microcrystalline form, which usually provides higher-quality MAS NMR spectra but in a physiological distant environment.[20-21] In both cases, extensive work has been done in order to obtain the most suitable conditions for the NMR analysis. Finally, we could perform the first MAS NMR characterizations of the protein in different environments and metallation states.

VI.3.1 Optimization of the expression and purification protocols

An essential step in the characterization of a protein sample by MAS NMR is represented by the optimization of the expression and purification protocols, which is of critical importance in order to obtain high-quality NMR data.[22] We therefore performed an optimization of the published protocols used in the crystallization studies[11-12] to adapt them for the MAS NMR analysis. The detailed protocol for the expression and purification of *Tm*CorA is reported in the Appendix 3. Here only the key steps are briefly summarized.

The protein is expressed in *E. coli* as fusion to an N-terminal six-histidine tag, in M9 minimal medium, in order to obtain isotopically enriched samples. After cell lysis, the membrane fraction is harvested by ultracentrifugation and homogenized in a buffer containing 1% of n-dodecyl-β-D-maltopyranoside (DMM), which has the function to solubilize membrane proteins. The solubilized protein is then purified by nickel affinity chromatography and, after the removal of the histidine tag, by gel filtration.

VI.3.2 Optimization of sample reconstitution in lipid bilayers

For the preparations in lipid bilayers the desired lipids are added to the purified protein solution in a determined protein-to-lipid ratio, and the solution is then extensively dialized against a buffer containing either 40 mM $MgCl_2$ or 20 mM $CoCl_2$ (for the metal-containing form), or 1 mM EDTA (for the metal-free form).

Reconstitution of protein in a membrane mimic environment represents a critical step in the MAS NMR of membrane proteins. Different strategies are used to reproduce this environment, including preparation in micelles, bicelles, liposomes or lipid nanodiscs.[23-24] Lipid bilayers represent the most attractive environment for membrane-protein sample preparation.[19] Membrane protein structure and function are often sensitive to the local environment,[25] and therefore for the protein reconstitution, the lipid composition and protein-to-lipid ratio should be screened in order to find the best compromise between physiological relevance and quality of experimental data.[19, 26]

We performed a series of screenings for the optimization of the composition of the bilayers used for the NMR analysis. We analyzed different lipids (Figure 47), notably 1,2-dimyristoyl-sn-glycero-3-phosphocholine (DMPC), 1,2-dipalmitoyl-sn-glycero-3-phosphocholine (DPPC), and 1,2-diphytanoyl-sn-glycero-3-phosphocholine (DPhPC). We tested also two different protein-to-lipid mass ratios (1:1 and 2:1).

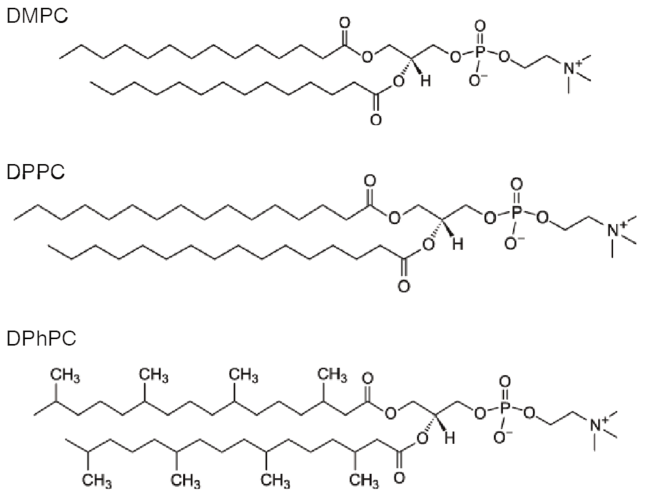

Figure 47. Lipids tested for *Tm*CorA reconstitution in bilayers in the present work.

The effect of different lipid content on the quality of the sample was monitored from the (H)NH spectra of the corresponding samples, acquired at different temperatures in order to identify the experimental conditions maximizing the quality of the NMR data.

All the acquired spectra displayed good signal dispersion, indicating that the protein is folded, and also some well-resolved signals can be identified. We observed that the sample

prepared with DMPC at 2:1 protein-to-lipid mass ratio at an approximate temperature of 300 K (Figure 48A) gave the best results compared to other preparations, such as the sample reconstituted in DPhPC at a protein-to-lipid ratio of 1:1 shown in Figure 48B.

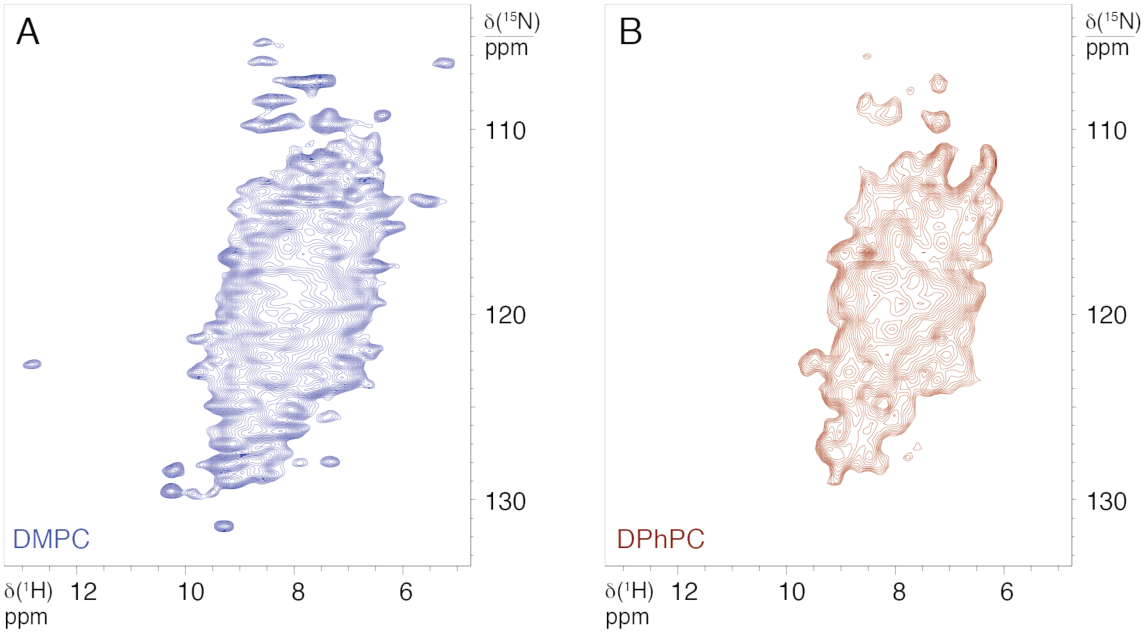

Figure 48. (H)NH spectra of [U-^{15}N]-labeled *Tm*CorA reconsitituted in A) DMPC lipid bilayers with a protein-to-lipid ratio of 2:1, and B) DPhPC lipid bilayers with a protein-to-lipid ratio of 1:1, in presence of $MgCl_2$ 40 mM, at ~300 K and 60 kHz MAS on a 700 MHz (16.4 T) spectrometer.

VI.3.3 MAS NMR of *Tm*CorA in the absence of Mg^{2+}

In parallel to the analysis of *Tm*CorA in the presence of Mg^{2+}, we also performed the first preliminary characterization of the protein in the presence of EDTA, where Mg^{2+} is expected to be depleted. The (H)NH spectrum of the Mg^{2+}-free form in DMPC bilayers, acquired at 60 kHz MAS on a 700 MHz (16.4 T) spectrometer (Figure 49, red), shows similar features compared to the one obtained in the presence of Mg^{2+} (Figure 49, blue), with the exception of minor shift changes observed for some of the few resolved resonances. This is quite surprising at a first sight: according to the cryo-EM structures, the Mg^{2+}-free form undergoes large conformational changes, which might affect the chemical shifts or even lead to peak splitting into several sets of resonances.

With the resolution available in these spectra, and lacking the information from a third ^{13}C dimension, it is hard to speculate on these data. However, it is still possible to make some considerations. Even if a considerable rearrangement of the quaternary structure of *Tm*CorA is observed in the cryo-EM structures of the open form, the secondary and tertiary structural elements are globally preserved, an this might induce only minor variations in the chemical shifts of most of the nuclei. This will translate into a slight inhomogeneous broadening of the

corresponding signals rather than the appearance of different set of resonances (indeed the spectrum of the Mg^{2+}-free form appears generally broadened). Moreover, considering the limited resolution, and the unavailability of the backbone assignment, even large shift variations occurring in the most crowded parts of the spectrum cannot be monitored here. Higher fields and MAS rates, combined with ^{13}C labeling, will be essential to investigate the system in the Mg^{2+}-free form with site-specific resolution in the future.

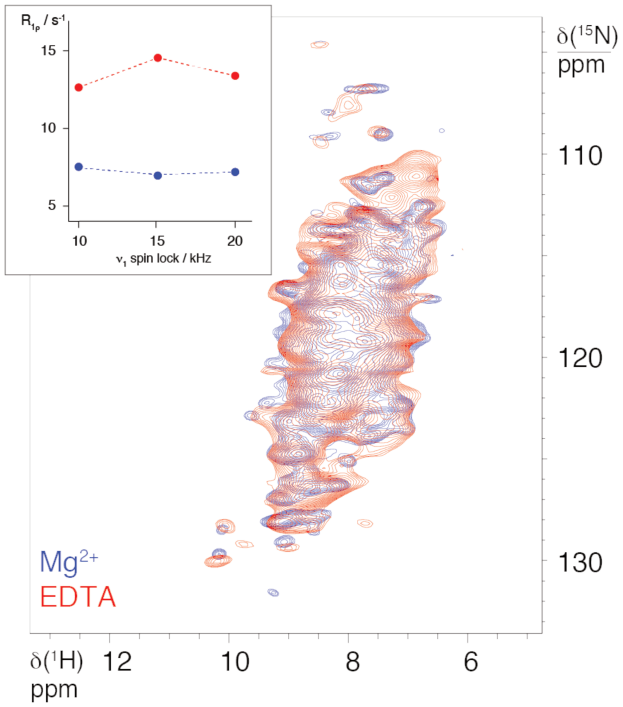

Figure 49. (H)NH spectra of [U-^{15}N]-labeled *Tm*CorA acquired at ~ 300 K, and 60 kHz MAS on a 700 MHz (16.4 T) spectrometer, in DMPC lipid bilayers in the presence (blue) and in the absence (red) of Mg^{2+}. The upper-left insert shows the bulk ^{15}N $R_{1\rho}$ relaxation dispersion profile.

Additional information can be provided from the analysis of *Tm*CorA dynamics. Indeed, it is expected that an increase in the mobility of the entire protein should be observed after Mg^{2+}-depletion.[15] NMR is a powerful tool to study protein dynamics, and in the past years solution NMR provided to be able to characterize different time scale motions in proteins, especially through relaxation measurements.[27-28] However, one of the major drawbacks of solution NMR is that internal dynamics slower than the overall tumbling cannot be detected by relaxation studies, which hinders the analysis of the microsecond-nanosecond range motions. This hampers the study of a variety of motions occurring in the protein, like large domain motions occurring usually in the microsecond-millisecond range,[29] which are often associated with the gating of ion channels.[30-31]

In this regard, MAS NMR represents a valuable technique to access this kind of motions, the molecular tumbling being abolished in a solid sample.[17] In particular, R_1 measurements

are sensitive to internal motions occurring in the nanosecond range, while $R_{1\rho}$ measurements can probe internal motions and conformational exchanges occurring in the microsecond-millisecond range.[32-35] ^{15}N $R_{1\rho}$ and R_1 measurements are so far the most used in MAS NMR, due to the well established modeling of the relaxation properties of this nucleus.[17]

We performed bulk ^{15}N $R_{1\rho}$ and R_1 measurements[32, 36] in order to investigate the dynamic properties of the two samples. In the MAS regime used in this preliminary analysis (60 kHz MAS), a significant contribution from coherent decay affects measured $R_{1\rho}$ values for spin-lock rf-fields below 10 kHz.[32] Therefore we explored the region comprised between 10 and 20 kHz (higher fields being potentially harmful for the sample and the instrumentation), where coherent contribution should be negligible. The obtained relaxation dispersion profiles for bulk ^{15}N $R_{1\rho}$ are shown in Figure 49. For the two samples, the profile is, within experimental error, flat. However, the two profiles have different plateau: $R_{1\rho}$ values of 7.1 and 13.4 s^{-1} (corresponding to $T_{1\rho}$ values of 140 and 75 ms) are observed, at 20 kHz spin-lock rf-field, for the Mg^{2+}-containing and the Mg^{2+}-free samples, respectively. This significant variation is a clear indication that the dynamics on the millisecond timescale between the two samples is different. This is in agreement with the presence of large domain motions that can be associated with the rearrangements of the subunits in *Tm*CorA pentamer during the gating process.

At the same time, the ^{15}N R_1 values measured in the two cases are almost identical (0.36 s^{-1} for the Mg^{2+}-containing form, and 0.38 s^{-1} for the Mg^{2+}-free form, corresponding to T_1 values of 28 and 26 s respectively), which indicate that internal dynamics in the nanosecond range is not significantly altered between the two forms.

In the future, more detailed information can be obtained by the analysis of site-specific relaxation measurements, potentially providing insights into the local change in dynamics associated with the gating of the channel.

VI.3.4 MAS NMR of microcrystalline *Tm*CorA

The long-range order observed in a microcrystalline sample usually produces higher-quality MAS NMR spectra, which display longer coherences lifetimes and higher resolution compared to samples in other aggregation states.[21, 37] At the same time, packing forces might induce some modification of non-physiological relevance in protein structures, and care has to been taken in the interpretation of the obtained data.[20]

We performed a screening of crystallization conditions (as reported in the Appendix), based on the ones used in the literature for the determination of the different crystal structures of *Tm*CorA.[11-13] We found that the best, needle-like shaped crystals are obtained in 2-3 weeks in sitting drops over a solution containting 100 mM $MgCl_2$, 10 % PEG 2000, and 100 mM Tris, at pH 8.0.

The (H)NH spectra of *Tm*CorA in microcrystalline form and reconstituted in lipid bilayers preparations are well comparable. Thanks also to the higher packing factor, an almost twofold increase in sensitivity is observed for the microcrystalline form. Only minor deviations in the peaks position or variation in relative intensity of some resonances, compared to the sample prepared in lipid bilayers, are observed (Figure 50). This indicates that the same fold is globally preserved between the two forms, which is consistent with the fact that the reported crystal structures are quite well comparable with the cryo-EM structure of *Tm*CorA obtained in lipid bilayer nanodiscs. However better resolved spectra, acquired at higher field and MAS rates, would be needed to address more specifically structural or dynamic differences between the two preparations.

Bulk T_2' measured for $^{1}H^{N}$ resonances at 60 kHz MAS on 700 MHz (16.4 T) spectrometer increase from 0.9 ms in DMPC lipid bilayers to 1.1 ms in microcrystalline preparation, while a more significant improvement is observed in the case of $^{15}N^{H}$, for which observed T_2' increase from 26 ms in lipid bilayers to 32 ms in microcrystals. Therefore only a limited improvement in the sensitivity of ^{1}H-detected spectra is expected for the microcrystalline form, even if still an improvement in resolution could be obtained if the inhomogeneous contribution to the linewidth were smaller in the microcrystalline form.

From ^{15}N $R_{1\rho}$ relaxation dispersion profiles it is clear that the dynamics in the millisecond-microsecond timescale is not significantly altered between *Tm*CorA in lipid bilayers and in microcrystalline form. However longer ^{15}N T_1 are measured in the microcrystalline sample (41 s compared to 28 s in lipid bilayers), which can be an indication of reduced side chains and loop dynamics, which usually occurs in the nanosecond timescale. This might translate into an increased local order and therefore better resolution, especially in side chains, which would be highly beneficial in the perspective of their assignment.

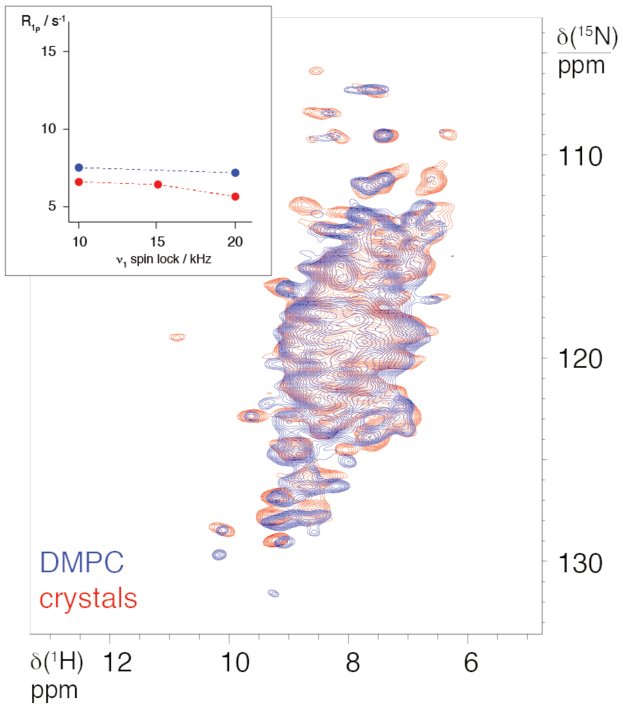

Figure 50. (H)NH spectra of [U-^{15}N]-labeled *Tm*CorA acquired at ~300 K, and 60 kHz MAS on a 700 MHz (16.4 T) spectrometer in the presence of Mg^{2+}, in DMPC lipid bilayers (blue) and in microcrystalline form (red). The upper-left insert shows the bulk ^{15}N $R_{1\rho}$ relaxation curve.

VI.3.5 Preliminary MAS NMR analysis of *Tm*CorA in the presence of Co^{2+}

All the results presented in the previous sections were obtained for samples in the absence of paramagnetic ions. However, as mentioned at the beginning of the chapter, *Tm*CorA can also transport other divalent cations, in particular Co^{2+}, probably with physiological relevance.[8-9] This represents an attractive aspect in order to exploit paramagnetic effects for structural investigations.

We performed a preliminary MAS NMR investigation of the protein in the presence of Co^{2+}. The protein was prepared in lipid bilayers exactly in the same way as the Mg^{2+}-containing form, just the reconstitution was performed in the presence of $CoCl_2$ and in the absence of Mg^{2+}. The (H)NH spectrum of Co^{2+}-containing [U-^{15}N] *Tm*CorA in lipid bilayers is shown in Figure 51. The spectrum is comparable to the one of the Mg^{2+}-containing protein, but it displays a considerable broadening and sensitivity loss, with the disappearance of some peaks. With the available resolution it is difficult to observe PCSs, which would be a distinctive feature of Co^{2+} binding. This would be eventually possible in a [U-^{15}N, ^{13}C]-labeled sample, exploiting the higher resolution of 3D experiments at higher field and MAS rates.

In the double-adiabatic spin-echo ^{1}H spectrum of Co^{2+}-containing [U-^{15}N] *Tm*CorA no contact-shifted signals can be identified. At this stage it is hard to provide a robust

explanation for this. As discussed in Section 2, different potential metal binding sites are found along the protein, however only in the M1 site the metal is directly coordinated to the protein, and therefore it might be expected that only ligands of the M1 site could experience appreciable contact shifts. According to the X-ray structures the metal cation in the M1 site should have an octahedral geometry.[16] In this geometry Co^{2+} is almost always in high-spin state (S=3/2), and has short electron relaxation times (τ_e~ 10^{-12} s),[38] which represents a very favorable situation for NMR, as discussed in Chapter II. Therefore contact-shifted signals should not be excessively broadened by PREs, and being detectable by NMR. This holds in the absence of chemical exchange. However it cannot be excluded that the metal ion is not tightly bound and that a certain degree of chemical exchange is present. This would not be completely surprising, considering that the gating of *Tm*CorA is probably regulated by the release of cations from the M1 and M2 sites. The presence of chemical exchange would affect the relaxation and the observed shifts of the nuclei of interest. However, with the available information it is not possible to draw any final conclusion, which will be possible in the future after further investigation and, eventually, a better optimization of the protocol for Co^{2+} inclusion in the protein.

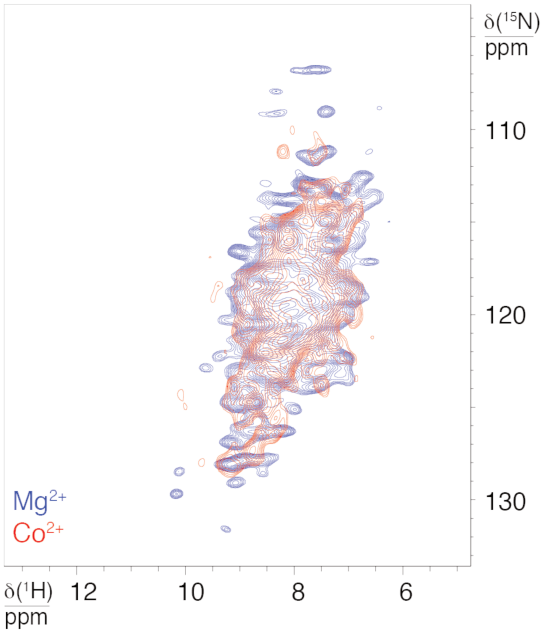

Figure 51. (H)NH spectra of *Tm*CorA reconstituted in DMPC lipid bilayers in the presence of Mg^{2+} (blue) and Co^{2+} (red). The double-adiabatic spin-echo spectrum of the Co^{2+}-containing form is shown in the upper-left panel. All spectra were acquired at ~ 300 K, and 60 kHz MAS, on a 700 MHz (16.4 T) spectrometer.

VI.3.6 Experiments for backbone assignment at ultrafast MAS

After these preliminary characterizations, we increased the magnetic field (B_0) and MAS frequency in order to improve the resolution of the NMR experiments, which are essential in the perspective of performing backbone and side chains assignment of a system of this size.

The (H)NH spectrum of Mg^{2+}-containing [U-^{13}C, ^{15}N]-labeled *Tm*CorA (Figure 52A) acquired at 107 kHz MAS on a 1 GHz (23.5 T) spectrometer displays a substantial improvement in resolution compared to the spectrum shown in Figure 48. Several well-resolved peaks are observable, and a good dispersion of the correlations is observed. Analogously, the (H)CH spectrum (Figure 52C) displays very good spectral quality, and several resolved peaks (especially in the C^{α}-H^{α} and methyl regions) are observable as well.

A considerable improvement of coherences lifetimes is observed in this MAS regime. Compared to experiments acquired at 60 kHz MAS at the same field, bulk transverse coherence lifetimes (T_2') increased from 1.1 to 3.0 ms for $^{1}H^{N}$ (comparing quite well to values observed in fully protonated microcrystalline samples, such as GB1[39]), and from 24 to 44 ms for $^{15}N^{H}$, while T_2' of 40 and 28 ms are observed, at 107 kHz MAS, for ^{13}CO and $^{13}C^{\alpha}$, respectively.

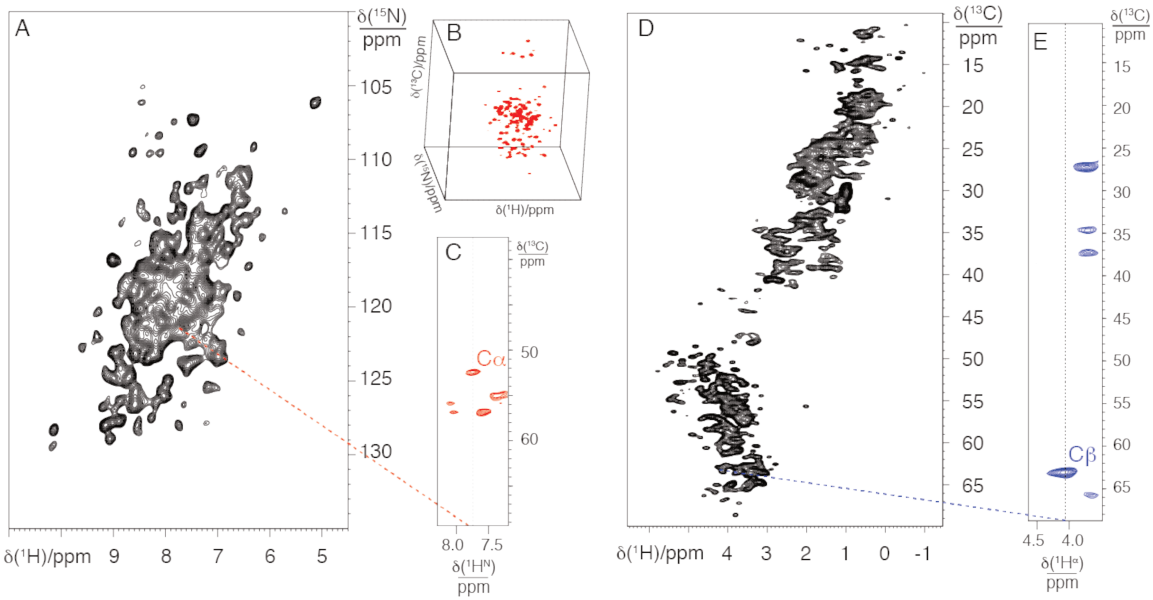

Figure 52. A) (H)NH, B) (H)CANH, and C) (H)CH spectra, and selected strip-plots from the (H)CANH (C), and (H)(CA)CBCAHA (E) spectra of [U-^{15}N, ^{13}C]-labeled *Tm*CorA in DMPC (2:1 protein-to-lipid ratio) bilayers and in presence of $MgCl_2$ 40 mM, acquired at ~300 K and 107 kHz MAS on a 1 GHz (23.5 T) spectrometer.

These favorable coherence lifetimes allow the acquisition of 3D experiments for backbone assignment. We acquired five $^{1}H^{N}$-detected experiments ((H)CANH, (H)CONH, (H)(CO)CA(CO)NH, (H)CO(CA)NH, (H)(CA)CB(CA)NH), and five $^{1}H^{\alpha}$-detected experiments ((H)NCAHA, (H)N(CO)CAH, (H)CO(N)CAHA, (H)COCAHA, (H)CBCAHA).

Acquisition of the (H)(CA)CB(CA)(CO)NH experiment was unfortunately hampered by low sensitivity. These experiments display a good resolution in the ^{13}C dimension, as shown for the (H)CANH spectrum (Figure 52B), and two selected strips of the (H)CANH (Figure 52C), and of the (H)(CA)CBCAHA spectrum (Figure 52D).

All together these experiments represent a large repertoire, whose high level of redundancy is fundamental for the reliable assignment of a system so complex. The assignment of the backbone resonances is currently under progress in our group. Several fragments were promptly identified and tentatively matched to the primary sequence. Still, the size of the protein represents a challenge for MAS NMR, CorA being one of the largest proteins ever approached so far by the technique. Despite the high quality of the data, extensive overlap occurs in some regions of the spectra. This could hinder the correct identification of different resonances and spin systems, especially in the case of less sensitive experiments, thus having a detrimental effect in the assignment procedure.

These problems can eventually be addressed in the future by acquisition of additional data. For example, higher-dimensionality experiments could in principle alleviate the effects of extensive overlap in some regions of the spectra, but they can also potentially suffer from low sensitivity and resolution deterioration due to truncation effects.

Another interesting approach in order to assist the assignment procedure might be represented by the use of alternative labeling schemes. For example, inverse fractional labeling (iFD)[31] constitutes an attractive option, based on the use of protonated solvents (100 % H_2O) and [U-^{2}H, ^{13}C]-labeled glucose for protein expression. In this way proteins that are fully protonated at the H^N and H^{α} nuclei are obtained, while extensive deuteration is observed in side chains. This labeling approach has been proven to improve considerably coherences lifetimes and $^{1}H^N$ and $^{1}H^{\alpha}$ linewidths compared to fully protonated samples at 60 kHz MAS, and allowed among others the backbone assignment of a potassium channel by MAS NMR.[31, 40] A meaningful decrease of linewidths even at 100 kHz was observed as well in relatively complex systems, notably a 2.5 MDa viral capsid.[40] The increase in resolution might be then highly beneficial to improve the quality of 3D spectra and facilitate the assignment procedure.

A reduction of spectral crowding in 3D experiments might also be obtained by washing the sample with D_2O. This would deuterate all the solvent-exposed exchangeable sites, reducing the crowding in (H)NH and $^{1}H^N$-detected 3D spectra, and select all the regions that are not exposed to the solvent, notably the TM regions, considerably simplifying their assignment.[31]

At the same time, this would leave all the non-exchangeable sites unaffected, in particular the H^{α} nuclei, keeping unaltered the accessibility of the whole protein by $^{1}H^{\alpha}$-detected methods.[41]

All the mentioned strategies are currently under investigation in our group, and will hopefully provide an extensive assignment of the protein in the future.

VI.4 Conclusions

In this chapter the preliminary investigation of a metal ion channel was provided. The data shown here represent the first step for the characterization of this interesting system by MAS NMR. High-quality NMR spectra for backbone resonance assignment have been acquired, and we are currently analyzing the data obtained. This will hopefully provide an extensive assignment of this system in the future, which represents an important step prior to any site specific and structural study. We showed also that studying dynamics through MAS NMR relaxation measurements could potentially provide important information on the gating mechanism.

This is still an undergoing project, and several aspects still need to be addressed. We are currently working on the production of *Tm*CorA with different labeling schemes, in order to support the assignment procedure, and provide site-specific structural and dynamic studies.

Another important issue that has to be investigated in the future is related to the analysis of *Tm*CorA in the presence of Co^{2+}. In this regard a careful optimization of the sample production has to be performed, in order to incorporate Co^{2+} in the desired sites of the protein. This would open an avenue to the use of paramagnetic effects for providing important information on the system, in particular with the application of the methods described in the previous chapters.

VI.5 References

(1) Maguire, M. E.; Cowan, J. A., Magnesium chemistry and biochemistry. *Biometals* **2002,** *15*, 203-210.

(2) Payandeh, J.; Pfoh, R.; Pai, E. F., The structure and regulation of magnesium selective ion channels. *Biochim. Biophys. Acta* **2013,** *1828*, 2778-2792.

(3) Nelson, D. L.; Kennedy, E. P., Magnesium transport in *Escherichia coli.* Inhibition by cobaltous ion. *J. Biol. Chem.* **1971,** *246*, 3042-9.

(4) Park, M. H.; Wong, B. B.; Lusk, J. E., Mutants in three genes affecting transport of magnesium in *Escherichia coli*: genetics and physiology. *J. Bacteriol.* **1976,** *126*, 1096-103.

(5) Papp-Wallace, K. M.; Maguire, M. E., Regulation of CorA Mg^{2+} channel function affects the virulence of *Salmonella enterica serovar typhimurium*. *J. Bacteriol.* **2008,** *190*, 6509-6516.

(6) Papp-Wallace, K. M.; Nartea, M.; Kehres, D. G.; Porwollik, S.; McClelland, M.; Libby, S. J.; Fang, F. C.; Maguire, M. E., The CorA Mg^{2+} channel is required for the virulence of *Salmonella enterica serovar typhimurium*. *J. Bacteriol.* **2008,** *190*, 6517-23.

(7) Hmiel, S. P.; Snavely, M. D.; Miller, C. G.; Maguire, M. E., Magnesium transport in *Salmonella typhimurium*: characterization of magnesium influx and cloning of a transport gene. *J. Bacteriol.* **1986,** *168*, 1444-1450.

(8) Xia, Y.; Lundback, A. K.; Sahaf, N.; Nordlund, G.; Brzezinski, P.; Eshaghi, S., Co^{2+} selectivity of Thermotoga maritima CorA and its inability to regulate Mg^{2+} homeostasis present a new class of CorA proteins. *J. Biol. Chem.* **2011,** *286*, 16525-32.

(9) Nordin, N.; Guskov, A.; Phua, T.; Sahaf, N.; Xia, Y.; Lu, S.; Eshaghi, H.; Eshaghi, S., Exploring the structure and function of *Thermotoga maritima* CorA reveals the mechanism of gating and ion selectivity in Co^{2+}/Mg^{2+} transport. *Biochem. J.* **2013,** *451*, 365-74.

(10) Holden, J. F.; Adams, M. W., Microbe-metal interactions in marine hydrothermal environments. *Curr. Opin. Chem. Biol.* **2003,** *7*, 160-165.

(11) Eshaghi, S.; Niegowski, D.; Kohl, A.; Martinez Molina, D.; Lesley, S. A.; Nordlund, P., Crystal structure of a divalent metal ion transporter CorA at 2.9 angstrom resolution. *Science* **2006,** *313*, 354-357.

(12) Lunin, V. V.; Dobrovetsky, E.; Khutoreskaya, G.; Zhang, R.; Joachimiak, A.; Doyle, D. A.; Bochkarev, A.; Maguire, M. E.; Edwards, A. M.; Koth, C. M., Crystal structure of the CorA Mg^{2+} transporter. *Nature* **2006,** *440*, 833-837.

(13) Payandeh, J.; Pai, E. F., A structural basis for Mg^{2+} homeostasis and the CorA translocation cycle. *EMBO J.* **2006,** *25*, 3762-3773.

(14) Pfoh, R.; Li, A.; Chakrabarti, N.; Payandeh, J.; Pomes, R.; Pai, E. F., Structural asymmetry in the magnesium channel CorA points to sequential allosteric regulation. *Proc. Natl. Acad. Sci. U. S. A.* **2012,** *109*, 18809-18814.

(15) Matthies, D.; Dalmas, O.; Borgnia, M. J.; Dominik, P. K.; Merk, A.; Rao, P.; Reddy, B. G.; Islam, S.; Bartesaghi, A.; Perozo, E.; Subramaniam, S., Cryo-EM structures of the magnesium channel CorA reveal symmetry break upon gating. *Cell* **2016,** *164*, 747-756.

(16) Dalmas, O.; Sompornpisut, P.; Bezanilla, F.; Perozo, E., Molecular mechanism of Mg^{2+}-dependent gating in CorA. *Nat. Commun.* **2014,** *5*, 3590.

(17) Schanda, P.; Ernst, M., Studying dynamics by magic-angle spinning solid-state NMR spectroscopy: principles and applications to biomolecules. *Prog. Nucl. Magn. Reson. Spectrosc.* **2016,** *96*, 1-46.
(18) Lewandowski, J. R., Advances in solid-state relaxation methodology for probing site-specific protein dynamics. *Acc. Chem. Res.* **2013,** *46*, 2018-2027.
(19) Wang, S.; Ladizhansky, V., Recent advances in magic angle spinning solid state NMR of membrane proteins. *Prog. Nucl. Magn. Reson. Spectrosc.* **2014,** *82*, 1-26.
(20) Acharya, K. R.; Lloyd, M. D., The advantages and limitations of protein crystal structures. *Trends Pharmacol. Sci.* **2005,** *26*, 10-14.
(21) Martin, R. W.; Zilm, K. W., Preparation of protein nanocrystals and their characterization by solid state NMR. *J. Magn. Reson.* **2003,** *165*, 162-174.
(22) Baker, L. A.; Folkers, G. E.; Sinnige, T.; Houben, K.; Kaplan, M.; van der Cruijsen, E. A. W.; Baldus, M., Chapter Fifteen - Magic-angle-spinning solid-state NMR of membrane proteins. In *Method. Enzymol.*, Shukla, A. K., Ed. Academic Press: 2015; Vol. 557, pp 307-328.
(23) Seddon, A. M.; Curnow, P.; Booth, P. J., Membrane proteins, lipids and detergents: not just a soap opera. *BBA - Biomembranes* **2004,** *1666*, 105-117.
(24) Lacabanne, D.; Kunert, B.; Gardiennet, C.; Meier, B. H.; Böckmann, A., Sample preparation for membrane protein structural studies by solid-state NMR. In *Membrane protein structure and function characterization: methods and protocols*, Lacapere, J.-J., Ed. Springer New York: New York, NY, 2017; pp 345-358.
(25) Zhou, H.-X.; Cross, T. A., Influences of membrane mimetic environments on membrane protein structures. *Annu. Rev. Biophys.* **2013,** *42*, 361-392.
(26) Baker, L. A.; Baldus, M., Characterization of membrane protein function by solid-state NMR spectroscopy. *Curr. Opin. Struc. Biol.* **2014,** *27*, 48-55.
(27) Palmer, A. G., 3rd, NMR characterization of the dynamics of biomacromolecules. *Chem. Rev.* **2004,** *104*, 3623-40.
(28) Ishima, R.; Torchia, D. A., Protein dynamics from NMR. *Nat. Struct. Biol.* **2000,** *7*, 740-3.
(29) Henzler-Wildman, K.; Kern, D., Dynamic personalities of proteins. *Nature* **2007,** *450*, 964-972.
(30) Chakrapani, S.; Cordero-Morales, J. F.; Jogini, V.; Pan, A. C.; Cortes, D. M.; Roux, B.; Perozo, E., On the structural basis of modal gating behavior in K(+) channels. *Nat. Struct. Mol. Biol.* **2011,** *18*, 67-74.
(31) Medeiros-Silva, J.; Mance, D.; Daniels, M.; Jekhmane, S.; Houben, K.; Baldus, M.; Weingarth, M., H-1-detected solid-state NMR studies of water-inaccessible proteins invitro and insitu. *Angew. Chem. Int. Ed.* **2016,** *55*, 13606-13610.
(32) Lewandowski, J. R.; Sass, H. J.; Grzesiek, S.; Blackledge, M.; Emsley, L., Site-specific measurement of slow motions in proteins. *J. Am. Chem. Soc.* **2011,** *133*, 16762-16765.
(33) Krushelnitsky, A.; Zinkevich, T.; Reif, B.; Saalwächter, K., Slow motions in microcrystalline proteins as observed by MAS-dependent ^{15}N rotating-frame NMR relaxation. *J. Magn. Reson.* **2014,** *248*, 8-12.
(34) Knight, M. J.; Pell, A. J.; Bertini, I.; Felli, I. C.; Gonnelli, L.; Pierattelli, R.; Herrmann, T.; Emsley, L.; Pintacuda, G., Structure and backbone dynamics of a microcrystalline metalloprotein by solid-state NMR. *Proc. Natl. Acad. Sci. U.S.A.* **2012,** *109*, 11095-11100.
(35) Ma, P.; Xue, Y.; Coquelle, N.; Haller, J. D.; Yuwen, T.; Ayala, I.; Mikhailovskii, O.; Willbold, D.; Colletier, J. P.; Skrynnikov, N. R.; Schanda, P., Observing the overall rocking motion of a protein in a crystal. *Nat. Commun.* **2015,** *6*, 8361.

(36) Schanda, P.; Meier, B. H.; Ernst, M., Quantitative analysis of protein backbone dynamics in microcrystalline ubiquitin by solid-state NMR spectroscopy. *J. Am. Chem. Soc.* **2010,** *132*, 15957-67.
(37) Muller, H.; Etzkorn, M.; Heise, H., Solid-state NMR spectroscopy of proteins. *Top. Curr. Chem.* **2013,** *335*, 121-56.
(38) Bertini, I.; Luchinat, C.; Parigi, G.; Ravera, E., *NMR of paramagnetic molecules. Applications to metallobiomolecules and models*. Elsevier: Boston, 2017.
(39) Andreas, L. B.; Jaudzems, K.; Stanek, J.; Lalli, D.; Bertarello, A.; Le Marchand, T.; Cala-De Paepe, D.; Kotelovica, S.; Akopjana, I.; Knott, B.; Wegner, S.; Engelke, F.; Lesage, A.; Emsley, L.; Tars, K.; Herrmann, T.; Pintacuda, G., Structure of fully protonated proteins by proton-detected magic-angle spinning NMR. *Proc. Natl. Acad. Sci. U.S.A.* **2016,** *113*, 9187-9192.
(40) Cala-De Paepe, D.; Stanek, J.; Jaudzems, K.; Tars, K.; Andreas, L. B.; Pintacuda, G., Is protein deuteration beneficial for proton detected solid-state NMR at and above 100 kHz magic-angle spinning? *Solid State Nucl. Magn. Reson.* **2017,** *87*, 126-136.
(41) Stanek, J.; Andreas, L. B.; Jaudzems, K.; Cala, D.; Lalli, D.; Bertarello, A.; Schubeis, T.; Akopjana, I.; Kotelovica, S.; Tars, K.; Pica, A.; Leone, S.; Picone, D.; Xu, Z. Q.; Dixon, N. E.; Martinez, D.; Berbon, M.; El Mammeri, N.; Noubhani, A.; Saupe, S.; Habenstein, B.; Loquet, A.; Pintacuda, G., NMR spectroscopic assignment of backbone and side-chain protons in fully protonated proteins: microcrystals, sedimented assemblies, and amyloid fibrils. *Angew. Chem. Int. Ed.* **2016,** *55*, 1-6.

Conclusions

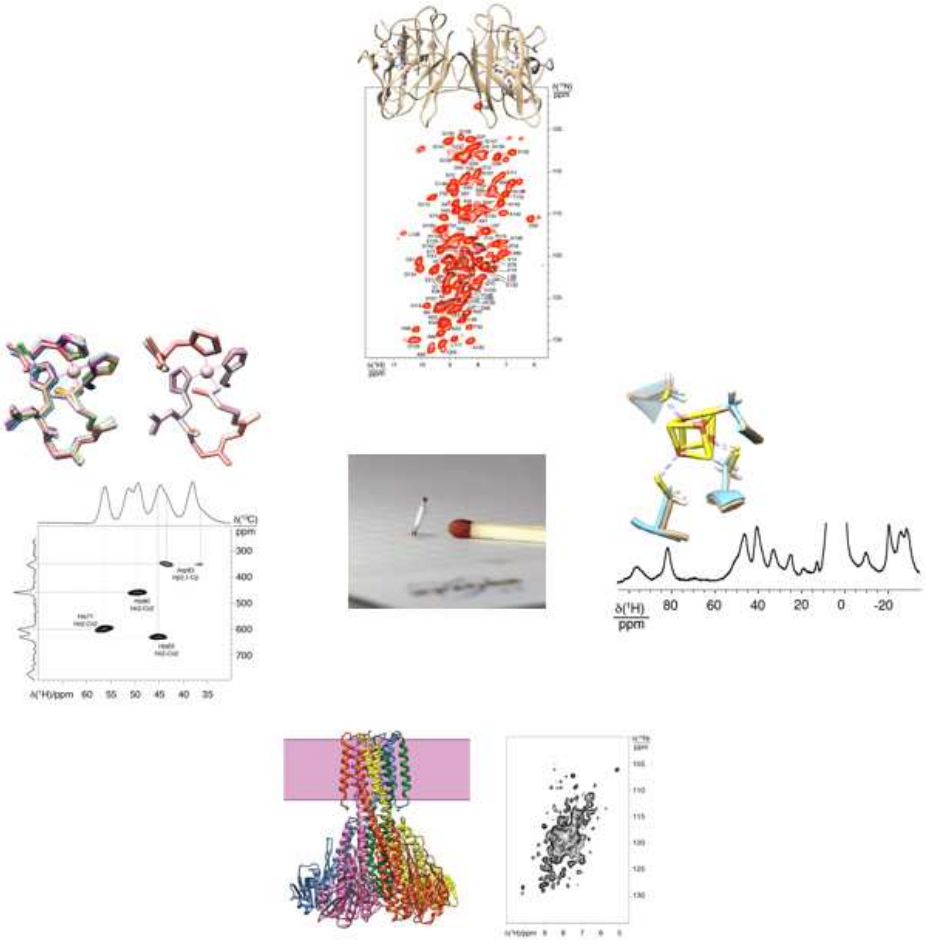

In conclusion, the work presented in this manuscript has addressed the main bottlenecks preventing the application of MAS NMR for the characterization of active sites in (large) paramagnetic metalloproteins.

On one hand, we have demonstrated that dramatic improvements in resolution and sensitivity are provided by proton-detected NMR approaches at ultrafast MAS rates (60-111 kHz). These developments allow the rapid acquisition of protein fingerprint spectra, of multidimensional maps for backbone and side chain assignment, and of structural restraints. Specifically, this methodology was successfully employed to two microcrystalline paramagnetic metalloproteins, the human superoxide dismutase (SOD) and the *E. halophila* high potential iron-sulfur protein I (*Eh*HiPIP I). The approach also allowed the first characterization of a metal ion channel, *Tm*CorA, in reconstituted lipid membranes, establishing a frame for the investigation of the gating mechanism. Backbone and side chains assignment, combined with site-specific dynamics studies, represent the following step towards the elucidation of the properties of this system in the future.

On the other hand, we have developed and applied a spectroscopic "toolkit" for the observation of nuclei in the close proximity of a paramagnetic metal center. This was based on NMR techniques previously designed for the analysis of highly paramagnetic materials, and allowed to overcome the severe drawbacks connected to the hyperfine couplings to unpaired electrons.

By the combination of ultra-fast MAS, short high-powered adiabatic pulses, short recoupling schemes, and state-of-the-art DFT and *ab initio* calculations, we were able to accomplish the detection and the assignment of signals associated to the ^{1}H, ^{13}C, and ^{15}N nuclei in the "blind" coordination sphere of paramagnetic Fe, Co, and Cu centers in *Eh*HiPIP I and SOD. The shift tensors of these signals are extremely sensitive to the fine details of the metal ion coordination, and can be converted into structural restraints for obtaining atomic-resolution geometries of active sites at ultra-high resolution.

Still, different aspects will require additional investigation in the future. In particular, we aim to extend the methodology presented in the thesis in the case of magnetically coupled systems, which are rather common in metalloproteins, for which a full theoretical framework for the interpretation of the PNMR shifts is not yet available, as discussed in the case of SOD. Besides this, we also aim to analyse a wider repertoire of systems, in particular membrane-embedded metalloenzymes, for which there is still a paucity of solved structures, with the result that many essential related biochemical processes are currently unknown. In this regard,

CorA represents an attractive target, and once optimized protocols for the inclusion of paramagnetic species will be established, we expect that the methodology described in the thesis will provide insights into the gating mechanism of the channel, paving the way to the study of other similar systems.

Overall, we believe that the techniques described in this thesis will be an essential tool to elucidate many currently unanswered questions about structure and function of metal sites in structural biology, representing a substantial step forward for biomolecular MAS NMR.

Appendices

Appendix 1. List of most important abbreviations

CP	Cross Polarization
DEER	Double Electron-Electron Resonance
DFT	Density Functional Theory
DMM	n-dodecyl-β-D-maltopyranoside
DMPC	1,2-dipalmitoyl-sn-glycero-3-phosphocholine
DPhPC	1,2-diphytanoyl-sn-glycero-3-phosphocholine
DPPC	1,2-dimyristoyl-sn-glycero-3-phosphocholine
EM	Electron Microscopy
EPR	Electron Paramagnetic Resonance
EXAFS	Extended X-ray Absorption Fine Structure
HFC	Hyperfine Coupling
HiPIP	High-Potential Iron-Sulfur Protein
IMAC	Immobilized Metal ion Affinity Chromatography
ISC	Iron-Sulfur Cluster
MAS	Magic Angle Spinning
MAT	Magic Angle Turning
MPD	2-Methyl-2,4-pentanediol
NMR	Nuclear Magnetic Resonance
PCS	Pseudo-Contact Shift
PDA	Point Dipole Approximation
PNMR	Paramagnetic NMR
PRE	Paramagnetic Relaxation Enhancement
RF	Radio Frequency
RFDR	Radio-Frequency Driven Recoupling
SA	Shift Anisotropy
SHAP	Short High-power Adiabatic Pulse
SOD	Superoxide dismutase
TCEP	Tris(2-carboxyethyl)phosphine
TEDOR	Transferred-Echo DOuble-Resonance
TM	Trans Membrane
XRD	X-Ray Diffraction
ZFS	Zero-Field Splitting

Appendix 2. Settings of ^{1}H-experiments for backbone assignment at 60 kHz MAS

90° nonselective pulses. For the nonselective 90°pulses no specific requirements are needed in principle, as long as they are powerful enough to properly excite the required spectral window. With the characteristic of the 1.3 mm probes used in our laboratory, these are usually set to 2.5 μs and 100 kHz rf-amplitude for ^{1}H, 5.0 μs and 50 kHz rf-amplitude for ^{15}N, and 3.12 μs and 80 kHz rf-amplitude for ^{13}C.

Cross-polarization. The optimal CP conditions are sample dependent, and they need to be carefully optimized. What it is experimentally found is that both zero-quantum (ZQ CP) and double-quantum (DQ CP) conditions are suitable.

^{1}H-^{15}N forward CP is usually achieved with contact times around 1 ms, while for the ^{15}N-^{1}H back CP shorter contact times, around 0.5 ms are used in order to avoid long-range transfers. For ZQ CP conditions ^{1}H rf-amplitude is set at about 100 kHz and ^{15}N rf-amplitude is set at about 40 kHz, while for the DQ CP conditions ^{1}H rf-amplitude is usually set at 20 kHz, with the ^{15}N rf-amplitude set at about 40 kHz. The ^{1}H rf-amplitude is usually ramped linearly across the optimal value, holding ^{15}N rf-amplitude constant, in order to achieve a broader selection of the Hartmann – Hahn condition.

^{1}H-^{13}C CP is usually achieved with contact times between 3 and 5 ms, using either the ZQ CP (100 kHz rf-amplitude for ^{1}H, 40 kHz rf-amplitude for ^{13}C) or the DQ CP (100 kHz rf-amplitude for ^{1}H, 20 kHz rf-amplitude for ^{13}C). Again, ^{1}H rf-amplitude is usually ramped linearly, helding ^{13}C rf-amplitude constant, like for ^{1}H-^{15}N CP.

^{15}N-^{13}C CP requires longer contact times, between 8 and 15 ms, and DQ CP is usually used, with ^{13}C rf-apmplitude held constant at about 35 kHz, and a tangent-modulated amplitude spin lock[1] of mean RF field amplitude of about 25 kHz on ^{15}N.

Decoupling and water suppression. Low-power heteronuclear decoupling is used in all the sequences. For ^{13}C and ^{15}N decoupling WALTZ-16[2] at an rf-amplitude of 10 kHz is usually applied, while for ^{1}H decoupling also the swept-low-power TPPM[3] sequence, applied at an rf-power of about 13 kHz is found to be equally effective, in addition to WALTZ-16. Water-suppression is achieved with the MISSISSIPPI pulse sequence,[4] without the use of homospoil gradients, with around 20 kHz irradiation for 100 to 300 ms.

^{13}C-^{13}C homonuclear transfers. The scalar $^{13}C^{\alpha}$-^{13}CO coherence transfer of the (H)CO(CA)NH experiment comprises two spin echoes with half-echo delays τ of duration 4.7

and 4.0 ms for the ^{13}CO and $^{13}C^{\alpha}$ sides of the transfer respectively (the durations for optimal transfer is sample dependent). Gaussian-cascade Q3 frequency-selective refocusing pulses[5] selective for the CO region (typical length ~350 μs) and the C^{α} region (typical length ~600 μs) are used for selective refocusing.

The (H)(CO)CA(CO)NH experiment comprises two spin echoes for the out-and-back ^{13}CO-$^{13}C^{\alpha}$ scalar transfer, of which the half-echo is typically 4.7 ms. Both the (H)(CA)CB(CA)NH and (H)(CA)CB(CA)(CO)NH experiments uses two spin echoes for the out-and-back $^{13}C^{\alpha}$-$^{13}C^{\beta}$ transfer, with Q3 refocusing pulse selective for the entire ^{13}C aliphatic region (typical length ~150 μs), and half-echo delays of 7.2 ms. In the (H)(CA)CB(CA)(CO)NH experiment, the second scalar transfer from $^{13}C^{\alpha}$ to ^{13}CO is performed using the same parameters as for the (H)(CO)CA(CO)NH sequence.

Appendix 3. Proteins preparation

Ubiquitin

Human ubiquitin was expressed with a C-terminal (His)6 tag from M15 cells transformed with a vector provided by ASLA Biotech (Riga, Latvia). Cells were grown in 3 mL LB medium at 37˚ C with 180 rpm shaking for 3h using Kanamycin and Ampicillin as antibiotics, then transferred in 15 mL of M9 medium supplied with ^{15}N labeled ammonium chloride and ^{2}H-^{13}C labeled glucose in 100 % D_2O, and let overnight at 37˚ C with 180 rpm shaking. The overnight culture was transferred to 500 mL of deuterated M9 medium and protein expression was induced with 1 mM IPTG when the optical density reached 0.55. At this point the temperature was reduced to 25˚ C and expression continued for 40 hours. Cells were harvested, suspended in 15 mL of phosphate buffer (50 mM sodium phosphate, 150 mM NaCl, pH 7.4 buffer) and lysed using and Avestin homogenizer (Mannheim, Germany). The lysate was incubated with 3 µg/mL DNAse I for 25 minutes at room temperature and centrifuged at 25000 g for 40 minutes. The supernatant was filtered and charged into a HiTrapTM IMAC HP 1 mL column equilibrated with loading buffer (50 mM sodium phosphate, 300 mM NaCl, 10 mM imidazole, pH 7.4). Protein was eluted using a linear gradient with elution buffer (50 mM sodium phosphate, 300 mM NaCl, 500 mM imidazole, pH 7.4), and the protein was recovered at 50 % of the gradient. Purity was confirmed by SDS PAGE gel. The protein was dialyzed three times against sodium citrate 20 mM, pH 4.05 and then concentrated up to 12 mg/mL. Crystallization[6] was induced by slowly adding 1.5 volumes of 2-Methyl-2,4-pentanediol (MPD) and left overnight at 4 °C. The solid was filled into a 1.3 mm rotor by centrifugation at 25000 g, and the rotor was sealed with FKM inserts (courtesy of Bruker Biospin) to avoid sample dehydration.

***Eh*HiPIP I**

Purified [U-^{13}C, ^{15}N] labeled oxidized HiPIP I from *E. halophila* was purchased from Giotto Biotech S.r.l. (Sesto Fiorentino, Italy). Protein solutions of 10 mg/mL were dialysed against 10 mM TRIS, pH 8. Protein crystals were grown by sitting drop vapor diffusion using a ratio of 1:1 (protein / reservoir). The reservoir solution consisted of 3.5 M Ammonium Sulfate, 100 mM MES, pH 5.6. Platelet-like crystals were obtained in 34 days. Crystals were harvested by centrifugation and packed in a 1.3 mm rotor using the ultracentrifugal device 1 (Bruker Biospin).[7] The rotor was centerpacked with FKM inserts (courtesy of Bruker Biospin) to avoid dehydration.

SOD

[U-^{13}C, ^{15}N]-labeled samples of the thermostable mutant of human Co^{II}-SOD and Cu^{II},Co^{II}-SOD, and [U-$^{1}H^{N}$, ^{2}H, ^{13}C, ^{15}N]-labeled sample of the thermostable mutant of human Cu^{II},Co^{II}-SOD, were expressed and purified as described previously.[8-9] For crystallization the sample were concentrated to 20 mg/mL in a 50 mM sodium acetate pH 5.0 buffer, mixed 1:1 with a precipitant solution of 20% PEG 4K in unbuffered water and crystals grown in sitting drops over a reservoir solution of the same precipitant supplemented with 2 M NaCl. Complete crystallization occurred in 3-4 days. The suspension of microcrystals was then packed into a 0.7 mm rotor by ultra-centrifugation, using the ultra-centifugal device provided by Giotto Biotech.[7]

***Tm*CorA**

Expression and purification of Tm*CorA*. *Tm*CorA was expressed with a N-terminal (His)6 tag from BL21(DE3) cells transformed with a pET15b vector. Cells were grown in 1.5 L of LB medium at 37˚C with 180 rpm shaking to an OD_{600} of ~0.6, harvested and then transferred to 1.5 L of M9 medium supplied with ^{15}N-labeled ammonium chloride and unlabeled or ^{13}C-labeled glucose in H_2O, using Ampicillin as antibiotic, for 30 minutes at 37˚C and 180 rpm shaking. Protein expression was induced with 1 mM IPTG and the culture was kept at 30˚C for 3-4 hours, until an OD_{600} of ~2. Cells were resuspended in 75 mL of binding buffer (50 mM HEPES, 500 mM NaCl, 5 % glycerol, pH 7.5), in the presence of 1mM PMSF, 3 μg/mL DNAse I and 1mM $MgCl_2$, and lysed using and Avestin homogenizer (Mannheim. Germany). The lysate was centrifuged at 8000 rpm for 15 minutes to remove cells debris and the corresponding supernatant was then centrifuged at 100000 g for 1 hour. The pellet was homogenized with 25 mL of binding buffer in the presence of 1mM PMSF and 1 % DMM and stirred gentle overnight. The solution was centrifuged at 100000 g to remove residual debris and, after addition of 10 mM imidazole, charged into a HiTrapTM IMAC HP 1 mL column equilibrated with binding buffer. The column was washed with ~ 20 column volumes of washing buffer (50 mM HEPES, 500 mM NaCl, 5 % glycerol, 35 mM imidazole, pH 7.5) and the protein eluted with ~3 mL of elution buffer (50 mM HEPES, 500 mM NaCl, 5 % glycerol, 400 mM imidazole, pH 7.5). The buffer was changed to binding buffer on a PD10 column and the resulting solution was incubated with TEV-protease and 0.5 mM TCEP overnight to remove the (His)6 tag. The solution was charged into HiTrapTM IMAC HP 1

mL column as in the previous step. The flow-through was concentrated to ~ 3mL and charged into a Superdex 200 column in 20 mM Tris, 150 mM NaCl, 0.5 mM TCEP and 0.02 % DDM.

Reconstitution of Tm*CorA in lipid bilayers*. For reconstitution in lipid bilayers the collected fractions from the previous steps were mixed with different lipids in defined protein-to-lipid ratios. In particular the following preparations were analyzed: DMPC 2:1; DMPC 1:1; DPPC 1:1; DPPC 2:1; DPhPC 1:1. The protein-lipids mixture was extensively dialyzed against 10 mM HEPES, 50 mM NaCl, 0.05 % NaN_3, pH 7.5 and $MgCl_2$ 40 mM (Mg^{2+}-containing form), or 20 mM $CoCl_2$ (Co^{2+}-containing form), or 1mM EDTA (metal-free form). The obtained precipitate was then packed into 1.3 mm or 0.7 mm rotors.

Crystallization of Tm*CorA*. For crystallization the collected fraction from the gel filtration was concentrated to 3 mg/mL and dialyzed overnight against 20 mM Tris, 1 mM $MgCl_2$, 0.02 % DMM, pH 8.0. Screening of crystallization conditions was performed by sitting-drop method, mixing 1 μL of protein solution with of 1 μL reservoir. The reservoir composition was changed by varying the buffer composition (Tris pH 8.0 or HEPES 7.5, either 100 or 300 mM), precipitating agent (PEG 400, PEG 1000 or PEG 2000, at 10 or 20 $\%_{w/v}$ concentration) and Mg^{2+} source ($MgCl_2$ or $MgNO_3$, either 100 mM or 300 mM). Different conditions produced needle-shaped crystals within 2 or 3 weeks. For NMR analysis the crystallization was performed using a 100 mM Tris, 100 mM $MgCl_2$, 10 $\%_{w/v}$ PEG 2000, pH 8.0 reservoir, mixing 15 μL of protein solution with 15 μL of reservoir. The crystals were then packed into an 1.3 mm rotor.

Appendix 4. NMR experiments

Backbone assignment of His6-tagged ubiquitin (Chapter II)

Experiments were acquired on a 800 MHz Bruker Avance III spectrometer equipped with a triple resonance 1.3 mm probe at 60 kHz MAS (Table 9).

Spectrum	Max indirect evolution	Spectral window (ppm)	Scans per point	Experimental time
(H)NH	40 ms	40 (^{1}H) 40 (^{15}N)	4	16 m
(H)CANH	 4 ms (^{13}C) 8 ms (^{15}N)	40 (^{1}H) 40 (^{13}C) 40 (^{15}N)	4	4 h
(H)CONH	 8 ms (^{13}C) 8 ms (^{15}N)	40 (^{1}H) 20 (^{13}C) 40 (^{15}N)	8	8 h
(H)CO(CA)NH	 8 ms (^{13}C) 8 ms (^{15}N)	40 (^{1}H) 20 (^{13}C) 40 (^{15}N)	16	16 h
(H)(CO)CA(CO)NH	 4 ms (^{13}C) 8 ms (^{15}N)	40 (^{1}H) 40 (^{13}C) 40 (^{15}N)	16	16 h
(H)(CA)CB(CA)NH	 4 ms (^{13}C) 8 ms (^{15}N)	40 (^{1}H) 80 (^{13}C) 40 (^{15}N)	8	16 h
(H)(CA)CB(CA)(CO)NH	 4 ms (^{13}C) 8 ms (^{15}N)	40 (^{1}H) 80 (^{13}C) 40 (^{15}N)	16	32 h
(H)N(CA)(CO)NH	 8 ms (^{13}C) 10.2 ms (^{15}N)	40 (^{1}H) 40 (^{13}C) 40 (^{15}N)	16	36 h
(H)N(CO)(CA)NH	 8 ms (^{13}C) 10.2 ms (^{15}N)	40 (^{1}H) 40 (^{13}C) 40 (^{15}N)	16	36 h

Table 9. Experimental parameters for the acquisition of NMR experiments for backbone assignment of Hi6-tagged ubiquitin.

Backbone assignment of Cu^{II},Co^{II}-SOD (Chapter II)

Experiments for backbone assignments (2D (H)NH, 3D (H)CANH, (H)(CO)CA(CO)NH, (H)CONH, (H)CO(CA)NH, (H)(CA)CB(CA)NH, and (H)(CA)CB(CA)(CO)NH)[10] were recorded on a 800 MHz Bruker Avance III spectrometer equipped with a triple resonance 1.3 mm probe at 60 kHz MAS. For each of these experiments the experimental parameters are listed in Table 10.

Spectrum	Max indirect evolution	Spectral window (ppm)	Scans per point	Experimental time
(H)NH	30 ms	60 (^{1}H) 35 (^{15}N)	8	16 m
(H)CANH	 4 ms (^{13}C) 8 ms (^{15}N)	40 (^{1}H) 40 (^{13}C) 35 (^{15}N)	24	26 h
(H)CONH	 8.6 ms (^{13}C) 8 ms (^{15}N)	40 (^{1}H) 16 (^{13}C) 35 (^{15}N)	16	16 h
(H)CO(CA)NH	 8.6 ms (^{13}C) 8 ms (^{15}N)	40 (^{1}H) 16 (^{13}C) 35 (^{15}N)	16	16 h
(H)(CO)CA(CO)NH	 4 ms (^{13}C) 8 ms (^{15}N)	40 (^{1}H) 40 (^{13}C) 35 (^{15}N)	32	32 h
(H)(CA)CB(CA)NH	 4 ms (^{13}C) 8 ms (^{15}N)	40 (^{1}H) 80 (^{13}C) 35 (^{15}N)	16	35 h
(H)(CA)CB(CA)(CO)NH	 4 ms (^{13}C) 8 ms (^{15}N)	40 (^{1}H) 80 (^{13}C) 35 (^{15}N)	32	70 h

Table 10. Experimental parameters for the acquisition of NMR experiments for backbone assignment of Cu^{II},Co^{II}-SOD.

Side chain assignment and contacts determination of GB1 (Chapter II)

Experiments were recorded on a 1 GHz Bruker Avance III spectrometer equipped with a triple resonance 0.7 mm probe at 111 kHz MAS. The experimental parameters are listed in Table 11.

Spectrum	Max indirect evolution	Spectral window (ppm)	Scans per point	Experimental time
(H)NH	20 ms	100 (^{1}H) 40 (^{15}N)	4	24 m
(H)CH	46 ms	100 (^{1}H) 88 (^{13}C)	8	5 h
(H)NCAHA	4 ms (^{13}C) 8 ms (^{15}N)	40 (^{1}H) 40 (^{13}C) 40 (^{15}N)	4	25 h
(H)CCH TOCSY	6.8 ms	40 (^{1}H) 88 (^{13}C)	2	32.5 h
(H)NHH$_{RFDR}$	6.9 ms (^{1}H) 13.6 ms (^{15}N)	40 (^{1}H) 14 (^{1}H) 40 (^{15}N)	4	15 h
(H)CHH$_{RFDR}$	2.6 ms (^{1}H) 5.3 ms (^{13}C)	40 (^{1}H) 14 (^{1}H) 75 (^{13}C)	4	67 h

Table 11. Experimental parameters for the acquisition of NMR experiments for side chains assignment and contacts determination of GB1.

Backbone and side chain assignment of *Eh*HiPIP I

Experiments for backbone assignments (2D (H)NH and (H)CH, 3D (H)CANH, (H)(CO)CA(CO)NH, (H)CONH, (H)CO(CA)NH, (H)NCAH, and (H)CHH)[10-11] were recorded on a 1 GHz Bruker Avance III spectrometer equipped with a triple resonance 0.7 mm probe at 111 kHz MAS (Table 12).

Spectrum	Max indirect evolution	Spectral window (ppm)	Scans per point	Experimental time
(H)NH	20 ms	100 (^{1}H) 50 (^{15}N)	16	20 m
(H)CANH	4 ms (^{13}C) 8 ms (^{15}N)	100 (^{1}H) 50 (^{13}C) 50 (^{15}N)	16	11 h
(H)CONH	5 ms (^{13}C) 8 ms (^{15}N)	100 (^{1}H) 20 (^{13}C) 50 (^{15}N)	16	6 h
(H)CO(CA)NH	5 ms (^{13}C) 8 ms (^{15}N)	100 (^{1}H) 20 (^{13}C) 50 (^{15}N)	32	11 h
(H)(CO)CA(CO)NH	4 ms (^{13}C) 8 ms (^{15}N)	100 (^{1}H) 40 (^{13}C) 50 (^{15}N)	64	39 h
(H)CH	46 ms	100 (^{1}H) 88 (^{13}C)	8	5 h
(H)NCAHA	4 ms (^{13}C) 8 ms (^{15}N)	40 (^{1}H) 40 (^{13}C) 50 (^{15}N)	24	25 h
(H)CCH TOCSY	6.8 ms	40 (^{1}H) 70 (^{13}C)	4	24 h

Table 12. Experimental parameters for the acquisition of NMR experiments for backbone and side chains assignment of *Eh*HiPIP I.

PNMR experiments for *Eh*HiPIP I (Chapter IV)

Paramagnetic solid-state NMR experiments were performed on a 500 MHz Bruker Avance III spectrometer equipped with a double-resonance 1.3 mm probe. All experiments were acquired at 60 kHz MAS. The temperature was regulated in order to obtain an estimated sample temperature of 298 K, unless otherwise specified. One dimensional ^{1}H spectra were acquired with the double-adiabatic spin-echo sequence using tanh/tan refocusing pulses at 200 kHz with a sweep width of 500 kHz over 50 μs.[12-13] The water signal was suppressed by presaturation using a continuous pulse of 2 kHz for 10 ms. The recycle delay was set to 20 ms. The ^{1}H-^{1}H radiofrequency driven recoupling (RFDR) spectrum[14] was acquired using a mixing time of 0.5 ms and a recycle delay of 20 ms.[15] The (^{1}H)^{13}C transferred echo double resonance (TEDOR)[16-17] was acquired with a recoupling period of 16.67 μs (one rotor period) and a recycle delay of 50 ms.

Spectrum	Max indirect evolution	Spectral window (ppm)	Scans per point	Experimental time
^{1}H		500	133 120	1 h
^{1}H^{1}H RFDR	0.50 ms	500 (ω_2) 500 (ω_1)	3072	5.5 h
(^{1}H)^{13}C TEDOR	1 ms	1000 (^{13}C) 260 (^{1}H)	17 408	3.2 d

Table 13. Experimental parameters for the acquisition of PNMR experiments for *Eh*HiPIP I.

PNMR experiments for Co^{II}-SOD (Chapter IV)

Paramagnetic solid-state NMR experiments were performed on a 500 MHz Bruker Avance III spectrometer with a triple-resonance 0.7 mm probe. All experiments were acquired at 100 kHz MAS and at an estimated sample temperature of 280 K, unless specified otherwise. In all experiments the highest allowed power was used for hard-pulses, corresponding to a ν_1 field of 350 kHz for ^{1}H, 190 kHz for ^{13}C, and 115 kHz for ^{15}N, respectively. Recycle delays were set to 25 ms in ^{1}H-detected experiments and 50 ms in ^{13}C-detected ones. The water signal was suppressed by presaturation using a continuous pulse of 2 kHz for 10 ms. One-dimensional ^{1}H and ^{13}C spectra were acquired with a rotor synchronized spin-echo sequence. The ^{1}H adiabatic magic angle turning (aMAT)[18] experiment was acquired at 40 kHz MAS using six tanh/tan short high-powered adiabatic pulses (SHAPs) that swept through 10 MHz in 50 μs. The ^{13}C aMAT experiment was acquired at 30 kHz MAS using six tanh/tan pulses sweeping through 5 MHz in 33.33 μs. The shifts anisotropies (SAs) were estimated using the program Dmfit.[19] For this purpose, rows corresponding to the spinning-sideband manifold of each nucleus were extracted from the aMAT spectra and fitted separately. The (H)CH and (H)NH transferred echo double resonance (TEDOR)[16-17] experiments were acquired using the same radio-frequency powers used in the 1D experiments; in both cases the recoupling period was set to four rotor periods. The (H)C(H)H TEDOR spectrum was acquired with the same parameters used for the (H)CH TEDOR, using a ^{1}H-^{1}H radio frequency driven recoupling scheme (RFDR),[14] with a mixing time of 0.64 ms (Table 14).

Spectrum	Max indirect evolution	Spectral window (ppm)	Scans per point	Experimental time
^{1}H spin echo	-	1500	92160	2 h
^{13}C spin echo	-	2980	614400	12.5 h
(H)NH TEDOR	0.2 ms	1500 (^{1}H) 1971 (^{15}N)	27136	10 h
(H)CH TEDOR	0.2 ms	1500 (^{1}H) 794 (^{13}C)	10240	6.5 h
(H)C(H)H TEDOR	0.2 ms	1500 (^{1}H) 794 (^{13}C)	25600	14 h
^{1}H aMAT	0.325 ms	800 (ω_2) 400 (ω_1)	5120	10.5 h
^{13}C aMAT	0.633 ms	1986 (ω_2) 1758 (ω_1)	24832	4.4 d

Table 14. Experimental parameters for the acquisition of PNMR experiments for Co^{II}-SOD.

Backbone assignment of *Tm*CorA (Chapter VI)

Experiments were recorded on a 1 GHz Bruker Avance III spectrometer equipped with a triple resonance 0.7 mm probe at 107 kHz MAS, or on a 800 MHz Bruker Avance III spectrometer equipped with a four-channels 0.7 mm probe at 107 khz MAS (Table 15).

Spectrum	Max indirect evolution	Spectral window (ppm)	Scans per point	Experimental time
(H)NH	30 ms	40 (^{1}H) 40 (^{15}N)	32	2 h
(H)CANH	 6.4 ms (^{13}C) 10 ms (^{15}N)	40 (^{1}H) 32 (^{13}C) 30 (^{15}N)	8	18 h
(H)CONH	 8 ms (^{13}C) 10 ms (^{15}N)	40 (^{1}H) 15 (^{13}C) 35 (^{15}N)	8	11.5 h
(H)CO(CA)NH	 8.6 ms (^{13}C) 8 ms (^{15}N)	40 (^{1}H) 15 (^{13}C) 35 (^{15}N)	16	23 h
(H)(CO)CA(CO)NH	 6.4 ms (^{13}C) 10 ms (^{15}N)	40 (^{1}H) 32 (^{13}C) 30 (^{15}N)	16	36 h
(H)(CA)CB(CA)NH*	 4 ms (^{13}C) 6 ms (^{15}N)	40 (^{1}H) 70 (^{13}C) 40 (^{15}N)	64	4 d
(H)CH	10 ms	100 (^{1}H) 80 (^{15}N)	32	4 h
(H)(CA)CBCAHA	 6 ms (^{13}CA) 6 ms (^{13}CB)	40 (^{1}H) 35 (^{13}CA) 65 (^{13}CB)	8	2 d
(H)NCAHA	 6.4 ms (^{13}C) 10 ms (^{15}N)	40 (^{1}H) 32 (^{13}C) 30 (^{15}N)	8	18 h
(H)COCAHA	 6.4 ms (^{13}CO) 7 ms (^{13}CA)	40 (^{1}H) 15 (^{13}CO) 30 (^{13}CA)	8	13.5 h
(H)N(CO)CAHA	 6.4 ms (^{13}C) 10 ms (^{15}N)	40 (^{1}H) 32 (^{13}C) 30 (^{15}N)	16	36 h
(H)CO(N)CAHA	 6.4 ms (^{13}CO) 7 ms (^{13}CA)	40 (^{1}H) 15 (^{13}CO) 30 (^{13}CA)	16	27 h

Table 15. Experimental parameters for the acquisition of NMR experiments for backbone assignment of *Tm*CorA. * Acquired at 800 MHz.

Appendix 5. Calculations for Co^{II}-SOD

Molecular models

Molecular models were built from the X-ray crystallographic structure of the thermostable mutant of human Cu,Zn-SOD (PDB ID 1SOS).[20] The crystal unit cell of 1SOS contains 10 protein chains labeled A–J. PNMR calculations were performed consistently for all of them, thus exploiting the natural structural variation occurring in the crystal.

Two molecular models of the Co^{II} (substituted for Zn^{II}) site were built (Figure 53) a larger one (*m1*, 86 atoms) for structure optimization, hyperfine coupling and orbital shielding calculations and a smaller one (*m0*, 32 atoms) for subsequent high-level *ab initio* calculations of EPR parameters. The larger model *m1* consists of the Co^{II} ion in place of the native Zn^{II}, two backbone segments between Cα atoms of residues 71–72 and 79–83, and side chains of metal-binding residues His63, His71, His80, and Asp83. All other side chains were removed and terminated with hydrogen atoms. The conformation of the metal-binding Asp83 side chain is stabilized by two hydrogen bonds to backbone amide protons of His80 and Gly72, both essential for the proper fold of the SOD Zn^{II} (Co^{II}) site and both properly included in model *m1*. The hydrogen atoms were added to the raw PDB structures with the REDUCE tool.[21] The *m1* structures were optimized with PBE0-D3BJ[22-25] method using TURBOMOLE.[26] The conductor-like-screening model[27] with dielectric constant ε = 4.0 was used to account for dielectric environmental effects in the protein. To keep the overall molecular fold intact the positions of C^{α} atoms (8 atoms out of 86) were fixed in space during the optimization while the rest was freely relaxed. The technique keeping the positions of C^{α} atoms fixed was chosen to preserve the overall fold of the metal center as encoded in the X-ray structures, while at the same time allowing the local geometry parameters to relax after the Co^{II} substitution for Zn^{II}. A locally dense Gaussian basis set was applied, using a def2-TZVP basis for Co and def2-SVP for the main-group elements.[28]

From each optimized *m1* structure, a model *m0* was built by truncating and terminating with hydrogen atoms followed by an optimization of positions of the newly added hydrogen atoms. The smaller model *m0* includes only the metal-binding imidazole rings of His63, His71, His80. The total charge was +1 for both models. All DFT and single-state CASSCF calculations were done for the high-spin ($S = 3/2$) ground state of the Co^{II} complex.

Calculation of PNMR shifts

PNMR shift tensors were obtained according to the Kurland–McGarvey theory[29] in its recent formulation by Vaara et al.,[30] where the hyperfine part of the PNMR shift tensor is expressed in terms of EPR property tensors. EPR *g*- and *D*-tensors were calculated in model *m0* applying a strongly contracted variant of the *N*-electron valence-state perturbation theory of second order (NEVPT2)[31] to a state-averaged complete-active-space self-consistent-field reference wave-function[32-33] with seven electrons in five active 3d-orbitals (SA-CASSCF(7,5)) as implemented in ORCA.[34] It is known that standard DFT functionals dramatically underestimate the magnitude of zero-field splitting (ZFS, *D*-tensor) in high-spin Co^{II} complexes and correlated multi-reference wave-function level of electronic structure theory is needed for reliable results.[35] The spin-orbit part of the *D*-tensor was evaluated using quasi-degenerate perturbation theory[36] (QDPT) applied to the NEVPT2 electronic structure. A test CAS-CI calculation with the converged SA-CASSCF(7,5) wave-function confirmed that the spin-spin part of the *D*-tensor is this case really negligible with all matrix elements being smaller than 0.15 cm^{-1}. EPR *g*-tensor was calculated on NEVPT2 level with the effective Hamiltonian approach.[37] For both D_{SO}- and *g*-tensors, the spin-orbit mean-field (SOMF) approximation[38-39] to the spin-orbit matrix elements in Breit-Pauli form was applied. The RI technique was applied in the orbital transformation step of NEVPT2. The state-averaging in SA-CASSCF involved all 10 quartet and 40 doublet roots implied by the (7,5) active space, all equally weighted. Single-state CASSCF(7,5) calculations for the $S = 3/2$ ground state were performed to obtain Mulliken spin densities at Co^{II} plotted in Figure 53. The atomic basis used for the DFT structure optimizations was in all multi-reference calculations enhanced with diffuse functions optimized for molecular properties.[40] We thus used the def2-TZVPD basis for Co and def2-SVPD for the main-group elements. In the DFT hyperfine coupling and orbital shielding calculations we employed the def2-TZVPD and IGLO-III[41] basis sets for Co and main-group elements, respectively.

The FC and SD terms of EPR hyperfine coupling tensors for the ^{1}H, ^{13}C, and ^{15}N nuclei in model *m1* were calculated using PBE0[22-23] and PBE50 functionals including 25% and 50% of Hartree–Fock exchange, respectively. GIAO orbital shielding tensors[42] were calculated on PBE0 level with GAUSSIAN.[43]

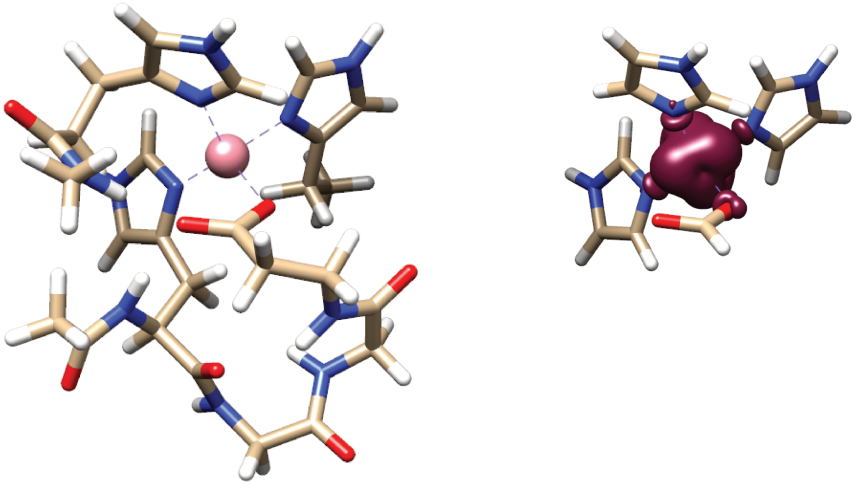

Figure 53. Left: the larger model *m1* used for DFT structure optimization and HFC calculations. Right: the smaller model *m0* used for ab initio calculations of *g*- and *D*-tensors with spin-density distribution (from SA-CASSCF(7,5) calculation, 0.002 a.u. isosurface).

Isotropic shifts δ_K were obtained from the total (orbital plus hyperfine) isotropic nuclear shieldings σ_K as

$$\delta_K = \sigma_K^{\mathrm{ref}} - \sigma_K \,, \tag{A.1}$$

where σ_K^{ref} is the reference nuclear shielding for a nucleus K. The calculations required to obtain σ_K^{ref} for ^{1}H, ^{13}C, and ^{15}N nuclei were performed with Gaussian 09, revision D.01 at conditions corresponding to the experimental NMR reference measurements44 (see Table 16). Structure of tetramethylsilane (TMS) was optimized with the PBE0-D3BJ/6-311++G (d,p) method and polarizable continuum model (PCM) of chloroform solvent. Orbital shielding tensors in TMS were calculated at the PBE0/IGLO-III level with PCM of chloroform.

In the case of ^{15}N reference shielding, to avoid difficult modeling of liquid ammonia, we employed neat liquid nitromethane as an easy-to-model secondary standard. The ^{15}N reference shielding was calculated according to the expression

$$\sigma^{\mathrm{NH_3}(l)} = \sigma^{\mathrm{CH_3NO_2}} + \frac{\Xi^{\mathrm{CH_3NO_2}}}{\Xi^{\mathrm{NH_3}(l)}} - 1 \,, \tag{A.2}$$

where $\sigma^{\mathrm{CH_3NO_2}}$ is the isotropic shielding of nitromethane and $\Xi^{\mathrm{CH_3NO_2}}/\Xi^{\mathrm{NH_3}(l)} - 1 =$ 380.5 ppm is the isotropic shift of nitromethane relative to the primary reference expressed in terms of standardized resonance frequency ratios.[44] Structure of nitromethane was optimized with the PBE0-D3BJ/6-311++G(d,p) method and polarizable continuum model (PCM) of nitromethane solvent. Orbital shielding tensors were calculated at the PBE0/IGLO-III level with PCM of nitromethane.

Nucleus	Experimental NMR reference	σ_K^{ref}
^{1}H	TMS [a]	31.6
^{13}C	TMS [a]	185.7
^{15}N	NH_3 (l)	218.7

Table 16. Isotropic shieldings used for reference. [a] 1 % solution with $CDCl_3$ solvent.

Appendix 6. Calculated shifts for models A-J of Co^{II}-SOD

Residue	Atom	A	B	C	D	E	F	G	H	I	J
His63	Cβ	300	280	264	294	261	308	274	300	335	246
	Cδ2	790	771	735	792	758	741	760	797	698	794
	Cε1	947	956	995	948	921	979	967	961	976	863
	Cγ	570	533	562	538	525	525	555	543	456	621
	Hβ2	-1	1	0	5	0	2	-3	-1	-3	-3
	Hβ1	-14	-17	-7	-13	-14	-17	-14	-16	-22	-13
	Hδ2	55	50	49	53	48	48	49	55	45	54
	Hε1	57	59	59	56	59	58	64	55	59	58
	Hε2	78	74	69	77	72	72	72	79	72	72
	Nδ1	17338	16426	16056	17236	16506	16210	15962	17735	15398	17187
	Nε2	1296	1268	1282	1320	1266	1264	1248	1318	1219	1280
His71	Cβ	204	216	184	211	199	184	212	215	175	188
	Cδ2	706	677	693	694	663	695	660	704	696	686
	Cε1	961	862	879	883	926	898	879	914	920	936
	Cγ	807	854	911	762	877	879	820	833	846	868
	Hβ2	-17	-16	-7	-17	-14	-8	-18	-16	-15	-7
	Hβ1	-2	1	0	0	-3	0	0	-1	-3	-1
	Hδ2	64	63	64	61	63	63	61	65	62	63
	Hε1	94	86	95	87	90	89	80	96	83	97
	Hε2	69	65	58	70	60	60	63	70	61	59
	Nδ1	16296	15373	15339	15970	15155	15363	15326	16109	15684	15442
	Nε2	1291	1235	1277	1249	1274	1276	1231	1278	1288	1290
His80	Cβ	153	92	131	150	107	126	79	162	90	199
	Cδ2	585	568	548	551	563	545	562	573	536	596
	Cε1	1299	1306	1331	1297	1308	1327	1267	1315	1244	1352
	Cγ	726	908	870	804	901	872	911	789	944	827
	Hβ2	-1	5	-2	-4	3	0	6	-5	13	-12
	Hβ1	5	4	3	4	3	5	5	3	9	-1
	Hδ2	59	59	60	60	60	59	58	60	61	60
	Hε1	93	101	108	99	105	107	96	97	111	98
	Hε2	62	47	50	55	50	48	45	61	40	65
	Nδ1	13710	11663	11870	12651	11981	11778	11506	13180	11961	13588
	Nε2	1355	1360	1374	1341	1364	1357	1338	1345	1355	1377
Asp83	Cα	288	256	244	270	236	262	240	272	256	243
	Cβ	215	568	475	328	531	477	581	258	621	292
	Cγ	-127	-2	-62	-88	-48	-44	-21	-108	81	-65
	Hα	5	7	7	8	7	8	6	7	7	7
	Hβ1	59	46	49	49	42	49	28	58	47	59
	Hβ2	27	40	42	34	45	39	57	31	40	32

Table 17. Calculated chemical shifts with PBE0 hyperfine coupling.

Residue	Atom	A	B	C	D	E	F	G	H	I	J
His63	Cβ	226	214	201	223	198	236	208	226	260	187
	Cδ2	636	607	577	630	601	586	601	637	547	640
	Cε1	711	728	749	716	693	741	737	723	761	619
	Cγ	415	384	413	388	378	373	401	388	320	463
	Hβ2	-3	-2	-2	2	-3	-3	-5	-4	-9	-6
	Hβ1	-16	-17	-9	-15	-15	-17	-16	-18	-21	-14
	Hδ2	38	34	34	37	32	32	33	37	30	36
	Hε1	43	45	43	42	44	42	49	41	44	43
	Hε2	63	59	55	62	58	58	58	64	58	58
	Nδ1	14875	13907	13638	14699	14040	13759	13498	15163	12993	14684
	Nε2	954	934	951	972	931	934	920	968	904	932
His71	Cβ	154	163	141	160	151	141	160	162	134	141
	Cδ2	544	521	526	536	504	527	504	545	529	522
	Cε1	652	598	597	610	645	613	613	620	642	625
	Cγ	612	668	724	572	691	692	639	636	656	693
	Hβ2	-15	-14	-5	-14	-12	-6	-16	-13	-13	-6
	Hβ1	-3	-1	0	-1	-3	-1	-2	-2	-3	-1
	Hδ2	44	45	46	42	45	45	43	44	45	45
	Hε1	78	71	77	74	74	73	66	81	68	79
	Hε2	53	50	44	54	46	45	49	53	47	44
	Nδ1	13571	12860	12795	13352	12647	12830	12800	13437	13155	12847
	Nε2	968	937	969	942	970	969	934	960	980	972
His80	Cβ	123	81	108	122	92	104	73	131	77	160
	Cδ2	434	412	400	408	409	399	406	427	390	446
	Cε1	932	931	946	926	933	938	896	943	869	971
	Cγ	566	740	708	645	730	714	747	618	794	638
	Hβ2	-1	7	0	-3	5	2	8	-4	14	-11
	Hβ1	4	5	4	4	4	5	6	2	10	-2
	Hδ2	45	47	47	46	48	47	46	45	49	45
	Hε1	73	78	85	78	82	83	73	77	85	80
	Hε2	48	37	39	43	39	37	35	47	30	50
	Nδ1	11332	9663	9838	10454	9949	9742	9500	10925	9888	11280
	Nε2	1031	1048	1057	1025	1053	1041	1030	1028	1029	1055
Asp83	Cα	191	170	163	180	157	174	158	180	170	163
	Cβ	100	369	299	189	340	299	378	135	410	163
	Cγ	-35	72	14	-9	37	23	51	-16	147	16
	Hα	6	7	8	8	8	8	6	8	7	8
	Hβ1	34	23	25	26	20	26	13	31	24	31
	Hβ2	17	24	25	22	27	24	35	20	24	20

Table 18. Calculated chemical shifts with PBE0 hyperfine coupling.

.

Appendix 7. Resonance assignments

Cu^{II},Co^{II}-SOD

Assignment for [U-$^{1}H^{N}$, ^{2}H, ^{13}C, ^{15}N] labeled microcrystalline Cu^{II},Co^{II}-SOD. All shifts are in ppm with respect to TMS.

Residue		$^{1}H^{N}$	$^{15}N^{H}$	^{13}CO	$^{13}C^{\alpha}$	$^{13}C^{\beta}$
ALA	1					
THR	2					
LYS	3			172.1		
ALA	4	9.1	122.9		47.6	20.2
VAL	5	9.5	121.2	168.1	56.5	29.0
ALA	6	9.2	125.8	170.3	47.6	20.0
VAL	7	9.0	123.7	172.6	58.4	28.0
LEU	8	8.9	126.4	173.1	51.0	38.7
LYS	9	8.4	121.4	172.3	51.7	33.4
GLY	10	8.8	111.4	170.4	42.3	
ASP	11	8.7	121.1	173.7	51.3	37.4
GLY	12	8.0	110.0	171.0	41.5	
PRO	13			173.7	60.6	
VAL	14	7.4	120.3	173.1	60.0	26.8
GLN	15	8.0	122.9	171.6	50.7	28.7
GLY	16	8.2	107.2	168.1	43.4	
ILE	17	7.9	120.4	173.2	58.1	37.7
ILE	18	8.6	125.3	169.3	53.4	34.3
ASN	19	8.7	123.5	169.3	49.1	37.6
PHE	20	8.4	114.3	173.4	51.9	39.8
GLU	21	9.6	121.7	170.7	52.7	31.7
GLN	22	9.3	130.4	171.4	50.8	28.7
LYS	23	9.0	128.4		56.1	
GLU	24					
SER	25					
ASN	26					
GLY	27	7.7	107.9		40.9	
PRO	28			173.8	60.0	
VAL	29	9.0	121.3	172.8	57.7	29.7
LYS	30	9.3	127.7	172.5	52.3	41.3
VAL	31	9.4	126.0	172.6	57.4	29.5
TRP	32	9.0	125.5	170.4	53.1	29.3
GLY	33	8.4	107.9	168.5	41.6	
SER	34	7.9	114.4	170.0	53.8	62.4
ILE	35	8.5	123.3	170.1	56.7	39.7
LYS	36	9.1	124.0	172.7	51.3	31.5

GLY	37	8.2	106.2	171.4	42.4	
LEU	38	8.2	120.6	174.5	50.2	40.5
THR	39	8.4	110.6	173.3	58.2	66.5
GLU	40	8.7	126.0	173.2	54.2	26.6
GLY	41	8.8	113.7	170.6	40.4	
LEU	42	8.3	120.7	174.6	52.3	40.8
HIS	43	8.7	114.5	171.9	50.8	28.3
GLY	44	8.4	108.5	167.7	42.9	
PHE	45	8.3	128.4		53.2	38.1
HIS	46					
VAL	47	9.2	120.5		58.4	36.0
HIS	48	10.2	128.6	173.5	52.9	61.8
GLU	49					
PHE	50	8.8	111.9	176.1	53.0	36.2
GLY	51	10.1	120.6	168.9	43.0	
ASP	52	6.1	115.5		49.0	39.0
ASN	53	9.0	127.5	174.5	48.6	36.5
THR	54	9.2	117.1		63.4	66.1
ALA	55	8.4	126.7	174.8	46.6	14.3
GLY	56	7.3	108.2	172.1	42.7	
CYS	57	8.5	120.8	175.5	55.6	
THR	58	8.5	119.5	173.1	63.4	65.6
SER	59	7.5	112.0	171.3	55.4	58.8
ALA	60	7.1	119.6	174.4	50.2	15.6
GLY	61	8.0	102.3		43.1	
PRO	62					
HIS	63					
PHE	64					
ASN	65					
PRO	66			174.6		
LEU	67	7.7	116.8	170.4	51.1	36.9
SER	68	7.3	111.0		55.2	60.5
ARG	69					
LYS	70					
HIS	71					
GLY	72					
GLY	73	8.3	107.4		43.4	
PRO	74			177.5		
LYS	75	9.2	115.4	174.0	51.9	28.2
ASP	76	7.4	120.8		59.7	
GLU	77	9.0	120.1		60.0	
GLU	78					
ARG	79	7.2	118.9		50.9	
HIS	80	8.3	118.2			
VAL	81					
GLY	82					

ASP	83					
LEU	84					
GLY	85	8.9	109.4	168.6	43.1	
ASN	86	8.0	118.8	174.4	49.7	41.5
VAL	87	8.8	112.6	171.9	56.2	28.7
THR	88	8.6	117.6	170.7	58.5	66.8
ALA	89	9.3	129.0	174.7	46.5	17.6
ASP	90	8.4	124.7	173.5	49.3	
LYS	91	8.1	115.1	172.9	51.1	28.6
ASP	92	8.3	120.4	173.6	51.8	
GLY	93	8.5	111.1	170.1	43.5	
VAL	94	7.9	119.1	173.8	58.6	37.7
ALA	95	9.7	131.1		47.0	16.7
ASP	96	8.5	125.4	173.4	58.7	29.0
VAL	97	8.8	126.0	173.8	58.9	34.2
SER	98	8.7	123.2	172.6	54.9	59.6
ILE	99	9.5	126.2		57.1	40.6
GLU	100	8.6	124.1		52.1	29.3
ASP	101	9.4	126.1	171.8	51.3	44.2
SER	102	9.0	118.6		55.2	61.0
VAL	103	8.1	123.6	176.1	61.8	28.8
ILE	104	7.9	111.2	169.4	60.0	36.3
SER	105	6.7	107.8		52.0	62.3
LEU	106	9.1	123.4	172.2	51.1	28.1
SER	107	8.1	110.5	171.1	54.5	62.3
GLY	108	8.6	105.9	175.4	42.4	
ASP	109					
HIS	110	9.2	117.4	170.5	50.0	
SER	111	7.1	110.4	174.4	54.5	60.6
ILE	112	7.7	117.0	171.6	57.4	32.8
ILE	113	7.5	121.5	174.1	58.4	31.4
GLY	114	9.6	113.0	169.9	42.1	
ARG	115	7.3	118.5	171.5	51.5	23.3
THR	116	7.0	112.6	170.7	59.3	67.8
LEU	117	8.8	129.8	171.6	50.7	40.0
VAL	118	9.8	125.9		57.7	31.9
VAL	119	7.7	121.1	170.8	55.0	31.0
HIS	120	8.5	125.2		53.5	56.2
GLU	121	8.9	122.5	172.7	55.8	37.8
LYS	122	8.4	115.3	172.0	50.4	31.5
ALA	123	7.7	121.5	173.3	48.9	16.4
ASP	124	10.0	121.5	175.0	49.2	41.4
ASP	125	10.2	129.9	175.8	51.1	35.6
LEU	126	10.6	117.2		52.4	34.3
GLY	127	8.6	107.7	174.0	42.5	
LYS	128	7.0	118.3	174.7	51.3	28.1

GLY	129	8.6	108.5	174.5	42.2	
GLY	130	9.0	106.2		42.5	
ASN	131	7.1	112.3		41.7	37.0
GLU	132	8.2	120.4	172.0	52.0	
GLU	133	8.9	118.3	173.5	55.0	
SER	134	7.8	114.6	172.9	58.0	60.1
THR	135	6.3	101.6		57.9	65.5
LYS	136					
THR	137					
GLY	138			171.6		
ASN	139	7.8	108.2	172.0	53.3	
ALA	140	7.1	114.9	172.7	50.9	16.7
GLY	141	9.0	106.4	174.4	42.8	
SER	142	9.3	119.2		56.3	60.6
ARG	143	8.9	122.2		51.2	
LEU	144	7.8	122.4	174.7	53.2	39.2
ALA	145	7.2	113.7	172.1	48.0	17.7
CYS	146	9.0	111.8	170.3	51.3	29.0
GLY	147	8.1	107.0	168.2	42.8	
VAL	148	8.4	124.5	172.5	59.5	28.5
ILE	149	8.5	127.5	172.3	59.3	33.5
GLY	150	9.3	116.8	170.6	40.1	
ILE	151	9.0	120.4	172.6	60.1	35.7
ALA	152	8.2	130.0	171.7	46.8	18.4
GLN	153					

***Eh*HiPIP I**

Assignment for [U-^{13}C, ^{15}N] labeled microcrystalline oxidized *Eh*HiPIP I. All shifts are in ppm with respect to TMS. Shifts for the two different diastereoisomers of the same nucleus are in two different lines. Shifts for the same spin in two different conformers are divided by a slashed bar.

Residue		H^N	N^H	H^α	C^α	H^β	C^β	H^γ	C^γ	H^δ	C^δ
ALA	1										
SER	2										
GLU	3										
PRO	4		126.0	4.5	62.1	1.6	32.9	2.0	27.4	3.6	50.2
						2.4		2.0		4.0	
ARG	5	8.4	119.7	4.0	56.3						
ALA	6	9.5	127.2	3.9	53.3	1.3	19.7				
GLU	7	8.8	120.9	4.7	54.0	1.9	31.4				
						1.9					
ASP	8	9.0	123.0	4.7	56.3	2.3	38.9				
						2.7					
GLY	9	10.4/10.6	111.8/112.4	4.5	45.1/45.7						
				4.5							
HIS	10	8.5	121.0	3.9	61.8	2.7	31.4				
						2.7					
ALA	11	7.1	110.8	4.2	51.5		22.1				
HIS	12	9.3/9.9	116.0/116.7	4.4	56.3	0.9	39.3/39.4				
ASP	13	9.3	112.9	4.6	55.6		39.3				
TYR	14	8.0	114.9	4.9	59.6	2.8	40.7				
						4.3					
VAL	15	8.6	124.5	4.3	58.5	2.3	34.6	0.9	24.1		
								0.8	20.8		
ASN	16	8.9	118.5	4.6	55.4		43.6				
GLU	17	8.3	118.2	4.4	54.5	1.7	30.0				
						2.0					
ALA	18	8.7	128.3	3.8	56.7	1.5	19.5				
ALA	19	8.4	114.8	3.8	54.7	1.4	18.5				
ASP	20	8.2	117.6	4.4	56.7		39.5				
ALA	21	8.2	123.5	4.4	51.4	0.9	20.4				
SER	22	6.8	111.2	2.9	60.4		63.1				
GLY	23	8.3	113.6	3.4	44.4						
				4.5							
HIS	24	8.8	128.1	4.5	57.0	3.1	31.4				
						3.3					
PRO	25		142.2	4.5	65.1	2.5	32.5	2.0	27.6	3.0	51.7
						2.1		2.0		3.9	

ARG	26	11.4/10.8	119.0/119.2	4.5/4.7	56.5/56.0	2.7/2.6	39.3/39.4			
						2.7/2.6				
TYR	27	8.0/8.1	120.9/121.3	3.9/4.1	60.2/59.9	1.8/1.8	38.8/39.4			
						2.5/2.6				
GLN	28	5.9/6.0	124.8/125.6	4.0	54.1/53.6		31.6/31.0			
GLU	29	8.3	122.8	3.6	58.2		29.3			
GLY	30	8.2	115.1	3.4	44.7					
				4.5						
GLN	31	7.5	120.7	4.0	56.7		27.9			
LEU	32	8.7	122.5	5.7	53.5	1.4	48.7	1.0	20.0	
						1.4				
CYS	33	9.7	127.8	3.9	53.0					
GLU	34									
ASN	35									
CYS	36									
ALA	37	8.8/7.5	156.2/156.4	5.0/4.1	54.0/59.9		18.8/19.0			
PHE	38									
TRP	39									
GLY	40	9.1	118.0		44.7					
GLU	41	7.3	117.9	4.1	59.7					
ALA	42	8.6	126.3	4.1	55.1	1.0	19.3			
VAL	43									
GLN	44	7.7	115.1	4.4	56.0					
ASP	45	9.7	124.7	3.9	56.1					
GLY	46	9.4	105.0	3.9	47.6					
				4.2						
TRP	47	8.3	121.9	4.0	56.1		33.5			
GLY	48	10.0	107.5	3.9	45.1					
				4.3						
ARG	49									
CYS	50									
THR	51	11.1	148.3	5.0/4.5	62.9/62.7	5.2	69.7/69.5	1.4	21.3	
HIS	52	9.4	122.7	5.5	56.6	3.3	31.4			
						3.3				
PRO	53									
ASP	54									
PHE	55	7.4	115.3	4.7	53.4	2.4	38.7			
						3.1				
ASP	56									
GLU	57									
VAL	58	7.1	107.4	5.0	58.7	1.9	35.9	0.6	22.7	
								0.1	17.8	
LEU	59	8.6	118.8	4.9	53.5	1.7	44.1	0.6	26.1	0.5 22.6
						1.7				1.0 23.9
VAL	60	9.1	112.4	5.5	60.0		33.8			
LYS	61	8.5	125.8	3.7	54.0	2.0	32.6	2.0	27.7	1.7 34.0

						2.0		2.0	2.2
ALA	62	8.9	126.3	3.8	55.6	1.5	19.5		
GLU	63	7.4	110.1	4.7	56.0				
GLY	64	8.0/8.1	108.6/109.5	3.62/3.67	43.1				
TRP	65	8.7	116.4	3.8	70.8				
CYS	66								
SER	67	8.9	117.8	3.7	59.6	3.2	63.6		
						4.2			
VAL	68								
TYR	69								
ALA	70								
PRO	71								
ALA	72	8.6	126.2	4.1	51.3	1.1	19.2		
SER	73								
GLY	89	10.6	112.4		45.7				
HIS	92	9.9	116.7	4.4	56.3		39.4		
ARG	106	10.8	119.2	4.7	56.0	2.6	39.4		
						2.6			
TYR	107	8.1	121.3	4.1	59.9	1.8	39.2		
						2.6			
GLN	108	6.0	125.6	4.0	53.6		31.0		
ALA	117	7.5	107.5	5.1	53.6		19.0		
THR	131			4.5	62.7	4.9	69.5		
GLY	144	8.1	109.5		43.5				

Appendix 8. References

(1) Zhang, Z.; Miao, Y.; Liu, X.; Yang, J.; Li, C.; Deng, F.; Fu, R., Dual-band selective double cross polarization for heteronuclear polarization transfer between dilute spins in solid-state MAS NMR. *J. Magn. Reson.* **2012,** *217*, 92-99.

(2) Shaka, A. J.; Keeler, J.; Frenkiel, T.; Freeman, R., An improved sequence for Broad-Band Decoupling - Waltz-16. *J. Magn. Reson.* **1983,** *52*, 335-338.

(3) Lewandowski, J. R.; Sein, J.; Blackledge, M.; Emsley, L., Anisotropic collective motion contributes to nuclear spin relaxation in crystalline proteins. *J. Am. Chem. Soc.* **2010,** *132*, 1246-1248.

(4) Zhou, D. H.; Rienstra, C. M., High-performance solvent suppression for proton detected solid-state NMR. *J. Magn. Reson.* **2008,** *192*, 167-72.

(5) Emsley, L.; Bodenhausen, G., Gaussian Pulse Cascades: New analytical functions for rectangular selective inversion and in-phase excitation in NMR. *Chem. Phys. Lett.* **1990,** *165*, 469-476.

(6) Igumenova, T. I.; Wand, A. J.; McDermott, A. E., Assignment of the backbone resonances for microcrystalline ubiquitin. *J. Am. Chem. Soc.* **2004,** *126*, 5323-5331.

(7) Bertini, I.; Engelke, F.; Gonnelli, L.; Knott, B.; Luchinat, C.; Osen, D.; Ravera, E., On the use of ultracentrifugal devices for sedimented solute NMR. *J. Biomol. NMR* **2012,** *54*, 123-127.

(8) Knight, M. J.; Webber, A. L.; Pell, A. J.; Guerry, P.; Barbet-Massin, E.; Bertini, I.; Felli, I. C.; Gonnelli, L.; Pierattelli, R.; Emsley, L.; Lesage, A.; Herrmann, T.; Pintacuda, G., Fast resonance assignment and fold determination of human superoxide dismutase by high-resolution proton-detected solid-state MAS NMR spectroscopy. *Angew. Chem. Int. Ed. Engl.* **2011,** *50*, 11697-11701.

(9) Knight, M. J.; Felli, I. C.; Pierattelli, R.; Bertini, I.; Emsley, L.; Herrmann, T.; Pintacuda, G., Rapid measurement of pseudocontact shifts in metalloproteins by proton-detected solid-state NMR spectroscopy. *J. Am. Chem. Soc.* **2012,** *134*, 14730-14733.

(10) Barbet-Massin, E.; Pell, A. J.; Retel, J. S.; Andreas, L. B.; Jaudzems, K.; Franks, W. T.; Nieuwkoop, A. J.; Hiller, M.; Higman, V.; Guerry, P.; Bertarello, A.; Knight, M. J.; Felletti, M.; Le Marchand, T.; Kotelovica, S.; Akopjana, I.; Tars, K.; Stoppini, M.; Bellotti, V.; Bolognesi, M.; Ricagno, S.; Chou, J. J.; Griffin, R. G.; Oschkinat, H.; Lesage, A.; Emsley, L.; Herrmann, T.; Pintacuda, G., Rapid proton-detected NMR assignment for proteins with fast magic angle spinning. *J. Am. Chem. Soc.* **2014,** *136*, 12489-12497.

(11) Andreas, L. B.; Jaudzems, K.; Stanek, J.; Lalli, D.; Bertarello, A.; Le Marchand, T.; Cala-De Paepe, D.; Kotelovica, S.; Akopjana, I.; Knott, B.; Wegner, S.; Engelke, F.; Lesage, A.; Emsley, L.; Tars, K.; Herrmann, T.; Pintacuda, G., Structure of fully protonated proteins by proton-detected magic-angle spinning NMR. *Proc. Natl. Acad. Sci. U.S.A.* **2016,** *113*, 9187-9192.

(12) Kervern, G.; Steuernagel, S.; Engelke, F.; Pintacuda, G.; Emsley, L., Absence of Curie relaxation in paramagnetic solids yields long H-1 coherence lifetimes. *J. Am. Chem. Soc.* **2007,** *129*, 14118-14119.

(13) Kervern, G.; Pintacuda, G.; Emsley, L., Fast adiabatic pulses for solid-state nmr of paramagnetic systems. *Chem. Phys. Lett.* **2007,** *435*, 157-162.

(14) Griffiths, J. M.; Griffin, R. G., Nuclear magnetic resonance methods for measuring dipolar couplings in rotating solids. *Anal. Chim. Acta* **1993,** *283*, 1081-1101.

(15) Zhang, R.; Nishiyama, Y.; Sun, P.; Ramamoorthy, A., Phase cycling schemes for finite-pulse-RFDR MAS solid state NMR experiments. *J. Magn. Reson.* **2015,** *252*, 55-66.
(16) Holl, S. M.; Marshall, G. R.; Beusen, D. D.; Kociolek, K.; Redlinski, A. S.; Leplawy, M. T.; McKay, R. A.; Vega, S.; Schaefer, J., Determination of an 8-Angstrom interatomic distance in a helical peptide by solid-state NMR-spectroscopy. *J. Am. Chem. Soc.* **1992,** *114*, 4830-4833.
(17) Saalwachter, K.; Graf, R.; Demco, D. E.; Spiess, H. W., Heteronuclear double-quantum MAS NMR spectroscopy in dipolar solids. *J. Magn. Reson.* **1999,** *139*, 287-301.
(18) Clement, R. J.; Pell, A. J.; Middlemiss, D. S.; Strobridge, F. C.; Miller, J. K.; Whittingham, M. S.; Emsley, L.; Grey, C. P.; Pintacuda, G., Spin-transfer pathways in paramagnetic lithium transition-metal phosphates from combined broadband isotropic solid-state MAS NMR spectroscopy and DFT calculations. *J. Am. Chem. Soc.* **2012,** *134*, 17178-17185.
(19) Massiot, D.; Fayon, F.; Capron, M.; King, I.; Le Calvé, S.; Alonso, B.; Durand, J.-O.; Bujoli, B.; Gan, Z.; Hoatson, G., Modelling one- and two-dimensional solid-state NMR spectra. *Magn. Reson. Chem.* **2002,** *40*, 70-76.
(20) Parge, H. E.; Hallewell, R. A.; Tainer, J. A., Atomic structures of wild-type and thermostable mutant recombinant human Cu,Zn superoxide dismutase. *Proc. Natl. Acad. Sci. U.S.A.* **1992,** *89*, 6109-6113.
(21) Word, J. M.; Lovell, S. C.; Richardson, J. S.; Richardson, D. C., Asparagine and glutamine: using hydrogen atom contacts in the choice of side-chain amide orientation. *J. Mol. Biol.* **1999,** *285*, 1735-1747.
(22) Perdew, J. P.; Burke, K.; Ernzerhof, M., Generalized Gradient Approximation Made Simple. *PBE1PBE* **1996,** *77*, 3865-3868.
(23) Perdew, J. P.; Ernzerhof, M.; Burke, K., Rationale for mixing exact exchange with density functional approximations. *J. Chem. Phys.* **1996,** *105*, 9982-9985.
(24) Grimme, S.; Antony, J.; Ehrlich, S.; Krieg, H., A consistent and accurate ab initio parametrization of density functional dispersion correction (DFT-D) for the 94 elements H-Pu. *J. Chem. Phys.* **2010,** *132*, 154104.
(25) Grimme, S.; Ehrlich, S.; Goerigk, L., Effect of the Damping Function in Dispersion Corrected Density Functional Theory. *J. Comput. Chem.* **2011,** *32*, 1456-1465.
(26) Ahlrichs, R.; Armbruster, M. K.; Bachorz, R. A.; Bär, M.; Baron, H.-P.; Bauernschmitt, R.; Bischoff, F. A.; Böcker, S.; Crawford, N.; Deglmann, P.; Della Sala, F.; Diedenhofen, M.; Ehrig, M.; Eichkorn, K.; Elliot, S.; Furche, F.; Glöß, A.; Haase, F.; Häser, M.; Hättig, C.; Hellweg, A.; Höfener, S.; Horn, H.; Huber, C.; Huniar, U.; Kattannek, M.; Klopper, W.; Köhn, A.; Kölmel, C.; Kollwitz, M.; May, K.; Nava, P.; Ochsenfeld, C.; Öhm, H.; Pabst, M.; Patzelt, H.; Rappoport, D.; Rubner, O.; Schäfer, A.; Schneider, U.; Sierka, M.; Tew, D. P.; Treutler, O.; Unterreiner, B.; von Arnim, M.; Weigend, F.; Weis, P.; Weiss, H.; Winter, N. *Turbomole, version 6.3.1, a development of University of Karlsruhe and Forschungszentrum Karlsruhe GmbH, 1989-2007, TURBOMOLE GmbH, since 2007.*, Turbomole 6.3.1; TURBOMOLE GmbH: 2011.
(27) Klamt, A.; Schuurmann, G., COSMO: A New Approach to Dielectric Screening in Solvent with Explicit Expression for the Screening Energy and its Gradient. *J. Chem. Soc., Perkin Trans. 2* **1993,** 799-805.
(28) Weigend, F.; Ahlrichs, R., Balanced basis sets of split valence, triple zeta valence and quadruple zeta valence quality for H to Rn: Design and assessment of accuracy. *Phys. Chem. Chem. Phys.* **2005,** *7*, 3297-3305.

(29) Kurland, R. J.; McGarvey, B. R., Isotropic NMR shifts in transition metal complexes: The calculation of the fermi contact and pseudocontact terms. *J. Magn. Reson.* **1970,** *2*, 286-301.
(30) Vaara, J.; Rouf, S. A.; Mareš, J., Magnetic couplings in the chemical shift of paramagnetic NMR. *J. Chem. Theory Comput.* **2015,** *11*, 4840-4849.
(31) Angeli, C.; Borini, S.; Cestari, M.; Cimiraglia, R., A quasidegenerate formulation of the second order n-electron valence state perturbation theory approach. *J. Chem. Phys.* **2004,** *121*, 4043-4049.
(32) Roos, B. O.; Taylor, P. R.; Siegbahn, P. E. M., A complete active space SCF method (CASSCF) using a density matrix formulated super-CI approach. *Chem. Phys.* **1980,** *48*, 157-173.
(33) Malmqvist, P.-Å.; Roos, B. O., The CASSCF state interaction method. *Chem. Phys. Lett.* **1989,** *155*, 189-194.
(34) Neese, F., The ORCA program system. *Wiley Interdiscip. Rev. Comput. Mol. Sci.* **2012,** *2*, 73-78.
(35) Maganas, D.; Sottini, S.; Kyritsis, P.; Groenen, E. J. J.; Neese, F., Theoretical analysis of the spin hamiltonian parameters in Co(ii)S4 complexes, using density functional theory and correlated *ab initio* methods. *Inorg. Chem.* **2011,** *50*, 8741-8754.
(36) Ganyushin, D.; Neese, F., First-principles calculations of zero-field splitting parameters. *J. Chem. Phys.* **2006,** *125*, 024103.
(37) Neese, F., Configuration interaction calculation of electronic g tensors in transition metal complexes*. *Int. J. Quantum Chem* **2001,** *83*, 104-114.
(38) Heß, B. A.; Marian, C. M.; Wahlgren, U.; Gropen, O., A mean-field spin-orbit method applicable to correlated wavefunctions. *Chem. Phys. Lett.* **1996,** *251*, 365-371.
(39) Neese, F., Efficient and accurate approximations to the molecular spin-orbit coupling operator and their use in molecular g-tensor calculations. *J. Chem. Phys.* **2005,** *122*, 034107.
(40) Rappoport, D.; Furche, F., Property-optimized Gaussian basis sets for molecular response calculations. *J. Chem. Phys.* **2010,** *133*, 134105.
(41) Kutzelnigg, W.; Fleischer, U.; Schindler, M., Deuterium and shift calculation. In *NMR - Basic Principles and Progress*, Springer: Heidelberg, 1990; Vol. 23, pp 165-262.
(42) Wolinski, K.; Hinton, J. F.; Pulay, P., Efficient implementation of the gauge-independent atomic orbital method for nmr chemical-shift calculations. *J. Am. Chem. Soc.* **1990,** *112*, 8251-8260.
(43) Frisch, M. J.; Trucks, G. W.; Schlegel, H. B.; Scuseria, G. E.; Robb, M. A.; Cheeseman, J. R.; Scalmani, G.; Barone, V.; Mennucci, B.; Petersson, G. A.; Nakatsuji, H.; Caricato, M.; Li, X.; Hratchian, H. P.; Izmaylov, A. F.; Bloino, J.; Zheng, G.; Sonnenberg, J. L.; Hada, M.; Ehara, M.; Toyota, K.; Fukuda, R.; Hasegawa, J.; Ishida, M.; Nakajima, T.; Honda, Y.; Kitao, O.; Nakai, H.; Vreven, T.; Montgomery Jr., J. A.; Peralta, J. E.; Ogliaro, F.; Bearpark, M. J.; Heyd, J.; Brothers, E. N.; Kudin, K. N.; Staroverov, V. N.; Kobayashi, R.; Normand, J.; Raghavachari, K.; Rendell, A. P.; Burant, J. C.; Iyengar, S. S.; Tomasi, J.; Cossi, M.; Rega, N.; Millam, N. J.; Klene, M.; Knox, J. E.; Cross, J. B.; Bakken, V.; Adamo, C.; Jaramillo, J.; Gomperts, R.; Stratmann, R. E.; Yazyev, O.; Austin, A. J.; Cammi, R.; Pomelli, C.; Ochterski, J. W.; Martin, R. L.; Morokuma, K.; Zakrzewski, V. G.; Voth, G. A.; Salvador, P.; Dannenberg, J. J.; Dapprich, S.; Daniels, A. D.; Farkas, Ö.; Foresman, J. B.; Ortiz, J. V.; Cioslowski, J.; Fox, D. J. *Gaussian 09, revision D.01*, Gaussian, Inc.: Wallingford, CT, USA, 2009.

(44) Harris, R. K.; Becker, E. D.; Cabral De Menezes, S. M.; Granger, P.; Hoffman, R. E.; Zilm, K. W., Further conventions for NMR shielding and chemical shifts IUPAC recommendations 2008. *Solid State Nucl. Magn. Reson.* **2008,** *33*, 41-56.

Publications

Peer-reviewed articles

A. Bertarello, L. Benda, K.J. Sanders, A. J. Pell, V. Pelmenschikov, I. C. Felli, M. Kaupp, L. Emsley, R. Pierattelli, G. Pintacuda, "Paramagnetic NMR crystallography: Theory and experiment meet at the catalytic center of a metalloprotein", *manuscript in preparation*.

K. Jaudzems, **A. Bertarello**, S. R. Chaudari, A. Pica, E. Barbet-Massin, A. J. Pell, I. Akopjana, S. Kotelovica, D. Gajan, O. Ouari, K. Tars, G. Pintacuda, A. Lesage, "Dynamic nuclear polarization enhanced biomolecular NMR spectroscopy at high magnetic field with fast magic-angle spinning", *Angew. Chem. Int. Ed., under revision*.

A. Bertarello, T. Schubeis, C. Fuccio, E. Ravera, M. Fragai, G. Parigi, L. Emsley, G. Pintacuda, C. Luchinat, "Paramagnetic properties of a crystalline iron−sulfur protein by magic-angle spinning NMR spectroscopy", *Inorg. Chem*. **2017**, 56, 6624-6629.

J. Stanek, L. B. Andreas, K. Jaudzems, D. Cala, D. Lalli, **A. Bertarello**, T. Schubeis, I. Akopjana, S. Kotelovica, K. Tars, A. Pica, S. Leone, D. Picone, Z.-Q. Xu, N. E. Dixon, D. Martinez, M. Berbon, N. El Mammeri, A. Noubhani, S. Saupe, B. Habenstein, A. Loquet, G. Pintacuda, "Backbone and side-chain proton NMR assignment in fully protonated proteins: microcrystals, sedimented assemblies, and amyloid fibrils", *Angew. Chem. Int. Ed.* **2016**, 55, 1-6; *Angew. Chem*. **2016**, 128, 15730-15735.

L. Andreas, K. Jaudzems, J. Stanek, D. Lalli, **A. Bertarello**, T. Le Marchand, D. Cala-De Paepe, S. Kotelovica, I. Akopjana, B. Knott, S. Wegner, F. Engelke, A. Lesage, L. Emsley, K. Tars, T. Herrmann, G. Pintacuda, "Structure of fully protonated proteins by proton-detected magic-angle spinning NMR", *Proc. Natl. Acad. Sci. U.S.A.* **2016**, 113, 9187-9192.

R. Gupta, M. Lu, G. Hou, M. Caporini, M. Rosay, W. Maas, J. Struppe, C. Suiter, J. Ahn, I.-J. Byeon, W. T. Franks, M. Orwick-Rydmark, **A. Bertarello**, H. Oschkinat, A. Lesage, G. Pintacuda, A. Gronenborn and T. Polenova, "Dynamic Nuclear Polarization Enhanced MAS NMR for Structural Analysis of HIV-1 Protein Assemblies", *J. Phys. Chem. B* **2016**, 120, 329-339.

L. B. Andreas, J. Stanek, T. Le Marchand, **A. Bertarello**, D. Cala-De Paepe, D. Lalli, M. Krejcikova, C. Doyen, C. Oester, B. Knott, S. Wegner, F. Engelke, I. C. Felli, R. Pierattelli, N. E. Dixon, L. Emsley, T. Herrmann, and G. Pintacuda, "Protein residue linking in a single spectrum for magic-angle spinning NMR assignment", *J. Biomol. NMR* **2015**, 62, 253-261.

E. Barbet-Massin, A. J. Pell, J. S. Retel, L. B. Andreas, K. Jaudzems, W. T. Franks, A. J. Nieuwkoop, M. Hiller, V. Higman, P. Guerry, **A. Bertarello**, M. J. Knight, M. Felletti, T. Le Marchand, S. Kotelovica, I. Akopjana, K. Tars, M. Stoppini, V. Bellotti, M. Bolognesi, S. Ricagno, J. J. Chou, R. G. Griffin, H. Oschkinat, A. Lesage, L. Emsley, T. Herrmann and G. Pintacuda "Rapid proton-detected NMR assignment for proteins with fast magic angle spinning", *J. Am. Chem. Soc*. **2014**, 136, 12489-12497.

Book chapters

A. Bertarello, G. Pintacuda, "Paramagnetism in the solid state", in "Paramagnetism in experimental biomolecular NMR", E. Ravera, G. Parigi and C. Luchinat eds, the Royal Society of Chemistry, Cambridge, 2018.

Oral communications at international conferences

A. Bertarello, L. Benda, K. J. Sanders, H. R. W. Dannatt, A. J. Pell, S. Wegner, F. Engelke, V. Pelmenschikov, M. Kaupp, L. Gonnelli, I. C. Felli, R. Pierattelli, G. Pintacuda, "Paramagnetic metalloproteins and fast-magic angle spinning", *Europe meets Italy with paramagnetic NMR*, Venice (Italy), 27 September – 30 September 2016.

A. Bertarello, L. Benda, K. Sanders, D. Lalli, A. J. Pell, H. R. W. Dannatt, L. Gonnelli, I. C. Felli, R. Pierattelli, L. Emsley, S. Wegner, F. Engelke, V. Pelmenschikov, M. Kaupp, G. Pintacuda, "Paramagnetic metalloproteins and fast magic-angle spinning: theory and experiments meet at the metal center", *Chianti Workshop – Magnetic Resonance for Cellular Structural Biology*, Grosseto (Italy), 5 June -10 June 2016.

A. Bertarello, K. J. Sanders, D. Lalli, A. Pell, H. Dannatt, I. Felli, L. Gonnelli, R. Pierattelli, B. Knott, S. Wegner, F. Engelke, L. Emsley, G. Pintacuda, "Paramagnetic metalloproteins with MAS over 100 kHz: NMR finally gets to the metal center", *9th Alpine Conference on Solid-State NMR*, Chamonix (France), 13 September – 17 September 2015.

A. Bertarello, K. J. Sanders, D. Lalli, A. J. Pell, H. R. W. Dannatt, L. Gonnelli, I. C. Felli, R. Pierattelli, G. Pintacuda, "Dynamics and reactivity at the core of a paramagnetic metalloprotein", *pNMR : from rags to riches,* Prague (Czech Republic), 4 July – 5 July 2015.

Poster presentations at international conferences

20th ISMAR meeting, Québec (Canada), 23 July – 28 July 2017

NMR: a tool for structural biology Xth, Paris (France), 30 January - 1 February 2017.

1ère Journée Grand-Sud de RMN, Montpellier (France), 30 May – 31 May 2016.

EUROMAR 2015, Prague (Czech Republic), 5 July – 10 July 2015.

XVI^{e} Journée Rhône-Alpes de RMN, Marseille (France), 12 June 2015.

4th Annual User group Meeting of Bio-NMR, Warsaw (Poland), 5 May – 9 May 2014.